UNIVERSITÉ de Liège

Faculté des Sciences **Département d'Astrophysique, Géophysique et Océanographie**

Astrophysical studies of extrasolar planetary systems using infrared interferometric techniques

THÈSE

présentée pour l'obtention du diplôme de

Docteur en Sciences

par

Olivier Absil

Soutenue publiquement le 17 mars 2006 devant le Jury composé de :

Président :	Pr. Jean-Pierre Swings
Directeur de thèse :	Pr. Jean Surdej
Examinateurs :	Dr. Vincent Coudé du Foresto
	Dr. Philippe Gondoin
	Pr. Jacques Henrard
	Pr. Claude Jamar
	Dr. Fabien Malbet

Institut d'Astrophysique et de Géophysique de Liège

Mis en page avec la classe thloria.

Acknowledgments

First and foremost, I want to express my deepest gratitude to my advisor, Professor Jean Surdej. I am forever indebted to him for striking my interest in interferometry back in my undergraduate student years; for introducing me to the world of scientific research and fostering so many international collaborations; for helping me put this work in perspective when I needed it most; and for guiding my steps, from the supervision of diploma thesis to the conclusion of my PhD studies. Thank you Jean, from the bottom of my heart!

My utmost gratitude also goes to Dr Vincent Coudé du Foresto for introducing me to the practical aspects and applications of stellar interferometry. Vincent's spirit is present throughout this work. I am grateful to him for having kindly hosted me in Meudon and granted me privileged access to the FLUOR instrument.

I am indebted to Dr Philippe Gondoin for giving me the opportunity to work on the GENIE project from its very beginning. Since that time and throughout the past four years, Philippe has continually encouraged and advised me, while giving me free rein to work on my favourite topics.

I am grateful to Professors Jean-Pierre Swings, Jacques Henrard, Claude Jamar and to Dr Fabien Malbet, members of my thesis committee, for accepting to read and evaluate my work.

This work would not have been possible without the help of Roland den Hartog, my comrade in arms on the GENIE and Darwin projects, who has become much more than a colleague over the past four years. I thank him for his incomparable support in developing GENIEsim, for the inordinate amount of time he has spent answering my emails and for his valuable comments on this dissertation. My gratitude also goes to the entire Darwin-GENIE team, including Malcolm, Anders, Lisa, Luigi, Pierre and Christian at ESA, Rainer, Philippe and Florence at ESO, and Eric at Leiden Observatory.

I would like to express my warmest thanks to the wonderful FLUOR team (past and present) at Observatoire de Paris-Meudon. I have particularly enjoyed the fruitful collaboration and discussions with Emmanuel, Antoine, Guy, Pierre K., Bertrand, Pascal, Julien and Aglaé, as well as with Jason and Steve on the NOAO side. Special thanks go to Professor Pierre Léna, for drawing my attention to GENIE and for arranging my stay in Paris. My gratitude also goes to the whole CHARA crew at Mount Wilson (Hal, Theo, Judit, Laszlo, Nils, Dave, PJ, ...), for allowing me to use their terrific Array. Thanks to all of you for so many enjoyable moments on the mountain top, meeting bears, snakes and black widows, eating pumpkin pies on Halloween with Jason (thanks for sharing the recipe!), taking pictures of deers, flowers (and mosquitoes) in the wild with Emmanuel, welding cables in the freezing outdoors with Guy, spending rainy nights playing ping-pong and listening to Aglaé play the piano, counting dust and pollen with PJ, and learning real-time data reduction with Antoine.

My thanks also go to my colleagues at Grenoble Observatory for their hearty welcome and enthusiasm. I am particularly grateful to Jean-Charles for his tireless advice and support on the study of debris disks, and to Mark for fruitful discussions on interferometry in Antarctica.

Contributions to large international projects such as GENIE, Darwin, Pegase or ALADDIN inevitably rely on the input of many people. Marc Barillot, Cyril Ruilier and Frédéric Cassaing have been three recurrent collaborators, with whom I have particularly enjoyed working. Thanks to them for sharing their great ideas and for so many fruitful discussions. I also take the opportunity to thank Marc Ollivier, Alain Léger, Fabien Malbet, Jean-Michel Le Duigou, Denis Mourard, and all the people involved.

I would like to acknowledge all my colleagues and friends at Institut d'Astrophysique et de Géo-

physique de Liège for making the past four years so enjoyable. Special thanks go to my roommates, Dimitri (aka Monsieur ZOG) and Pierre (aka Poulpy, supplier of chocolate bread and psychedelic music) for countless discussions on interferometry, coronagraphy, as well as many less serious topics. I also wish to thank Emilie and Denis, who are beautifully carrying this work forward, Denise for taking care of my travels and refunds, and the regulars of the "pops" for so many feasty afternoons, evenings and nights!

Finally, I take a particular pleasure in thanking all members of my family, in particular my parents for their moral support (especially when I needed it most) and their inspiration, not only during my PhD studies, but also for a long time before. Special thanks also to André and P-A for their careful reading of this dissertation. Last, but far from least, my most tender thanks go to Muriel for her unconditional love and support, always, and in particular during the final stages of this work (when she became a LaTeX expert in less than two days). This thesis is dedicated to her.

This research was supported by a fellowship from the Belgian National Science Foundation ("Aspirant du F.N.R.S."). During his stay at the Observatoire de Paris-Meudon, the author was supported by a European Community Marie Curie Fellowship.

Contents

Notations and acronyms **1**

Introduction **3**

Exoplanets galore! . . . 3
Direct imaging and the quest for life outside the solar system . . . 5
Debris disks: getting warmer... . . . 7
Objectives and outline of this work . . . 9

I Study of debris disks with stellar interferometry **13**

1 An overview of stellar interferometry **15**

1.1 Principles of stellar interferometry . . . 15
1.1.1 Fringe contrast . . . 16
1.1.2 Phase measurements and image reconstruction . . . 17
1.1.3 Practical design of a stellar interferometer . . . 18
1.2 Current interferometric facilities . . . 19
1.2.1 Facilities from the 1980s and 90s . . . 19
1.2.2 A new generation of arrays . . . 21
1.3 Application of stellar interferometry to circumstellar disks . . . 23
1.3.1 The interferometric view of Herbig Ae/Be stars . . . 24
1.3.2 The interferometric view of T Tauri stars . . . 25
1.3.3 First attempts at detecting debris disks . . . 26

2 A study of debris disks with CHARA-FLUOR **27**

2.1 Principle and goals of the study . . . 27
2.1.1 Strategy for near-infrared debris disk detection . . . 28
2.1.2 The FLUOR instrument at the CHARA Array . . . 30
2.2 A prototypical debris disk star: Vega . . . 33
2.2.1 The observations . . . 33
2.2.2 Article: *Circumstellar material in the Vega inner system revealed by CHARA-FLUOR* . . . 34

2.3 Ongoing work and future prospects . . . 45
2.3.1 Follow-up observations of Vega . . . 45
2.3.2 Our next target: ϵ Eridani . . . 45
2.3.3 Perspectives at the CHARA Array and the VLTI . . . 47

II Ground-based nulling interferometry: towards exozodiacal disks 51

3 An introduction to ground-based nulling interferometry 53
3.1 Principle of nulling interferometry . . . 54
3.1.1 Principle of a two-telescope (Bracewell) nulling interferometer . . . 54
3.1.2 Geometric and instrumental stellar leakage . . . 57
3.1.3 Spatial and modal filtering . . . 58
3.1.4 Disentanglement of the astrophysical sources . . . 59
3.2 Scientific and technological preparation of Darwin/TPF-I . . . 61
3.3 A first generation of ground-based nulling instruments . . . 61
3.3.1 BLINC at the MMT . . . 61
3.3.2 The Keck Interferometer Nuller (KIN) . . . 62
3.3.3 The Large Binocular Telescope Interferometer (LBTI) . . . 64
3.4 The European effort: GENIE . . . 65
3.4.1 The VLTI infrastructure . . . 65
3.4.2 Nulling configurations at VLTI . . . 67
3.4.3 Background subtraction techniques . . . 69
3.4.4 The need for a GENIE simulator . . . 73

4 Simulated performance of ground-based nulling interferometers 75
4.1 GENIEsim: the GENIE simulation software . . . 75
4.1.1 Principle and architecture of the simulator . . . 76
4.1.2 Real-time correction of atmospheric turbulence . . . 78
4.1.3 Modal filtering and the fluctuations of coupling efficiency . . . 81
4.2 A performance study of the GENIE instrument . . . 84
4.2.1 Article: *Performance study of ground-based infrared Bracewell interferometers* . . . 84

5 Selected scientific applications of the GENIE instrument 99
5.1 Characterisation of debris disks around Vega-type stars . . . 99
5.1.1 The debris disk around ζ Lep . . . 100
5.1.2 Observing procedure . . . 102
5.1.3 Influence of the disk morphology . . . 104
5.1.4 Influence of the grain size and composition . . . 107

5.1.5 Conclusions . . . 109
5.2 Spectroscopy of hot Extrasolar Giant Planets . . . 110
5.2.1 Classical detection method and calibration issues . . . 111
5.2.2 Perspectives: OPD modulation and colour-differential techniques . . . 112

6 Potential of nulling interferometry in Antarctica 115
6.1 The Antarctic plateau as an astronomical site . . . 116
6.1.1 Atmospheric turbulence at Dome C . . . 117
6.1.2 Water vapour, sky transparency and sky brightness . . . 119
6.1.3 The potential gain for interferometry . . . 121
6.2 ALADDIN: an optimised nulling interferometer . . . 121
6.2.1 The interferometric infrastructure . . . 121
6.2.2 The nulling instrument . . . 122
6.3 Preliminary performance study at Dome C . . . 123
6.3.1 Expected performance for the baseline design . . . 123
6.3.2 Influence of the accuracy on stellar angular diameters . . . 127
6.3.3 Influence of integration time . . . 127
6.3.4 Influence of pupil diameter . . . 129

III The quest for extrasolar planets from space 131

7 Pegase: a space-based precursor to Darwin 133
7.1 Context and objectives of the Pegase space mission . . . 134
7.1.1 Scientific objectives of Pegase . . . 134
7.1.2 Overview of the Pegase design . . . 137
7.2 The prime targets: hot Extrasolar Giant Planets . . . 139
7.2.1 Modelling the infrared emission of EGPs . . . 139
7.2.2 Observing scenario . . . 143
7.3 Simulated performance of Pegase . . . 146
7.3.1 Geometric stellar leakage and calibration issues . . . 146
7.3.2 Instrumental stellar leakage and real-time control . . . 147
7.3.3 The thermal background and its fluctuations . . . 149
7.3.4 Total signal-to-noise ratio and target selection . . . 151
7.3.5 Wavelength dependence of the signal-to-noise ratio . . . 154

8 Aperture configurations for the Darwin mission 157
8.1 A study of phase chopping techniques . . . 158
8.1.1 The need for high-frequency chopping techniques . . . 158
8.1.2 Principle of internal modulation . . . 160

8.1.3 High-rejection configurations with internal modulation 162
8.1.4 Principle of inherent modulation 165
8.1.5 High-rejection configurations with inherent modulation 166
8.2 The resurgence of low-rejection configurations 167
8.2.1 The trade-off between low- and high-rejection configurations 168
8.2.2 A new concept: the Three Telescope Nuller (TTN) 171

Conclusion **177**
Objectives and results 177
Perspectives 178

Bibliography **179**

Appendix **197**

A Thermal background fluctuations at 10 micron measured with VLTI-MIDI **199**

Notations and acronyms

Atmospheric windows

J band	from 1.15 to 1.4 μm
H band	from 1.5 to 1.8 μm
K band	from 2.0 to 2.4 μm
L′ band	from 3.5 to 4.1 μm
M band	from 4.5 to 5.1 μm
N band	from 8 to 13 μm

Units

arcmin (or ′)	minute of arc (2.90888×10^{-4} radian)
arcsec (or ″)	second of arc (4.848137×10^{-6} radian)
mas	milli-arcsec (10^{-3} arcsec)
AU	Astronomical Unit (1.495978×10^{11} m)
pc	parsec (3.085678×10^{17} m)
Jy	Jansky (10^{-26} W m^{-2} Hz^{-1})
Myr	Mega-years (one million years)
Gyr	Giga-years (one billion years)
zodi	density unit for dust disks, equivalent to the solar zodiacal disk

Notations

$M_\odot$	Mass of the Sun (1.98892×10^{30} kg)
$R_\odot$	Radius of the Sun (6.96×10^{8} m)
$L_\odot$	Luminosity of the Sun (3.846×10^{26} W)
$M_{\rm Jup}$	Mass of Jupiter (1.8987×10^{27} kg)
$R_{\rm Jup}$	Radius of Jupiter (7.1492×10^{7} m)
$M_\oplus$	Mass of the Earth (5.97370×10^{24} kg)
$R_\oplus$	Radius of the Earth (6.37814×10^{6} m)
$M_\star$, $T_\star$, $L_\star$	Mass, effective temperature and luminosity of a star
$B_\star$	Photospheric surface brightness of a star
$R_\star$, $\theta_\star$	Linear and angular radius of a star
$\theta_{\rm UD}$, $\theta_{\rm LD}$	Uniform disk and limb-darkened disk stellar angular *diameters*
b, $b_\perp$	Interferometric baseline length, its projection on the sky plane
a	Semimajor orbital axis for a planet, or diameter for a dust grain

Acronyms

ALADDIN	Antarctic L-band Astrophysics Discovery Demonstrator for Interferometric Nulling
AMBER	Astronomical Multiple Beam Recombiner (at the VLTI)
AO	Adaptive Optics
AT	VLTI Auxiliary Telescope (1.8-m diameter)
BLINC	BracewelL Infrared Nulling Cryostat (for the MMT)
CHARA	Center for High Angular Resolution Astronomy (Georgia State University)
CNES	Centre National d'Études Spatiales
DAC	Degenerated Angel Cross
Darwin	Not an acronym—infrared space interferometer (ESA project)
EGP	Extrasolar Giant Planet
ESA	European Space Agency
ESO	European Southern Observatory
FINITO	Fringe Tracking Instrument of Nice and Torino (at the VLTI)
FLUOR	Fiber Linked Unit for Optical Recombination (at the CHARA Array)
FSU	Fringe Sensing Unit
GAC	Generalised Angel Cross
GENIE	Ground-based European Nulling Interferometry Experiment (for the VLTI)
IRAS	Infra-Red Astronomical Satellite
ISO	Infrared Space Observatory
JCMT	James Clerk Maxwell Telescope
JPL	Jet Propulsion Laboratory
KIN	Keck Interferometer Nuller
MACAO	Multi Application Curvature Adaptive Optics (at the VLTI)
MIDI	Mid-Infrared instrument for the VLTI
MIRC	Michigan Infra-Red Combiner (for the CHARA Array)
MMT	Multiple Mirror Telescope
OB	Observation Block
OPD	Optical Path Difference
Pegase	Not an acronym—infrared space interferometer (CNES)
PID	Proportional, Differential and Integrator (controller)
PRIMA	Phase-Referenced Imaging and Microarcsecond Astrometry (for the VLTI)
PSD	Power Spectral Density
SCUBA	Submillimeter Common Used Bolometer Array (at the JCMT)
SED	Spectral Energy Distribution
SNR	Signal-to-Noise Ratio
STRAP	System for Tip-tilt Removal with Avalanche Photodiodes (at the VLTI)
TPF-I	Terrestrial Planet Finder Interferometer (NASA project)
TTN	Three Telescope Nuller
UKIRT	United Kingdom Infra-Red Telescope
UT	VLTI Unit Telescope (8-m diameter)
VCM	Variable Curvature Mirror (at the VLTI)
VISA	VLT Interferometer Sub-Array
VLTI	Very Large Telescope Interferometer (ESO)
YSO	Young Stellar Object

Introduction

There are countless suns and countless earths all rotating around their sun in exactly the same way as the seven planets of our system. We see only the suns because they are the largest bodies and are luminous, but their planets remain invisible to us because they are smaller and non-luminous. The countless worlds in the universe are no worse and no less inhabited than our Earth.

Giordano Bruno, "De l'Infinito, Universo e Mondi" (1584)

Surrounded by a seemingly limitless ocean of stars, mankind has long speculated about the existence of planetary systems other than our own, and the possibility of development of life elsewhere in the Universe. Four centuries after Giordano Bruno's visionary reflections, we now live in a remarkable time where human beings have finally attained the possibility of finding the first answers to some of these most meaningful questions.

Exoplanets galore!

The first discovery, by Mayor & Queloz (1995), of a planet orbiting another star than our Sun (namely, 51 Peg) was undoubtedly one of the major scientific breakthroughs of the 1990s, not only because it opened the path to countless advances in the theory and observation of extrasolar planetary systems, but also because it brought to light an unexpected new type of planets: hot Extrasolar Giant Planets (EGPs). With a minimum mass[1] of $0.468 M_{\rm Jup}$ and an orbital period of 4.23 days, "51 Peg b" has become the prototype of this class of planets, which are heated up to about 1000 K due to the proximity to their parent star. To date, about 40 similar planets with orbital periods shorter than 10 days have been found, i.e., with semimajor orbital axes $a \lesssim 0.1$ AU (see Figure 1). These discoveries were most often the result of precise measurements of the host star's radial velocity through spectroscopic observations, showing small Doppler shifts in the stellar spectral lines (typically tens of metres per second) as the star moves back and forth due to the gravitational pull of its planet. Another successful technique for EGP detection relies on the dimming of the apparent stellar flux as the planet transits in front of the stellar photosphere. Even though the probability to detect such a transit is rather low ($p = R_\star/a \sim 10\%$ for a hot EGP, with $R_\star$ the stellar radius), nine hot EGPs have been either found or confirmed using this technique.

In addition to hot planets, radial velocity measurements have also led to the discovery of cool extrasolar planets located farther away from their stars, with semimajor axes up to 5.3 AU. Most of these are thought to be gaseous giants similar to the Jovian planets of our solar system, as 105 of the 170 planets discovered to date have a minimum mass larger than that of Jupiter (see Figure 1). Such a large spread

[1] The standard detection method, based on radial velocity measurements of the parent star, provides a measurement of $M \sin i$, i.e., the planetary mass multiplied by the sine of the planetary system's inclination with respect to the plane of the sky. The latter being generally unknown, only a lower limit can be inferred on the planetary mass.

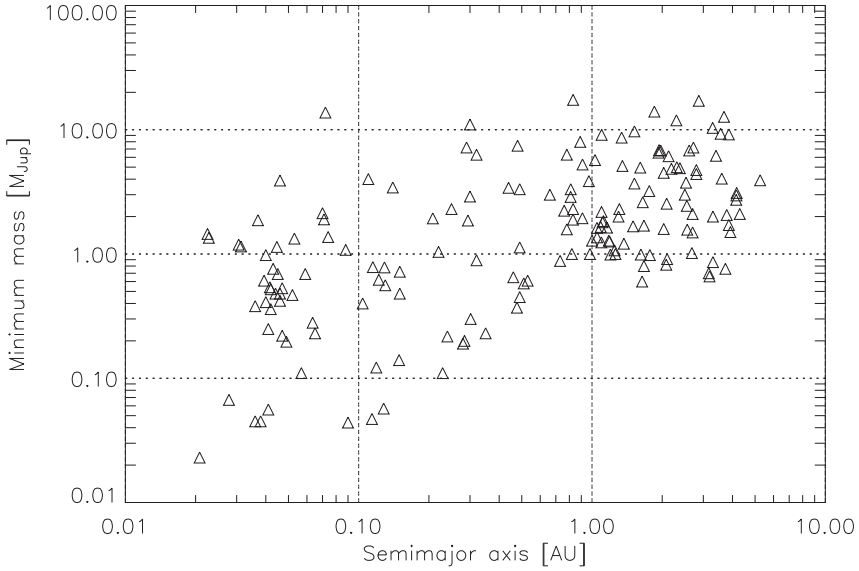

Figure 1: Distribution of minimum mass versus semimajor axis for the extrasolar planets detected to date (data taken from Schneider (2006)). Note that the current detection techniques are strongly biased towards high-mass planets with short orbital periods (i.e., small semimajor axes).

of semimajor axes was not expected for giant planets in the classical planet formation theory and thus required a revision of the standard scenario, as we now discuss.

According to the classical scenario of planet formation (Pollack 1984), giant planets form by core accretion of solid particles in the outer part of protoplanetary disks surrounding young stars, beyond the "snow line" (Sasselov & Lecar 2000), where the $\sim 10 M_\oplus$ protoplanetary cores can later on capture substantial amounts of gas from the disk in a runaway accretion process lasting about 10 Myr (Pollack et al. 1996). Because this timescale is uncomfortably close to the typical lifetime of protoplanetary disks, believed to be of the order of 1–10 Myr (Haisch et al. 2001), a long-discarded mechanism, based on local gravitational collapse of the protoplanetary disk, has been reevaluated by Boss (1998) to allow for a more rapid formation of giant planets. In any case, formation scenarios require giant planets to be formed in the outer part of protoplanetary disks. These theories are obviously incompatible with the observation of giant planets orbiting close to their parent star, where a sufficient amount of gas is not available to form such large bodies. This apparent contradiction is now understood in the framework of migration processes: in the protoplanetary disk, the planets are assumed to excite density waves that propagate on both sides of their orbit (Goldreich & Tremaine 1979). The torque exerted by these waves can cause the planets to migrate inwards in the disk, a mechanism believed to be at the origin of the observed distribution of extrasolar planet orbital periods. Even though the updated formation theories have gained much credibility through successful planet hunting programmes, they need to be further validated with new types of observations, especially at the early stages of planet formation when planet-disk interactions are taking place.

In addition to validating the new formation theories, the bonanza of extrasolar planet discoveries has allowed the inference of statistical properties. The incidence of planets around solar-type stars has been estimated by Lineweaver & Grether (2003). At least ~9% of Sun-like stars[2] have planets in the mass and orbital period ranges $M \sin i > 0.3\, M_{\rm Jup}$ and $P < 13$ years, and at least ~22% have planets in the larger range $M \sin i > 0.1\, M_{\rm Jup}$ and $P < 60$ years. These estimates might still be lower limits to the true fraction of Sun-like stars with planets, which could be close to 100%. Statistical studies have also shown

[2]Stars with spectral types ranging from F to K and with luminosity class IV or V.

some unexpected behaviours, such as correlations between stellar metallicity and planet occurrence rate, high eccentricities of planetary orbits, or the dearth of planets with periods shorter than 3 days, leading to further refinements of the formation theories. The period-eccentricity relations of extrasolar planets, significantly different from those of binary stars (Halbwachs et al. 2005), and the absence of companions with masses in the range $10\,M_{\rm Jup} < M < 100\,M_{\rm Jup}$ (the "brown dwarf desert") provide strong reasons to believe that extrasolar planets are formed by a different mechanism than low-mass companion stars and thus favour the core-accretion scenario.

Almost all planet discoveries to date have been realised with indirect methods, i.e., radial velocities, photometric transits, gravitational lensing or astrometry, which rely on the effect of the planet on its parent star or on a background star. The current limitations of these methods have so far prevented the detection of Earth-like bodies: the smallest two planets discovered to date have estimated masses of 7.5 and $5.5\,M_\oplus$ respectively (Rivera et al. 2005; Beaulieu et al. 2006). Although future space-based missions for transit searches (CoRoT, Kepler) or astrometric surveys (SIM, Gaia) are expected to push this limit down to one or a few Earth masses, they will still be restricted to the measurements of orbital parameters and will therefore provide only limited information on the physics of these supposedly rocky bodies. Indirect methods surely still have many bright years ahead, but will gradually be complemented and replaced by direct methods, which aim at extrasolar planet imaging and could eventually lead to the detection of signposts of life outside our solar system.

Direct imaging and the quest for life outside the solar system

The next major step in the study of extrasolar planets consists in characterising their composition by means of spectroscopy. Such investigations should eventually lead to the assessment of the possible presence of life on rocky planets. The simultaneous presence of water vapour, carbon dioxide and ozone is indeed generally considered to be a robust indicator of biological activity at the surface of a planet (Selsis et al. 2002). However, a spectroscopic study requires that the planetary and stellar spectra be separated, which is only possible by spatially resolving the two components of the system. Indirect methods are therefore not appropriate for such a task.[3]

Direct imaging of planetary systems is however still in its infancy: it has only recently allowed three extrasolar planets to be imaged, in very favourable cases where the flux ratio between the star and its planet is only a few hundreds (Chauvin et al. 2005a,b; Neuhäuser et al. 2005). These discoveries have been made possible thanks to the advent of adaptive optics (AO) systems on large ground-based telescopes, which correct for the distortion induced by the Earth's atmosphere in order to provide sharp images of relatively bright astronomical objects. The addition of a coronagraphic mask in the focal plane, designed to dim the stellar light, enhances the capability of large AO-corrected telescopes to distinguish giant planets around nearby stars with contrasts up to a few thousands. However, the challenge of rocky planet detection is much harder due to the huge contrast: the flux reflected by Earth-like planets is not expected to represent more than a few 10^{-10} of the stellar flux in the visible range, while its thermal emission only amounts to a few 10^{-7} of the stellar flux around 10 μm where it peaks. The mid-infrared wavelength range is therefore generally considered best for the investigation of planetary atmospheres in the context of life detection, all the more so because spectral bands associated with water, carbon dioxide and ozone can be found between 6 and 18 μm.

In addition to the high contrast between the two bodies, another major problem comes from their minute angular separation. The development of life on a rocky planet requires it to be located in the

[3] Among indirect methods, only the dimming of the system's flux during planetary transits can provide (limited) information on the atmospheric composition of the planets, when the contrast is not too large.

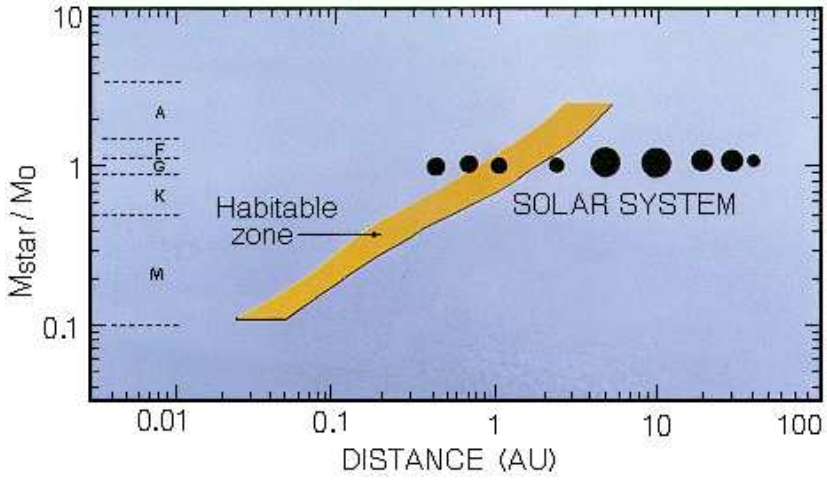

Figure 2: The habitable zone around different types of main-sequence stars, centred around 1 AU for a solar-type star. The nine planets of our own solar system are shown. Adapted from Kasting & Catling (2003).

habitable zone around its parent star (at about 1 AU from a Sun-like star, see Figure 2), where liquid water can be present at its surface (Kasting & Catling 2003). Accordingly, the angular separation between the star and its Earth-like companion is expected to be about 100 milliarcseconds (mas) for a Sun-like star located at 10 parsecs (pc). Such an angular resolution cannot be achieved with current monolithic telescopes in the mid-infrared regime, where their resolution λ/D is limited to about 200 mas. Larger telescopes, up to 100 m in diameter, are currently being developed but, as such large apertures are not expected to be feasible in space, they still will be limited by the presence of the Earth's atmosphere which degrades the images and restricts the observations to the infrared transparency windows (i.e., only between 8 and 13 μm in the mid-infrared). In order to benefit both from the full infrared electromagnetic spectrum and from a high angular resolution, space-based interferometers have been proposed, both at the European Space Agency (ESA) with the Darwin mission (Fridlund 2004b), and at NASA with the Terrestrial Planet Finder Interferometer (TPF-I, Beichman et al. 1999).

The principle of interferometry is to synthesise the resolving power of a large monolithic telescope by combining the light collected by several smaller telescopes, separated by a distance equivalent to the required diameter of the large telescope. In addition to increasing the angular resolution, interferometry also provides a natural way to dim the stellar light, by using its wave properties: by inserting phase-shifting devices in the path of the light beams, one can adjust their respective phases in order to produce a totally destructive interference on the optical axis. This technique, first proposed by Bracewell (1978), is referred to as *nulling interferometry* and is currently considered for both Darwin and TPF-I.

Since the pioneering work of Bracewell, nulling interferometry has been studied and improved by many researchers, leading to the current view of the future Earth-like planet finding missions (Fridlund 2004a): a flotilla of 3 to 6 free-flying telescopes of moderate diameter (~3 m) capable of searching for planets around the 150 closest F, G and K type stars in a 5 year mission (see Figure 3). A road map of technological developments has been laid out by both ESA and NASA in order to reach that goal in the 2015 time frame with the Darwin and TPF-I missions. However, there remain two major unknown parameters critical to the design of these missions: the occurrence rate of Earth-like planets around nearby stars, and the amount of dust to be expected in their habitable zone.

The first parameter will be addressed to a large extent by the future space missions that will search for planets with the transit method (CoRoT and Kepler), as they are expected to be sensitive down to one Earth radius (Bordé et al. 2003b). The second parameter, which is at the heart of the present work,

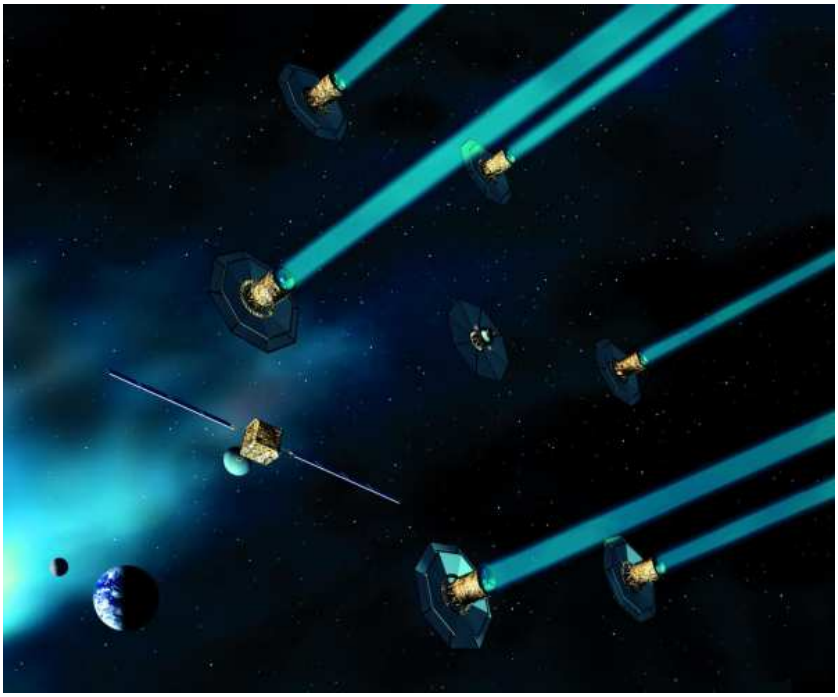

Figure 3: Artist impression of the Darwin space interferometer in its original hexagonal version, deployed and observing at the Sun-Earth Lagrange point L2. Added to the six telescopes are a central beam combining spacecraft and a satellite dedicated to communication and control (© 2002, ESA).

is more difficult to assess with current instruments because it requires both high angular resolution and high dynamic range imaging capabilities. In fact, our knowledge of the dust distribution in the first few AUs around solar-type stars is currently mostly limited to the observations of the solar zodiacal disk, a sparse structure of warm silicate grains 10 to 100 μm in diameter, which is the most luminous component of the solar system after the Sun. Its optical depth is only $\sim 10^{-7}$, but its integrated emission at 10 μm is about 300 times larger than the flux of an Earth-size planet. The presence of similar disks around the Darwin/TPF-I targets (*exozodiacal disks*) may present a severe limitation to the Earth-like planet detection capabilities of these missions, as warm exozodiacal dust becomes the main source of noise if it is more than 20 times as dense as in the solar zodiacal disk (Absil 2001). The prevalence of dust in the habitable zone around nearby solar-type stars must therefore be assessed before finalising the design of the Darwin/TPF-I missions. In this context, the present work aims at the detection and characterisation of warm dust around main sequence stars, starting with those already known to harbour significant amounts of cold debris in their outskirts.

Debris disks: getting warmer...

First evidence for the presence of circumstellar dust around a main sequence star dates back to the launch of the InfraRed Astronomical Satellite (IRAS), with which Aumann et al. (1984) quickly found Vega's far-infrared flux to be larger than the expected photospheric flux. Similar excesses were then soon discovered around a large sample of main sequence stars using photometric observations with infrared space telescopes such as IRAS (e.g. Aumann 1988; Stencel & Backman 1991; Mannings & Barlow 1998) or ISO (e.g. Fajardo-Acosta et al. 1999; Decin et al. 2000; Habing et al. 2001; Laureijs et al. 2002). These studies have shown that about 10% of main sequence stars have excess emission in the 25 μm region, with a larger occurrence rate around early-type stars, and that this proportion increases to about 17% at 60 μm. Infrared excesses around main-sequence stars are now commonly understood as the signature of

cold second-generation dust grains arranged in disk-like structures referred to as *debris disks*, originating from collisions between small bodies (asteroids) or from the evaporation of comets (Backman & Paresce 1993). Similarly to the solar zodiacal disk, debris disks are thought to be continuously replenished because dust grains have a limited lifetime of a few Myr at most due to the effects of collisions, radiation pressure and Poynting-Robertson drag (Dominik & Decin 2003). These two types of second-generation dust disks have to be distinguished from the optically thick protoplanetary disks of gas and dust detected around young pre-main sequence stars, which originate from primordial interstellar medium, are at the origin of the formation of planetary systems and dissipate on timescales of 10 Myr (Mamajek et al. 2004).

In fact, debris disks are different from exozodiacal disks only in that they are much more massive and mainly composed of cold dust grains located at several tens of AU from their parent star. Such dust structures are actually more reminiscent of the solar Kuiper Belt, a reservoir of small icy bodies extending roughly from 30 to 50 AU from the Sun. This similarity has been confirmed by obtaining resolved images for some of these debris disks, first in the visible regime where stellar light scattered by dust particles has been detected around young main-sequence stars such as β Pic (Smith & Terrile 1984) or AU Mic (Kalas et al. 2004), and then in the sub-millimetric and millimetric regimes where ring-like structures of cold dust were first discovered around the *Fabulous Four* Vega, β Pic, Fomalhaut and ϵ Eri (Holland et al. 1998; Greaves et al. 1998; Koerner et al. 2001). These images suggest that planets may be forming or may have already formed in these systems, because they generally show planet-related features such as the presence of warps, clumps, rings or central clearings inside the cold dust ring (see Figure 4). However, the lack of high angular resolution and/or dynamic range has limited these techniques to the outer parts of only a dozen debris disks, which are not relevant in the context of future life-finding missions.

The presence of hot (~1000 K) and/or warm (~300 K) dust grains around main sequence stars, which would mostly emit in the near- and mid-infrared, has long been and still remains elusive. Their expected excesses ($\lesssim$ 1%) are in fact barely detectable by classical aperture photometry because the precision on both the measurements and the models of stellar photospheric emission is around 2% at best in the

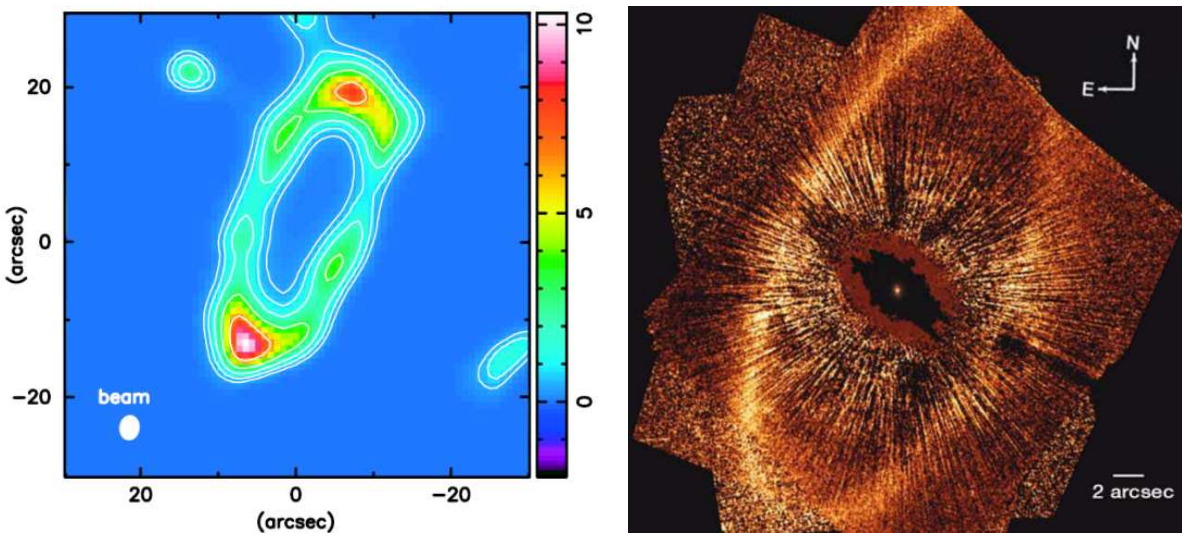

Figure 4: The debris disk around Fomalhaut, as detected in the sub-millimetric domain (left, adapted from Marsh et al. 2005) and in the visible domain (right, adapted from Kalas et al. 2005). This circumstellar dust ring, inclined by 66° with respect to the plane of the sky, has an extent of about 20 arcsec corresponding to a linear distance of 150 AU, where the dust grains are expected to have temperatures around 50 K. A lack of circumstellar material inside a radius of 120 AU is evident in both images.

infrared regime (Mégessier 1995). In a survey of nearby Vega-like stars with known infrared excesses at 12 μm, Aumann & Probst (1991) found that the presence of warm dust could be confirmed for only two targets (β Pic and ζ Lep) out of 548 with ground-based photometric measurements at 10 μm. More recently, Fajardo-Acosta et al. (1998) detected only 5 systems with weak 10 μm excess emission using the InfraRed Telescope Facility (IRTF), and derived disk models typically spanning between 1 and 10 AU with median grain temperatures ranging between 200 and 350 K. Infrared imaging did not provide better results: β Pic remains the only main-sequence star around which the thermal emission of warm grains has been imaged in the mid-infrared (Telesco et al. 1988; Lagage & Pantin 1994).

The advent of NASA's infrared Spitzer Space Telescope has recently brought new hints on the prevalence of dust in the inner regions of debris disks. For instance, Stapelfeldt et al. (2004) have found Fomalhaut's cold circumstellar ring to be at least partially filled with emission from warm dust, even though the available angular resolution has not allowed for a unique determination of its spatial distribution. Similarly, an excess emission relative to the stellar photosphere has been found between 8 and 35 μm around HD 69830 (Beichman et al. 2005a), showing strong spectral features attributable to crystalline silicates. The absence of excess at 70 μm suggests that this circumstellar material is quite warm (~400 K) and confined within a few AU from the star. Yet another study with Spitzer revealed two other main sequence stars to be surrounded by warm grains at about 400 K (Chen et al. 2005), while a survey of the Galactic H II region RCW 49 further suggested the presence of warm dust around 18 main sequence stars (Uzpen et al. 2005).

All aforementioned studies have demonstrated that cold dusty disks are frequently found in the outskirts of a large variety of main sequence stars. Further studies have reached the same conclusions in the case of brown dwarfs (Jayawardhana et al. 2003) and even white dwarfs (Reach et al. 2005). Recent results also suggest that small amounts of warm dust grains might be common in the inner planetary zone of debris disks, produced by the sublimation of cometary bodies or by a collisional cascade of asteroids. However, even these latest results do not provide very useful information for the future Darwin/TPF-I missions, as they are limited to dust disks about 10^3 times denser than the solar zodiacal disk, and do not provide the required angular resolution to image the most important planetary zone. In order to improve the sensitivity and angular resolution in the search for exozodiacal disks, we propose to make use of infrared interferometry.

Objectives and outline of this work

Thanks to its high angular resolution capabilities and to its potential for high contrast imaging, interferometry is the best-suited technique to investigate the inner regions of exozodiacal disks around main sequence stars. The present work aims at demonstrating the high dynamic range capabilities of infrared interferometers in the context of the future Darwin and TPF-I planet finding missions. In addition to providing much needed information on the prevalence of dust in the habitable zones around nearby main sequence stars, the development of high contrast interferometric techniques will also largely contribute to the validation of the proposed concepts for the Darwin and TPF-I space interferometers.

Our work follows a stepwise approach, focusing first on existing interferometric facilities. We undertake to demonstrate their high dynamic range capabilities by studying the inner regions of optically thin debris disks around nearby main sequence stars. In Chapter 1, we recall the basic principles of stellar interferometry and review the main scientific achievements of current interferometers, with a particular emphasis on their success in characterising optically thick circumstellar disks around Young Stellar Objects (YSO). This success is contrasted with the failure of the first attempts at detecting debris disks, for which the contrast between the star and the disk is much larger. In Chapter 2, we propose a general

method for the investigation of optically thin disks around main sequence stars, and apply it to the prototypical debris disk star Vega using the FLUOR near-infrared interferometer at the CHARA Array. Our observations lead to the first convincing detection of warm dust in the inner region (< 10 AU) of a debris disk by stellar interferometry. Complementing our measured K-band flux ratio with archival near- and mid-infrared photometric data, we investigate the physical properties of the dust grains and propose a possible scenario for their production, which is most probably related to the evaporation of comets. The second chapter ends with the presentation of preliminary results on another debris disk star (ϵ Eri) and of the perspectives for the years to come.

Even though existing interferometric facilities have the capability of studying debris disks with infrared flux ratios in the range 0.1 – 1% with respect to their parent star, their current precision does not allow for the detection of faint exozodiacal disks with typical infrared flux ratios below 10^{-4}. In order to improve the dynamic range of these facilities, the second part of this work aims at the development of ground-based nulling interferometry. In Chapter 3 are presented the principles and limitations of this concept. We review the efforts currently undertaken around the world to develop and build nulling interferometers and describe the general design of these instruments. A particular emphasis is put on the Ground-based European Nulling Interferometer Experiment (GENIE), an instrument to be installed at the ESO Very Large Telescope Interferometer (Figure 5) to which we have largely contributed. Chapter 4 is dedicated to a thorough performance study of ground-based nulling interferometers. For that purpose, we have developed a specific software simulator, which takes into account atmospheric turbulence in a realistic way. Based on this simulator, we compute the expected performance of the real-time control loops dedicated to the correction of atmospheric perturbations and deduce the global performance of ground-based nullers. Our work suggests that GENIE will detect circumstellar emission down to a few 10^{-4} of the stellar flux in the infrared L′ band. In Chapter 5, we further investigate the science case and performance of GENIE in the context of extrasolar planetary systems. It is shown that this nulling instrument could largely improve our knowledge of debris disks by investigating both their morphology and their composition, and thereby constrain the current models for the formation and evolution of planetary systems. The capability of GENIE to detect hot EGPs is also discussed and indicates that low-resolution

Figure 5: The ESO Very Large Telescope Interferometer with its four 8-m Unit Telescopes, three of its four 1.8-m Auxiliary Telescopes (artist impression) and its central beam combining laboratory (© 2000, ESO).

spectroscopy will be possible for a handful of planets.

A major limitation to the performance of ground-based nulling interferometers comes from the harmful influence of atmospheric turbulence. The obvious solution to this issue is to launch an interferometer into space. However, as shown in Chapter 6, a significant gain can already be obtained by installing the interferometer at supposedly the best astronomical site on Earth: the high Antarctic plateau. Recent measurements of the atmospheric conditions at Dome C, one of the highest points of the plateau, are used to assess the performance of a nulling interferometer optimised for the Antarctic. Our simulations suggest that the sensitivity of such an interferometer to faint exozodiacal disks could be significantly improved with respect to a similar instrument at a temperate site while using much smaller telescopes.

The third and last part of this work focuses on the final steps in the quest for habitable planets, i.e., the design of space missions. Because the detection of Earth-like planets is such an ambitious goal, space-based precursor missions are currently investigated to demonstrate in orbit the concept and required technologies of Darwin. Chapter 7 describes the science case and expected performance of one of these precursor missions: Pegase. This French proposal for a formation flying near-infrared nulling interferometer aims at the characterisation of known hot EGPs. Based on a simple model for the thermal emission of EGPs, we show that Pegase will be able to perform low-resolution spectroscopy on about 20 planets with masses similar or larger than that of Uranus. Finally, Chapter 8 describes our contribution to the design of the Darwin mission, which mainly focuses on the global architecture of the interferometer. We review the concept of phase chopping and propose new configurations which significantly enhance the performance of the original hexagonal configuration represented in Figure 3. We discuss how the Darwin concept has evolved in the past few years and present the new three-telescope mission model with some detail.

Part I

Study of debris disks with stellar interferometry

1

An overview of stellar interferometry

Contents

1.1 Principles of stellar interferometry 15
1.1.1 Fringe contrast 16
1.1.2 Phase measurements and image reconstruction 17
1.1.3 Practical design of a stellar interferometer 18
1.2 Current interferometric facilities 19
1.2.1 Facilities from the 1980s and 90s 19
1.2.2 A new generation of arrays 21
1.3 Application of stellar interferometry to circumstellar disks 23
1.3.1 The interferometric view of Herbig Ae/Be stars 24
1.3.2 The interferometric view of T Tauri stars 25
1.3.3 First attempts at detecting debris disks 26

In this chapter, we review the principles of stellar interferometry and introduce the required concepts for the next chapters, as well as some technical aspects. Then, we give a brief description of the characteristics and major scientific results of current interferometric facilities, and discuss the main features of upcoming facilities. A particular emphasis is put on the application of stellar interferometry to the study of optically thick circumstellar disks around Young Stellar Objects (YSO), which has strongly benefitted from the high angular resolution capabilities of infrared interferometers. We conclude by noting that the first attempts at detecting debris disks around main sequence stars have been mostly inconclusive due to the high contrast between the near-infrared emission of the disk and the stellar photosphere.

1.1 Principles of stellar interferometry

The capability of distinguishing very small details in visible and infrared images has been a major design driver for telescopes and astronomical instrumentation during the past few decades. The angular resolution $\theta = 1.22\lambda/D$ of a single-dish telescope being limited by its diameter D for a given incident light wavelength λ, larger and larger mirrors have been built over the 20th century, finally reaching 10 m with the most recent telescopes. Adaptive optics systems have been designed to achieve the full potential of these giant dishes in terms of angular resolution, overcoming the harmful perturbations of atmospheric

turbulence. Even larger telescopes (up to 100 m) are foreseen to be built within the next ten years, but these heavy and cumbersome structures are not expected to grow in size indefinitely because of technical limitations. Therefore, another way to improve the angular resolution of astronomical images without building a telescope of enormous size has been developed: optical interferometry.[4] The idea is to synthesise a large aperture by combining light beams from several small telescopes. Even though the technique itself dates back to Fizeau (1868) and Michelson & Pease (1921), the first application to two separate telescopes was achieved only 30 years ago by Labeyrie (1975). At that time, a maximum angular resolution $\theta = \lambda/2b$ of 5 mas was achieved in the visible range on a $b = 12$ m baseline. Since this pioneering work, many interferometric facilities have been built around the world with enhanced capabilities, as described in Section 1.2.

1.1.1 Fringe contrast

In a two-telescope interferometer, the fundamental observable is the contrast of the interference fringes formed by the combination of the two light beams. The fringe contrast, historically called the visibility, is defined as the ratio between the fringe amplitude and the average intensity:

$$\mathcal{V} = \frac{I_{\max} - I_{\min}}{I_{\max} + I_{\min}} \,, \tag{1.1}$$

where $I_{\max}$ and $I_{\min}$ denote the maximum and minimum intensity of the fringes. The Van Cittert-Zernike theorem (Thompson et al. 2001) relates the contrast of an interferometer's fringes to a unique Fourier component of the impinging brightness distribution. In fact, the visibility is exactly proportional to the amplitude of the image Fourier component corresponding to the spatial frequency $u = b/\lambda$ related to the baseline (expressed in rad^{-1}). Also, the phase of the fringe pattern is equal to the Fourier phase of the same spatial frequency component. However, the phase of the complex visibility is generally corrupted by atmospheric or internal fluctuations of the optical pathlength difference (OPD), which erases information about the intrinsic phase arising from the source structure. Under these circumstances, it is usually better to work with the squared visibility $\mathcal{V}^2$ rather than $\mathcal{V}$ itself, because $\mathcal{V}^2$ estimators can be constructed that properly take into account the noise bias (Perrin 2003).

The fringe contrast measured on a simple object such as a single star is directly related to its physical size. Assuming a uniform disk (UD) model for the brightness distribution of a single star of angular diameter θ_{UD}, the squared visibility measured by a two-telescope interferometer is given by (Boden 2000):

$$\mathcal{V}^2(b_\perp, \lambda, \theta_{\mathrm{UD}}) = \left(\frac{2J_1(\pi\theta_{\mathrm{UD}} b_\perp/\lambda)}{\pi\theta_{\mathrm{UD}} b_\perp/\lambda} \right)^2 \,, \tag{1.2}$$

where $b_\perp$ is the length of the baseline vector projected onto the sky plane. For an unresolved star ($\theta_{\mathrm{UD}} \ll \lambda/b_\perp$), the visibility is close to 1. It decreases for increasing baseline lengths and finally reaches 0 for $\theta_{\mathrm{UD}} \simeq 1.22\lambda/b_\perp$. The star is then said to be resolved.

In practice, interferometric fringes never have a perfect contrast ($\mathcal{V} = 1$), even for a point source, because of atmospheric and instrumental effects. One must therefore accompany each measurement of the target by a similar measurement of an unresolved calibration source. The true visibility of the object is then the observed visibility of the object divided by the observed visibility of the calibrator.

[4] The terminology "optical" refers here to the way of handling the routing and beam combination of light, using optics, and thereby restricts the application to the visible and infrared domains.

1.1.2 Phase measurements and image reconstruction

As stated above, the fringe visibility measured using a particular baseline provides one component of the object's Fourier transform. However, a Fourier transform is a complex quantity, having both an amplitude and phase. While the amplitude is given by the fringe visibility, the phase is given by the position of the fringes. In principle, image reconstruction can be achieved from the measurements of Fourier components (amplitude and phase) in the spatial frequency plane (or (u, v)-plane), provided that the sampling of the (u, v)-plane is dense enough. Reconstruction algorithms such as CLEAN (Högbom 1974) or the maximum entropy method (MEM, Skilling & Bryan 1984) are routinely used in radio-interferometry. A good sampling of the (u, v)-plane can be achieved either by repeating the interferometric measurements with various telescope pairs or by using the Earth's diurnal rotation. The latter method, called supersynthesis, has been extensively used in the past years as most interferometric facilities are composed of a limited number of fixed telescopes. By observing the same star at different moments in time with the same (fixed) telescopes, one obtains information at different spatial frequencies since the projected baseline length ($b_\perp$) and orientation changes with the object's position.

However, until the mid-1990s, only fringe contrast measurements were achieved by stellar interferometers, while phase information could not be retrieved due to atmospheric turbulence: because the rms atmospheric phase shift is generally larger than 1 radian, even averaging over many realisations of the atmosphere does not provide an estimate of the intrinsic source phase (Monnier 2000). The information obtained on the Fourier transform of the source's brightness distribution is then only partial, and image reconstruction generally fails. Fortunately, a number of strategies have been developed to circumvent these difficulties.

Phase referencing

Phase referencing uses a reference object to determine the atmospheric phase and to correct the phase of the target source accordingly. For this technique to work, the target and reference sources must be affected by the same atmospheric turbulence, i.e., be separated by an angle smaller than the isoplanetic angle (the angle over which image distortions are correlated). Because the isoplanetic angle is only a few arcseconds in the optical regime, this technique is limited by the presence of a sufficiently bright source close to the target. It has been applied to narrow-angle astrometry where fringe phase information is used for determining precise relative position of nearby stars (Shao & Colavita 1992). This technique can also be used to increase the effective atmospheric coherence time, allowing longer coherent integrations on the target source.

Closure phases

A simple way to retrieve (part of) the phase information can be used if three (or more) telescopes are simultaneously combined pair-wise. The three sets of fringes are all affected by atmospheric turbulence, which adds a random phase $\phi(i)$ for each telescope i, but their phase fluctuations are not independent: their relative positions contain information on the intrinsic phase Φ_0 of the source. In fact, the three fringe phases measured pair-wised, $\Phi(i-j) = \Phi_0(i-j) + [\phi(j) - \phi(i)]$, have their sum insensitive to the phase corruption introduced by atmospheric turbulence as the phase error $\phi(i)$ on each telescope i is counted once positively and once negatively in the sum of the measured fringe phases. The closure phase $\Phi(i-j-k) = \Phi_0(i-j) + \Phi_0(j-k) + \Phi_0(k-i)$ therefore only depends on the brightness distribution of the source, so that one third of the phase information can be retrieved from phase closure measurements on a single triplet of telescopes. If $N > 3$ telescopes are used simultaneously, the number of independent closure phases measured on triplets of telescopes is given by $\binom{N-1}{2} = (N-1)(N-2)/2$, equivalent

to holding one telescope fixed and forming all possible triangles with that telescope (Monnier 2000). Because there are $\binom{N}{2} = N(N-1)/2$ independent Fourier phases, the information provided by closure phase measurements is incomplete, and given by $(N-2)/N$. For example, for a 10-telescope array, 80% of the phase information can be retrieved if the baselines are not redundant.

1.1.3 Practical design of a stellar interferometer

The essential functions of an optical interferometer, illustrated in Figure 1.1, can be divided into four main components:

- **Beam collection.** This function is performed either by classical telescopes, or by siderostats. The latter are flat steerable mirrors, used to send the light directly to the interferometer or to a fixed (generally horizontal) telescope serving as beam compressor. Telescope sizes were at first limited by the atmosphere coherence length r_0 (Fried parameter), ranging from 10 cm in the visible to about 50 cm in the near-infrared. With the advent of adaptive optics, larger telescopes are now being used in new generations of arrays (see Section 1.2.2).
- **Beam transport.** A set of optical elements, referred to as optical train, is used to propagate the light beams from the output of the telescopes to the location where they will be combined. The latter is generally placed in a dedicated laboratory. Particular attention is paid to mirror geometry

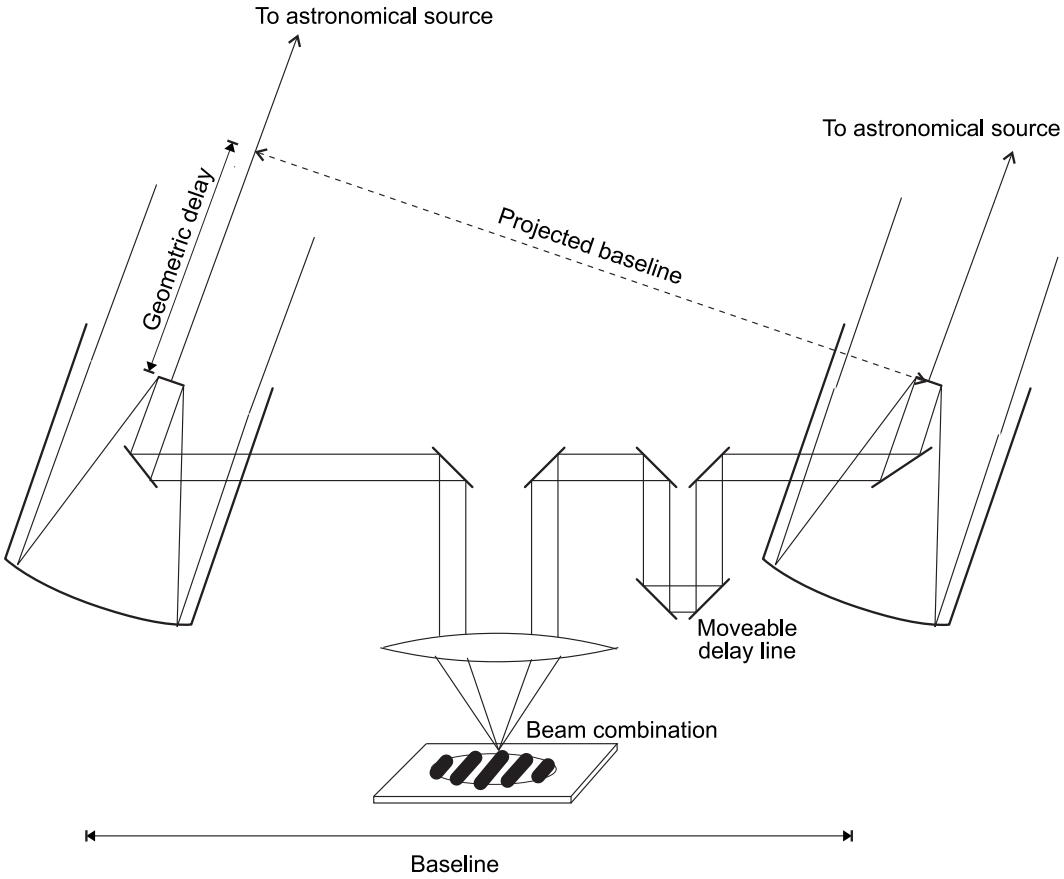

Figure 1.1: General design of an optical interferometer. The light beams collected by two (or more) telescopes are brought together by means of optical elements, and their optical paths are equalised by means of an optical delay line. The combination of the light beams produces interference fringes, spatially encoded in the image plane (as represented) or temporally encoded in the pupil plane by modulating the optical path difference (OPD) between the beams.

and coating in order to preserve the relative polarisation of the beams. A moveable delay line is used to compensate for the external delay, which constantly changes due to the Earth's rotation.

- **Beam combination.** There are essentially two types of beam combination, depending on the arrangement of the beams when they are brought together. Co-axial beam combination, the most widely used technique, consists in superposing the beams on a 50/50 beam splitter, and only works pair-wise. Alternately, the beams can also be brought together at a common focus from various directions, in an arrangement called multi-axial beam combination producing the equivalent of Young's fringes. This is the case depicted in Figure 1.1. Advanced beam combination methods, such as pupil densification (Labeyrie 1996) and related techniques will not be discussed here.
- **Detection.** Fringe detection is generally performed in a image plane for multi-axial beam combination and in a pupil plane for co-axial beam combination. In the first case, the fringes are encoded spatially on a focal plane array, and are seen as an intensity modulation of a classical Airy pattern as the actual delay between the beams varies at different points of the focal plane. In the latter case, the fringes are encoded temporally on two single-pixel detectors placed at each output of the beam splitter by modulating the optical path in one of the two beams by means of a dither mirror. In both cases, the detection of the full interferogram has to be faster than the atmospheric coherence time (typically $1 - 10$ msec), and requires low-noise, high read-out speed detectors.

Another important functionality of an optical interferometer is the ability to actively track the white-light fringe, which moves by up to hundreds of microns within sub-second timescales due to atmospheric turbulence (see Section 4.2.1). There are two levels of fringe stabilisation: *coherencing* and *co-phasing* (or simply *fringe tracking*). The first one consists in tracking the full interferogram to a precision of a few wavelengths. This can be done on a rather leisurely timescale, since large optical path distance (OPD) fluctuations occur on longer timescales: update rates of $\sim$1 Hz are sufficient except for the worst seeing conditions. In the case of fringe tracking, the OPD is tracked in real time within a small fraction of wavelength . This technique will be further described in Chapter 4, together with a more detailed description of the effects of atmospheric turbulence. Other standard functions in interferometry, such as wavefront cleaning by spatial or modal filtering, will also be described in this dissertation (see Sections 3.1.3 and 4.1.3).

1.2 Current interferometric facilities

1.2.1 Facilities from the 1980s and 90s

Following the successful demonstration of stellar interferometry with separate telescopes (Labeyrie 1975), various interferometric projects have been pursued around the world. A number of permanent interferometric facilities have been built between the mid-1980s and the mid-1990s and used up to now. They are generally characterised by the use of small telescopes, modest baselines ($\lesssim$ 100 m) and operation in the visible or near-infrared domains. In the following paragraph, we briefly review some technical aspects and the major scientific results achieved with these facilities, starting with the oldest ones.

- **Grand Interféromètre à 2 Télescopes (GI2T, 1985).** Operating since 1985 with two 1.5 m telescopes separated by up to 65 m, GI2T works nowadays with a visible beam combiner (REGAIN) including a spectrograph providing spectral resolution up to 30000. GI2T has been successful in studying the circumstellar environment of active hot stars (Be stars) thanks to the combination of high angular resolution and high spectral resolution (Stee 2003). In addition, the polarimetric mode of the GI2T is a powerful tool to study stellar magnetism and activity (Rousselet-Perraut et al. 2004).

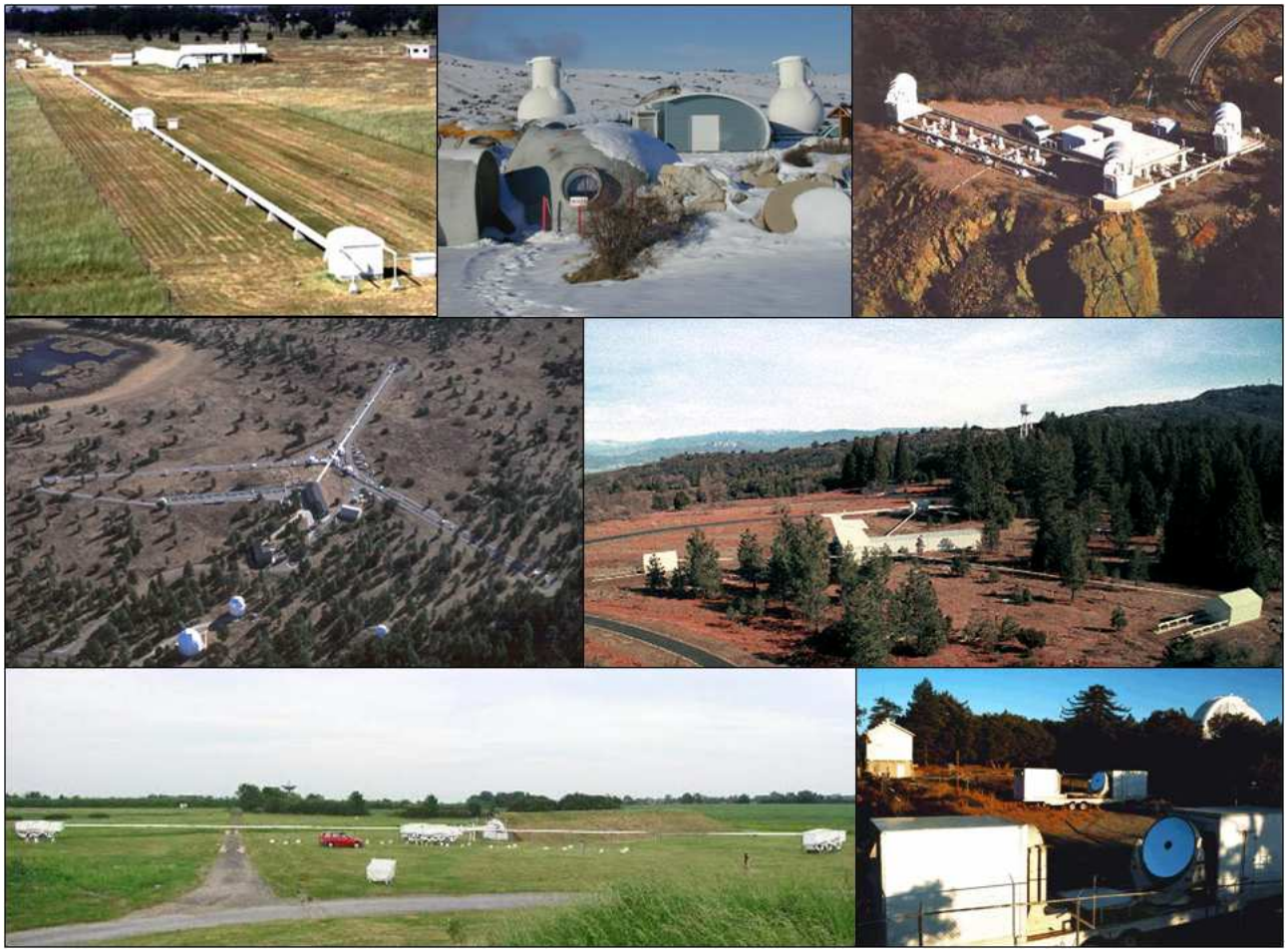

Figure 1.2: Pictures of interferometric facilities around the world. From left to right and top to bottom: SUSI, GI2T, IOTA, NPOI, PTI, COAST and ISI.

- **Infrared Spatial Interferometer (ISI, 1988).** ISI is the only infrared stellar interferometer working with heterodyne beam combination, using CO_2 lasers as local oscillators at wavelengths around 10 μm. With its three 1.65 m telescopes arranged over baselines up to 70 m, it provides some imaging capabilities thanks to closure-phase measurements. Thanks to ISI, the diameters of supergiant and Mira stars were found to be significantly (up to twice) larger in the mid-infrared than in the near-infrared (Weiner et al. 2003), suggesting the presence of a semiopaque H_2O shell surrounding the star (Weiner 2004). ISI was also used to image the dust disks around young stars (Tuthill et al. 2002).

- **Sydney University Stellar Interferometer (SUSI, 1992).** With its 11 aligned 20 cm siderostats, SUSI has potential baselines up to 640 m, but the longest operational baseline is currently restricted to 160 m. Pair-wise beam combination is performed in the visible range. While scientific results from SUSI have been mostly limited to the measurement of fundamental stellar parameters in the past, including binaries (Davis et al. 2005), scattering by atmospheric dust around Mira-type stars has recently been observed in the polarimetric mode (Ireland et al. 2005).

- **Cambridge Optical Aperture Synthesis Telescope (COAST, 1992).** The facility comprises five 40-cm siderostats arranged in a Y-shaped configuration, with baselines up to 67 m. It was the first interferometer to produce true synthesis images at optical wavelengths (visible and near-infrared). Scientific results from COAST include stellar surface imaging, leading for instance to the discovery of brightness asymmetries on Betelgeuse's photosphere (Young et al. 2000).

- **Infrared-Optical Telescope Array (IOTA, 1993).** With its three 45-cm siderostats arranged on short baselines (< 40 m), IOTA has been one of the most successful facilities so far. It has been extensively used to measure the diameters of Mira and supergiant stars, especially with the innovative near-infrared fibre-linked beam combiner FLUOR (at IOTA until 2003). These studies have led to a new model for the structure of these stars, which are now understood to be surrounded by an extremely thin and nearly transparent molecular envelope whose opacity in the infrared is dominated by a single high layer (Perrin et al. 2004a). The study of Young Stellar Objects (YSO) has also greatly benefited from the IOTA capabilities, with the important result that the characteristic sizes of the near-infrared emitting regions are larger than previously thought (Millan-Gabet et al. 2001). The addition of a third telescope and of a new 3-way integrated optics beam combiner (IONIC) has improved the facility with imaging capabilities.
- **Navy Prototype Optical Interferometer (NPOI, 1994).** Two operational modes are available at NPOI: a Y-shaped, 6-element array with baselines up to 437 m is used for imaging, while a kite-shaped, 4-element array is used for wide-angle astrometry. The arrays are composed of 50-cm siderostats connected by vacuum pipes and work in the visible. The 6-way imaging beam combiner has provided scientific results on various objects, such as elongated rapidly rotating stars (Peterson et al. 2004), multiple stars (Hummel et al. 2003), stellar surfaces (Ohishi et al. 2004) or the environment of Be stars (Tycner et al. 2005). The astrometric mode is still under commissioning.
- **Palomar Testbed Interferometer (PTI, 1995).** Built as a testbed for interferometric techniques such as dual-star narrow-angle astrometry, phase referencing and fringe tracking, the PTI has been one of the most scientifically productive interferometers. Three 40-cm apertures are combined pair-wise in the near-infrared K band with baselines between 85 m and 110 m. Recent results include high-precision astrometric measurements of multiple stars (Muterspaugh et al. 2005; Lane & Muterspaugh 2004) as well as "classical" $\mathcal{V}^2$ observations of various objets. For instance, the oblateness of rapidly rotating stars was first demonstrated at PTI (van Belle et al. 2001). Other major results concern the inner region of dusty disks around late- and early-type young stars (Akeson et al. 2005b; Eisner et al. 2004) or a revised distance to the Pleiades star cluster (Pan et al. 2004).
- **Mitaka optical and InfraRed Array (MIRA, 1998).** MIRA is a Japanese interferometer consisting of two 30-cm siderostats separated by 30 m. It has been mainly used for technical purposes and has not provided scientific results up to now (Nishikawa et al. 2004).

1.2.2 A new generation of arrays

Based on the success of the facilities from the 1990s, new interferometers with improved performances have been and are currently being built. There are various features distinguishing the new facilities from the old ones. First, they generally benefit from larger telescopes, equipped with adaptive optics in order to provide a stable image despite atmospheric turbulence. This is a major improvement as it largely increases the (usually low) sensitivity of interferometers and allows extragalactic targets to be observed. In the same context, fringe tracking is now becoming a standard feature, and also increases the sensitivity of the instruments as they are not forced to record the interferograms within the coherence time of the atmosphere (typically a few milliseconds). The use of spatial filtering, which provides a stable interferometric throughput, is also becoming a standard. Dual-feed capabilities are also being developed to allow for precise astrometric measurements. The new arrays also benefit from new beam combination techniques and are generally equipped with state-of-the-art infrared detectors.

Current facilities

Among the new facilities already in use, the Very Large Telescope Interferometer (VLTI) and the Keck Interferometer are the most prominent. Both have obtained their first fringes in 2001 and are based on a combination of large 10-m class telescopes with smaller 2-m class auxiliary ones. They are equipped with various instruments with a wavelength coverage from the near- to the mid-infrared. Technical details related to the Keck-I and the VLTI will be further discussed in Chapter 3. Another facility, more modest yet very performing, is the CHARA Array, commissioned in 1999 but extensively used for science only since 2004. Its 1-m class telescopes provide a good sensitivity, but cannot compete with the two big arrays. Yet, CHARA has some major advantages, namely long and numerous baselines, which will be described in more detail in Section 2.1.2.

Upcoming facilities

The Large Binocular Telescope (LBT), consisting of two 8.4-m primary mirrors on a single mounting, will be the next facility to see its first fringes, expectedly in late 2006 (Herbst & Hinz 2004). With its 14.4 m centre-to-centre spacing, it provides a spatial resolution equivalent to a 22.8 m telescope in the Fizeau imaging mode (between the outer edges of the two pupils). It will also host a nulling beam combiner with 14.4 m baseline. Both instruments will strongly benefit from the original design of the LBT, where delay lines are not needed and a small number of mirrors are required to propagate the light to the (cryogenic) interferometric beam combiner.

At Mauna Kea, Perrin et al. (2004b) intend to combine the light collected by various 10-m class telescopes thanks to a fibre-linked instrument (‘OHANA). The maximum telescope separation of 800 m can provide an angular resolution as good as 0.25 milliarcseconds (mas) at 1.2 μm. The combination of long baselines and large apertures will open the path to more discoveries in the field of extragalactic studies. Injection of stellar light into the fibres has already been demonstrated, as well as a first fibre-linked combination of the two Keck telescopes (Perrin 2005).

Let us also cite the Magdalena Ridge Observatory Interferometer (Creech-Eakman et al. 2004), which is envisaged to comprise ten 1.4-m movable telescopes in a Y-shaped configuration with baselines extending from 8 to 400 metres, delay lines capable of tracking well-placed sources during 6 continuous hours, fringe-tracking in the near-infrared, and to undertake science observations at both near-infrared and optical wavelengths. Its first fringes are expected for 2007.

In addition, new extensions of current facilities are foreseen within the next few years. For example, at the VLTI, a dual feed facility (PRIMA) will soon allow astrometric measurements with an accuracy of a few tens of microarcseconds and also increase the limiting magnitude of the first generation instruments thanks to fringe tracking (Quirrenbach et al. 2004). Still at the VLTI, several concepts for second generation instruments are currently under evaluation for implementation around 2010, such as a 4 to 8-way integrated optics near-infrared imager (Malbet et al. 2004), a mid-infrared 4-way spectro-interferometer (Lopez et al. 2004), or a demonstrator of nulling interferometry (see Section 3.4).

Major scientific results

Although they have only been used for a few years, these new facilities have opened the path to more discoveries and have brought major scientific results in various fields. One of the major breakthroughs is related to extragalactic studies: both the Keck-I and the VLTI have been used to study Active Galactic Nuclei (AGN). In the near-infrared, the Keck-I has revealed an unexpectedly compact nucleus for NGC 4151 (Swain et al. 2003), suggesting that the emission mainly originates in the central accre-

tion disk. Measurements with the VINCI instrument at VLTI (Wittkowski et al. 2004) favour a multi-component model for the intensity distribution of NGC 1068, where a part of the flux originates from scales smaller than 5 mas (0.4 pc) and another part of the flux from larger scales. Finally, additional observations of NGC 1068 obtained with MIDI at VLTI (Jaffe et al. 2004) reveal warm (320 K) dust in a structure 2.1 pc thick and 3.4 pc in diameter, surrounding a smaller hot structure. Such a configuration requires a continual input of kinetic energy to the cloud system from a source coexistent with the AGN.

Another field where the new facilities have brought an important contribution is the study of Cepheids. Thanks to precise measurements of their angular diameters and pulsations with the VLTI (Kervella et al. 2004b), the distances to several of these "standard candles" have been precisely determined, using a modified version of the Baade-Wesselink method. Moreover, these observations have allowed for the calibration of the period-radius and period-luminosity relations (Kervella et al. 2004a), which are at the basis of extragalactic distance measurements. Another critical parameter weighing in distance estimations, the projection factor, has recently been determined with the FLUOR instrument at the CHARA Array (Mérand et al. 2005).

The VLTI has been very productive in various topics of stellar physics. The coupling of interferometric and asteroseismic observations have provided new insights on the evolutionary status of various stars (Kervella et al. 2003; Thévenin et al. 2005). Radius measurements of very low mass stars have been obtained for the first time (Ségransan et al. 2003), showing a good agreement with theoretical models. Rapid rotating stars have also largely benefitted from the new interferometers, with the first oblateness measurement of a Be star (Domiciano de Souza et al. 2003), direct measurements of stellar winds (van Boekel et al. 2003), and first estimations of the gravity darkening coefficient, both at the VLTI (Domiciano de Souza et al. 2005) and the CHARA Array (McAlister et al. 2005). The study of evolved stars such as Miras, AGBs and supergiants has also been pursued with the new facilities, greatly benefitting from multi-wavelength observations and providing more precise models for these stars and their environments. Finally, young stars and their environment have also been extensively observed, leading to important results as discussed in the next section.

1.3 Application of stellar interferometry to circumstellar disks

During the last decade, the study of circumstellar disks by stellar interferometry has been mostly limited to Young Stellar Objects (YSO), i.e., pre-main-sequence stars with ages of 1 to 10 Myr, surrounded by significant amounts of dust and gas arranged in optically thick accretion disks. These disks are the remnants of the molecular clouds from which the central stars were born, and are expected to evolve into optically thin debris disks as the circumstellar material either accretes onto the central star, coagulates into planetesimals, or is blown out of the system. Characterising the inner disk properties is of utmost importance for understanding the initial conditions and steps of planet formation.

In fact, YSOs have been one of the prime targets of infrared interferometers, as they are currently the most suited instruments for the investigation of the inner region of their disks (10 AU corresponds to 67 mas at 150 pc, the typical distance of YSOs). In particular, infrared interferometers directly probe the temperature and density structure of gas and dust within the first few AU of YSO disks, which are critical ingredients in any recipe for planet formation. The discoveries brought by interferometry have been strongly supported by major advances in theoretical models of YSO in the past ten years, which have seen simple accretion scenarios of passively-heated disks (Hartmann et al. 1993; Chiang & Goldreich 1997) be complemented by a richer set of phenomena. These results are summarised below, separately for the two classes of YSOs: Herbig Ae/Be and T Tauri stars, respectively with masses above and below $2M_{\odot}$. The first attempts at detecting optically thin debris disks around main sequence stars are also discussed.

1.3.1 The interferometric view of Herbig Ae/Be stars

The first Herbig Ae/Be star to be resolved by interferometry was AB Aur, by Millan-Gabet et al. (1999) who found, using the IOTA interferometer, that its near-infrared emission has to be much larger than expected from the models. This discovery was then confirmed by a survey of 15 similar stars at IOTA (Millan-Gabet et al. 2001). An important result from this survey was that the sizes measured, when combined with the observed spectral energy distributions, essentially ruled out accretion disk models represented by blackbody disks with the canonical $T(r) \propto r^{-3/4}$ law. In addition, no variation of the visibilities was observed as the baseline orientation was changed, favouring a spherical envelope for the dust emission. The same survey, complemented by observations of T Tauri stars, was used by Monnier & Millan-Gabet (2002) to produce a diagram showing significant correlation between the size of the near-infrared excess emission and the luminosity of the star, as one would expect for an inner dust disk (or envelope) truncated by dust evaporation close to the star. An optically thin cavity was thus suggested around YSOs, while the classical model assumed the presence of optically thick gas (Figure 1.3). This result was later confirmed by additional observations at the Keck-I (Monnier et al. 2005). In parallel, another survey at PTI led essentially to the same conclusion of a revised size for the inner disk (Eisner et al. 2004), also favouring disk models with a puffed-up inner rim as proposed by Dullemond et al. (2001) except for the most massive Herbig Be stars. Unlike the previous one, this survey allowed for a determination of the disk inclination for most targets, which reconciles the interferometric view with a disk-like geometry.

The VLTI has also recently obtained important results on Herbig Ae/Be stars. In particular, the MIDI instrument has provided the first spatially and spectrally resolved mid-infrared view of these objects, with

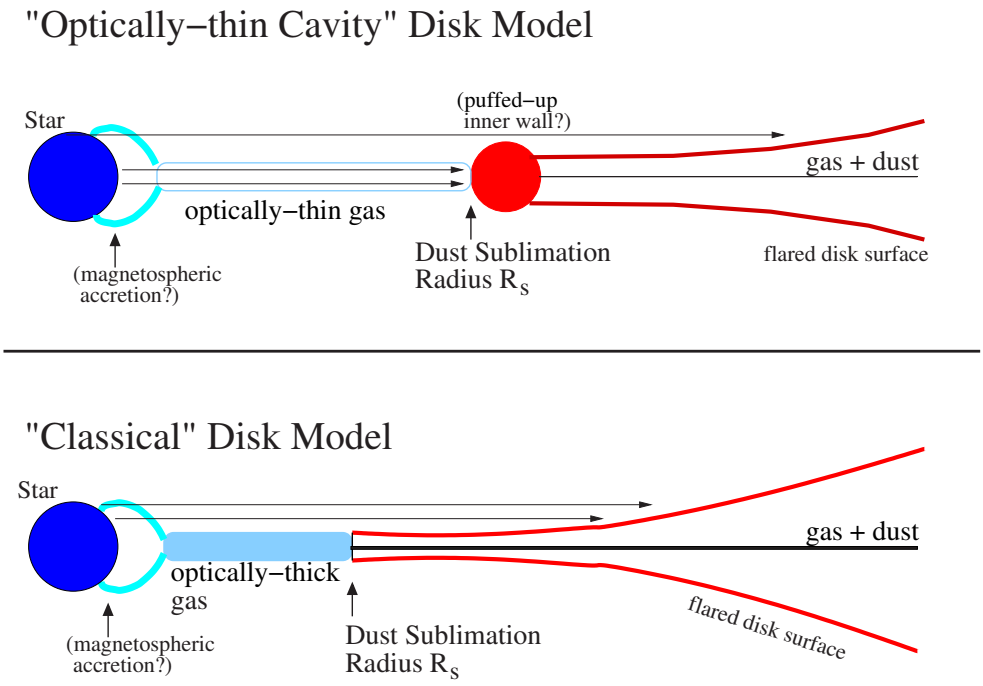

Figure 1.3: Top: Cross section in the inner disk region for the "inner cavity" disk model proposed by Monnier et al. (2005) to explain interferometric observations of Herbig Ae/Be stars. The presence of a puffed-up inner rim is predicted by theoretical models (Natta et al. 2001; Dullemond et al. 2001) and seems in agreement with recent observations (Eisner et al. 2004). Bottom: Classical accretion disk model. The presence of optically thick gas in the midplane partially shields the innermost dust from stellar radiation, causing the dust sublimation radius to shrink for the same sublimation temperature. Courtesy of J. Monnier.

characteristic sizes of 1 to 10 AU for the mid-infrared emitting regions (Leinert et al. 2004). Although in qualitative agreement with the predictions from passively heated models, the data show quantitative discrepancies with these models and therefore ask for a next step in the modelling of circumstellar disks. This study supports the phenomenological classification of Herbig Ae/Be stars into categories by their mid-infrared colour and the distinction of these categories by flaring-dominated versus non-flaring-dominated circumstellar dust distributions. The spectroscopic capabilities have also contributed to the study of these stars, showing the dust in the innermost regions of the disk to be highly crystallised and to be dominated by olivine, while outer regions have a lower degree of crystallinity (van Boekel et al. 2004). These observations imply that silicates crystallise before any terrestrial planets are formed. Even more recently, the first scientific results of the AMBER instrument have focused on MWC 297, an embedded Be star, showing the star to be surrounded by a possibly still accreting flat equatorial disk and an outflowing wind which has a much higher velocity in the polar region than at the equator (Malbet et al. 2006).

Finally, nulling interferometry (on a single masked pupil) has obtained one of its first on-sky results on Herbig Ae/Be stars, showing the spatial extent of their mid-infrared emission to be much smaller than predicted (Hinz et al. 2001). This result, wich contradicts after interferometric studies, has still to be confirmed by a broader survey, currently underway at the MMT and Magellan telescopes. Further observations have suggested the presence of a large inner gap in the flared disk around the Herbig Ae star HD 100546 (Liu et al. 2003), and a more complex structure of AB Aur's circumstellar environment than anticipated (Liu et al. 2005).

1.3.2 The interferometric view of T Tauri stars

The study of T Tauri stars by infrared interferometry has been somewhat more limited than in the case of Herbig Ae/Be stars, in part due to the lower luminosity of these less massive sources. Yet, the first Young Stellar Object to be observed by interferometry was FU Ori, a rare type of T Tauri star whose emission is dominated by accretion luminosity (Malbet et al. 1998). The disk size was then found to be roughly consistent with expectations from a simple flat disk model. Four T Tauri stars were then resolved by Akeson et al. (2000) at PTI, revealing a larger near-infrared emitting region than predicted by simple accretion models. This result was confirmed two years later (Akeson et al. 2002) by additional observations of T Tau and SU Aur, and by the first scientific observations of the Keck-I on DG Tau (Colavita et al. 2003).

Based on these observations, new models have been built, including disk flaring and puffed-up inner rims as in the case of Herbig Ae/Be stars. Further observations at PTI (Akeson et al. 2005b) and Keck-I (Eisner et al. 2005) are generally in agreement with these revised models, and show that the presence of gas within the sublimation radius of dust, probably extending down to the magnetospheric truncation radius, can also be a significant component to the inner disk flux. A range of inner dust disk properties have been recently suggested by Akeson et al. (2005a) with the Keck-I, possibly related to the various evolutionary statuses of the target sources. These observations also have important implications for planet formation scenarios, as the measured inner dust radii (typically ranging from 0.04 to 0.3 AU) prove the presence of dust in the habitable zone (near 1 AU) at early stages of planet formation. This suggests that giant planets can penetrate the sublimation zone by migration mechanisms triggered by the large quantity of gas. Finally, new observations of FU Ori (Malbet et al. 2005) have confirmed that, unlike most T Tauri stars, this source is compatible with a standard disk model, i.e., geometrically flat and optically thick with a temperature law index close to $3/4$. This may be due to the enhanced accretion rate, as suggested by Eisner et al. (2005) on another accretion-dominated source. Such a behaviour has also been observed on massive Herbig Be stars (Eisner et al. 2004). However, recent observations of three

FU Orionis objects by Millan-Gabet et al. (2006) contradict these conclusions, as a simple accretion disk does not reproduce the low visibilities measured with the Keck Interferometer. A significant contribution to the near-infrared flux might come from scattering in the upper atmosphere of the disk (the presence of an optically thin inner disk is very implausible in the case of FU Orionis objects). This scenario is supported by recent models where circumstellar haloes account for both infrared spectroscopic and imaging data (Vinković et al. 2006).

1.3.3 First attempts at detecting debris disks

Even though many issues are still to be addressed in the context of Young Stellar Objects, interferometric studies are already trying to access the next step in planetary formation: debris disks around main sequence stars, which reveal the presence of small bodies orbiting these stars, as they are understood to be composed of second-generation dust grains produced by comet evaporation, asteroid collisions, etc. The main difficulty in the detection of these disks comes from their faintness: they are not expected to represent more than a few percent of the stellar flux in the near- and mid-infrared. Here again, stellar interferometry is only sensitive to the inner part of these disks, where the dust grains are heated up to about 1500 K. The outer part, where large quantities of dust have been found by far-infrared and sub-millimetric studies, not only does not produce a significant near-infrared contribution, but also generally lies outside the interferometric field-of-view.

The first attempt at detecting a debris disk was performed at PTI by Ciardi et al. (2001) on the prototypical debris disk star Vega. Fitting the data with a stellar limb-darkened disk model led to significant residuals displaying an organised structure. Among the possible explanations for these residuals, Ciardi et al. (2001) proposed a simple debris disk model, with 3 – 6% of Vega's near-infrared flux emanating from the disk at $r \leq 4$ AU. However, the long baseline (110 m) and limited spatial frequency range were far from ideal in order to investigate the debris disks (see Section 2.1.1), which explains why the conclusion was not unique and the determination of the circumstellar flux rather imprecise.

A second, more thorough study, was then performed by di Folco et al. (2004) with the VINCI instrument at VLTI on five Vega-like stars, including the prototypical β Pic, α PsA and ϵ Eri. Due to the limited precision of the VLTI observations at that time, and to the unavailability of short baselines, this study did not allow an unambiguous detection of warm dust around these stars. An additional difficulty came from the fact that three of the target stars are rapid rotators, thereby producing a visibility modulation similar to the signature of circumstellar dust at the available baselines. Nevertheless, the analysis provided upper limits ranging from 2 to 4% for the dust-to-star flux ratio in the K band.

Finally, the third and last published study on debris disks by interferometry has been performed by Liu et al. (2004) with the BLINC nulling instrument, working with two parts of the MMT 6.5 m telescope (see Section 3.3 for more details on this instrument). The nulling ratio measured on Vega in the N band was found to be consistent with the point-source calibrators within a 1σ uncertainty of 0.7%. This allowed for a 3σ upper limit of 2.1% to be placed on the circumstellar emission of Vega relative to its photosphere at 10.6 μm, valid for separations greater than 0.8 AU (equivalent to the resolution of BLINC at MMT). When compared to the large excess flux detected in the far-infrared regime around Vega, this result suggests a lack for warm material in the inner debris disk, which could be attributed to the sweeping influence of a giant planet within 40 AU from Vega. This conjecture will be contradicted in the next chapter, where we present the first convincing detection of warm dust around Vega.

2

A study of debris disks with CHARA-FLUOR

Contents

2.1 Principle and goals of the study 27

2.1.1 Strategy for near-infrared debris disk detection 28

2.1.2 The FLUOR instrument at the CHARA Array 30

2.2 A prototypical debris disk star: Vega 33

2.2.1 The observations 33

2.2.2 Article: *Circumstellar material in the Vega inner system revealed by CHARA-FLUOR* 34

2.3 Ongoing work and future prospects 45

2.3.1 Follow-up observations of Vega 45

2.3.2 Our next target: ϵ Eridani 45

2.3.3 Perspectives at the CHARA Array and the VLTI 47

We have shown in the previous chapter that the first attempts at detecting warm dust around debris disk stars with infrared interferometry have been mostly inconclusive, even though they have placed useful upper limits of a few percent on the star-to-disk contrast in the near- and mid-infrared. In this chapter, we further develop and refine the interferometric method for debris disk detection. We introduce the facility (CHARA) and the instrument (FLUOR) that have been used to carry out our observations, and then present the first convincing detection of hot dust around Vega, one of the "Fabulous Four" debris disk stars. Based on our measurement of the K band emission of the disk and on archival photometric data, we investigate the composition, morphology and size distribution of the warm dust surrounding Vega. This chapter ends with a brief review of the ongoing work and perspectives.

2.1 Principle and goals of the study

We have explained in the introduction of this thesis that the study of the inner part of debris disks is an important step for the understanding of the formation and evolution of planetary systems, and why it is so crucial for the future space missions dedicated to Earth-like planet detection and characterisation. Inner debris disks are expected to harbour small but significant amounts of dust, heated up to hundreds of Kelvin by the stellar radiation. Their spectrum therefore peaks in the near-infrared. Until now, traditional

methods such as photometry and single-aperture imaging have been essentially incapable of detecting the signature of these disks in the near-infrared, even around stars known the be surrounded by large amounts of cold dust in Kuiper Belt-like structures. The main challenge with the study of inner debris disks comes from the high contrast, supposed to be generally larger than 100, between the star and the disk in the near-infrared. Owing to its high dynamic range and high angular resolution, stellar interferometry is currently the best way to peer into these faint circumstellar structures.

2.1.1 Strategy for near-infrared debris disk detection

The principle of the detection comes from the fact that the extended structure (debris disk) and the compact source (stellar photosphere) have very different signatures in the Fourier spatial frequency plane: because of its extension, the debris disk is resolved at much shorter baselines than the stellar photosphere. The square visibility of the star-disk system is given by the weighed sum of the two components (with the visibility of the star given by Equation 1.2):

$$\mathcal{V}^2(b,\lambda) = \left((1-f)\frac{2J_1(\pi\theta_{\rm UD}b/\lambda)}{\pi\theta_{\rm UD}b/\lambda} + f\mathcal{V}_{\rm disk}(b,\lambda)\right)^2 , \tag{2.1}$$

assuming that the disk contributes a fraction f of the total flux of the system and has a visibility $\mathcal{V}_{\rm disk}(b,\lambda)$. Because it is resolved at shorter baselines, the disk has a lower visibility than the star, and thus reduces the visibility of the system compared to a single star. For the baselines at which the disk is completely resolved, we have $\mathcal{V}_{\rm disk} \simeq 0$ (equivalent to a purely incoherent emission) and thus, assuming that the star is not resolved ($\theta_{\rm UD} < \lambda/b$):

$$\mathcal{V}^2(b,\lambda) \simeq (1-f)^2\left(\frac{2J_1(\pi\theta_{\rm UD}b/\lambda)}{\pi\theta_{\rm UD}b/\lambda}\right)^2 . \tag{2.2}$$

Assuming a small flux ratio ($f \ll 1$), this equation becomes

$$\mathcal{V}^2(b,\lambda) \simeq (1-2f)\left(\frac{2J_1(\pi\theta_{\rm UD}b/\lambda)}{\pi\theta_{\rm UD}b/\lambda}\right)^2 , \tag{2.3}$$

showing a visibility deficit of twice the flux ratio with respect to a single star. This behaviour is illustrated in Figure 2.1 for various morphologies of the debris disk, assuring a flux ratio $f = 1\%$ between the stellar photosphere and the integrated disk brightness in all cases. The shape of the visibility deficit as a function of baseline depends on the particular morphology of the circumstellar emission, but its value at short baselines is essentially equal to twice the flux ratio. For instance, a uniform circumstellar emission, spread over the entire field-of-view, produces a smooth visibility deficit as it acts as a purely incoherent source and therefore produces a *relative* deficit of 2% at all baselines. On the other hand, a ring-like structure produces sinusoidal fluctuations of the visibility deficit around its mean, because it is more compact.

As shown in Figure 2.1, detecting a faint debris disk is a difficult task because it only weakly affects the visibility with respect to a simple star model. The best strategy to detect its presence is to use a combination of short and long baselines. Even though the presence of the debris disk has an influence on the measurements at all baselines, visibilities obtained in the lower first lobe and/or second lobe can provide a precise and almost unbiased estimation of the stellar angular radius. In fact, the contribution of the circumstellar emission at these spatial frequencies is generally negligible as compared to other effects appearing at high frequencies, such as limb-darkening, spots, or even bandwidth smearing. Moreover, it does not affect the position of the first null in the visibility curve.

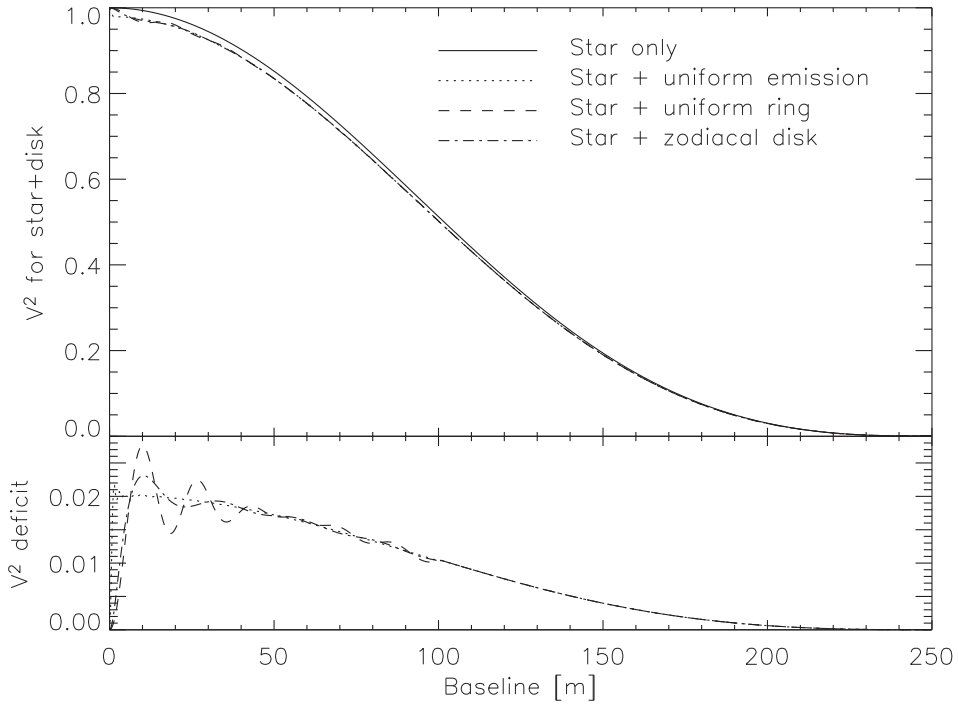

Figure 2.1: Visibility of a star surrounded by circumstellar emission compared to the visibility of the star only (an A0V star at 10 pc for this illustration), observed in the K band. Three different morphologies have been assumed for the circumstellar emission: a uniform emission spread over the whole field-of-view, a ring-like structure located between 0.2 AU (sublimation radius) and 0.3 AU from the star, and a more realistic debris disk model similar to the solar zodiacal disk. All have been scaled so that their integrated brightness represents 1% of the photospheric emission.

Once a simple uniform disk (UD) stellar model is obtained, one can compare the visibilities obtained at short baselines to the predictions of this model. If the data points are significantly below the expected visibility, the presence of an extended emission can be inferred, as it is the only possible "astrophysical" source for a deficit of visibilities at short baselines. But even at short baselines, detecting the signature of a debris disk requires a very good precision on the measured visibilities (about 1% in the case illustrated here). If many different short baselines were used, one could potentially study the morphology of the circumstellar emission. However, this would require an even better precision (a few 0.1%), which is not yet within reach with the most precise interferometers. In the following study, our only goal therefore restricts to the detection of the disk and the evaluation of the star-to-disk contrast. More ambitious goals would require a major observational effort with the current facilities.

Another difficulty in the study comes from the possible inclination of the system. A debris disk does not have the same signature when it is inclined with respect to the line of sight: it will appear more compact along one direction. Baselines with different orientations will therefore measure different visibility deficits. Such a behaviour can be easily confused with the signature of an oblate stellar photosphere, which has different angular diameters along the equatorial and polar directions. In fact, a large fraction of Vega-type stars are expected to be elongated as they are usually of rather early spectral type (typically A type) and often show a significant rotational velocity. For instance, the measured $v \sin i$ on β Pic and Fomalhaut are respectively of 130 and 93 km/s (Royer et al. 2002). Fortunately, the two targets that have been observed up to now in our programme (Vega and epsilon Eridani) are close to pole-on, so that they appear circular and their debris disks are seen face-on.

With just one precise measurement of the flux ratio between the star and disk at a given near-infrared wavelength, and using the upper limits on the disk brightness provided at other wavelengths by single-

aperture photometry, one can already estimate some of the major parameters of the inner debris disk, such as its mass and fractional bolometric luminosity. Some physical properties of the dust grains can also be inferred, but with rather large uncertainties due to the poor constraints provided by photometry. The power of this method is illustrated in the article presented in Section 2.2.2. One of the future goals of our study will be to obtain interferometric measurements at different wavelengths to improve our modelling of the disks.

2.1.2 The FLUOR instrument at the CHARA Array

Because it requires such a high precision, our observing programme could not be carried out without a suitable combination of interferometric facility and instrument, providing at the same time a large variety of baselines and a high precision on visibility measurements. Such a combination became available in the Summer of 2002, when the Fiber Linked Unit for Optical Recombination (FLUOR, Coudé du Foresto et al. 2003) was moved to the CHARA Array (ten Brummelaar et al. 2005).[5] Thanks to our collaboration with the Observatoire de Paris-Meudon and the Georgia State University, we were privileged with an access to the facility during its science commissioning period, starting in 2003. In the next sections, we briefly describe the main features of the facility and instrument.

The CHARA Array

The CHARA Array is an optical/infrared interferometer consisting of six 1-m telescopes located on top of Mount Wilson (California). It was designed and built, and is now operated by the Center for High Angular Resolution Astronomy of Georgia State University (ten Brummelaar et al. 2005). The aperture telescopes are arranged in a nonredundant Y-shaped configuration yielding 15 baselines ranging from 34 to 331 m, providing a maximum angular resolution of 1.6 mas in K band. The telescopes are named from the direction of the interferometric arm to which they belong: E1 and E2 along the East arm, W1 and W2 along the West arm, S1 and S2 along the South arm (see Figure 2.2).

The telescopes are based on 1-m primary mirrors mounted on an alt-az fork-style structures with seven-mirror coudé beam extraction. They have been placed on massive pedestals with a coudé area below where the extracted beam is polarisation compensated and directed to the central laboratory. The beam routing is performed in vacuum pipes in order to reduce dispersion (especially in the visible) and to provide good imaging quality. The delay lines, beam management subsystems, and beam combination subsystems are all housed in the central beam synthesis facility, which is thermally controlled and designed to minimise vibrations. Path length equalisation is carried out in two stages. The first stage occurs while still in vacuum with six parallel tube systems (referred to as the "Pipes of Pan" or PoPs) having assemblies with fixed delay intervals. The second stage is provided by the Optical Path Length Equalisers (OPLEs). They are out of vacuum and based on a classical cat's-eye arrangement. After passing through a longitudinal dispersion compensator, the beams are then separated into visible and infrared components and finally routed to the optical tables where the instruments are installed. The Beam Combination Laboratory (BCL) currently houses five optical tables based on functionality of subsystems. These tables contain the visible beam combiner, the infrared beam combiner ("CHARA Classic", a simple pupil-plane beam combiner), an He-Ne laser for bore sighting/alignment and a white-light source for internal fringe generation, detectors for fringe and tip/tilt tracking, and the FLUOR instrument.

[5] The same level of performance and (u, v)-plane coverage can be achieved with VINCI, a conceptual copy of FLUOR installed at VLTI. This instrument is unfortunately now unavailable to the scientific community, as its only purpose was to commission the VLTI infrastructure. The AMBER instrument should soon reach the same level of performance.

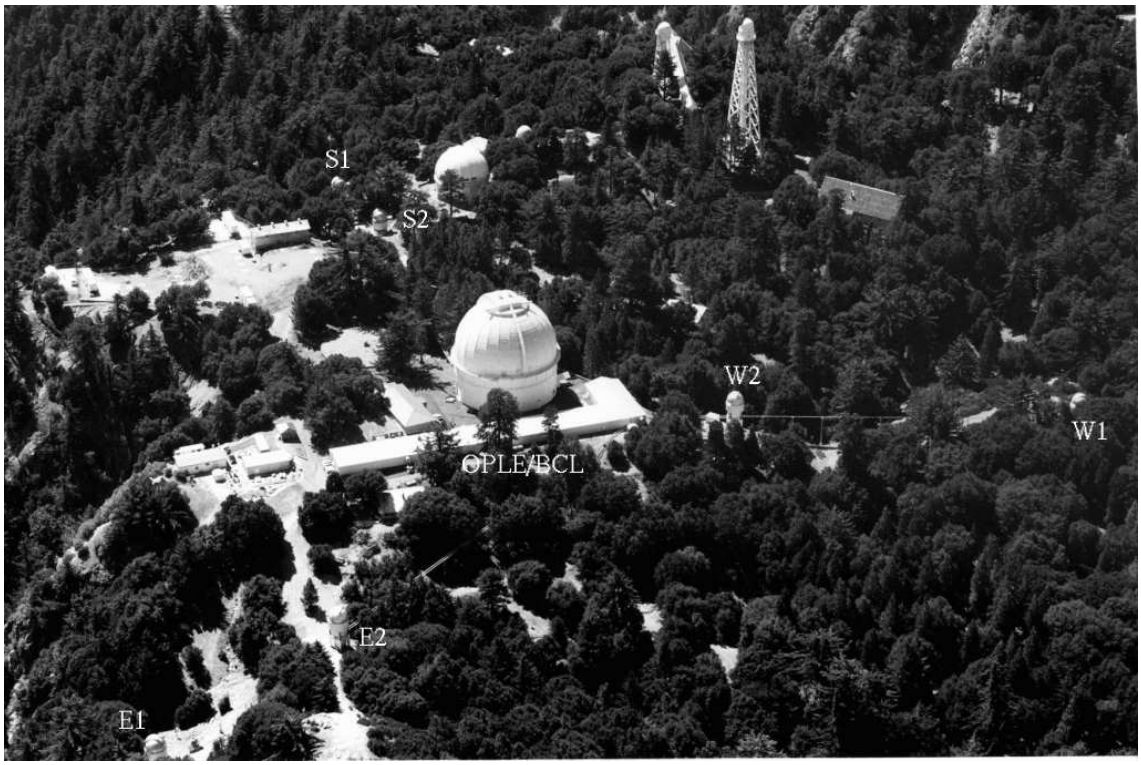

Figure 2.2: Picture of the CHARA Array taken from the North looking South. The six 1 m telescopes are identified by their name, as well as the Optical Path Length Equaliser and Beam Combination Laboratory (OPLE/BCL).

The FLUOR beam combiner

The FLUOR interferometric beam combiner started as a prototype experiment on Kitt Peak (Coudé du Foresto & Ridgway 1991) to demonstrate the potential of modal filtering for accurate visibility measurements. After a successful testing period, a modified version of the instrument was moved to Mount Hopkins (Arizona) where it became one of the focal instruments of the IOTA interferometer (Coudé du Foresto et al. 1998). It has been used at IOTA until June 2002, when it was finally moved to the CHARA Array (Coudé du Foresto et al. 2003). A thorough description of the current status of the FLUOR instrument can be found in Mérand (2005).

The principle of the FLUOR instrument (see Figure 2.3) is to use single-mode fibres for modal filtering of the light beams and for beam combination. When injected into the fibre, the electromagnetic field is forced to follow the fundamental mode of the fibre: the single-mode fibres thereby reject all the turbulent modes of the atmosphere present in the input wavefront (see Section 3.1.3). This ensures that the beams are perfectly coherent. The only residual of the atmospheric perturbations comes from the injection efficiency into the waveguide, which depends on the wavefront shape: the coupling efficiency is given by the overlap integral of the incoming wavefront with the fundamental mode of the fibre. The beam combination itself is achieved by coupling evanescent fields into an X-coupler, providing the same function as a standard beam combiner but in a small integrated component avoiding potential misalignments. In addition, a pair of Y-couplers are used to monitor the intensity fluctuations of the light injected at each telescope. This is mandatory in order to correct the interferograms for randomly unbalanced intensities in each arm. The result is an interferometric efficiency (fringe contrast on point sources) stable within typically 1% night after night, around 85% since the installation at the CHARA Array. This efficiency is further optimised with polarisation-controlling fibre loops, which are adjusted to maximise the relative degree of internal coherence between the two arms.

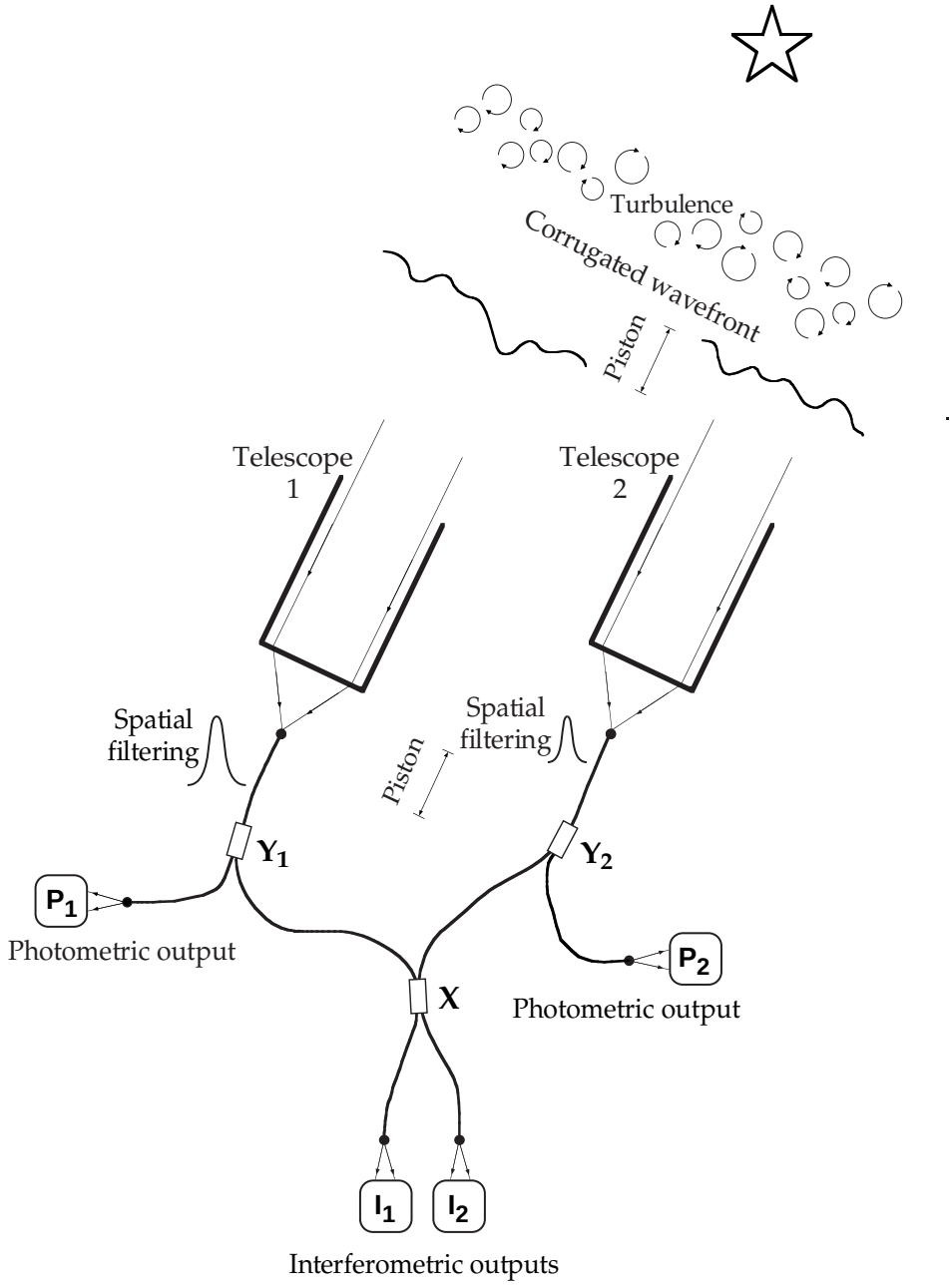

Figure 2.3: Principle of the FLUOR instrument (courtesy of V. Coudé du Foresto).

Because beam combination is done in the pupil plane, the fringe packet has to be recorded by temporally modulating the optical path in one of the two arms. This function is provided by a piezo-activated scanning mirror, which performs an optical path modulation of ∼110 μm in typically half a second. The fringe scanning frequency is set by the coherence time of the atmosphere: the piston mode of turbulence should not make the fringes drift by too large an amount during the acquisition in order to record a clean interferogram.[6] For each scan, the location of the central fringe is identified, compared with the expectation, and the OPD error so measured is fed back to the CHARA delay line. The OPD scanning frequency determines the sensitivity of the instrument: the source must be bright enough in order to produce a sufficiently large number of photons in a few milliseconds (the typical read-out frequency of the detector is of 500 Hz). The magnitude limit of the FLUOR instrument at the CHARA Array is currently $K \simeq 5$.

[6]See Section 4.2.1 for a thorough discussion of piston and its influence on interferometric measurements.

On-source scans are collected by batches of a few hundreds and complemented by off-source and single-beam calibration signals. The visibility of the fringe packet is estimated from the recorded interferogram using a data reduction software based on wavelet analysis (Kervella et al. 2004c). The statistical error on the estimation of the final visibility, related to the detection process, is typically of the order of 1%. Another source of error comes from the imperfect knowledge of the instrumental efficiency, which is estimated by observing calibration stars before and after the target source. This contribution can generally be reduced down to or below the level of statistical errors by a careful choice of the calibration stars.

2.2 A prototypical debris disk star: Vega

Vega was an obvious choice as a first target for our programme because it is the only one of the *Fabulous Four* debris disk stars to be located in the northern hemisphere, and because it has been extensively studied by various instruments. Vega is in fact the first star for which a far-infrared excess was detected, using the IRAS satellite (Aumann et al. 1984). Moreover, its near-infrared photometry has been extensively measured by many single-aperture telescopes, as it is the traditional calibration standard for photometric measurements. In addition, it is the only debris disk star to have been observed both in the near- and the mid-infrared by interferometric instruments (Ciardi et al. 2001; Liu et al. 2004).

2.2.1 The observations

After an unsuccessful attempt at observing Vega in July 2003 (due to nearby forest fires), we prepared a one-month observing programme entirely devoted to Vega for Spring 2005. The objective of this observing programme was two-fold: on one hand detect or at least put an upper limit on the near-infrared emission from the debris disk, and on the other hand study Vega's photospheric brightness distribution in order to constrain its physical parameters and its rotation velocity.

Between May 20th and June 17th 2005, we have obtained a large quantity of data on Vega at various baselines: S1−S2, W2−E2, S1−W2, W1−E2, S1−E2 and W1−E1, with respective ground lengths of 34, 156, 211, 251, 279 and 314 meters. Among the recorded batches, only 39 made it through the quality test of the data reduction software. The (u, v) coordinates of these data points are illustrated in Figure 2.4, overlayed on a model for Vega's two-dimensional Fourier appearance. The data acquired at long baselines (lower first lobe and second lobe) were used by Aufdenberg et al. (2006) to derive a complete model for Vega's physical parameters, showing that a Roche-von Zeipel model atmosphere rotating at 91 ± 3% of the angular break-up rate provides a very good match to the data. The inclination of the rotating axis has been estimated to $5.3^{+0.7}_{-0.3}$ degrees, i.e., very close to pole-on. In the following discussion, we will assume Vega to be seen pole-on, an approximation valid in our case because such a small inclination has a negligible influence on the projected image of the debris disk at our level of precision. In addition, the model proposed by Aufdenberg et al. (2006) predicts that Vega's spectral energy distribution viewed from its equatorial plane is significantly cooler than viewed from its pole. This equatorial spectrum may have a significant influence on the modelling of Vega's debris disk, but was not taken into account in our study (performed before this new model was available).

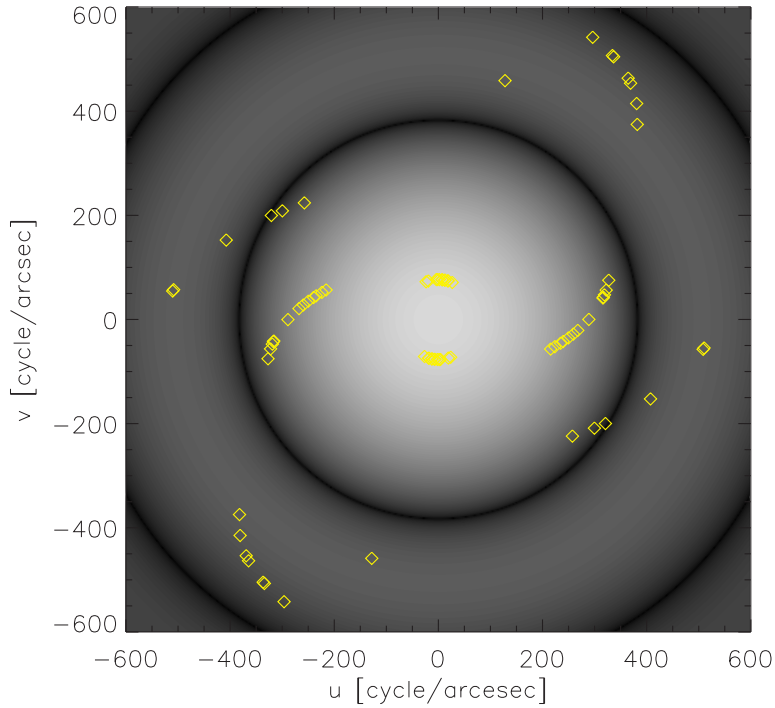

Figure 2.4: The sampling of the (u, v)-plane for the CHARA-FLUOR Vega data set. The diamonds represent the monochromatic sampling at 2.145 μm within the K band. Two-telescope observations have a 180° ambiguity in the position angle, therefore we plot two coordinates, (u, v) and $(-u, -v)$, for each of the 39 data points. These (u, v) points overlay a model for Vega's two-dimensional monochromatic Fourier appearance. The CHARA baselines sample the first lobe, first null, and second lobe of Vega's visibility curve.

2.2.2 Article: *Circumstellar material in the Vega inner system revealed by CHARA-FLUOR*

In the following paper (Absil et al. 2006b, accepted for publication in Astronomy & Astrophysics), we present the results of our interferometric observations of Vega and provide the first precise estimation of the near-infrared excess due to hot dust around a main sequence star. The discussion has been restricted to the measurements obtained in the first lobe of Vega's visibility curve, as the combination of lower first lobe data with short baseline data is sufficient to derive both a precise uniform disk (UD) stellar diameter and an estimation of the total circumstellar emission at short baselines. Second-lobe data are mostly sensitive to the actual photospheric brightness distribution, which is of little interest in our case.

Astronomy & Astrophysics manuscript no. 4522
February 22, 2006
© ESO 2006

Circumstellar material in the Vega inner system revealed by CHARA/FLUOR

O. Absil[1,⋆], E. di Folco[2,3], A. Mérand[2], J.-C. Augereau[4], V. Coudé du Foresto[2], J. P. Aufdenberg[5], P. Kervella[2], S. T. Ridgway[5,6], D. H. Berger[6], T. A. ten Brummelaar[6], J. Sturmann[6], L. Sturmann[6], N. H. Turner[6], and H. A. McAlister[6]

[1] Institut d'Astrophysique et de Géophysique, Université de Liège, 17 Allée du Six Août, B-4000 Liège, Belgium
e-mail: absil@astro.ulg.ac.be
[2] LESIA, UMR8109, Observatoire de Paris-Meudon, 5 place Jules Janssen, F-92195 Meudon, France
[3] Observatoire de Genève, 51 chemin des Maillettes, CH-1290 Sauverny, Switzerland
[4] Laboratoire d'Astrophysique de l'Observatoire de Grenoble, UMR CNRS/UJF 5571, BP 53, F-38041 Grenoble Cedex 9, France
[5] National Optical Astronomical Observatory, 950 North Cherry Avenue, Tucson, AZ 85719, USA
[6] Center for High Angular Resolution Astronomy, Georgia State University, PO Box 3969, Atlanta, Georgia 30302-3965, USA

Received 16 November 2005 / Accepted 6 February 2006

ABSTRACT

Context. Only a handful of debris disks have been imaged up to now. Due to the need for high dynamic range and high angular resolution, very little is known about the inner planetary region, where small amounts of warm dust are expected to be found.
Aims. We investigate the close neighbourhood of Vega with the help of infrared stellar interferometry and estimate the integrated *K*-band flux originating from the central 8 AU of the debris disk.
Methods. We performed precise visibility measurements at both short (~30 m) and long (~150 m) baselines with the FLUOR beam-combiner installed at the CHARA Array (Mt Wilson, California) in order to separately resolve the emissions from the extended debris disk (short baselines) and from the stellar photosphere (long baselines).
Results. After revising Vega's *K*-band angular diameter ($\theta_{\rm UD} = 3.202 \pm 0.005$ mas), we show that a significant deficit in squared visibility ($\Delta V^2 = 1.88 \pm 0.34\%$) is detected at small baselines with respect to the best-fit uniform disk stellar model. This deficit can be either attributed to the presence of a low-mass stellar companion around Vega, or as the signature of the thermal and scattered emissions from the debris disk. We show that the presence of a close companion is highly unlikely, as well as other possible perturbations (stellar morphology, calibration), and deduce that we have most probably detected the presence of dust in the close neighbourhood of Vega. The resulting flux ratio between the stellar photosphere and the debris disk amounts to $1.29 \pm 0.19\%$ within the FLUOR field-of-view (~7.8 AU). Finally, we complement our *K*-band study with archival photometric and interferometric data in order to evaluate the main physical properties of the inner dust disk. The inferred properties suggest that the Vega system could be currently undergoing major dynamical perturbations.

Key words. Stars: individual: Vega – Circumstellar matter – Techniques: interferometric

1. Introduction

Vega (HD 172167, A0V, 7.76 pc) is probably one of the most important stars in astrophysics, as it has been used as a photometric standard for more than a century (Hearnshaw 1996). However, with the advent of infrared space-based telescopes, it was discovered to have a large infrared excess beyond 12 μm with respect to its expected photospheric flux (Aumann et al. 1984). This was identified as the thermal emission from a circumstellar disk of cool dust located at about 85 AU from Vega. Since this first discovery of a circumstellar dust around a main-sequence (MS) star, photometric surveys with IRAS (Fajardo-Acosta et al. 1999) and ISO (Laureijs et al. 2002) have shown that about 10% of MS stars have significant infrared excess in the 20 – 25 μm region.

Since the mid-1980s, great attention has been paid to Vega and other Vega-like stars. They have been imaged from the millimetric domain down to the visible, revealing circumstellar dust arranged in various shapes. For instance, Vega is known to be surrounded by a smooth annular structure similar to the solar Kuiper Belt, containing about $3 \times 10^{-3} \mathcal{M}_\oplus$ of dust grains (Holland et al. 1998; Su et al. 2005), which also shows some clumpy components (Koerner et al. 2001; Wilner et al. 2002). However, due to the limitation in angular resolution of current telescopes, very little is known about the innermost part

Send offprint requests to: O. Absil

⋆ O. A. acknowledges the financial support of the Belgian National Fund for Scientific Research (FNRS).

Table 1. Individual measurements. Columns are: (1, 2) date and time of observation; (3, 4) projected baseline length and position angle (measured East of North); (5) squared visibility after calibration and error; (6, 9) HD number of calibrators used prior and after the given data point respectively, 0 means that there was no calibrator; (7, 8, 10, 11) quantities used for computing the correlation matrix as in Eq. (26) of Perrin (2003): σ_{V^2} are errors on the estimated visibility of the calibrators.

Date	UT	Projected baseline (m)	Position angle (°)	Calibrated V^2 (×100)	HD_a	α	$\sigma_{V_a^2}$	HD_b	β	$\sigma_{V_b^2}$
2005/05/21	06:17	101.60	-76.85	20.4 ± 1.14	0	0.000	0.000	165683	0.330	0.870
	07:31	127.86	-90.04	6.1 ± 0.25	176527	0.050	0.870	176527	0.060	1.025
	08:20	141.07	-97.43	2.6 ± 0.08	176527	0.026	1.025	173780	0.039	0.896
	08:59	148.55	-102.96	1.3 ± 0.04	173780	0.024	0.896	173780	0.017	0.895
2005/05/22	06:05	98.63	-75.25	23.2 ± 0.22	159501	0.240	0.467	159501	0.064	0.624
	06:24	105.77	-79.02	18.2 ± 0.20	159501	0.142	0.467	159501	0.101	0.624
	06:29	107.70	-80.00	16.8 ± 0.18	159501	0.120	0.467	159501	0.107	0.624
	06:39	111.61	-81.97	14.4 ± 0.15	159501	0.082	0.467	159501	0.115	0.624
	06:49	115.39	-83.83	12.2 ± 0.14	159501	0.052	0.467	159501	0.117	0.624
	06:59	118.79	-85.51	10.4 ± 0.12	159501	0.030	0.467	159501	0.115	0.624
	08:18	141.45	-97.68	2.6 ± 0.07	173780	0.014	0.624	173780	0.051	0.897
	08:23	142.62	-98.45	2.4 ± 0.06	173780	0.011	0.624	173780	0.051	0.897
	08:34	144.75	-99.93	2.0 ± 0.06	173780	0.005	0.624	173780	0.049	0.897
2005/06/13	05:22	33.59	20.55	84.2 ± 1.42	168775	0.543	0.152	168775	0.362	0.153
	06:15	33.85	13.58	83.4 ± 0.92	168775	0.269	0.153	168775	0.628	0.153
	06:46	33.92	9.33	84.5 ± 0.73	168775	0.419	0.153	163770	0.523	0.272
	07:14	33.96	5.49	80.8 ± 0.99	163770	0.510	0.272	163770	0.419	0.272
	07:43	33.97	1.37	82.8 ± 1.35	163770	0.514	0.272	163770	0.438	0.272
	08:13	33.97	-2.95	84.5 ± 1.19	163770	0.833	0.272	168775	0.129	0.152
	09:37	33.82	-14.54	83.6 ± 0.67	163770	0.123	0.272	168775	0.784	0.152
	10:04	33.70	-18.05	83.9 ± 0.66	168775	0.574	0.152	176670	0.330	0.167
2005/06/14	07:58	33.98	-1.26	85.0 ± 0.90	176670	0.521	0.166	176670	0.400	0.166
2005/06/15	06:03	33.83	14.15	84.4 ± 1.16	176670	0.458	0.167	176670	0.457	0.167
	06:39	33.92	9.18	86.5 ± 1.35	176670	0.363	0.167	176670	0.575	0.166
	07:07	33.96	5.37	84.2 ± 1.41	176670	0.544	0.166	163770	0.392	0.272

of these debris disks, which could potentially harbour warm dust ($\gtrsim$ 300 K) heated by the star as suggested by Fajardo-Acosta et al. (1998). Such warm dust would have a signature in the near- and mid-infrared that only photometric studies have attempted to detect until recently. Indeed, Vega's near-infrared (*K*, *L*, *M*) flux was shown to be significantly above the modelled photospheric level (Mountain et al. 1985), but this discrepancy was most likely due to an inadequate photospheric model since Vega's flux is consistent with other A-type stars to within standard photometric precision of 2 − 5% (Leggett et al. 1986). In the N band, the best constraint on the thermal emission from warm dust has been obtained by nulling interferometry, with no resolved emission above 2.1% of the level of stellar photospheric emission at separations larger than 0.8 AU (Liu et al. 2004). At longer wavelengths, the recent measurements obtained with Spitzer in the far-infrared (Su et al. 2005) have not allowed for an investigation of the inner part of Vega's disk because of the limited resolution (47 AU at the distance of Vega) and because hot dust is not expected to contribute significantly to the far-infrared flux.

In this paper, we use infrared stellar interferometry to investigate the inner part of Vega's debris disk. Such an attempt had already been made by Ciardi et al. (2001), who observed Vega with the PTI interferometer on a 110 m long baseline in dispersed mode. The poor spatial frequency coverage of their observations did not allow clear conclusions, although a simple model of a star and a uniform dust disk with a 3 – 6% flux ratio was proposed to explain the observations. A more thorough study of Vega-type stars was performed with the VLTI by di Folco et al. (2004), using short and long baselines to separately resolve the two components of the system (stellar photosphere at long baselines and circumstellar emission at short baselines). Unfortunately, the visibility precision and the available baselines at the VLTI only allowed upper limits to be inferred on the flux of the inner disks. In order to better constrain the near-infrared brightness of Vega's disk, we have used the same method at the CHARA Array (ten Brummelaar et al. 2005) with an optimised set of baselines.

2. Observations and data reduction

Interferometric observations were obtained in the infrared *K* band (1.94 − 2.34 μm) with FLUOR, the Fiber Linked Unit for Optical Recombination (Coudé du Foresto et al. 2003), using the S1–S2 and E2–W2 baselines of the CHARA Array, 34 and 156 metres respectively. Observations took place during Spring 2005, on May 21st and May 22nd for E2–W2, and between June 13th and June 15th for S1–S2 (see Table 1). The FLUOR field-of-view, limited by the use of single-mode fibers, has a Gaussian shape resulting from the overlap integral of the turbulent stellar image with the fundamental mode of the fiber (Guyon 2002). Under typical seeing conditions, it has a radius

Table 2. Calibrators with spectral type, *K* magnitude, limb-darkened disk (LD) angular diameter in *K* band (in milliarcsec) and baseline (Bordé et al. 2002; Mérand et al. 2005).

	S. type	*K* mag	LD diam. (mas)	Baseline
HD 159501	K1 III	3.14	1.200 ± 0.014	E2–W2
HD 163770	K1 IIa	1.03	3.150 ± 0.034	S1–S2
HD 165683	K0 III	2.9	1.152 ± 0.014	E2–W2
HD 168775	K2 IIIab	1.74	2.280 ± 0.025	S1–S2
HD 173780	K2 III	2.0	1.950 ± 0.021	E2–W2
HD 176527	K2 III	2.04	1.765 ± 0.024	E2–W2
HD 176670	K2.5 III	1.6	2.410 ± 0.026	S1–S2

of 1″ (distance at which the coupling efficiency falls to 3% of its on-axis value).

The FLUOR Data Reduction Software (Coudé du Foresto et al. 1997; Kervella et al. 2004) was used to extract the squared modulus of the coherence factor between the two independent apertures. The interferometric transfer function of the instrument was estimated by observing calibrators before and after each Vega data point. All calibrator stars (Table 2) were chosen from two catalogues developed for this specific purpose (Bordé et al. 2002; Mérand et al. 2005). Calibrators chosen in this study are all K giants, whereas Vega is an A0 dwarf. The spectral type difference is properly taken into account in the Data Reduction Software, even though it has no significant influence on the final result. The efficiency of CHARA/FLUOR was consistent between all calibrators and stable night after night to around 85%. Data that share a calibrator are affected by a common systematic error due to the uncertainty of the a priori angular diameter of this calibrator. In order to interpret our data properly, we used a specific formalism (Perrin 2003) tailored to propagate these correlations into the model fitting process. All diameters are derived from the visibility data points using a full model of the FLUOR instrument including the spectral bandwidth effects (Kervella et al. 2003).

3. Data analysis

3.1. Stellar diameter

The measurements obtained with the long E2–W2 baseline are particularly appropriate for a precise diameter determination, because they provide good spatial frequency coverage of the end of the first lobe of the visibility curve (see Fig. 1). Previous interferometric measurements obtained in the visible by Hanbury Brown et al. (1974) and Mozurkewich et al. (2003) were used to derive uniform disk (UD) diameters $\theta_{\rm UD}$ = 3.08 ± 0.07 (λ = 440 nm) and $\theta_{\rm UD}$ = 3.15 ± 0.03 (λ = 800 nm) respectively. In the *K* band, where the limb-darkening effect is not as strong, Ciardi et al. (2001) estimated the UD diameter to be $\theta_{\rm UD} = 3.24 \pm 0.01$ mas. We have fitted a uniform stellar disk model to our E2–W2 data, assuming that Vega's photospheric intensity $I(\phi, \lambda)$ equals the Planck function with an effective temperature of 9550 K for all angles ϕ. The best-fit diameter is $\theta_{\rm UD}$ = 3.218 ± 0.005 mas for an effective wavelength of 2.118 μm, which significantly revises the previously obtained

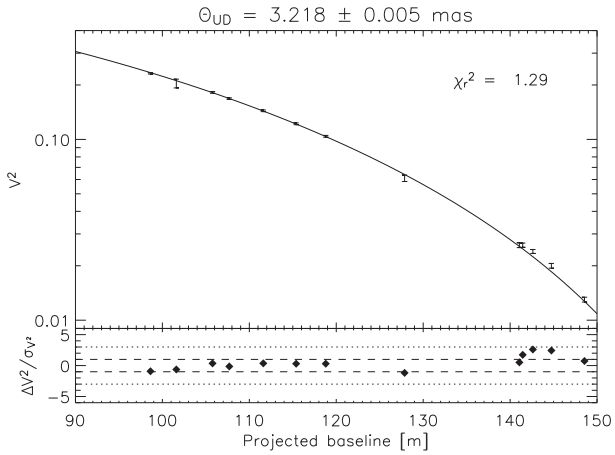

Fig. 1. Fit of a uniform stellar disk model to the E2–W2 data. The quality of the fit is satisfactory (reduced χ^2 of 1.29), with small residuals that do not display any obvious trend except for a small underestimation of the actual data for baselines between 140 and 150 m.

estimates[1]. The quality of the fit is quite good (χ^2_r = 1.29). Unlike in the PTI data of Ciardi et al. (2001), we do not see any obvious trend in the residuals of the fit, except for three points at projected baselines between 140 and 150 m which are slightly above the fit (by ∼1.5σ). In fact, Fig. 3 not only shows a significant discrepancy between the CHARA/FLUOR and the PTI data, but also between the 1999 and 2000 PTI data. Our observations do not support the scenario of Ciardi et al. (2001), who proposed a uniform dust ring with a 3 – 6% integrated flux relative to the Vega photosphere in *K* band to account for the trend that they observed in the residuals of the fit obtained with a simple limb-darkened disk (LD) stellar model.

Note that fitting an LD stellar model to our data would only marginally improve the fit (see Table 3), as the shape of the first-lobe visibility curve is not very sensitive to limb darkening. Moreover, the actual limb-darkening parameter may be significantly larger than standard tabulated values because Vega is suspected to be a fast rotating star viewed nearly pole-on and the equatorial darkening may bias the limb profile (Gulliver et al. 1994; Peterson et al. 2004). Complementary observations to our data set, obtained by Aufdenberg et al. (2006) at ∼250 m baselines, confirm this fact and lead to an accurate estimation of the *K*-band limb profile, which mostly affects visibilities beyond the first null and will not be discussed here.

3.2. Visibility deficit at short baselines

With this precise diameter estimation, we can now have a look at the short-baseline data. In fact, these points do not significantly contribute to the UD fit because of the low spatial frequencies they sample. Including all the data points in the fitting procedure gives a best-fit diameter $\theta_{\rm UD}$ = 3.217 ± 0.013 mas, but with a poor χ^2_r = 3.36. We show the reason for this poor reduced χ^2 in Fig. 2, where the S1–S2 data points are plotted as

[1] The *K*-band diameter proposed by Ciardi et al. (2001) was computed with the assumption of a flat spectrum for the Vega intensity. This explains a large part of the discrepancy with our new value.

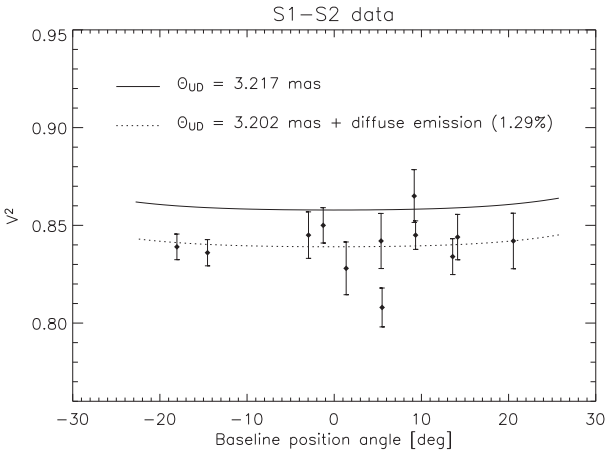

Fig. 2. The data obtained with the S1–S2 baseline (~34 m) are displayed as a function of the projected baseline's position angle together with the best UD fit computed over the whole data set (3.217 mas). The data points are significantly below the best UD fit, with a mean visibility deficit $\Delta V^2 \simeq 2\%$. The addition of a uniform diffuse source of emission in the FLUOR field-of-view reconciles the best fit with the data (dotted line). Note that there is no obvious dependence of the data points with respect to position angle, which would be indicative of an asymmetric extended emission.

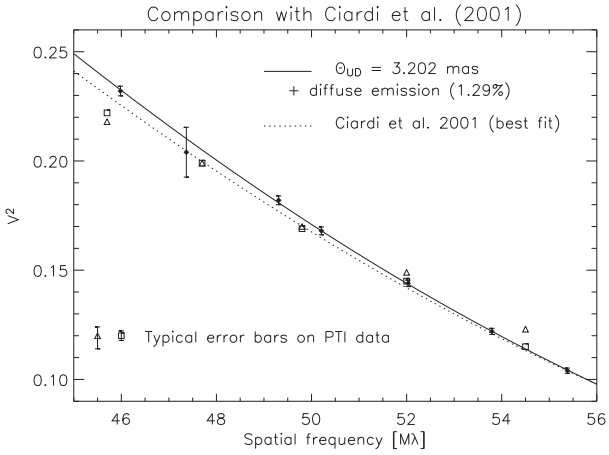

Fig. 3. Comparison of our E2-W2 data (black dots) with the observations of Ciardi et al. (2001) obtained at PTI (triangles: data acquired in 1999, squares: data acquired in 2000). The data are displayed as a function of spatial frequency, taking an equivalent wavelength of 2.145 μm for the FLUOR instrument (computed for a flat stellar spectrum as in the study of Ciardi et al. (2001)). The 1σ errors on the PTI data are shown at the bottom of the figure for the sake of clarity.

a function of position angle together with the best UD fit (solid line). The observations are consistently below the fit, with a $\Delta V^2 = 1.88 \pm 0.34\%$.

Systematic errors in the estimation of the calibrator diameters or limb-darkened profiles are possible sources of bias in interferometric observations. In order to explain the measured visibility deficit in the S1–S2 data, the diameters of the first three calibrators of Table 2 should have been underestimated by 0.26, 0.35 and 0.33 mas respectively, which represent about 10 times the estimated error on their diameters. We have made sure that such improbable errors were not present in our calibration procedure by cross-calibrating the three calibrators. No significant departure from the expected LD diameters was measured, and the calibrated visibilities of Vega do not depend on the chosen calibrator. Therefore, it appears extremely unlikely that the calibration process may have induced the observed visibility deficit.

A limb-darkened stellar model for Vega will not reconcile the best-fit stellar model with the S1–S2 data points (see Table 3), because low spatial frequencies are not sensitive to limb darkening. One may think of stellar asymmetry as a possible reason for the visibility deficit at short baselines, since the position angles of the short and long baselines are almost perpendicular (see Table 1). However, an oblateness ratio of 1.07 for Vega would be needed to explain the deficit, which would strongly contradict previous interferometric studies (van Belle et al. 2001; Peterson et al. 2004). Other stellar features such as spots would not explain this deficit either as they can only appear in the second and higher lobes of the visibility function. In fact, a natural explanation to the observed visibility deficit would be the presence of an extended source of emission in the interferometric field-of-view (e.g. disk or companion), which would be resolved with the S1–S2 baseline (i.e., incoherent emission).

In order to assess the amount of incoherent emission needed to explain the observed visibility deficit, we have added a diffuse emission, uniformly distributed in the CHARA/FLUOR field-of-view, to our UD stellar model. Fitting this new model to the complete data set gives the following final result: $\theta_{\rm UD} = 3.202 \pm 0.005$ mas, K-band flux ratio = $1.29 \pm 0.19\%$, with a significantly decreased $\chi^2_r = 1.10$ (instead of 3.36). This result is almost independent of the extended source morphology, as the spatial frequency coverage of our interferometric data is too scarce to constrain its spatial distribution. The extended structure, detected with very good confidence (almost 7σ), would thus have a relative flux contribution of 1.29% with respect to the Vega photosphere in K band when integrated over the whole field-of-view (7.8 AU in radius). Such an excess does not contradict photometric measurements in the K band, which have typical accuracies of 2 – 3% (Mégessier 1995). The result of the fit is displayed in Fig. 2 (dotted line) and Fig. 3 (solid line), as well as in Fig. 4 for a realistic debris disk model (see Sect. 4.2), which gives the same best-fit parameters.

4. Discussion

In this section, we discuss the possible sources of incoherent flux around Vega that could account for the observed visibility deficit at short baselines.

4.1. Point source

Because of our sparse sampling of spatial frequencies, a point source located in the FLUOR field-of-view could also be the origin of the observed visibility deficit. Regardless of the bound

Table 3. Influence of the limb-darkening parameter α on the best-fit diameter and the associated reduced χ^2 using the whole data set, assuming a brightness distribution $I(\mu) = \mu^\alpha$ with $\mu = \cos\theta$ the cosine of the azimuth of a surface element of the star (Hestroffer 1997). The visibility deficit measured at short baselines (S1–S2) with respect to the best-fit model is given in the last column, showing a weak dependence on the limb-darkening model.

α	Best-fit $\theta_{\rm LD}$ (mas)	χ^2_r (all data)	ΔV^2 (S1–S2)
0.0	3.217 ± 0.013	3.36	1.88%
0.1	3.264 ± 0.013	3.14	1.83%
0.2	3.310 ± 0.012	2.96	1.78%
0.3	3.356 ± 0.012	2.82	1.73%
0.4	3.402 ± 0.011	2.71	1.67%
0.5	3.447 ± 0.011	2.64	1.62%
0.6	3.491 ± 0.011	2.61	1.58%
0.7	3.536 ± 0.012	2.60	1.53%
0.8	3.579 ± 0.012	2.62	1.49%
0.9	3.623 ± 0.012	2.66	1.44%

or unbound character of the companion, there are essentially two regimes to be considered when computing the visibility of a binary system, depending on whether the fringe packet associated with the companion falls into the FLUOR observation window or not. The observation window is defined as the total optical path $L_{\rm OPD}$ scanned by the FLUOR dither mirror, which is used to temporally record the fringes. The secondary fringe packet lies outside the observation window if $|B\alpha\cos\theta| > L_{\rm OPD}/2$, where B is the baseline length, α the angular separation of the binary system, θ the angle between the baseline and the orientation of the binary system, and $L_{\rm OPD} = 102$ μm. In that case, e.g. for an angular separation larger than 350 mas at a baseline of 34 m, the flux from the secondary will contribute incoherently and will lead to the same signature as a diffuse emission in the FLUOR field-of-view. A binary star with a separation ranging between 350 and 1000 mas could therefore reproduce the observed visibilities. On the other hand, if the secondary fringe packet is inside the observation window, it will lead either to a visibility modulation of twice the flux ratio as a function of baseline azimuth if the fringe packets are superposed, or to an enhancement of the measured visibility if the fringe packets are separated. Even if such behaviour does not seem compatible with the observed visibilities, our sparse data cannot definitely rule out a solution with a close companion.

The presence of a point source located within the FLUOR field-of-view could thus possibly explain our observations. The minimum K-band flux ratio between the point source and Vega is 1.29 ± 0.19%, valid for a very close companion ($\lesssim$ 50 mas). Because of the Gaussian shape of the off-axis transmission, the companion would have a larger flux if located farther away from the star. For instance, the flux should be increased by 10% at 100 mas, by 50% at 200 mas and by 3000% at 500 mas from the star in order to reproduce the observed visibility deficit. Based on a minimum K-band flux ratio of 1.29 ± 0.19% and a K magnitude of 0.02 for Vega (Mégessier 1995), we deduce an upper limit of $K = 4.74 \pm 0.17$ for a companion.

4.1.1. Field star

Although Vega is known to be surrounded by a number of faint objects ($V > 9$) with low proper motion since the beginning of the 20th century (Dommanget & Nys 2002), these objects are far enough from Vega (at least 1′) so that they do not interfere with our measurements. In the infrared, neither adaptive optics studies (Macintosh et al. 2003; Metchev et al. 2003) nor the 2MASS survey (Cutri et al. 2003) identified any $K < 5$ object within 1′ of Vega. In fact, the local density of such objects is about 5×10^{-4} per arcmin^2 according to the 2MASS survey, so that the probability to find a $K < 5$ source within 1″ of Vega is smaller than 4.3×10^{-7}.

4.1.2. Physical companion

At the distance of Vega, the putative companion would have a maximum absolute magnitude $M_K = 5.15 \pm 0.17$. Assuming this companion to be a star of the same age as Vega itself, comprised between 267 and 383 Myr (Song et al. 2001), we use the evolutionary models developed by Baraffe et al. (1998) to deduce the range of effective temperature and mass for the companion: $T_{\rm eff} = 3890 \pm 70$ K and $\mathcal{M} = 0.60 \pm 0.025$ $\mathcal{M}_\odot$. This roughly corresponds to an M0V star (Delfosse et al. 2000).

With a $V - K$ of 3.65 (Bessel & Brett 1988), the M0V companion would have a V magnitude of 8.41 and would therefore have remained undetected in high resolution visible spectra of Vega (M. Gerbaldi, personal communication). Adaptive optics studies in the near-infrared would not have noticed the companion either, due to its very small angular distance from the bright Vega (< 1″). At longer wavelengths, the expected infrared excess due to an M0V companion is not large enough to be detected by classical photometry as its does not exceed 2% between 10 and 100 μm. Indirect methods are in fact much more appropriate to detect this kind of companion.

Astrometric measurements of Vega with Hipparcos did not detect the presence of any companion, with an astrometric precision of 0.5 mas (Perryman 1997). With a mass ratio of 4.2 between Vega ($2.5\mathcal{M}_\odot$) and its putative M0V companion ($0.6\mathcal{M}_\odot$), a 3σ astrometric stability of 1.5 mas implies that the orbital semi-major axis of the putative companion cannot be larger than 6.3 mas[2] (= 0.05 AU = $4R_\star$) with a 99% confidence assuming a circular orbit, which is anticipated for such a small separation. Such a close companion, which could also fit the interferometric data, would have an appreciable signature in radial velocity measurements, unless the binary system is seen almost exactly pole-on. Precise measurements recently obtained with the ELODIE spectrometre have shown a relative stability of Vega's radial velocity over several months, with amplitudes lower than 100 m/s and a precision of order of 30 m/s each (F. Galland, private communication). Assuming that the orbital plane of the M0V companion is perpendicular to Vega's rotation axis, inclined by 5.1° with respect to the line-of-sight (Gulliver et al. 1994), the companion should be farther than 80 AU from Vega to be compatible with the measured radial

[2] The astrometric signature of a low-mass companion is given by the ratio between the orbital semi-major axis and the mass ratio (Perryman 2000).

velocity stability. In fact, for an M0V companion at 0.05 AU from Vega not to display any radial velocity signature at the 100 m/s level, its orbital inclination needs to coincide with the plane of the sky to within ±0.13° (Perryman 2000). Even if such an inclination is possible, the probability for the system to be so close to pole-on is very low (it ranges between about 6×10^{-4} and 10^{-6} depending on the assumptions on the statistical distribution of low-mass companion orbital planes). In conclusion, even though the presence of an M0V companion close to Vega could explain the interferometric data, there is strong evidence that such a companion does not exist.

4.2. Circumstellar material

Circumstellar disks around MS stars are understood to be composed of second-generation dust grains originating from collisions between small bodies (asteroids) or from the evaporation of comets (Backman & Paresce 1993). They are assumed to be continuously replenished since dust grains have a limited lifetime (< 10 Myr) due to radiation pressure, Poynting-Robertson (P-R) drag and collisional destruction (Dominik & Decin 2003). Several studies have shown Vega to harbour a cold circumstellar dust ring ∼85 AU in radius (Holland et al. 1998; Heinrichsen et al. 1998; Koerner et al. 2001; Wilner et al. 2002). Su et al. (2005) interpreted the extended dust emission (up to 600 AU, i.e., 77″) detected by Spitzer as the signature of dust grains being expelled by radiation pressure from the Vega system as a result of a recent collision in the main planetesimal ring and subsequent collisional cascade. Even if the presence of dust in the inner part of the disk has not been detected yet due to instrumental limitations, an equivalent to the solar zodiacal cloud is expected to be found around Vega. The thermal and scattered emissions from warm grains surrounding Vega could thus be a natural explanation to the visibility deficit observed at short baselines, provided that a sufficient quantity of dust is present within 8 AU from the star.

In order to assess the adequacy of a circumstellar disk to reproduce the observations, we have fitted our full data set with the only known model for an inner debris disk, i.e., the zodiacal disk model of Kelsall et al. (1998)[3], assuming that the inner dust distribution around Vega follows the same density and temperature power-laws as for the solar zodiacal cloud. The result is displayed in Fig. 4 wherein all data points are nicely spread around the best-fit model (as expected, because our interferometric data are not sensitive to the particular morphology of the incoherent emission). The long-baseline data are also better fitted than with a simple UD model, because the presence of the dust disk has some influence on the slope of the visibility curve at long baselines (di Folco et al. 2004). The resulting flux ratio between the whole circumstellar disk and the stellar photosphere ($1.29 \pm 0.19\%$) is the same as with a simple model of uniform diffuse emission (Sect. 3.2), with the same reduced χ^2 of 1.10. Using the model of Kelsall et al. (1998), a flux ratio of 1.29% in *K* band would suggest that the dust density level in the inner Vega system is about 3000 times larger

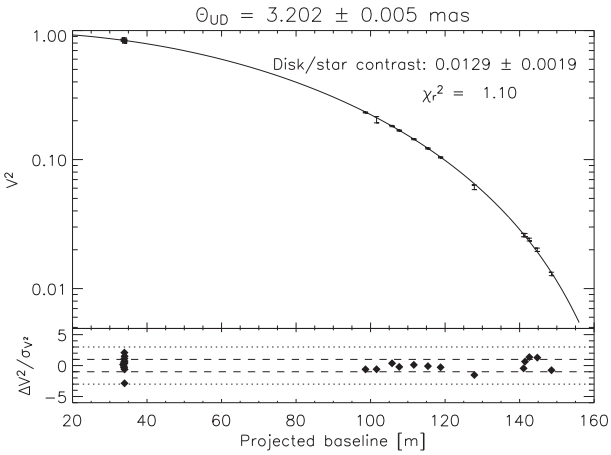

Fig. 4. Fit of a uniform stellar disk + circumstellar disk model to our full data set, using the model of Kelsall et al. (1998).

than in the solar zodiacal cloud. However, we will see later on that this model is not appropriate to represent Vega's inner disk (it would largely overestimate its mid-infrared flux), so that the comparison is not actually pertinent.

4.2.1. Physical properties of the dust grains

Let us now try to evaluate the main physical properties of the dust grains in the inner debris disk. Table 4 gives the photometric constraints on the near- and mid-infrared excess flux around Vega currently available in the literature. Photometric constraints at wavelengths longer than 12 μm are not appropriate for our purpose as they are mostly sensitive to the cold outer disk (the inner disk is not supposed to produce a significant photometric contribution in the far-infrared). The large error bars on the photometric measurements take into account both the actual error on photometric measurements and the estimated accuracy of photospheric models for Vega, to which the measurements are compared. Our study is compatible with previous near-infrared measurements but provides a much stronger constraint on the inner disk, because interferometry spatially resolves the disk from the stellar photosphere and focuses on the inner part of the disk thanks to the small field-of-view. Nulling interferometry at the MMT with the BLINC instrument also provides a valuable constraint on the mid-infrared excess (Liu et al. 2004). The sinusoidal transmission map of this nulling interferometer restricts however the observation to the part of the disk located farther than about 125 mas (∼ 1 AU) from the star. This explains why the result of this study is significantly below the estimated mid-infrared photometric excesses, as it is not sensitive to hot grains in the innermost part of the disk.

We have tried to reproduce the Spectral Energy Distribution (SED) of the infrared excess as listed in Table 4 with the debris disk model developed by Augereau et al. (1999). For that purpose, we took for Vega a NextGen model atmosphere spectrum (Hauschildt et al. 1999) with $T_{\rm eff}$ = 9600 K and $\log(g)$ = 4.0, scaled to match the observed visible magnitude (V = 0.03) at a distance of 7.76 pc, which gives a luminosity of $58.7 L_\odot$.

[3] This model was implemented in an IDL package called ZODIPIC by M. Kuchner (http://www.astro.princeton.edu/~mkuchner/).

Table 4. Available constraints on the near- and mid-infrared excess around Vega. The upper limits on the photometric excess are given as the 1σ errors on non-detections. References: (1) Campins et al. (1985); (2) Blackwell et al. (1983); (3) Rieke et al. (1985); (4) Liu et al. (2004); (5) Cohen et al. (1992), with the absolute photometric error estimated by Aumann et al. (1984). The photometric data in references (1), (2) and (3) have been compared to the most recent Kurucz photospheric model of Vega (Bohlin & Gilliland 2004), which has a typical uncertainty of 2% in the infrared (this uncertainty has been added to the estimated errors on the measurements). Note that the interferometric data from FLUOR and BLINC only sample a specific part of the inner disk, while the photometric studies include Vega's entire environment.

Wavelength	Excess	Instruments	References
1.26 μm	2.4 ± 2.9%	Catalina, UKIRT	(1), (2)
1.60 μm	−2.4 ± 3.6%	Catalina	(1)
2.12 μm	1.29 ± 0.19%	CHARA/FLUOR	This study
2.20 μm	4.1 ± 3.0%	Catalina, UKIRT	(1), (2)
3.54 μm	3.1 ± 3.0%	Catalina, UKIRT	(1), (2)
4.80 μm	7.1 ± 5.1%	Catalina, UKIRT	(1), (2)
10 μm	6 ± 4.5%	Various	(3)
10.6 μm	0.2 ± 0.7%	MMT/BLINC	(4)
12 μm	1.2 ± 5%	IRAS	(5)

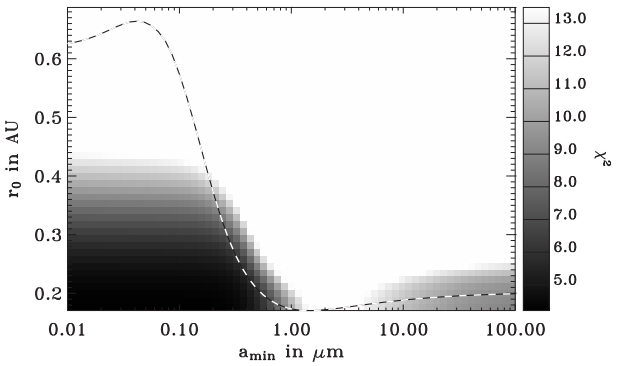

Fig. 5. Map of the χ^2 as a function of minimum grain size $a_{\rm min}$ and inner radius r_0, obtained by fitting the circumstellar disk model of Augereau et al. (1999) to the SED data of Table 4. We have assumed a surface density power-law $\Sigma(r) \propto r^{-4}$ and a grain size distribution $dn(a) \propto a^{-3.7}da$, with a maximum size of 1500 μm. In this simulation, the disk is composed of 50% amorphous carbons and 50% glassy olivines (see text). The dashed line represents the distance at which sublimation happens for dust grains of a given size (isotherm T = 1700 K). The axis labels should therefore read "a in μm" and "sublimation radius in AU" for this curve.

Various grain compositions and size distributions were used in the disk model, as well as various radial density profiles, assuming no azimuthal dependence. In each model, the sublimation temperature of the grains is set to $T_{\rm sub}$ = 1700 K. At a given distance and for a given size distribution, only grains large enough to survive the sublimation process can actually coexist (see dashed curve in Fig 5). The normalised differential size distribution between $a_{\rm min}$ and $a_{\rm max}$ (fixed) is thus truncated at $a_{\rm sub}$, which depends on the radial distance to the star. For each model, a χ^2 map is computed for all possible values of $a_{\rm min}$ (minimum grain size) and r_0 (inner radius where the disk is artificially truncated), adjusting the surface density at r_0 by a least-squares method (see Fig. 5). The most constraining observations in this process are the two interferometric measurements at 2.12 and 10.6 μm, so that the fit procedure mainly boils down to adjusting the near-infrared flux without producing a too strong 10.6 μm emission feature. Comparison of χ^2 values allowed us to infer most probable physical properties for the inner debris disk.

– **Size distribution:** The inner disk seems to be mainly composed of hot (~1500 K) and small ($<$ 1 μm) dust grains, which emit mostly in the near-infrared. Although larger grains ($\geq$ 10 μm) cannot be ruled out as the main source of the excess, such grains generally produce too large a mid-infrared flux as they emit more efficiently in this wavelength range. This suggests a steep size distribution with a small minimum grain size ($a_{\rm min} \leq$ 0.3 μm, assuming compact grains). For instance, we find that a size distribution similar to that inferred by Hanner (1984) for cometary grains provides a good fit to the SED, as well as the interstellar size distribution of Mathis et al. (1977). Both have power-law exponents of −3.5 or steeper. On the contrary, the size distribution of Grün et al. (1985) for interplanetary dust particles does not allow for a good reproduction of the disk's SED, so that the grain size distribution is most probably different from that of the solar zodiacal cloud described by Reach et al. (2003).
– **Composition:** Large amounts of highly refractive grains, such as graphites (Laor & Draine 1993) or amorphous carbons (Zubko et al. 1996), are most probably present in the inner disk. This is required in order to explain the lack of significant silicate emission features around 10 μm (Gaidos & Koresko 2004), which are especially prominent for small grains. Silicate grains can still be present in the disk, but with a maximum volume ratio of ~70%, using the astronomical silicates of Weingartner & Draine (2001) or the glassy olivines ($Mg_{2y}Fe_{2-2y}SiO_4$) of Dorschner et al. (1995) with y = 0.5. This is another difference from the solar zodiacal cloud, which is thought to contain about 90% of silicate grains (Reach et al. 2003). Such a mixing ratio would only be possible around Vega if the grains were sufficiently big ($a_{\rm min} \geq$ 10 μm), so that the silicate emission feature around 10 μm would not be too prominent.
– **Density profile:** The inner radius r_0 of the dusty disk is estimated to be between 0.17 and 0.3 AU. Assuming a sublimation temperature of 1700 K, dust grains larger than 0.5 μm would survive at such distances (see dashed curve in Fig. 5) while smaller grains, which are hotter, sublimate farther from the star (e.g. at ~0.6 AU for a 0.1 μm grain). A steep power-law for the radial surface density distribution has also been inferred from our investigations. A power-law exponent of −4 or steeper provides a good fit to the SED, as it reduces the amount of dust in the regions farther than 1 AU and thereby explains the non-detection with MMT/BLINC reported by Liu et al. (2004). In contrast, the zodiacal disk model of Kelsall et al. (1998) has a flat surface density power-law with an exponent around −0.34.

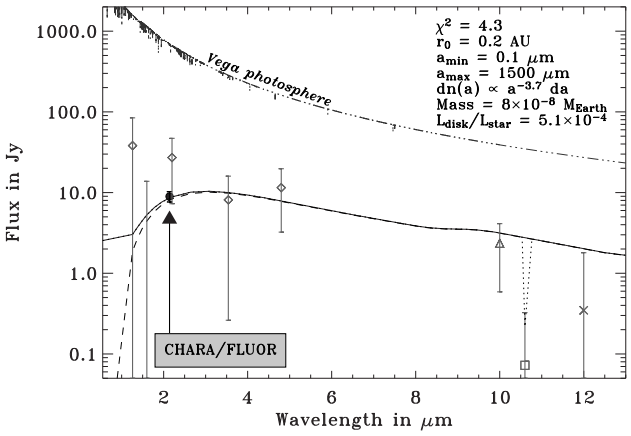

Fig. 6. A possible fit of our debris disk model (Augereau et al. 1999) to the photometric and interferometric constraints of Table 4: the diamonds correspond to references (1) and (2), the filled circle to this study, the triangle to (3), the square to (4) and the cross to (5). The model used here has a size distribution $dn(a) \propto a^{-3.7}da$ with limiting grain sizes $a_{\rm min} = 0.1$ μm and $a_{\rm max} = 1500$ μm, a surface density power-law $\Sigma(r) \propto r^{-4}$ with an inner radius $r_0 = 0.2$ AU, and assumes a disk composed of 50% amorphous carbon and 50% glassy olivine. The solid and dotted lines represent the total emission from the disk on a 8 AU field-of-view, respectively without and with the spatial filtering of interferometric studies, while the dashed line takes only the thermal emission into account. The photospheric SED, simulated by a NextGen model atmosphere (see text), is represented as a dashed-dotted line for comparison.

Using these most probable parameters for the inner disk and a mixed composition of 50% amorphous carbons (Zubko et al. 1996) and 50% glassy olivines ($MgFeSiO_4$, Dorschner et al. 1995), we have obtained a relatively good fit to the SED as illustrated in Fig. 6, where we see that the thermal emission from the hot grains supersedes the contribution from scattered light at wavelengths longer than 1.3 μm. Based on our model and assuming a size distribution $dn(a) \propto a^{-3.7}da$ with $a_{\rm min} = 0.1$ μm and $a_{\rm max} = 1500$ μm, we can deduce estimations for the dust mass in the inner 10 AU of the disk ($\mathcal{M}_{\rm dust} \sim 8 \times 10^{-8}\mathcal{M}_\oplus$, equivalent to the mass of an asteroid about 70 km in diameter) and for the bolometric luminosity ratio between the inner disk and the star ($L_{\rm disk}/L_\star \sim 5 \times 10^{-4}$). Because of the high temperature of the grains, the luminosity of the inner disk is more than one order of magnitude larger than the luminosity of the outer disk estimated by Heinrichsen et al. (1998), even though it is almost 10^5 times less massive than the outer disk. These results need to be confirmed by future studies, as the SED of the inner disk is still relatively poorly constrained. They have been included in this paper to demonstrate that the presence of warm circumstellar dust can reproduce the various observations, and to provide a plausible dust-production scenario as discussed below.

4.2.2. A possible scenario for the presence of hot dust

In fact, three main scenarios may explain the presence of small dust grains so close to Vega. As in the case of the solar zodiacal cloud, they could be produced locally, e.g. by collisions between larger bodies arranged in a structure similar to the solar asteroidal belt. Another local source of small grains is the evaporation of comets originating from the reservoir of small bodies at ~85 AU from Vega or from an inner population of icy bodies as in the case of β Pic (Beust & Morbidelli 2000). Finally, dust grains produced by collisions in the outer disk could drift towards the inner region because of P-R drag. However, this latter scenario cannot be connected to the recent collision(s) in the outer disk suggested by Su et al. (2005), because of the long timescale of P-R drag (2×10^7 yr, Dent et al. 2000). Moreover, due to the much shorter collisional timescale (5×10^5 yr in the outer disk), this process is not very efficient and is therefore unlikely to produce the observed amount of dust in Vega's inner system. Our observations cannot discriminate between the two remaining scenarios, even though a cometary origin is favoured by the steep size distribution of dust grains (Hanner 1984) and by the small inner disk radius.

Due to radiation pressure, small grains will not survive in the Vega inner disk more than a few years before being ejected toward cooler regions (Krivov et al. 2000). Larger grains would survive somewhat longer, but not more than a few tens of years due to the high collision rate in the inner disk. A large dust production rate ($\sim 10^{-8}\mathcal{M}_\oplus$/yr) is thus needed to explain our observations, suggesting that major dynamical perturbations are currently ongoing in the Vega system. An attractive scenario would be an equivalent to the Late Heavy Bombardment that happened in the solar system in the 700 Myr following the formation of the planets (Hartmann et al. 2000), i.e., at a period compatible with the age of Vega (~350 Myr). Such a bombardment, most probably triggered by the outward migration of giant planets (Gomes et al. 2005), could explain the presence of small grains around Vega both in its outer disk, due to an enhanced collision rate in this part of the disk, and in its inner disk, due to the high number of comets sent toward the star by gravitational interaction with the migrating planets. Although the presence of giant planets around Vega has not been confirmed yet, Wyatt (2003) has suggested that the outward migration of a Neptune-sized body from 40 to 65 AU could explain the observed clumpy structure in Vega's outer disk.

5. Conclusion

In this paper, we have presented high precision visibility measurements obtained on Vega at the CHARA Array with the FLUOR beam-combiner. The presence of a significant deficit of visibility at short baselines with respect to a simple uniform disk stellar model led us to the conclusion that an additional source of *K*-band emission is present in the FLUOR field-of-view centred around Vega (1″ in radius), with an estimated excess of 1.29 ± 0.19% relative to the photospheric emission. Among the possible sources for this excess emission, the presence of dust grains in the close vicinity of Vega, heated by the star and radiating mostly in the near-infrared, is proposed as the most probable one. Vega, a prototypical debris-disk star surrounded by a large quantity of dust at about 85 AU, was already suspected by several authors to harbour warm dust grains arranged in an inner circumstellar disk. Previous studies were

however limited to a precision of a few percent on the total infrared flux of the Vega system and therefore did not provide a precise estimation of the excess emission associated with the inner disk.

Thanks to our precise determination of the integrated *K*-band emission emanating from the inner 8 AU of the Vega debris disk, we are able to infer some physical properties of the dust, which is suspected to be mainly composed of submicronic highly refractive grains mainly concentrated in the first AU around Vega and heated up to 1700 K. An estimated dust mass of $8 \times 10^{-8} \mathcal{M}_{\oplus}$ and a fractional luminosity of $\sim 5 \times 10^{-4}$ are derived from our best-fit model. We propose that a major dynamical event, similar to the solar system Late Heavy Bombardment, might be the cause for the presence of small dust grains in the inner disk of Vega.

Acknowledgements. We thank P.J. Goldfinger and G. Romano for their assistance with the operation of CHARA and FLUOR respectively. The CHARA Array is operated by the Center for High Angular Resolution Astronomy with support from Georgia State University and the National Science Foundation, the W.M. Keck Foundation and the David and Lucile Packard Foundation. This research has made use of NASA's Astrophysics Data System and of the SIMBAD database, operated at CDS (Strasbourg, France).

References

Aufdenberg, J. A., Mérand, A., Coudé du Foresto, V., et al. 2006, ApJ, submitted
Augereau, J. C., Lagrange, A. M., Mouillet, D., Papaloizou, J. C. B., & Grorod, P. A. 1999, A&A, 348, 557
Aumann, H., Beichman, C., Gillett, F., et al. 1984, ApJ, 278, L23
Backman, D. & Paresce, F. 1993, in Protostar and Planet III, ed. E. Levy & J. Lunine (Tucson, Univ. of Arizona Press), 1253–1304
Baraffe, I., Chabrier, G., Allard, F., & Hauschildt, P. H. 1998, A&A, 337, 403
Bessel, M. & Brett, J. 1988, PASP, 100, 1134
Beust, H. & Morbidelli, A. 2000, Icarus, 143, 170
Blackwell, D. E., Leggett, S. K., Petford, A. D., Mountain, C. M., & Selby, M. J. 1983, MNRAS, 205, 897
Bohlin, R. C. & Gilliland, R. L. 2004, AJ, 127, 3508
Bordé, P., Coudé du Foresto, V., Chagnon, G., & Perrin, G. 2002, A&A, 393, 183
Campins, H., Rieke, G. H., & Lebofsky, M. J. 1985, AJ, 90, 896
Ciardi, D., van Belle, G., Akeson, R., Thompson, R., & Lada, E. 2001, ApJ, 559, 1147
Cohen, M., Walker, R. G., Barlow, M. J., & Deacon, J. R. 1992, AJ, 104, 1650
Coudé du Foresto, V., Bordé, P. J., Mérand, A., et al. 2003, in Proc. SPIE, Vol. 4838, Interferometry in Optical Astronomy II, ed. W. Traub, 280–285
Coudé du Foresto, V., Ridgway, S., & Mariotti, J.-M. 1997, A&AS, 121, 379
Cutri, R. M., Skrutskie, M. F., van Dyk, S., et al. 2003, VizieR Online Data Catalog, 2246, 0
Delfosse, X., Forveille, T., Ségransan, D., et al. 2000, A&A, 364, 217
Dent, W. R. F., Walker, H. J., Holland, W. S., & Greaves, J. S. 2000, MNRAS, 314, 702
di Folco, E., Thévenin, F., Kervella, P., et al. 2004, A&A, 426, 601
Dominik, C. & Decin, G. 2003, ApJ, 598, 626
Dommanget, J. & Nys, O. 2002, VizieR Online Data Catalog, 1269, 0
Dorschner, J., Begemann, B., Henning, T., Jaeger, C., & Mutschke, H. 1995, A&A, 300, 503
Fajardo-Acosta, S., Telesco, C., & Knacke, R. 1998, AJ, 115, 2101
Fajardo-Acosta, S. B., Stencel, R. E., Backman, D. E., & Thakur, N. 1999, ApJ, 520, 215
Gaidos, E. & Koresko, C. 2004, New Astronomy, 9, 33
Gomes, R., Levison, H. F., Tsiganis, K., & Morbidelli, A. 2005, Nature, 435, 466
Grün, E., Zook, H. A., Fechtig, H., & Giese, R. H. 1985, Icarus, 62, 244
Gulliver, A. F., Hill, G., & Adelman, S. J. 1994, ApJ, 429, L81
Guyon, O. 2002, A&A, 387, 366
Hanbury Brown, R., Davis, J., & Allen, L. 1974, MNRAS, 167, 121
Hanner, M. S. 1984, Advances in Space Research, 4, 189
Hartmann, W. K., Ryder, G., Dones, L., & Grinspoon, D. 2000, in Origin of the Earth and Moon, ed. R. M. Canup & K. Righter (Tucson, Univ. of Arizona Press.), 493–512
Hauschildt, P. H., Allard, F., & Baron, E. 1999, ApJ, 512, 377
Hearnshaw, J. B. 1996, The Measurement of Starlight, Two Centuries of Astronomical Photometry (Cambridge: Cambridge University Press)
Heinrichsen, I., Walker, H. J., & Klaas, U. 1998, MNRAS, 293, L78
Hestroffer, D. 1997, A&A, 327, 199
Holland, W. S., Greaves, J. S., Zuckerman, B., et al. 1998, Nature, 392, 788
Kelsall, T., Weiland, J. L., Franz, B. A., et al. 1998, ApJ, 508, 44
Kervella, P., Ségransan, D., & Coudé du Foresto, V. 2004, A&A, 425, 1161
Kervella, P., Thévenin, F., Ségransan, D., et al. 2003, A&A, 404, 1087
Koerner, D. W., Sargent, A. I., & Ostroff, N. A. 2001, ApJ, 560, L181
Krivov, A. V., Mann, I., & Krivova, N. A. 2000, A&A, 362, 1127
Laor, A. & Draine, B. T. 1993, ApJ, 402, 441
Laureijs, R. J., Jourdain de Muizon, M., Leech, K., et al. 2002, A&A, 387, 285
Leggett, S. K., Bartholomew, M., Mountain, C. M., & Selby, M. J. 1986, MNRAS, 223, 443
Liu, W. M., Hinz, P. M., Hoffmann, W. F., et al. 2004, ApJ, 610, L125
Macintosh, B. A., Becklin, E. E., Kaisler, D., Konopacky, Q., & Zuckerman, B. 2003, ApJ, 594, 538
Mathis, J. S., Rumpl, W., & Nordsieck, K. H. 1977, ApJ, 217, 425

Mégessier, C. 1995, A&A, 296, 771
Mérand, A., Bordé, P., & Coudé du Foresto, V. 2005, A&A, 433, 1155
Metchev, S. A., Hillenbrand, L. A., & White, R. J. 2003, ApJ, 582, 1102
Mountain, C. M., Leggett, S. K., Selby, M. J., Blackwell, D. E., & Petford, A. D. 1985, A&A, 151, 399
Mozurkewich, D., Armstrong, J. T., Hindsley, R. B., et al. 2003, AJ, 126, 2502
Perrin, G. 2003, A&A, 400, 1173
Perryman, M. 2000, Rep. Prog. Phys., 63, 1209
Perryman, M. A. C. 1997, ESA SP Series, Vol. 1200, The HIPPARCOS and TYCHO catalogues. (Noordwijk, The Netherlands: ESA Publications Division)
Peterson, D. M., Hummel, C. A., Pauls, T. A., et al. 2004, in Proc. SPIE, Vol. 5491, New Frontiers in Stellar Interferometry, ed. W. Traub, 65–72
Reach, W. T., Morris, P., Boulanger, F., & Okumura, K. 2003, Icarus, 164, 384
Rieke, G. H., Lebofsky, M. J., & Low, F. J. 1985, AJ, 90, 900
Song, I., Caillaut, J.-P., Barrado y Navascuès, D., & Stauffer, J. 2001, ApJ, 546, 352
Su, K. Y. L., Rieke, G. H., Misselt, K. A., et al. 2005, ApJ, 628, 487
ten Brummelaar, T. A., McAlister, H. A., Ridgway, S. T., et al. 2005, ApJ, 628, 453
van Belle, G. T., Ciardi, D. R., Thompson, R. R., Akeson, R. L., & Lada, E. A. 2001, ApJ, 559, 1155
Weingartner, J. C. & Draine, B. T. 2001, ApJ, 548, 296
Wilner, D. J., Holman, M. J., Kuchner, M. J., & Ho, P. T. P. 2002, ApJ, 569, L115
Wyatt, M. C. 2003, ApJ, 598, 1321
Zubko, V. G., Mennella, V., Colangeli, L., & Bussoletti, E. 1996, MNRAS, 282, 1321

2.3 Ongoing work and future prospects

2.3.1 Follow-up observations of Vega

Our investigations of Vega at the CHARA Array are considered as completed, because the current capabilities of the FLUOR instrument and the available baselines cannot provide more information on the debris disk than what we have already obtained. The only improvement would be to reduce the error bar on the K band flux ratio between the star and the disk by obtaining more observations at short baselines. We will therefore seek to confirm the detection of Vega's debris disk in the near-infrared with other interferometric facilities. In the northern hemisphere, the interferometric facilities open to the community are rare. Among them, IOTA is the most appropriate to perform follow-up observations. With its three telescopes arranged in an L-shaped array with baselines up to 38 m, it provides simultaneous visibility measurements on three short baselines and additional phase information through closure phase measurements. Moreover, with the IONIC integrated optics beam combiner (Berger et al. 2003), a precision of a few percent can be achieved on the measured visibilities in the H band.

From our model of the disk SED (Absil et al. 2006b), we have estimated that the disk-star contrast in the H band, where IONIC routinely operates, is only about 0.6%. This makes the detection even more difficult, but this perspective is very appealing as the confirmation of the detection at a different wavelength would allow us to improve our model of the inner disk. Another complication comes from the fact that a good knowledge of Vega's angular diameter is required in order to detect the deficit, while long baselines are not available at IOTA to directly measure Vega's H band diameter. Therefore, we will rely on the precise photospheric model of Vega developed by Aufdenberg et al. (2006), based on long-baseline K band measurements at the CHARA Array. This model can predict both the angular diameter and the limb-darkened profile in H band with a sufficient accuracy for our purpose.

The additional measurements of closure phases can also be useful, especially to assess the possible asymmetry of the excess emission. With a typical accuracy of 0.5° on the closure phases, it will be possible to discriminate between a low-mass companion (which could not be ruled out with our previous CHARA-FLUOR observations) and a (supposedly symmetric) face-on disk.

2.3.2 Our next target: ϵ Eridani

The second target in our list is ϵ Eridani, another member of the *Fabulous Four*. Even though it has a negative declination of $-09°27'30''$, ϵ Eri (HD 22049) can be observed from Mount Wilson in autumn (it culminates 46° above the horizon and can be observed during about 5h30). This close K2V star (3.22 pc) is known to be surrounded by a large but faint debris disk, detected at sub-millimetric wavelengths with SCUBA at the JCMT (Greaves et al. 1998, 2005). The sub-millimetric images show a clumpy, asymmetric face-on ring with a cleared region interior to 10 arcsec (~30 AU), which is understood to be comparable to our own Kuiper Belt. Besides this cold component, ϵ Eri's disk is also suspected to harbour warm dust in its inner part with an unknown density level, as suggested by recent measurements on the prototypical Fomalhaut (Stapelfeldt et al. 2004) and by our study of Vega. ϵ Eri is also known to host a giant planet, detected by the radial velocity method (Hatzes et al. 2000). It has a minimum mass of 0.86 $M_{\rm Jup}$ and orbits at a mean distance of 3.4 AU from the star with a large eccentricity (0.61). Assuming the orbit to be seen face-on as well, the angular separation between the star and the planet ranges between 410 mas and 1700 mas, so that the planet could reside on the edge of the FLUOR field-of-view (about 1 arcsec in radius). However, the expected K-band contrast between the star and planet is very low ($\sim 10^{-6}$), so that the planet does not interfere with our observations. The presence of other planets has been suggested by numerical simulations (Ozernoy et al. 2000; Quillen & Thorndike 2002).

JD−JD$_0$	Projected baseline (m)	Position angle (°)	Calibrated $\mathcal{V}^2$ (×100)	HD$_a$	HD$_b$
0.307582	24.60	-1.91	95.01 ± 1.17	10550	25165
0.385567	26.87	-21.36	93.90 ± 1.92	25165	25165
0.406565	27.92	-25.20	93.02 ± 2.37	25165	29063

Table 2.1: Individual measurements of ϵ Eri with CHARA-FLUOR. Columns are: (1) date of observation, JD$_0$ = 2453680.5; (2, 3) projected baseline length and position angle (measured East of North); (4) squared visibility after calibration and error; (5, 6) HD number of calibrators, prior (a) and after (b) the given data point respectively.

Because of their large semi-major axes, these putative planets would in any case lie outside the FLUOR field-of-view.

Like Vega, ϵ Eri is a very interesting target because, in addition to the presence of a cold debris disk, it has already been observed by interferometry. In their search for debris disks at the VLTI, di Folco et al. (2004) have obtained a large quantity of measurements of ϵ Eri with VINCI, leading to the first precise estimation of its stellar diameter: $\theta_{\rm UD} = 2.093 \pm 0.029$ mas using a uniform disk stellar model, or $\theta_{\rm LD} = 2.148 \pm 0.039$ mas using a limb-darkened stellar model with the tabulated limb-darkening coefficients of Claret (2000). Combining measurements at 66 m and 140 m baselines, the authors have also been able to set an upper limit of about 2.5% on the K-band excess flux due to the presence of hot dust.

The observations

In fact, ϵ Eri should have been the first star in our survey, as an observing programme had been proposed and accepted in 2004. However, the bad weather conditions over the Pacific in October 2004 have prevented us from obtaining a single visibility measurement during the two weeks of the observation run! The programme was thus re-scheduled for November 2005. This time, the weather was somewhat better, with observations carried out on 8 nights out of 20. However, these good nights had to be shared with two other observing programmes, so that only a limited number of data points have been obtained on ϵ Eri, mostly with the short S1–S2 baseline (34 m). Unfortunately, the data were not of very good quality due to technical problems (strong intermittent noise in the camera) and to the changing weather. At the end, we are left with only three data points of sufficient quality, all obtained at the short baseline (see Table 2.1). The absence of data at long baselines makes it impossible to directly evaluate ϵ Eri's diameter, so that we have to rely on the VINCI data set.

Because of the small number of additional data points with respect to the previous observations of di Folco et al. (2004), this study needs to be complemented with new observations in Fall 2006. Nevertheless, we present in the next paragraphs the preliminary results of our observations.

Preliminary result

In order to reconcile the measurements of VINCI and FLUOR, we had to take into account the transmission of the two instruments, including the atmosphere. In practice, the computation of the synthetic visibilities from the model should take into account the effect of bandwidth smearing (as was done in Section 2.2.2):

$$\mathcal{V}^2_{\rm band}(b) = \frac{\int_0^\infty T(\lambda)^2 F_\lambda^2 \mathcal{V}^2(b,\lambda)\lambda^2 {\rm d}\lambda}{\int_0^\infty T(\lambda)^2 F_\lambda^2 \lambda^2 {\rm d}\lambda}\,, \tag{2.4}$$

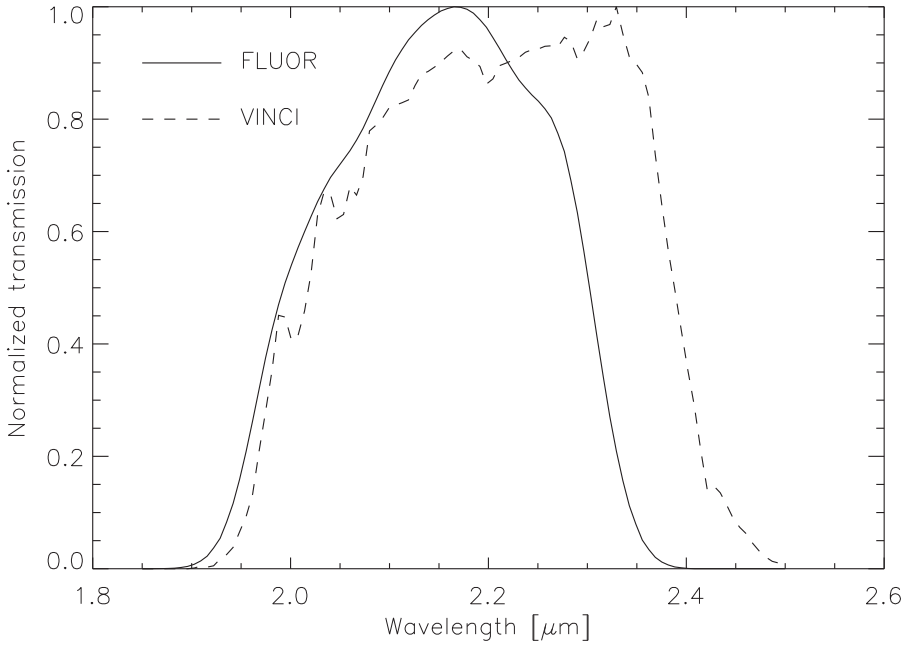

Figure 2.5: Transmission of the FLUOR and VINCI K-band filters, including atmospheric transmission and detector response (courtesy of A. Mérand and P. Kervella).

with $T(\lambda)$ the instrumental transmission curve, F_λ the stellar flux in units of photon cm^{-2} s^{-1} and $\mathcal{V}(b,\lambda)$ the monochromatic visibility of the model computed at baseline b and wavelength λ. Because the instruments have different transmission profiles (Figure 2.5), this formula could not be used, and we replaced $\mathcal{V}_{\rm band}(b)$ by the monochromatic visibility $\mathcal{V}(b,\lambda_{\rm eff})$ computed at the effective wavelength:

$$\lambda_{\rm eff} = \left(\frac{\int_0^\infty \lambda^{-1} T(\lambda) F_\lambda {\rm d}\lambda}{\int_0^\infty T(\lambda) F_\lambda {\rm d}\lambda} \right)^{-1} . \tag{2.5}$$

This approximation is valid as long as the squared visibilities are above ∼20%, where the broadband effect becomes significant.

We fitted a UD stellar model to the whole data set: the best-fit UD diameter of di Folco et al. (2004) was not affected by the three additional points at short baselines. Figure 2.6 shows that all of the three new points are below the expected visibility of the UD stellar model, by about 1σ. The small number of data at short baselines makes it impossible to conclude at this point, but it might well be that a small part of ϵ Eri's near-infrared flux comes from an extended structure, which could be once again related to the presence of hot dust around the star. Additional observations in Fall 2006 should allow us to confirm this preliminary result.

2.3.3 Perspectives at the CHARA Array and the VLTI

The performance of the interferometric instruments at the VLTI has prevented debris disk studies up to now, but AMBER will soon deliver the required accuracy to carry out such observations on the VLT Interferometer Sub-Array (VISA) composed of four 1.8-m Auxiliary Telescopes (ATs). The use of AMBER on three ATs should considerably improve the observing efficiency with respect to CHARA-FLUOR, as three visibility measurements will be obtained together with one closure phase measurement simultaneously in H and K bands with a low spectral resolution. One observation with a triplet of short

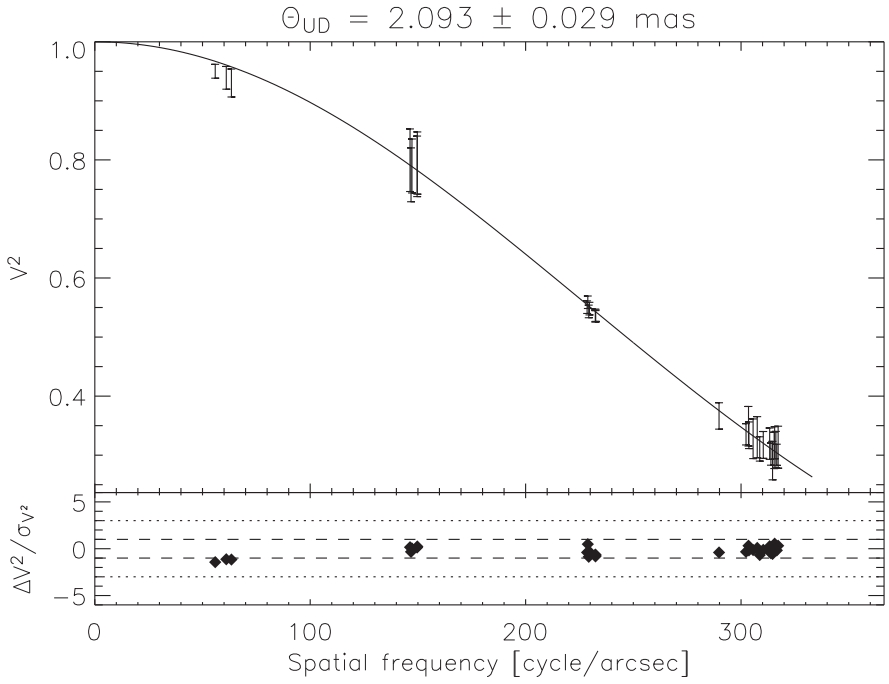

Figure 2.6: Preliminary results on ϵ Eri. The visibility is plotted as a function of spatial frequency ($b/\lambda_{\rm eff}$) in order to include the data from both VINCI ($\lambda_{\rm eff}$ = 2.180 μm) and FLUOR ($\lambda_{\rm eff}$ = 2.134 μm) in the same plot. The three points obtained with FLUOR with the short S1–S2 baseline seem to indicate the presence of a small deficit of visibility at low spatial frequencies, but need to be confirmed by further observations.

baselines followed by one observation with a triplet of long baselines will provide an estimation of the contribution of the disk in both bands, or at least place an upper limit on its flux. On the other hand, the mid-infrared instrument of the VLTI (MIDI) does not currently provide sufficient accuracy on the measured visibilities (about 5% at best) to detect faint circumstellar features representing only a few percent of the stellar flux.

At the CHARA Array, we will pursue our investigations with the FLUOR instrument, with a lower efficiency as only one visibility can be acquired at a time. When it becomes available, the Michigan InfraRed Combiner (MIRC, Monnier et al. 2004), the future 6-way imaging interferometer for the CHARA Array, will improve the efficiency of the survey. This instrument has an architecture similar to AMBER and will use a separate fringe tracker to improve its sensitivity. It will provide as much as 15 visibilities and 10 independent closure phases in a single observation.

Our next objective concerning debris disks is to carry out a small survey of near-infrared excesses around bright Vega-type stars in both the northern and southern hemispheres, with CHARA-FLUOR and VISA-AMBER. One of the main objectives of the survey is to identify new targets with significant near-infrared excess ($\gtrsim$ 1%), which will then be observed in more details at various wavelengths and spatial resolutions. A detailed model of the disks will then be derived from the available constraints on the SED, as was done in the case of Vega.

As already mentioned in the introduction, infrared space missions have detected a large quantity of candidate Vega-type stars through the presence of significant mid- to far-infrared emission in excess to the expected stellar photospheric flux. Among these candidates, we have selected 57 potential targets in Table 2.2 with $K < 5$ as a criterion, in order to stay within the current limitations of both CHARA-FLUOR and VISA-AMBER. The star coordinates and magnitudes in Table 2.2 are taken from the SIMBAD data base. When not available, K magnitudes have been estimated from V magnitudes and spectral types (values between brackets in the table). Most targets have been studied by more than one author.

Star	R.A.	Dec.	Dist. (pc)	Type	V	K	Reference
σ Her	16h34m06s	+42°26′13″	93	B9V	4.2	4.1	Fajardo-Acosta et al. (1998)
Vega	18h36m56s	+38°47′01″	7.8	A0V	0.0	0.0	(see text)
α Crb	15h34m41s	+26°42′52″	23	A0V	2.2	2.2	Song et al. (2001)
γ Uma	11h53m50s	+53°41′41″	26	A0V	2.4	2.3	Dunkin et al. (1997)
ζ Aql	19h05m25s	+13°51′49″	26	A0V	2.9	2.9	Chen et al. (2005)
γ Oph	17h47m54s	+02°42′26″	29	A0V	3.7	3.6	Fajardo-Acosta et al. (1998)
30 Mon	08h25m39s	−03°54′23″	38	A0V	3.9	3.9	Song et al. (2001)
7 Ori	04h54m54s	+10°09′03″	37	A0V	4.7	(4.7)	Jura et al. (2004)
ρ Vir	12h41m53s	+10°14′08″	37	A0V	4.9	4.9	Fajardo-Acosta et al. (1997)
β Uma	11h01m50s	+56°22′56″	24	A1V	2.4	2.3	Song et al. (2001)
α Lac	22h31m17s	+50°16′56″	31	A1V	3.8	3.8	Fajardo-Acosta et al. (1997)
HD 88955	10h14m44s	−42°07′19″	32	A1V	3.8	3.7	Mannings & Barlow (1998)
γ Tri	02h17m18s	+33°50′49″	36	A1V	4.0	(3.9)	Song et al. (2001)
HD 91375	10h30m20s	−71°59′34″	79	A1V	4.7	(4.6)	Mannings & Barlow (1998)
ι Cen	13h20m36s	−36°42′44″	18	A2V	2.7	2.8	Mannings & Barlow (1998)
ζ Lep	05h46m57s	−14°49′19″	22	A2V	3.6	3.4	Fajardo-Acosta et al. (1998)
τ Cen	12h37m42s	−48°32′28″	40	A2V	3.9	3.7	Fajardo-Acosta et al. (1997)
α Cra	19h09m28s	−37°54′16″	40	A2V	4.1	(3.9)	Song et al. (2001)
μ Ori	06h02m23s	+09°38′50″	46	A2V	4.1	(3.9)	Song et al. (2001)
ρ Aql	20h14m16s	+15°11′51″	47	A2V	5.0	(4.8)	Song et al. (2001)
29 Cyg	20h14m32s	+36°48′22″	41	A2V	5.0	4.5	Fajardo-Acosta et al. (1997)
Fomalhaut	22h57m39s	−29°37′20″	7.7	A3V	1.2	0.9	Fajardo-Acosta et al. (1997)
β Leo	11h49m03s	+14°34′19″	11	A3V	2.1	1.9	Habing et al. (2001)
β Cir	15h17m30s	−58°48′04″	30	A3V	4.0	3.9	Song et al. (2001)
β Pic	05h47m17s	−51°03′59″	19	A5V	3.9	3.5	Backman et al. (1992)
HD 172555	18h45m26s	−64°52′16″	29	A5V	4.9	(4.5)	Song et al. (2001)
α Pic	06h48m11s	−61°56′29″	30	A7IV	3.3	2.6	Song et al. (2001)
κ Phe	00h26m12s	−43°40′47″	24	A7V	3.9	(3.4)	Chen et al. (2005)
HD 91312	10h33m13s	+40°25′32″	34	A7IV	4.7	(4.2)	Song et al. (2001)
θ Cas	01h11m06s	+55°09′00″	42	A7V	4.3	4.0	Song et al. (2001)
δ Dor	05h44m46s	−65°44′07″	45	A7V	4.4	3.7	Song et al. (2001)
21 Lmi	10h07m26s	+35°14′41″	28	A7V	4.5	4.0	Song et al. (2001)
η Lep	05h56m24s	−14°10′04″	15	F1V	3.7	2.9	Mannings & Barlow (1998)
η Crv	12h32m04s	+16°11′46″	18	F2V	4.3	3.5	Wyatt et al. (2005)
σ Boo	14h34m41s	+29°44′42″	16	F2V	4.4	3.5	Habing et al. (2001)
8 Lib	14h50m41s	−15°59′50″	24	F3V	5.2	4.1	Chen et al. (2005)
1 Eri	02h45m06s	−18°34′21″	14	F5V	4.5	3.3	Sheret et al. (2004)
HD 139664	15h41m11s	−44°39′40″	18	F5V	4.6	(3.4)	Habing et al. (2001)
γ Lep	05h44m28s	−22°26′54″	9.0	F7V	3.6	2.4	Sheret et al. (2004)
γ Pav	21h26m27s	−65°21′58″	9.2	F7V	4.2	2.9	Mannings & Barlow (1998)
α For	03h12m05s	−28°59′15″	14	F8IV	3.9	2.5	Oudmaijer et al. (1992)
10 Tau	03h36m52s	+00°24′06″	14	F9V	4.3	2.9	Habing et al. (2001)
ζ Tuc	00h20m04s	−64°52′29″	8.6	G0V	4.2	2.8	Habing et al. (2001)
HD 207129	21h48m16s	−47°18′13″	16	G0V	5.6	4.1	Habing et al. (2001)
HD 52265	07h00m18s	−05°22′02″	28	G0V	6.3	(4.8)	Beichman et al. (2005b)
70 Vir	13h28m26s	+13°46′44″	18	G2.5V	5.0	3.3	Beichman et al. (2005b)
104 Tau	05h07m27s	+18°38′42″	16	G4V	5.0	3.2	Oudmaijer et al. (1992)
HD 73752	08h39m07s	−22°39′42″	20	G4V	5.1	(3.3)	Song et al. (2000)
τ Cet	01h44m04s	−15°56′15″	3.7	G8V	3.5	1.7	Habing et al. (2001)
82 Eri	03h19m56s	−43°04′11″	6.1	G8V	4.3	2.5	Decin et al. (2000)
54 Psc	00h39m22s	+21°15′01″	11	K0V	5.8	3.8	Fajardo-Acosta et al. (1997)
HD 69830	08h18m23s	−12°37′55″	13	K0V	6.0	4.2	Beichman et al. (2005a)
ϵ Eri	03h32m56s	−09°27′29″	3.2	K2V	3.7	1.6	(see text)
HD 191408	20h11m11s	−36°06′04″	6.1	K3V	5.3	2.9	Laureijs et al. (2002)
AU Mic	20h45m10s	−31°20′27″	9.9	M1V	8.6	4.7	Krist et al. (2005)
Gl 784	20h13m53s	−45°09′50″	6.2	M1-2V	8.0	4.1	Fajardo-Acosta et al. (1997)
Gl 725A	18h42m47s	+59°37′49″	3.6	M4	8.9	3.6	Fajardo-Acosta et al. (1997)

Table 2.2: 57 targets with $K < 5$ for an interferometric survey of Vega-type stars (see text).

The references given in the table are generally the most relevant for the purpose of the survey. We have not included spectral types earlier than A in this list, because hot stars are short-lived and are therefore not expected to form long-lasting planetary systems nor harbour large quantities of second-generation dust grains. Moreover, they generally undergo other physical processes such as strong stellar winds that could be confused with the presence of dust.

Among the targets listed in Table 2.2 are a few very interesting cases. First, β Pic and Fomalhaut, the remaining two members of the *Fabulous Four*, can be accessed from Cerro Paranal. Another prototypical Vega-type star is ζ Lep, which, together with β Pic, is the only star to have a mid-infrared excess confirmed by ground-based photometry at 10 μm (Aumann & Probst 1991) in addition to being detected at 12 μm with IRAS. HD 69830 is, together with Fomalhaut, one of the first stars around which the Spitzer Space Telescope found clear evidences for warm dust (Beichman et al. 2005a; Stapelfeldt et al. 2004). Another interesting star is η Crv: Wyatt et al. (2005) recently suggested the presence of a migrating Neptune-mass planet around it, which could potentially trigger the infall of large bodies towards the star. These bodies could then produce dust particles close to the star and thus be responsible for the detected infrared excess with IRAS above 12 μm (Mannings & Barlow 1998). HD 52265 and 70 Vir will also be subject of much attention, as they both are known to harbour giant planets orbiting at about 0.5 AU from them, i.e., much closer than in the case of ϵ Eri (3.3 AU). These giant planets are supposed to have formed farther out in the protoplanetary disk and to have migrated inwards due to their interaction with gas and dust (Ward 1997). The search for dust within 0.5 AU from the star would be a critical test for the current planet formation theories, especially in the context of disk-planet interactions.

In addition to identifying suitable targets for follow-up observations, this small survey will also provide a first statistical information on the prevalence of hot dust around main-sequence stars. Although the sample is strongly biased, as all targets are known to be surrounded by a substantial amount of cold dust, this will already be an indicator of the level of exozodiacal emission that the future planet finding missions will have to deal with. Finally, this survey will also provide a list of interesting targets to be observed with GENIE, the future ground-based nulling interferometer currently studied at ESA and ESO (see next chapter).

Part II

Ground-based nulling interferometry: towards exozodiacal disks

3

An introduction to ground-based nulling interferometry

Contents

3.1 Principle of nulling interferometry 54

3.1.1 Principle of a two-telescope (Bracewell) nulling interferometer 54

3.1.2 Geometric and instrumental stellar leakage 57

3.1.3 Spatial and modal filtering 58

3.1.4 Disentanglement of the astrophysical sources 59

3.2 Scientific and technological preparation of Darwin/TPF-I 61

3.3 A first generation of ground-based nulling instruments 61

3.3.1 BLINC at the MMT 61

3.3.2 The Keck Interferometer Nuller (KIN) 62

3.3.3 The Large Binocular Telescope Interferometer (LBTI) 64

3.4 The European effort: GENIE 65

3.4.1 The VLTI infrastructure 65

3.4.2 Nulling configurations at VLTI 67

3.4.3 Background subtraction techniques 69

3.4.4 The need for a GENIE simulator 73

We have seen in the previous part that major advances in the study of debris disks can be achieved with the help of stellar interferometry. However, the dynamic range of state-of-the-art stellar interferometers is limited to a few 0.1%, so that only dense debris disks can be investigated. In order to increase the capabilities of interferometry and open the path towards the detection of faint circumstellar disks similar to the solar zodiacal disk, we discuss in this chapter the technique of nulling interferometry. After reviewing the principle of this technique, we show how it can be applied on the ground to prepare both the technical aspects and the scientific programme of the future planet-finding missions, Darwin and TPF-I, through a survey of exozodiacal disks around nearby stars. We describe the first ground-based experiments currently under development in the United States, review their preliminary results, and finally present the prospects for a Ground-based European Nulling Interferometer Experiment (GENIE).

3.1 Principle of nulling interferometry

The basic principle of nulling interferometry dates back to almost 30 years, when Bracewell (1978) proposed in a letter to Nature to "detect nonsolar planets by spinning infrared interferometer". The rationale of this proposal was already based on the limited performances of indirect techniques (astrometry, radial velocity) and on the inability of "direct photography" to detect small and faint extrasolar planets around bright stars: even when a telescope's point spread function is very well calibrated and subtracted, the shot noise associated with stellar light remains, outshining any faint signal nearby. Bracewell thus proposed a way to enhance the planet over star flux ratio by placing an interference null on the star. An interference pattern $\sin^2(\pi\theta/\Phi)$ has a maximum on a planet at $\theta = \Phi/2$ while the response to a star at $\theta = 0$ is minimised. His initial proposal was aiming at the detection of Jupiter-like planets in the far-infrared (40 μm) with a moderate interferometer baseline (7.7 m), but the key features of future missions for Earth-like planet detection were already included. In this section, we review the technique proposed by Bracewell and how it has evolved in the context of the Darwin and TPF-I proposals.

3.1.1 Principle of a two-telescope (Bracewell) nulling interferometer

When overlapping the light beams collected by two telescopes on a balanced beam splitter, one can tune their respective phases by means of phase-shifting devices so that all the on-axis stellar light is sent to only one of the two complementary outputs of the beam splitter (see Figure 3.1). Such a configuration happens when a phase shift of π radians is maintained between the two input beams. This is in contrast with classical pupil-plane interferometry, where the optical path difference between the beams is modulated in order to record a complete interferogram. In order to avoid any spurious stellar light at the detector, the beam combination can only be done in a co-axial way, i.e., using a pupil plane arrangement, since multi-axial beam combination would produce interference fringes for the stellar light in the focal plane whatever the beam's phases.

A pupil plane interferometer is characterised by its intensity response $R(\vec{\theta})$ where $\vec{\theta} = (\theta, \alpha)$ is the position in the plane of the sky with respect to the optical axis (see Figure 3.2). This response is obtained

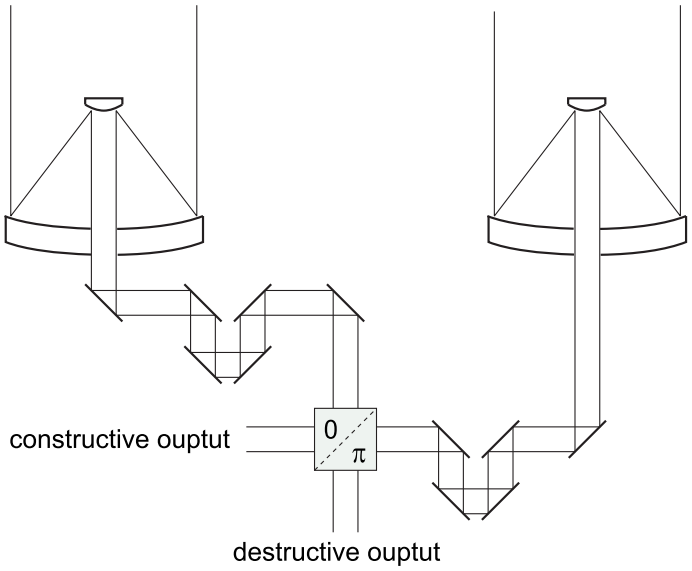

Figure 3.1: Principle of a Bracewell nulling interferometer. The beam-combining system produces a destructive interference by applying an achromatic π phase shift to one of the two input beams and by superposing them in a co-axial way.

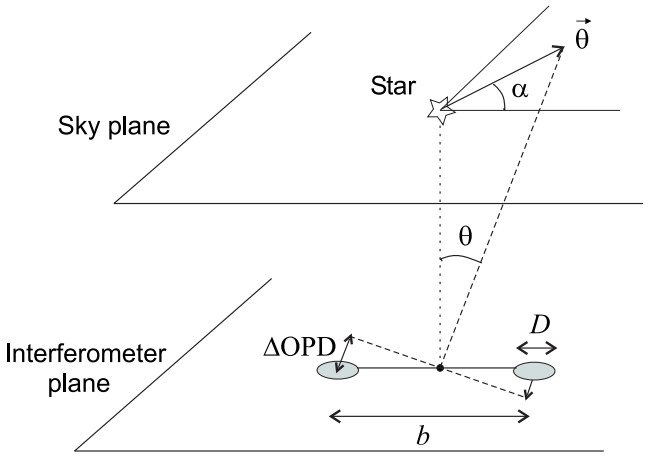

Figure 3.2: Geometrical configuration of the interferometer and of the stellar system. The two angular coordinates (θ, α) denote the position in the sky plane. In this sketch, we assume that the line-of-sight is perpendicular to the plane of the interferometer.

by adding the complex amplitudes of the electrical fields in the overlapped pupil. At any point $\vec{r}$ of the pupil, the total electrical field is given by:

$$\mathbf{E}(\vec{\theta},\vec{r}) = \Pi(r/R)\left(\mathbf{E}_1(\vec{\theta})e^{i\phi_1} + \mathbf{E}_2(\vec{\theta})e^{i\phi_2}\right) , \tag{3.1}$$

where $\Pi(r/R)$ is the top hat function, $R = \frac{D}{2}$ the radius of the pupil and ϕ_k an additional phase shift applied to the beam collected by telescope k. The expression of the complex electrical fields $\mathbf{E}_k(\vec{\theta})$ depends on its modulus E_k, proportional to the telescope diameter, and on its phase. Assuming the optical paths to be balanced for an on-axis source, the additional phase associated with a slightly off-axis source due to its differential external path ΔOPD equals $\pm\pi\frac{b\theta}{\lambda}\cos\alpha$. Taking into account the fact that each beam is divided into two equal parts by the balanced beam splitter, and assuming that they were collected by two telescopes of unitary size, we have $|\mathbf{E}_1|^2 = |\mathbf{E}_2|^2 = 1/2$. At the destructive output of the beam splitter, where a phase shift of $\phi_2 - \phi_1 = \pi$ radians is applied to the second telescope with respect to the first one, the total electrical field thus writes (using the notations of Figure 3.2):

$$\begin{aligned}\mathbf{E}(\vec{\theta},\vec{r}) &= \Pi(r/R)\frac{1}{\sqrt{2}}\left(e^{i\pi(b\theta/\lambda)\cos\alpha} + e^{-i\pi(b\theta/\lambda)\cos\alpha}\, e^{i\pi}\right) &(3.2)\\ &= \Pi(r/R)\frac{2i}{\sqrt{2}}\sin\left(\pi\frac{b\theta}{\lambda}\cos\alpha\right) . &(3.3)\end{aligned}$$

An equivalent expression can be obtained for the distribution of complex amplitude in the focal plane, by means of a Fourier transform of the pupil plane distribution. Denoting θ_f the angular coordinate in the focal plane and $\otimes$ the convolution sign, we obtain:

$$\widetilde{\mathbf{E}}(\vec{\theta},\vec{\theta_f}) = \left(\frac{2J_1(\pi D\theta/\lambda)}{\pi D\theta/\lambda} \otimes \delta(|\vec{\theta_f} - \vec{\theta}|)\right) i\sqrt{2}\sin\left(\pi\frac{b\theta}{\lambda}\cos\alpha\right) . \tag{3.4}$$

In this expression, the first term (between brackets) represents the classical response of a single aperture, i.e., an Airy pattern $2J_1(x)/x$ centred at the position $\vec{\theta}$ of any point-like object. The last term is the sinusoidal pattern associated with the interference process. Because only intensities are recorded, the square modulus of this term represents the response of the interferometer:

$$R_\lambda(\theta,\alpha) = 2\sin^2\left(\pi\frac{b\theta}{\lambda}\cos\alpha\right) . \tag{3.5}$$

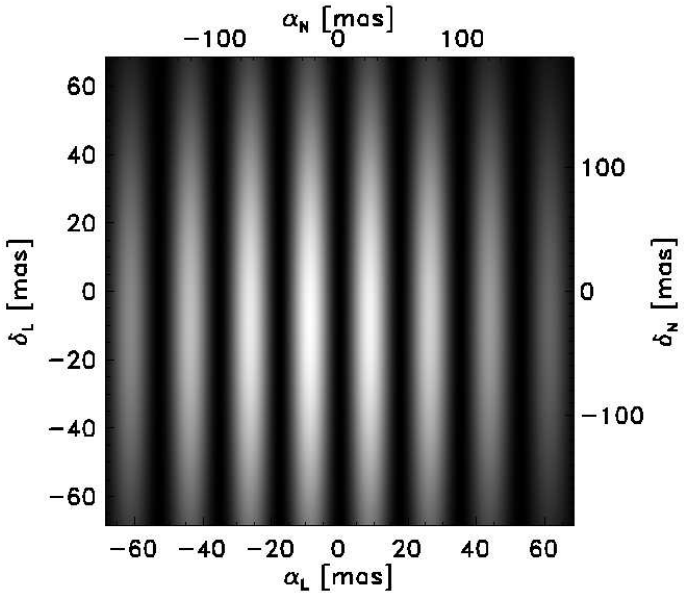

Figure 3.3: Monochromatic transmission map for a 47 m Bracewell interferometer formed of two 8-m telescopes. The interferometric field-of-view is diffraction-limited: $\Omega = \lambda^2/S$, with S the telescope surface. Its diameter is respectively of 137 mas and 378 mas at 3.8 μm (L′ band) and 10.5 μm (N band). The transmission map acts as a "photon sieve": it shows the parts of the field that are transmitted (white stripes) and those that are blocked (dark stripes, including the central dark fringe) by the interference process.

The intensity response projected on the plane of the sky forms the so-called *transmission map* of the interferometer. This map defines which parts of the field-of-view are transmitted by constructive interference, and which are blocked by destructive interference. It is represented in Figure 3.3, where the field-of-view has been restricted to the diffraction-limited beam of an individual telescope (λ/D). In theory, there is no real limitation to the field-of-view of a nulling interferometer, although the crests and troughs of the transmission map wash out for angular distances larger than $\lambda^2/(b\,\Delta\lambda)$ due to the effect of the finite bandwidth $\Delta\lambda$. Additionally, the zone of interest is generally limited to the size of the diffraction pattern of individual telescopes, as larger angular separations could easily be investigated with a single dish supplied with a coronagraph. This is one of the reasons[7] why the field-of-view of nulling interferometers (and of most pupil-plane interferometers) is generally limited to the size of an Airy pattern by the use of spatial or modal filtering.

The final detection can be done either in a pupil plane or in an image plane. In the first case, a single-pixel detector is sufficient to record the total flux in the output pupil, emanating from all the sources in the diffraction-limited field-of-view. In the latter, an image similar to that of a single telescope is formed, except that the relative contribution of each source is affected by the interferometer's intensity response at its location. In any case, no fringes are formed nor recorded, and the final output generally consists of a single value: the total intensity in the diffraction-limited field-of-view. In the following study, we will assume that detection is done in a pupil plane with a single-pixel detector. The final output then writes:

$$F(\lambda,t) = T_{\rm tot}(\lambda) \int_\alpha \int_\theta \frac{2J_1(\pi D\theta/\lambda)}{\pi D\theta/\lambda} \Big[R_\lambda(\theta,\alpha,t)B(\theta,\alpha,\lambda) + B_{\rm bckg}(\theta,\alpha,\lambda,t)\Big]\, \theta\, {\rm d}\theta\, {\rm d}\alpha\ , \qquad (3.6)$$

with $T_{\rm tot}(\lambda)$ the wavelength-dependent total throughput of the interferometer, taking into account telescope size, optical losses and detector efficiency; $R_\lambda(\theta,\alpha,t)$ the time-dependent transmission map of the

[7] The other main reasons are the improvement of the wavefront quality and the reduction of the background emission—see Section 3.1.3 for more details on spatial and modal filtering.

interferometer, possibly degraded by random instrumental errors (see Section 3.1.2); and with $B(\theta, \alpha, \lambda)$ the brightness distribution of all coherent sources in the diffraction-limited field-of-view. $B_{\text{bckg}}(\theta, \alpha, \lambda, t)$ is the time-dependent brightness of the incoherent background that includes the thermal emission from the sky, the telescope and the optical beam train. In practice, the expression of the field-of-view $(2J_1(x)/x)$ will be affected by the use of modal filtering.

3.1.2 Geometric and instrumental stellar leakage

When the off-axis angle is small compared to the fringe spacing ($\theta \ll \lambda/b$), the expression of the transmission map can be simplified as follows in the case of a two-telescope interferometer:

$$R_\lambda(\theta, \alpha) \simeq 2\left(\pi \frac{b\theta}{\lambda} \cos\alpha\right)^2 . \tag{3.7}$$

The transmission close to the centre of the field-of-view is thus proportional to the square of the off-axis angle θ, so that the Bracewell configuration is called a "θ^2 configuration". Even with an ideal Bracewell interferometer, the stellar signal is thus perfectly cancelled only on the optical axis. Part of the light will therefore leak through the transmission map due to the finite size of the stellar photosphere, an effect referred to as *geometric stellar leakage* because it is related to the physical arrangement of the telescopes and to the angular size of the stellar photosphere. Its expression can be derived by integrating the expression of the interferometer response over the finite stellar photosphere of angular radius $\theta_\star$, noting that $\frac{2J_1(\pi\theta D/\lambda)}{\pi\theta D/\lambda} \simeq 1$ for an unresolved star:

$$\begin{aligned} F_{\text{leak}}(\lambda) &= T_{\text{tot}}(\lambda) \int_0^{2\pi} \int_0^{\theta_\star} R_\lambda(\theta, \alpha) B_\star(\theta, \alpha, \lambda)\, \theta \,\mathrm{d}\theta \,\mathrm{d}\alpha \\ &\simeq T_{\text{tot}}(\lambda) B_\star(\lambda) \int_0^{2\pi} \int_0^{\theta_\star} 2\pi^2 \frac{b^2\theta^2 \cos^2\alpha}{\lambda^2}\, \theta \,\mathrm{d}\theta \,\mathrm{d}\alpha \end{aligned} \tag{3.8}$$

where the stellar brightness per square metre per steradian $B_\star(\lambda)$ is assumed to be constant over the whole stellar surface. When computing the integral, the above expression becomes

$$F_{\text{leak}}(\lambda) = T_{\text{tot}}(\lambda) B_\star(\lambda) \frac{\pi^3 b^2 \theta_\star^4}{2\lambda^2} . \tag{3.9}$$

The *nulling ratio N* is defined as the ratio between the transmitted stellar flux and the initial stellar flux at the input of the beam-combiner (flux coming from both telescopes):[8]

$$N = \frac{F_{\text{leak}}(\lambda)}{2\, T_{\text{tot}}(\lambda) B_\star(\lambda) \pi \theta_\star^2} = \frac{\pi^2}{4}\left(\frac{b\theta_\star}{\lambda}\right)^2 . \tag{3.10}$$

The *rejection ratio* ρ is then defined as the inverse of the nulling ratio:

$$\rho = \frac{4}{\pi^2}\left(\frac{\lambda/b}{\theta_\star}\right)^2 . \tag{3.11}$$

It depends on two parameters: the ratio of wavelength to baseline, which sets the angular resolution of the interferometer, and the angular radius of the star $\theta_\star$. The rejection ratio decreases for longer baselines (or shorter wavelengths) as the stars gets more and more resolved.

[8] In the case of a Bracewell interferometer, the nulling ratio is generally also the ratio of the stellar fluxes in the destructive and constructive outputs, because the stellar signal recorded in the constructive output is approximately equal to the total flux collected by the interferometer.

The expression 3.11 of the rejection rate is valid only for a perfect Bracewell interferometer. In practice, the rejection rate is degraded by atmospheric turbulence and various instrumental effects causing imperfect co-phasing of the light beams, wavefront errors, intensity mismatches and polarisation errors (Ollivier 1999). This contribution, called *instrumental stellar leakage* and independent of the stellar diameter to the first order, adds to the geometric leakage at the destructive output of the interferometer. Approximate expressions can be derived for the various contributors to instrumental leakage, although in practice it is dominated by non-linear, second order error terms (Lay 2004).

- **Phase error.** The effect of a global phase error between the two beams is to shift the position of the fringes in the transmission map: the dark fringe is not centred any longer on the optical axis. For a small phase error $\Delta\phi(\lambda)$ between the two beams, the shifting of the dark fringe produces a non-null on-axis transmission (Ollivier 1999):

$$R_\lambda(0,0) = \frac{\Delta\phi^2(\lambda)}{4} \ . \tag{3.12}$$

- **Wavefront error.** The corrugation of the wavefronts due to turbulence or imperfect optics produces a mismatch between the shapes of the two beams to be combined. If $\sigma^2_{\phi_{1,2}}(\lambda)$ designates the phase variance over each pupil, the on-axis transmission becomes (Mennesson et al. 2002):

$$R_\lambda(0,0) = \frac{1}{4}\left(\sigma^2_{\phi_1}(\lambda) + \sigma^2_{\phi_2}(\lambda)\right) \ . \tag{3.13}$$

- **Intensity error.** The effect of unequal intensities in the two arms of the interferometer is to induce a non-null transmission on the optical axis: the additional amount of light in one of the beams will not interfere and thus contribute as a background emission. Letting $\Delta I(\lambda)$ be the relative intensity error between the two beams, the expression of the central transmission is (Ollivier 1999):

$$R_\lambda(0,0) = \frac{\Delta I^2(\lambda)}{16} \ . \tag{3.14}$$

- **Polarisation error.** There are various types of polarisation errors, but they can always be converted into phase or intensity errors. For instance, a differential phase shift between the two components *s* and *p* of light can be seen as a phase error between the two beams for each component separately, while differential rotation can be seen as an intensity error when projecting the rotated polarisation components onto the initial direction of the *s* and *p* vectors. In practice, Serabyn (2000) has shown that polarisation errors lead to the following central transmission:

$$R_\lambda(0,0) = \frac{1}{4}\left(\Delta\phi^2_{s-p}(\lambda) + \alpha^2_{\text{rot}}(\lambda)\right) \ , \tag{3.15}$$

  where $\Delta\phi_{s-p}$ is the differential $s-p$ phase delay and α_{rot} the relative polarisation rotation angle between the two beams.

Instrumental leakage has two effects on the performance of the nuller: first, it introduces a *bias*, the mean contribution of instrumental leakage, and second, it introduces an additional *stochastic noise* through its fluctuations. Section 4.2 will essentially deal with the ways to reduce these two contributions.

3.1.3 Spatial and modal filtering

One of the most harmful contributors to instrumental leakage is the corrugation of wavefronts, especially for ground-based instruments where atmospheric turbulence produces large phase errors across

the pupils. For instance, if a rejection ratio of 10^3 is required, Equation 3.13 shows that the standard deviation σ_ϕ of the phase across the pupil cannot be larger than 4.5×10^{-2} radian, which corresponds to a $\lambda/140$ rms wavefront quality. Such low wavefront aberration is extremely challenging to reach from the ground, even in the mid-infrared. It corresponds to a Strehl ratio of 99.8% while state-of-the-art adaptive optics system on large telescopes provide a Strehl ratio hardly above 50% in the near-infrared K band, or about 97% in the mid-infrared N band.

In order to solve this problem, Ollivier & Mariotti (1997) proposed to use spatial filtering, which strongly reduces the wavefront imperfections appearing at high spatial frequencies. For instance, placing a pinhole in the focal plane with a size equivalent to and centred on the Airy disk associated with the on-axis star eliminates the most distorted part of the telescope's point spread function. However, the quality of the filtering is only satisfactory for uncomfortably small pinhole sizes (a fraction of an Airy disk), so that the total throughput of the instrument would be significantly reduced. A better solution has been proposed soon after by Mennesson et al. (2002), based on modal filtering with single-mode fibres.

When a single-mode waveguide is used, the incoming wavefront excites the fundamental mode of the guide. This is the only mode that is allowed to propagate in the waveguide. Its amplitude profile is fully determined by the physical properties of the guide, independently of the incoming wavefront. The shape of the initial wavefront only affects the amount of energy coupled into the guide. It is commonly stated that such a guide transforms wave-front corrugations into fluctuations of the injected starlight: phase errors are traded against intensity errors. All phase defects besides residual OPD errors are thus corrected by single-mode fibres. The temporal variations of phase defects only induce fluctuations of the signals injected in each fibre and thus intensity mismatching at the beam combination stage. The coupling efficiency of a corrugated wavefront into a single-mode fibre results from the overlap integral of the wavefront with the fundamental mode of the fibre. It can be shown that the injection efficiency of a weakly aberrated incoming wavefront into a single-mode waveguide is proportional to its Strehl ratio $S = \exp(-\sigma_\phi^2)$ (Ruilier & Cassaing 2001). The effect of the phase variance $\sigma^2_{\phi_{1,2}}(\lambda)$ across the two pupils is therefore given by $R_\lambda(0,0) = (\sigma^2_{\phi_1}(\lambda) - \sigma^2_{\phi_2}(\lambda))^2/16$ (Mennesson et al. 2002). This expression has to be compared with the initial expression 3.13 of the corrugation-related instrumental leakage. It significantly relaxes the requirements on the adaptive optics system as a rejection ratio of 10^3 is now obtained with a $\lambda/18$ rms wavefront quality (i.e., a Strehl ratio of 88%, still challenging in the near-infrared).

In the following study, it will always be assumed that modal filtering is used to clean the shape of the wavefronts. The field-of-view is then determined by the overlap integral of the fibre's fundamental mode with the classical Airy diffraction pattern, and can be approximated by a Gaussian distribution. A maximum of 82% of the beam's energy can be coupled into the waveguide when the focal length is matched to the fibre core radius in the absence of central obscuration. In that case, the $1/e$ width of the field-of-view equals $0.71\lambda/D$ (Ruilier & Cassaing 2001). Further details on modal filtering and its side-effects can be found in Section 4.1.3.

3.1.4 Disentanglement of the astrophysical sources

A major limitation of nulling interferometry is the fact that all sources located in the diffraction-limited field-of-view contribute to the detected signal and thus cannot be distinguished if a single detection is performed. This is the reason why Bracewell initially proposed to rotate his (space-based) nulling interferometer: if the interferometer spins around its optical axis oriented towards the star, the stellar signal will not vary while the planet transmission will be successively subject to crests and troughs in the transmission map and will therefore be modulated with a frequency related to the rotation period. Since then, several improvements have been added to the initial concept in order to better distinguish the various contributors. These improvements generally concern space-based interferometry dedicated

to Earth-like planet detection, but can also be applied on the ground to some extent.

Improving the rejection ratio

Although the residual stellar leakage can theoretically be removed by rotational modulation, the shot noise associated with the detected leakage still remains and generally represents one of the major noise contributions in the context of Earth-like planet detection. This limitation can be overcome by using more than two telescopes to produce the destructive interference. This idea was first considered by Angel (1990), who proposed to use a four-telescope array to reach a deeper nulling ratio, proportional to θ^4 close to the optical axis instead of θ^2 for the two-telescope Bracewell interferometer.

The potential of multi-telescope arrays was then exploited in the context of the initial Darwin and TPF-I proposals: an array of four to five telescopes arranged on a circle and providing a θ^4 central transmission was suggested for the Darwin mission (Léger et al. 1996), while a four-telescope linear array with a θ^6 central transmission was proposed for the TPF-I mission (Angel & Woolf 1997). Later on, a general condition was derived by Absil (2001) to reach a θ^{2p} transmission for an arbitrary telescope array (see Section 8.1.1), from which he deduced a classification for the behaviour of nulling interferometers: four telescopes are required for a circular configuration to provide a θ^4 central transmission, while three telescopes are sufficient on a linear array. An additional telescope is required in both cases if one wants to use phase shifts different from 0 or π in the beam combination scheme.

Subtracting the background sources

Besides stellar leakage, another difficulty in nulling interferometry comes from the emission of the other sources located in the field-of-view. One of the main noise contributors both in ground-based and space-based nulling is the background emission, due to the thermal environment (Earth atmosphere for ground-based instruments, local zodiacal dust for space-based instrument) and to the emission of the telescope and optical train. This emission may be nonuniform and fluctuate in time. Its average contribution can be subtracted by rotating the array for a space-based instrument. However, even in a stable space-based environment, thermal drifts and other variations in the background emission can lead to significant residuals.

In the case of Earth-like planet detection, another major source of noise is the potential presence of warm dust around the target star. Considering an exozodiacal dust disk similar to the solar zodiacal disk, its integrated flux over the first 5 AU is about 300 times larger than the planetary emission at 10 μm. The main problem with the exozodiacal disk is that its emission is also modulated by rotation of the array, unless it is seen face-on and has perfect circular symmetry, so that it can be confused with a planet.

To alleviate these limitations, fast modulation techniques have been proposed. The principle of these techniques is to synthesise two different transmission maps with the same telescope array, by applying different phase shifts in the beam combination process. In order to remove all point-symmetric sources in the field-of-view (star, background, exozodiacal disk) while keeping off-axis point-like sources (planets), the two maps must be linked to each other by point symmetry. These techniques of *phase chopping* can be implemented in various ways, and are now an essential part of the future space-based planet finding missions. They generally require one additional telescope to be used compared to simple rotating arrays if one wants to achieve the same rejection ratio. For instance, a θ^2 configuration with phase chopping requires at least three telescopes, while a θ^4 configuration requires at least four aligned telescopes or five telescopes on a circle. Phase chopping will be further discussed in Chapter 8.

3.2 Scientific and technological preparation of Darwin/TPF-I

In order to prepare the future planet-finding missions, a number of technologies have to be first validated on the ground. For that purpose, many R&D activities are currently underway both in the United States and in Europe. One of the important activities currently underway is the validation of nulling interferometry on a laboratory breadboard. Critical subsystems such as achromatic phase shifters, mid-infrared single-mode waveguides or space-borne delay lines and tracking systems are also being developed. However, both ESA and NASA soon understood that ground-based on-sky validation of nulling interferometry could be used not only to test all these subsystems in an integrated instrument, but would also be a great opportunity to carry out critical astrophysical observations for the preparation of the Darwin/TPF-I scientific programmes. In particular, we have discussed in the introduction that the presence of circumstellar dust around the target stars could outshine faint Earth-like planets and thus prevent their detection. Ground-based nulling interferometry in the near- to mid-infrared would provide both the angular resolution and the dynamic range to carry out a survey for exozodiacal disks around nearby main-sequence stars.

3.3 A first generation of ground-based nulling instruments

3.3.1 BLINC at the MMT

The first and only nulling experiment to have published astrophysical results so far is the Bracewell Infrared Nulling Cryostat (BLINC). This instrument was first installed on the segmented version of the Multi-Mirror Telescope (MMT), using the beams from two of its 1.8-m segments (Hinz et al. 1998a), and produced first scientific results on late-type giant stars around which dust outflows were detected (Hinz et al. 1998b). After the refurbishment of the MMT in 1999, BLINC was re-installed on the new 6.5-m monolithic telescope (Hinz et al. 2000). It was also used in the southern hemisphere, at the Magellan I (Baade) telescope.

The principle of the instrument is to divide the pupil of the telescope into two halves, thereby creating an artificial 4-m baseline (Figure 3.4) and to overlap them on a 50/50 beam splitter. Such a baseline provides an angular resolution of 258 mas at 10 μm. The orientation of the interferometer can be adjusted since the MMT is an altitude-azimuth-mounted telescope equipped with the ability to derotate the instrument. The derotator stays fixed for nulling observations, with its orientation determining the interferometer baseline's position angle on the sky. Because it works in the infrared N band (8–13 μm), where the thermal emission from room-temperature optical elements is an important source of noise, the instrument is enclosed in a cryostat. Alignment and phasing of the instrument is performed under cold and vacuum conditions by means of feedthrough actuators. The phase shift between the beam is implemented as a slight excess of path-length in one beam balanced by a suitable thickness of dielectric in the opposite beam, which can be slightly rotated to minimise chromatic errors. A sufficient degree of achromaticity can be achieved for the phase shift in that way. The design of the beam splitter provides a $3/4$ wave phase shift at 2.2 μm when it is a $1/2$ wave at 11 μm. The two interferometric outputs in the K band are thus halfway between constructive and destructive and can be used to monitor the pathlength variations between the two arms: any departure from zero OPD will dim one of the outputs while raising the other one.

During its first years of operation on the refurbished MMT, the performance of BLINC was limited to a null depth of 4% due to atmospheric turbulence. Detector frames were then recorded at a high frequency (~500 Hz) in order to freeze the turbulent pattern of the atmosphere and the best frames were selected based on the amount of residual light in the destructive output as compared to the constructive

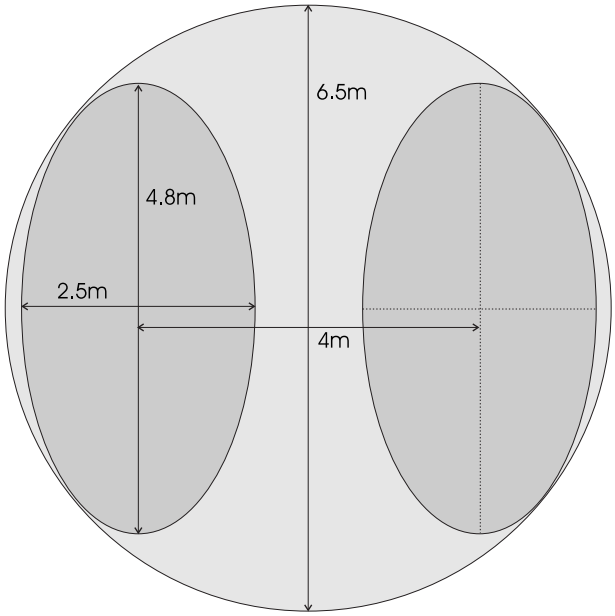

Figure 3.4: Division of the MMT pupil by the BLINC instrument to artificially produce a baseline of 4 m between two oval sub-pupils and perform destructive beam combination.

one. The measured null depth (ratio of the flux of the nulled image to the flux of the constructively interfered image) was then compared to the null depth measured on a point-like calibration source, in order to obtain the "source null" (intrinsic to the chosen target). Soon after its refurbishment, the MMT was equipped with an adaptive secondary mirror to correct for atmospheric turbulence on the wavefronts, thereby allowing a precise adjustment the path difference between the two beams of the interferometer and thus deeper nulling. Doing the correction at the secondary mirrors optimises the throughput and decreases background emissivity in the mid-infrared by avoiding the use of extra warm optics. However, even with adaptive optics, the performance of BLINC is limited to about 3% in null depth because of mechanical vibrations. It still obtained nice results on Young Stellar Objects and Vega-type stars, as discussed in Sections 1.3.1 and 1.3.3 (Liu et al. 2003, 2004, 2005).

Theoretically, a null depth of a few tenths of percent is achievable with BLINC on the MMT. This level of performance should be reached when the internal servo loop for active correction of phase difference in K band will become operational. A null depth of about 10^{-3} in the N band should enable the detection of exozodiacal disks about 50 to 100 times as dense as the solar zodiacal disk (50- to 100-*zodi* disks). Using the refined nulling observations, the BLINC team is planning a survey of nearby main-sequence A-type stars to search for evidence of exozodiacal dust. The ultimate performance of the BLINC instrument will also depend on the ability to subtract background emission with a very high precision, as the integrated background emission in a diffraction-limited field-of-view produced by the atmosphere is about 2×10^4 times larger than the flux coming from a 50-zodi disk at 10 parsec in the N band. The current technique for background subtraction is based on the chopping method, where off-source frames are taken in between each set of observations of the target source. However, the frequency at which off-source observations are currently performed (no more than once per minute) raises doubts on the background stability at a $\sim 10^{-5}$ level over such periods of time.

3.3.2 The Keck Interferometer Nuller (KIN)

Because it operates in the mid-infrared (10–12 μm), where the background emission is huge (especially for a non-cryogenic instrument), the KIN implements an original way of removing the background emis-

sion in addition to the removal of the stellar light. This method is based on phase chopping, a technique currently considered for the Darwin and TPF-I space missions (see Section 8.1). In order to modulate the signal from off-axis sources in front of the background emission, a dual-baseline nuller is synthesised by creating two distinct sub-apertures on each of the two Keck telescopes (Figure 3.5) and then cross-combining the outputs of the two individual nulling beam combiners with a standard interferometric beam combiner (Serabyn et al. 2004). The beam combination in the two individual nullers is performed with modified Mach-Zehnder beam combiners (Serabyn & Colavita 2001). A pair of rapid-scan mirrors provides the phase modulation between the two nulled beams by scanning an OPD equal to the wavelength. The useful signal can then be separated from the background and its fluctuations thanks to high frequency modulation. A potential limitation of this technique comes from the fact that the background emission present in the outputs of the two nuller must be perfectly incoherent in order not to produce a modulated pattern in the final output. The fact that some optical elements are in common between the two nullers may lead to a significant amount of coherent background and thus limit the subtraction accuracy.

A number of control subsystems are added to the basic architecture of the nuller to achieve deep nulling ratios. First, adaptive optics systems are installed on the two telescopes, providing typical Strehl ratios of 50% in the K band, i.e., about 97% at 10 μm. The K-band light is split after beam transport and used to perform fringe tracking. Dedicated N-band delay lines are precisely stabilised at the zero OPD position using the information provided by the K band fringe tracker and the metrology signals, which (among other things) monitor the non-common paths. Atmospheric dispersion compensators correct for the phase gradient within the observing band and also provide the necessary π-radian phase shift (Koresko et al. 2003). Intensity control is performed by obscuring vanes and spatial filtering is implemented in the mid-infrared camera KALI.

The KIN was designed to achieve exozodiacal disk detection at the 30-zodi level around a G2V star located at 10 pc. This level of performance requires a deep and stable instrumental nulling ratio of at least 10^3 at 10 μm. The integration and test laboratory of the Keck Interferometer at JPL was used to

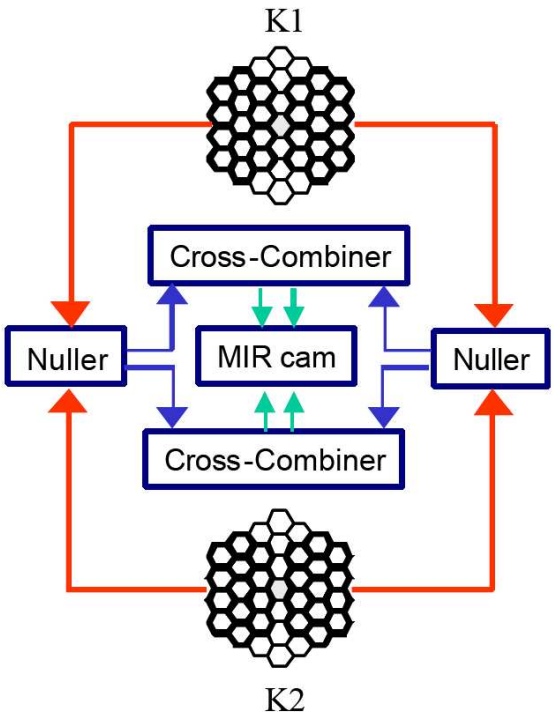

Figure 3.5: Dual-baseline nulling architecture of the KIN (Serabyn et al. 2004).

demonstrate the capability of the instrument to reach such a performance: a broad band null depth better than 10^{-3} was obtained and stabilised for periods of many minutes (Serabyn et al. 2004). This led to the decision to deploy the hardware at the Mauna Kea Observatory, where it is currently in commissioning phase (first N-band fringes obtained in August 2004, first stable null at 10^{-2} obtained in May 2005) and should soon provide its first scientific results. Its ultimate performance will depend on a number of environmental parameters, as discussed in Chapter 4.

3.3.3 The Large Binocular Telescope Interferometer (LBTI)

The LBT Interferometer, which combines the light from two 8.4-m telescopes placed side by side on a single rigid alt-azimuth mount, is very well suited to develop and exploit the basic Bracewell nulling method. With its short baseline of 14.4 m, it provides an angular resolution of 70 mas in the mid-infrared, which corresponds to the typical angular size of habitable zones around nearby G-type stars (see Figure 8.11). The LBTI instrument is composed of a Universal Beam Combiner (UBC) which reimages the two telescope beams to a common focal plane, the Nulling Interferometer for the LBT (NIL) which interferes the light from the telescopes out of phase to suppress the stellar light, and the Nulling Optimised Mid-Infrared Camera (NOMIC), which forms an image of the field around the star and is capable of detecting infrared emission from surrounding dust disks and planets. A second instrument (LINC-NIRVANA), focusing on wide-field interferometric imagery, will be installed as well (Herbst & Hinz 2004).

The NIL instrument relies on an upgraded version of the BLINC instrument developed at University of Arizona (Hinz et al. 2000). It will strongly benefit from the original architecture of the LBT, which is optimised for mid-infrared observations. Thanks to the use of adaptive secondary mirrors, and because delay lines are not required, only three warm mirrors, primary, secondary and Nasmyth flat, are used to direct the beams toward the cryostats where the instruments (UBC, NIL and NOMIC) are installed. This architecture minimises the contribution of the thermal background to the detected signal. In order to remove the background emission, an imaging detector is used and the secondaries will be rapidly tilted ($\sim$10 Hz) to translate the (nulled) star vertically through several diffraction widths along the line of null. In this way the zodiacal flux is always being detected, and the sky flux is simultaneously determined with an equivalent integration time. As in the case of the BLINC instrument, NIL will use the K-band output of the beam combiner to perform co-phasing of the beams.

The targeted null depth with the NIL instrument is 10^{-4}, with the objective to detect exozodiacal disks similar to the solar zodiacal disk (1-zodi level). A number of limitations could however prevent such a null depth with the current design of the nulling instrument. First, the absence of spatial filtering, which was intended to improve the throughput and increase the field-of-view, imposes tight requirements on the adaptive optics performances (Strehl ratio of 99.9% in N band), which might be difficult to reach even with the 670-actuator deformable secondary mirror. A second limitation comes from the fact that the co-phasing of beams in the K band does not ensure perfect co-phasing in the N band. A dispersion compensator might be needed to reach the required level of performance, as in the case of the KIN. Finally, background subtraction will definitely be challenging, as the integrated background emission from the atmosphere in a diffraction-limited field-of-view will be about 10^6 times larger than the emission from a 1-zodi disk. Background subtraction at such a level of precision has never been demonstrated. Moreover, the proposed technique for background subtraction at the LBTI might be sensitive to spatial nonuniformities.

The first 8.4-m mirror of the LBT was installed and achieved its first light in 2005. The second primary mirror has recently been transported from the University of Arizona to Mount Graham and has also been installed. By fall 2006, the LBT will be fully operational with both its enormous eyes wide

open. The nulling instrument will be used to perform a survey called NIREST (Nulling Infra-Red survey of Exo-Systems for TPF) of 80 TPF-I candidate stars. Its purpose is to search for and measure zodiacal dust emission strong enough to compromise TPF-I's performance. A by-product of the survey will be the detection of thermal emission from extrasolar giant planets.

3.4 The European effort: GENIE

In the context of the Darwin programme, the European Space Agency (ESA) and the European Southern Observatory (ESO) have initiated a definition study for a ground-based technology and science demonstrator called GENIE (Ground-based European Nulling Interferometry Experiment). This collaboration was initiated because ESO's VLT Interferometer (Cerro Paranal, Chile) was soon identified to be the best place to install a European nulling instrument. A letter of intent, signed by the two agencies, was sent to the European astronomy community in mid-2001, identifying the objectives of the GENIE instrument:

1. To gain required technological experience and demonstrate the technique of nulling interferometry with a breadboard representative of the Darwin mission;
2. To carry out required precursor science viz.
   - Detection and measurement of exozodiacal disks associated with the Darwin targets,
   - Detection and characterisation of large sub-stellar companions around the Darwin targets;
3. To allow European scientists to gain experience with a nulling interferometer in doing practical astronomy, and to train a new generation of "interferometrists" in preparation of the utilisation of Darwin;
4. To carry out unique and valuable science.

Studying the possible implementation of a nulling instrument at the VLTI was a natural continuation of my Diploma thesis on the Darwin configurations (Absil 2001), and it was therefore decided that I would assist ESA in the definition of the GENIE instrument during my PhD work. In this context, my first objective was to study and identify convenient candidate concepts for GENIE at VLTI, i.e., aperture configurations and associated modulation techniques. This work was part of the process leading to the issuing of an invitation to tender to industry for a phase-A study on the GENIE instrument. My work on the GENIE configurations and modulation techniques was pursued during the phase-A study (11/2003 – 11/2004) in collaboration with a consortium of industries and academic institutes regrouped around Alcatel Space.[9] This contribution is summarised in the rest of this chapter.

3.4.1 The VLTI infrastructure

The ESO Very Large Telescope (VLT) at the Cerro Paranal Observatory (Chile) is one of the world's largest and most advanced optical telescope. It presently comprises four 8-m reflecting Unit Telescopes (UTs) and three (soon four) 1.8-m Auxiliary Telescopes (ATs). The light beams collected by the various telescopes can be brought together by means of subterranean relay optics and coherently combined in this world-leading interferometric facility. Baselines ranging from 47 m to 130 m can be formed with the fixed UTs, while the movable ATs allow for baselines ranging from 8 m to 202 m (see Figure 3.6: the grid of AT stations has an 8 m fundamental spacing). Six of the eight delay line tracks are already furbished, theoretically allowing for six beams to be combined at the same time. The VLTI is currently

[9] Another consortium, regrouped around EADS Astrium, also performed a phase-A study on GENIE and essentially came to the same conclusions concerning the top-level requirements and functions of the instrument.

equipped with two scientific instruments, AMBER and MIDI, and a test instrument called VINCI, which obtained the first VLTI fringes in March 2001.

The VLTI infrastructure also comprises a number of subsystems improving the global performance of the facility. First, the four UTs are all equipped with an adaptive optics system called MACAO (Arsenault et al. 2004), providing typical Strehl ratios of 50% in the K band, while tip-tilt correction is performed on the ATs with the STRAP system. Two of the six delay lines are already equipped with Variable Curvature Mirrors (VCM) ensuring reimaging of the telescope exit pupil on the instrument entrance pupil even when the delay lines are moving. FINITO, a three beam fringe tracker operating in the H band, is currently under commissioning (Gai et al. 2004). When optimisation at VLTI will be completed, FINITO is expected to co-phase the beams with a residual OPD as small as 100 nm rms. A second-generation fringe tracker called PRIMA-FSU, based on a more robust design with simultaneous detection of four outputs (ABCD fringe detection scheme), should achieve the same order of performance on two beams in the K band. In addition, PRIMA will also provide a star separator system, a laser metrology system and differential delay lines (Quirrenbach et al. 2004). Finally, an infrared tip-tilt tracker (IRIS) is available in the interferometric laboratory and corrects for tip-tilt perturbations in the delay line tunnel at the 10 mas level and a frequency of 10 Hz.

The following discussion of a nulling instrument at VLTI will be restricted to two atmospheric win-

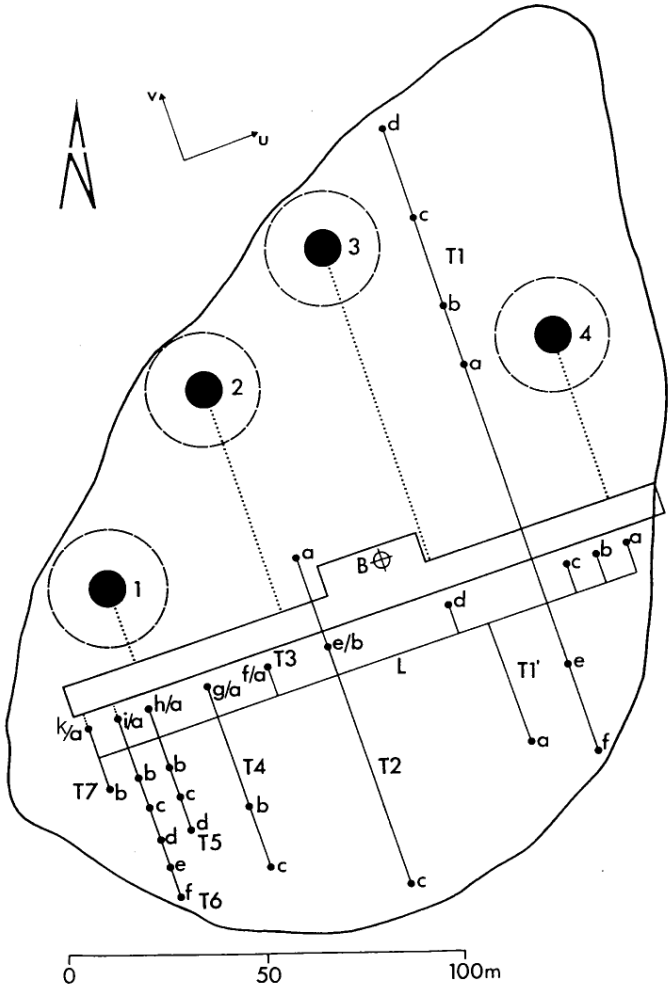

Figure 3.6: Layout of the individual VLTI elements. Unit Telescopes are shown as large, filled circles, while the AT locations are indicated by small, filled circles. The sizes of these circles are scaled to the diameters of the primary mirrors. Solid lines show the tracks for transporting the ATs between stations.

dows, the L′ (3.5 – 4.1 μm) and N (8 – 13 μm) bands, which were early identified as the most promising ones in the context of exozodiacal dust detection because they are most sensitive to dust temperatures in the range 200 – 800 K and provide good transmission over a wide bandpass. The $1/e$ radius of the field-of-view, limited by the use of single-mode fibres (Section 3.1.3), equals 70 mas and 192 mas respectively in the L′ and N bands for an 8-m UT (see Figure 3.3), while ATs have a field-of-view radius of 309 mas and 854 mas respectively in these bands. This has to be compared with the typical angular distance of habitable zones around Darwin/TPF-I candidate targets. According to Kaltenegger et al. (2006), this distance is smaller than 50 mas for most K and M-type dwarfs, while it is typically comprised between 40 and 100 mas for F and G-type dwarfs (see Figure 8.11). The UTs might therefore not be appropriate to study the habitable zone of some stars in the L′ band. However, it must be noted that the maximum emission from an exozodiacal disk in the L′ band comes from a region smaller than the habitable zone, typically at about 0.25 AU from a G-type star (instead of 1 AU for the habitable zone). If the L′ band is used to survey exozodiacal disks in the context of Darwin/TPF-I, some extrapolation will therefore be required to deduce the actual dust density in the habitable zone.

As far as field-of-view is concerned, it appears that ATs and UTs can both be used in the L′ and N bands to survey the Darwin/TPF-I star catalogue for the presence of dust. However, we will see in Section 4.2.1 that the reduced collecting area of the Auxiliary Telescopes does not allow the detection of faint exozodiacal disks around Darwin/TPF-I targets in the N band due to the huge thermal emission from the atmosphere and the instrument itself. The use of ATs will therefore be restricted to the L′ band.

3.4.2 Nulling configurations at VLTI

Two main configurations have been considered for implementation of nulling interferometry at VLTI: a two telescope Bracewell configuration and a three telescope *Degenerate Angel Cross* (DAC). The main trade-off criterion between these configurations is their ability to suppress the stellar light deeply enough so as to reveal faint circumstellar dust features. While instrumental leakage does not depend on the chosen configuration to the first order (Lay 2004), geometric leakage can be drastically reduced by using configurations with a high order central transmission (θ^4 or higher). The ability of a nulling concept to calibrate the residual stellar photons in the destructive output of the nuller is another important issue. The quality of a configuration is thus measured by the combination of both the performance on starlight rejection and the achievable calibration accuracy on geometric leakage.

Technical complexity and cost are two other major criteria that will eventually drive the choice for one or the other configuration. The ability to operate both UTs and ATs in the nulling mode is another important criterion, as it would allow for the commissioning phase and regular observations to be performed on the ATs while still permitting operation on the UTs for faint (remote) targets.

The Bracewell configuration

With its simple two-telescope configuration, the Bracewell nulling interferometer achieves the poorest rejection rates due to its θ^2 central transmission. Table 3.1 gives the geometric rejection ratio achieved by a Bracewell interferometer with a 46.7 m baseline (shortest UT-UT pair for the highest rejection ratio) on typical main-sequence targets at various distances. The expected ratio between the stellar flux and the integrated flux from a 20-zodi disk is given for comparison, showing that the residual stellar light generally exceeds the flux from the circumstellar disk. Fortunately, this contribution can be calibrated analytically by means of Equation 3.11, provided that the stellar angular radius $\theta_\star$ is known with a sufficiently good accuracy. Assuming that a signal-to-noise ratio (SNR) of 3 is required to detect the

	Star/disk		Rejection rate		Calibration	
Star	L′	N	L′	N	L′	N
K0V - 5pc	13200	1270	183	1397	0.2%	18%
G5V - 10pc	10100	961	625	4770	1.0%	83%
G0V - 20pc	9200	865	1748	13348	3.2%	257%
G0V - 30pc	9200	865	3933	29979	7.1%	578%

Table 3.1: Geometric rejection ratio for a 46.7 m Bracewell interferometer observing typical Darwin/TPF-I targets. The star/disk contrast is given for comparison in the case of a 20-zodi disk (based on the ZODIPIC package, see Section 4.1.1). The calibration accuracy is deduced so as to obtain a residual stellar leakage six times smaller than the flux from the exozodiacal disk.

disk, and that the four main contributors[10] to the total noise all have the same magnitude, we deduce that an SNR of 6 is required for each individual contributor and derive the required calibration accuracy on the geometric leakage. This value can be translated into a requirement on the knowledge of the stellar angular diameter of typical Darwin/TPF-I candidate targets, as a simple differentiation of Equation 3.10 gives $\Delta\theta_\star/\theta_\star = 0.5\Delta N/N$.

The tightest specifications on geometric leakage calibration come from the closest targets. Table 3.1 shows that, in the L′ band, the required knowledge on the stellar angular diameter is a few tenths of a percent, while in the N band an accuracy of 10% is sufficient. We argue in Section 4.2.1 that the L′-band angular diameter of most Darwin/TPF-I candidate targets can be measured or estimated with a precision of about 0.5%, which is only marginally compliant with the requirements. In fact, this requirement would be significantly relaxed if shorter baselines could be used. Operation with two ATs in the L′ band is therefore of great interest for the closest sources of the Darwin/TPF-I catalogue. For instance, observing a K0V star at 5 pc on a 16 m AT-AT baseline would increase the rejection rate by a factor ∼10 and thus relax the calibration accuracy to about 2%. This baseline is also better optimised to search for dust around such a close target, as its associated angular resolution (50 mas in the L′ band) better corresponds to the zone of interest (0.25 AU) than a longer baseline, which would largely over-resolve the habitable zone.

Higher-rejection configurations

Because the geometric rejection ratio provided by UT-UT configurations is not sufficient to reduce the stellar light below the planetary emission level, configurations with a higher order central transmission have been investigated. The simplest configuration that achieves a θ^4 central transmission is the Degenerate Angel Cross (DAC), composed of three aligned telescopes (Mennesson et al. 2005). The contribution of the central telescope in the beam combination scheme must be twice as large and π radians out of phase with respect to the two outer ones. Because it requires three aligned telescopes to produce a θ^4 central transmission, the DAC can only be used with ATs: three aligned UTs are not available at VLTI. As a consequence, this configuration is restricted to the L′ band. Due to the strongly reduced sensitivity of ATs with respect to UTs, the performance of the DAC on the faintest targets of the Darwin/TPF-I catalogue will therefore significantly trail those of the Bracewell, which can be operated on UTs for these targets.

The rejection rate of a DAC can be expressed in an analytical way, as was done for the Bracewell configuration in Section 3.1.2, by integrating its intensity response on the stellar photosphere. As expected,

[10]These main contributors are the residuals of geometric leakage calibration, instrumental leakage, the residuals of background subtraction and the global detection noise (including shot noise, read-out noise, etc).

the result is inversely proportional to the fourth power of the stellar angular radius $\theta_\star$:

$$\rho = \frac{32}{\pi^4}\left(\frac{\lambda/b}{\theta_\star}\right)^4 . \tag{3.16}$$

The available baselines for three aligned ATs range from 16 m to 182 m, so that the angular resolution of the configuration can be tuned to the observed target by placing the first bright fringe of the transmission map on the zone where the dust is at $\sim$ 800 K. In that case, the rejection ratio achieved on the stellar light typically ranges between 10^5 and 10^6. With such a performance, Table 3.1 shows that calibration of the stellar residuals would not be needed any more, as the initial star/disk contrast is typically 10^4 in the L′ band.

Besides its restriction to ATs, an important limitation of the DAC configuration comes from its technical complexity. A two-stage beam combination is required, as the two outer telescopes must be combined together before being destructively interfered with the central telescope (Mennesson et al. 2005). Other configurations with a θ^4 rejection rate would be even more complex as they would require four beams to be co-phased, balanced and combined.

Conclusion

The choice of a nulling configuration at VLTI depends on the considered wavelength. In the N band, where UTs are needed to reach the required sensitivity, the Bracewell configuration is the only viable option. On the other hand, in the L′ band where ATs can be used as well, high-rejection configurations such as the DAC would be better suited owing to their better rejection rate. However, the complexity of these configurations[11] and the restriction to the ATs are two serious drawbacks with respect to the Bracewell configuration. The latter should in fact provide sufficient performance on most Darwin/TPF-I candidate targets if ATs are used on short baselines for the closest subset (< 10 pc) while UTs are used on longer baselines for the remote targets (> 10 pc). Preparatory observations will however be required for the Bracewell configuration to efficiently operate in the L′ band, as stellar diameters will have to be known with a typical accuracy of 0.5%. Precise photometry, combined with surface-brightness relations (Kervella et al. 2004d), seems sufficient to predict stellar diameters with the required accuracy (see Section 4.2.1). In addition to providing the required starlight subtraction on most targets, the Bracewell is by far the simplest and cheapest configuration, and it can be used both with UTs and ATs. For these reasons, it has been selected as the baseline concept for the GENIE instrument.

3.4.3 Background subtraction techniques

Accurate background subtraction is an essential step for the detection of the faint exozodiacal signal behind the huge thermal emission from the atmosphere and the infrastructure. We show in Section 4.2.1 that the signal from a 20-zodi disk is typically 10^4 (resp. 6×10^6) times smaller than the background in the L′ (resp. N) band. In order to obtain an SNR of 6 for this noise contributor as in the case of residual geometric leakage, a background calibration accuracy of the order of 10^{-5} (resp. 2×10^{-8}) is required.

The quality of a background subtraction technique is determined by its ability to obtain background measurements as close as possible, both in the space and time domains, to the background signal actually present in the science data. The off-source measurements should also be as clean as possible, i.e., not contaminated by other sources such as the star or the exozodiacal disk. If possible, the on-source and off-source beams should also follow the same path in the optical train in order to avoid systematic errors in the estimation of the background.

[11] in particular, the fact that all control subsystems have to be duplicated due to the two levels of beam combination

Background subtraction by chopping-nodding

The classical *chopping-nodding* technique for background subtraction consists in tilting the secondary mirror of the telescope by a small quantity (a few arcseconds) in order to measure the background in an empty sky region close to the source and subtract it from the on-source measurements. The chopping sequence is repeated at a few Hertz. Nodding consists in repeating the whole chopping sequence off-source, by slightly tilting the telescope, in order to remove potential gradients associated with spatial variations of the thermal emission from both the sky and the optical train.

In the context of the GENIE phase-A, I have studied in collaboration with E. Bakker (NEVEC, Leiden) and M. Schöller (ESO, Santiago) the temporal fluctuations of the background emission at 10 μm recorded at the VLTI with the MIDI instrument (Absil et al. 2004a, see Appendix A). The main output of this study is a characterisation of the Power Spectral Density (PSD) of temporal background fluctuation and of its standard deviation, which is shown to be about 10^{-3} times smaller than the total background emission on a 10 min observation. Based on this model, we have estimated the requirements on the chopping frequency, and conclude that a frequency of about 150 Hz is required to reach a background subtraction accuracy of 10^{-4}, which is still a factor 10 above the requirement in the L′ band and a factor 5000 above the requirement in the N band (see Appendix A). Moreover, the precision of background subtraction increases very slowly with the chopping frequency f_c, proportionally to $f_c^{0.25}$ in our model.[12] Classical chopping with the secondary mirror of the VLTI cannot be performed at such a high frequency (it is limited to a frequency of 5 Hz). Even though a smaller chopping mirror could be used, placed downstream in the optical train, unrealistic chopping frequencies of at least a few kHz would be needed to achieve the required background subtraction accuracy. Therefore, advanced chopping techniques allowing for higher chopping frequencies or simultaneous measurements should be used for GENIE.

Background subtraction with multiple fibres

The purpose of this technique is to measure the background within the field-of-view available at VLTI (2″ for UTs, < 9.7″ for ATs) by inserting additional single-mode "background fibres" close to the on-axis "science fibre" centred on the star. This technique allows for background calibration simultaneous to the science measurement, which is indeed equivalent to an infinite chopping frequency. A similar technique, using pinholes, has already been proposed for the MIDI instrument.

Simultaneous measurements are done at the expense of separate spatial positions for the science and background channel, so that the technique is inherently sensitive to spatial gradients in the background emission. This drawback can be overcome by interpolating the actual value of the background in the science fibre from measurements at different locations within the field-of-view. Possible systematic errors due for instance to different throughputs for the various fibres can be removed by exchanging the positions of the fibres (Figure 3.7). A careful calibration of the fibres and detectors during the commissioning phase might also be sufficient. Another drawback associated with the spatial separation of the fibres is that the science and background beams hit different parts of the mirrors in their path from the telescope to the instrument, which could lead to slightly different values of the instrumental background. This effect can however be calibrated by nodding the telescope to an empty sky region.

A critical issue for this technique is the amount of stellar light coupled into the "background fibres". This quantity strongly depends on the quality of the wavefront correction performed by the adaptive optics system: if too much stellar light remains in the incoherent halo, the required accuracy of background subtraction cannot be reached as stellar light would bias the off-axis background measurements. Here

[12] The actual behaviour might deviate from this model as fluctuations of the background at frequencies above 10 Hz were hidden by shot noise in our measurements.

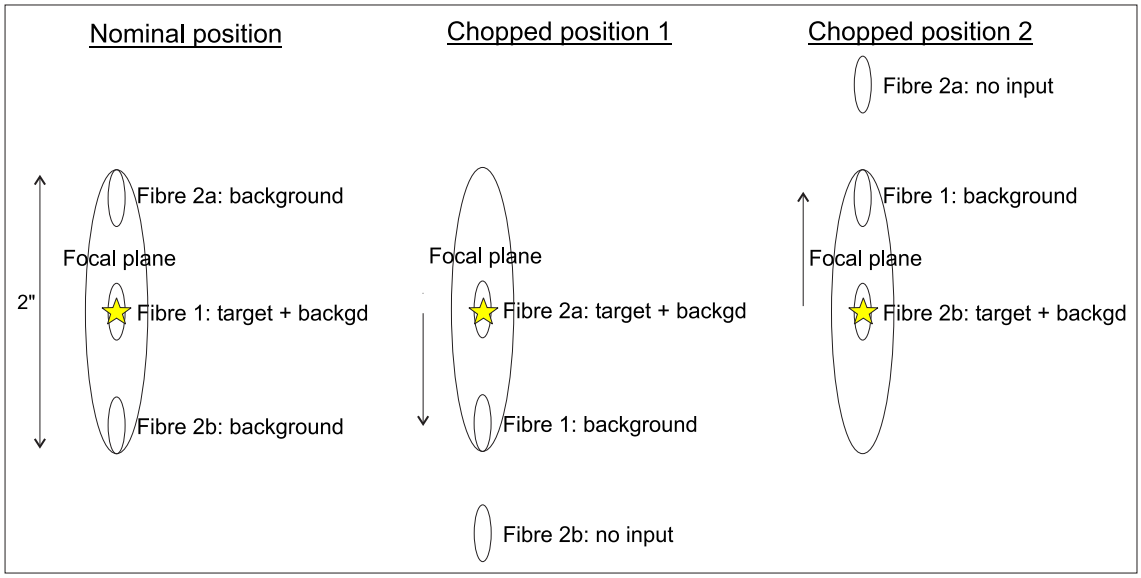

Figure 3.7: Principle of background subtraction with multiple fibres. Three single-mode fibres are inserted in the 2″ field-of-view of the VLTI (case of UTs). Chopped positions are used to avoid systematic errors (fibre throughput, detector efficiency, etc).

again, the fraction of stellar light coupled into the background fibre should be at least 6 times smaller than the signal from the exozodiacal disk. From Table 3.1, one can deduce that the residual stellar light in the background fibre should not exceed about 10^{-5} (resp. 10^{-4}) of the total stellar flux in the L′ (resp. N) band. Adaptive optics simulations performed at ONERA have shown that the residual stellar light at 1″ from the axis should amount to 2×10^{-4} (resp. 2×10^{-3}) in the L′ (resp. N) band after wavefront correction by the MACAO system. This problem has been further studied by G. Perrin in the context of the phase-A study (Barillot 2004b), and led to the conclusion that the required accuracy could still be reached by carefully calibrating the point spread function after correction by adaptive optics. This study has also shown that the expected spatial inhomogeneities of the background emission should not be a major source of bias owing to the small angular separation of on-source and off-source measurements.

Another issue is the technical feasibility of putting three fibres very close to each other in a common focal plane. The recent development of fibre optics and integrated optics techniques in the thermal infrared domain should however soon provide the required optical components.

Background subtraction by phase modulation with pupil division

As discussed in Sections 3.1.4 and 8.1, phase modulation is a powerful technique to extract a coherent signal from the incoherent thermal background radiation. However, phase modulation can be achieved only if two different nulled signals are available. The principle of phase modulation with pupil division, also referred to as the *split-pupil configuration*, is illustrated in Figure 3.8. It is similar to the concept of the Keck Interferometer Nuller. In order to produce two different nulled signals, the pupils of the UTs (or ATs) are divided into two equal semi-circular parts. The corresponding halves of the two telescopes are combined using a classical Bracewell nulling scheme. Two nulled signals are thus obtained, which can then be combined and phase-modulated in order to extract the useful signal from the incoherent background. Assuming that the final beam combination is done in a co-axial way on a lossless beam combiner, the same background flux will be measured in both outputs of the beam splitter, simultaneously in time, allowing in theory a perfect background subtraction.

The extraction of the coherent signals from the background can be done in two different ways:

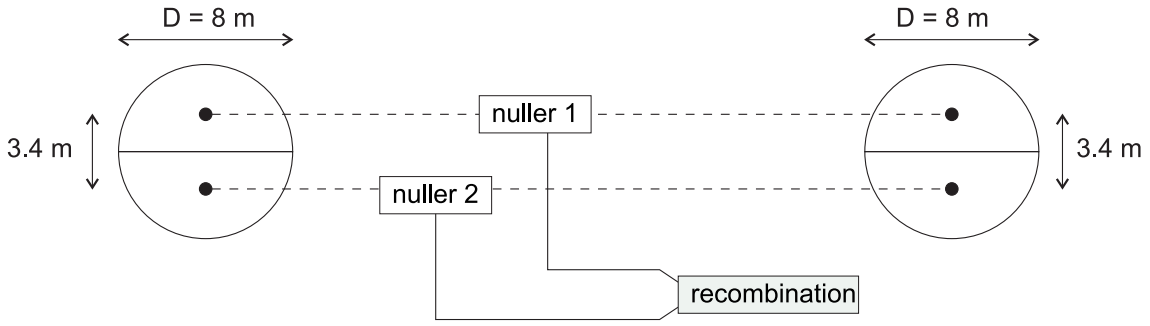

Figure 3.8: Principle of phase modulation with pupil division ("split-pupil Bracewell"), illustrated in the case of 8-m UTs.

- **Discrete phase modulation.** In this method, an achromatic phase shift is applied to one of the two nulled beams before the final combination so that the half pupils are put out of phase. In this condition, all coherent signals will be directed to only one of the two outputs of the beam splitter. A simple subtraction of the two detected fluxes will thus be sufficient to single out the coherent signals. In order to avoid potential systematic errors, the role of the two outputs should be repeatedly changed by putting the phase shift alternately in one or the other nulled beam. The transmission map of the total instrument, including the final beam combination, is illustrated in Figure 3.9, where the first and third images correspond to a phase shift of 0 or π radian between the semi-pupils.

- **Continuous phase modulation.** Phase modulation can also be implemented as a variation of the OPD in one arm of the interferometer (chromatic phase modulation). In this configuration, the background subtraction can benefit both from the variation of coherent signals in each output, as the transmission map takes all possible states between the four illustrated in Figure 3.9, and from the fact that two complementary outputs are available. Moreover, additional information on the morphology of the circumstellar disk can be retrieved from the shape of the time-modulated signals. For instance, if the brightness of the disk mainly comes from the inner region, the modulation will show steep gradients as the wide fringe pattern associated with the short baseline scans this region. An extended disk emission, on the other hand, will produce a smooth modulation curve. Disk asymmetries could also be detected, because they produce a slightly asymmetric modulation curve.

Although this concept provides in theory a very clean background subtraction, it also has some drawbacks. The main limitation is that the division of the pupils introduces significant additional complexity: instead of only having one nuller, this configuration comprises two nullers and an additional beam combiner. Most of the hardware will thus be duplicated, including the required control subsystem such as fringe tracking, intensity control, etc. The possibility to co-phase and balance the beams before pupil division has been considered, but was not found to be acceptable as it does not ensure a sufficient co-phasing and balancing of each of the half pupils. Another major limitation is the fact that the background emission present in the outputs of the two nullers is not completely incoherent, because the beams associated with the two halves of a same pupil have travelled the same path in the VLTI optical train, and thus essentially experienced the same "instrumental" background. A significant part of the background emission could therefore be confused with the coherent sources that are to be isolated. These two major drawbacks have urged to choose the concept of multiple fibres as a baseline concept for GENIE.

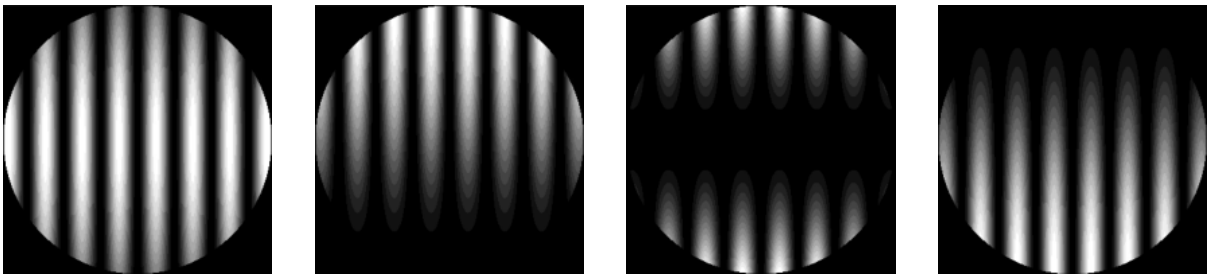

Figure 3.9: Monochromatic transmission maps of the split-pupil Bracewell after final beam combination, resulting from the superposition of a narrow fringe pattern associated with the long baseline and a wide perpendicular pattern associated with the short baseline between the two halves of each pupil. The four maps have been obtained with various phase differences between the outputs of the two nullers: 0, $\pi/2$, π and $3\pi/2$ radians (from left to right).

3.4.4 The need for a GENIE simulator

It was soon recognised that a software simulator of the GENIE instrument and of its environment (atmosphere, VLTI) would be a key element to compare the various concepts and to eventually choose the major design guidelines for GENIE. In particular, this simulator could provide the required performance estimations to choose between the two wavelength bands considered so far. In this context, a major role of the simulator would thus be to model the atmospheric and instrumental perturbations and derive the level of instrumental stellar leakage to be expected in both bands. A realistic simulation of fringe tracking, adaptive optics systems, modal filtering and intensity control is therefore one of the key elements of the simulator. This simulation would also provide the requirements on the quality of beam co-phasing and balancing, in order to reach the appropriate sensitivity of ~20 zodis. Another key feature of the simulator, which has in fact already been used in the previous paragraphs, is the estimation of the background emission, coming from both the atmosphere and the instrument.

My major contribution to the GENIE project has therefore focused on the development of such a simulator, in collaboration with Roland den Hartog (ESA/ESTEC). In the next chapter, some of the critical elements of this simulator are presented, as well as its major results. A particular emphasis will be put on control loops, which constitute the heart of the GENIE instrument and which I studied in detail during the phase-A.

4

Simulated performance of ground-based nulling interferometers

Contents

4.1 GENIEsim: the GENIE simulation software 75

4.1.1 Principle and architecture of the simulator 76

4.1.2 Real-time correction of atmospheric turbulence 78

4.1.3 Modal filtering and the fluctuations of coupling efficiency 81

4.2 A performance study of the GENIE instrument 84

4.2.1 Article: *Performance study of ground-based infrared Bracewell interferometers* 84

In the design of a complex instrument such as GENIE, early access to simulation software is a valuable asset. For example, the choice of the operational wavelength and the design of the control subsystems are two critical issues that cannot be addressed without a realistic simulation of the instrument operation. Therefore, we have developed an IDL package called GENIEsim to simulate future observations with the GENIE instrument, taking into account all noise sources encountered in ground-based interferometry. In this chapter, we present the principle and general architecture of GENIEsim. Two major building blocks of the simulator are then discussed in detail: real-time control loops and modal filtering. Finally, an end-to-end performance study of ground-based nulling interferometers is presented and illustrated in the case of the GENIE instrument.

4.1 GENIEsim: the GENIE simulation software

The implementation of simulation software for the GENIE instrument began in September 2001, in the context of the present PhD work, with the description of the astrophysical sources and the interferometric response. These basic features were soon improved and complemented by a fruitful collaboration with Roland den Hartog (ESA/ESTEC), who shares the fatherhood and development of this software. GENIEsim is now a complete end-to-end simulator of the VLTI infrastructure equipped with a nulling instrument, and consists of about 35000 lines of IDL code. While its implementation is strongly connected to the VLTI and to the design options of the GENIE instrument, the simulator was developed so as to be easily transposed to other nulling instruments, with two telescopes or more, a capability that is

exploited in Chapter 6. The versatility of GENIEsim also comes from the fact that it can be operated in any infrared atmospheric window, even though it is more specifically designed for the L′ and N bands, which are the preferred wavelengths for the GENIE instrument. The original objectives of GENIEsim can be summarised as follow:

- to define the basic GENIE functions, operation and calibration modes;
- to define top-level specifications on the GENIE instrument and on the VLTI;
- to quantify the impact of the atmosphere on the sensitivity of GENIE;
- to perform trade-offs between different concepts and/or designs proposed by the industrial partners;
- to estimate the global GENIE performance for these various concepts;
- to simulate GENIE commissioning tests and observing scenarios, in preparation for future scientific exploitation of the instrument;
- to test data reduction and analysis procedures.

In this section, we describe the global architecture of GENIEsim and its main building blocks. More details on the physics that was included in the simulator can be found in Absil (2003), where are presented all the phenomena that would eventually be implemented. Most of them are also summarised in the article included in Section 4.2.1, together with the expected performance of the GENIE instrument. The interested reader is also referred to the GENIEsim Release Notes (version 8), and to the fully commented IDL code of GENIEsim available on request (from Roland den Hartog: `rdhartog@rssd.esa.int`).

4.1.1 Principle and architecture of the simulator

The basic principle of the simulator is to produce an instantaneous transmission map of the nulling interferometer, taking into account all perturbations related to the instrument and its environment. This map is projected on the plane of the sky in order to compute the transmitted flux from all astrophysical sources located within the field-of-view of the instrument. Unlike a ray-tracing tool, GENIEsim relies on the physical modelling of individual subsystems or phenomena, taking into account the characteristics of the target source, the instrumental set-up and the environmental parameters. The main outcome of the simulator consists of a number of detected photo-electrons as a function of time and wavelength, at both the constructive and destructive outputs of the nulling interferometer. The basic action of the simulator can be expressed as in Equation 3.6, by a 2D-integral performed in the plane of the sky, where the instantaneous transmission map $R_\lambda(\theta, \alpha, t)$ is affected by atmospheric and instrumental perturbations. In this integral, the various astrophysical sources are treated in different ways:

- The contribution of stellar leakage is computed in a semi-analytical way following Equation 3.8, using the 2D numerical integration routine of IDL (`int_2d.pro`) with an analytical expression for both the stellar limb profile and the instantaneous transmission map. This process gives a very accurate estimation of stellar leakage.
- The image of circumstellar disks can be provided by three different packages integrated to the simulator. The ZODIPIC package, developed by M. Kuchner,[13] provides an image of the solar zodiacal disk as seen from outside the solar system. DISKPIC is a package that I developed to simulate optically thin disks with simple geometries. Finally, YSOPIC has recently been added in collaboration with E. Herwats to simulate optically thick disks around young stellar objects. All of them provide digital images of the simulated disks, generally on 128×128 pixels. The transmitted signal from a circumstellar disk is then computed by multiplying the disk image by a digitised transmission map, followed by a standard tabulated integration of the resulting intensity pattern.

[13] The ZODIPIC package is available at `http://www.astro.princeton.edu/~mkuchner/`.

- Potential planets are considered as point-like sources, and are thus only affected by the value of the transmission map at the position of their centre.
- Finally, the background emission is assumed to be perfectly incoherent so that the resulting signal can be computed by a simple integration over the field-of-view.

Description of the simulation sequence

The simulation sequence begins with the initialisation of various parameters related to the interferometer configuration, the target sources, the observing scenario, the atmospheric conditions, and to the detector and control loop performance. These parameters are stored in two ASCII files, which are read by a dedicated routine and transferred to the top-level routine by means of common blocks. From the instrumental specifications, a table is computed for the single-mode fibre coupling efficiency as a function of off-axis angle (see Section 4.1.3). This process also defines the extent of the field-of-view. The second important step is the definition of the astrophysical sources: from the physical parameters stored in the "observational" ASCII file, the intensity distributions of all sources are computed across the field-of-view.

GENIEsim is then structured in a number of stacked loops over wavelength and time (see Figure 4.1). Three different time scales are used in the simulator: observation blocks, detector frames and elementary time step. The outermost loop runs over observation blocks (OBs), which have a typical length of a few tens of seconds. This duration was chosen both for physical and technical reasons (mainly limitation in RAM memory). We assume that the global atmospheric conditions are constant during an OB and generate random time series for all turbulent parameters, such as piston, dispersion, wavefront errors, scintillation, etc, with a typical resolution of 0.1 msec. Such a small elementary time step is mandatory in order to include the effect of fluctuations up to the frequency at which they become negligible in the error budget. This time step is also related to the maximum repetition frequency of real-time control loops. The initialisation of control loops is one of the first actions performed in the time loop on OBs. This critical process is described in some detail in Section 4.1.2.

Once the random fluctuations of atmospheric parameters are generated, taking into account the influence of real-time control loops, a second loop begins on the detector frames, with a typical timescale of 100 msec. The purpose of this loop is to produce the signals actually recorded during an elementary integration and subsequent read-out of the relevant pixels on the detector. This loop is subdivided into the user-defined wavelength channels, which are recorded by different pixels and produce different results.

The inner time loop, with a typical elementary step of 0.1 msec, is the heart of the simulator. It consists in computing the instantaneous transmission map as a function of atmospheric and instrumental perturbations. The coupling efficiency is also computed in real-time as it is affected by random perturbations as well. The instantaneous transmission map is then used to compute the transmitted signal for each time step by a 2D integral over the field-of-view. These instantaneous signals are then added to produce the simulated read-outs of the detector. The loops over wavelength channels and detector frames are repeated until the full observation block is simulated. This process is then repeated for each OB and finally produces a number of arrays containing the detected signals as a function of time. A number of intermediate results are also produced by the simulator, as well as various diagnostic outputs. For instance, the random sequences for all atmospheric parameters are stored in IDL binary files.

Fundamental building blocks

The simulator is composed of a number of routines acting as building blocks, which are called in turn by the top-level routine (`geniesim.pro`). A thorough description of these building blocks is given in the GENIEsim Release Notes. The most important routines are stored in a dedicated subdirectory

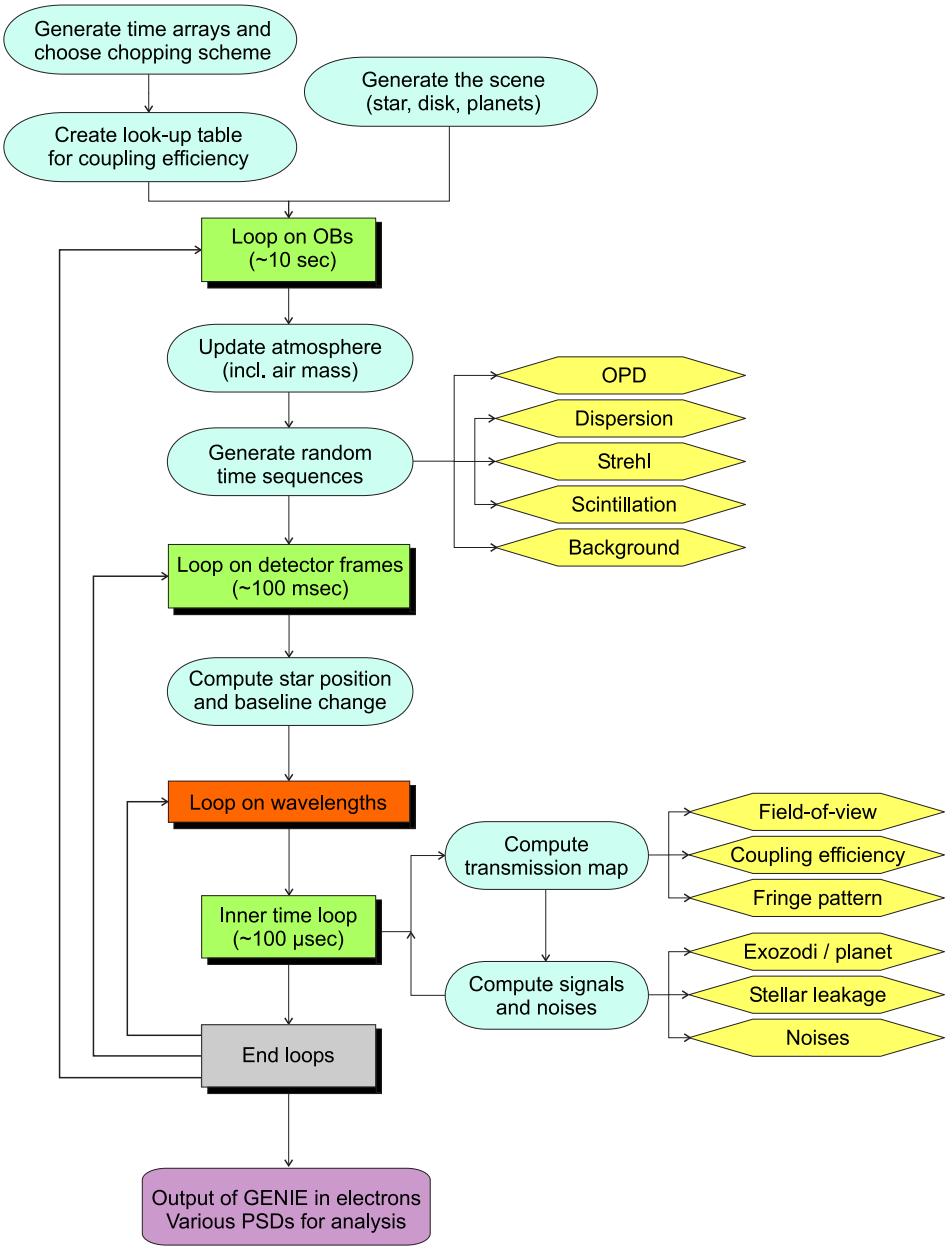

Figure 4.1: Top-level architecture of the GENIE simulator.

called `/main`. Besides the top-level routine which simulates the observation sequence, this directory contains the routines related to the simulation of control loops, the generation of random time series for atmospheric turbulence, the computation of the fibre injection properties including coupling efficiency, and the computation of the transmission map. These routines form the backbone of the simulator and are described with some details in the next sections (except for the latter, which simply consists in adding the complex amplitudes of the electrical fields collected by all telescopes).

4.1.2 Real-time correction of atmospheric turbulence

A large number of control loops are required for the operation of both the VLTI and the nulling instrument. At VLTI, wavefront correction is performed by the MACAO adaptive optics systems on the UTs, by the STRAP tip-tilt units on the ATs, and by the IRIS tip-tilt sensor in the interferometric laboratory.

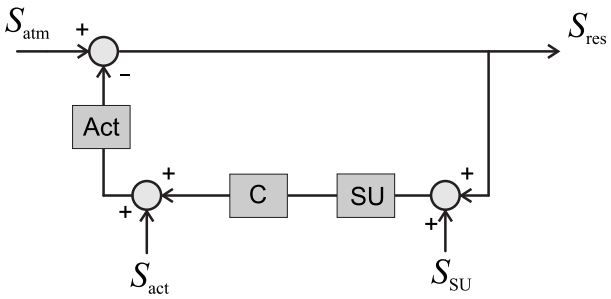

Figure 4.2: Simplified block-diagram of a fringe tracking system (see text for details).

Fringe tracking is performed either by the FINITO or the PRIMA fringe sensors, which are used to drive the VLTI delay lines. Additional control loops, specific to the nulling instrument, are needed to produce deep and stable nulling ratios. As discussed in Section 4.2.1, three dedicated control loops should equip the GENIE instrument: high-precision fringe tracking with dedicated delay lines, dispersion compensation and intensity matching between the beams coming from both telescopes.

Atmospheric turbulence and the real-time control loops are closely connected in their implementation, with the objective of producing random time series of turbulent parameters after closed-loop correction. The simulation of real-time control generally requires a large amount of computing power, especially if the simulation is performed in the time domain. In GENIEsim, we have chosen an implementation in the frequency domain, which also allows us to optimise the parameters of the control loops as a function of the observed target and of the actual atmospheric conditions. The general principle of this optimisation procedure is described in the next paragraphs.

Optimisation of the repetition frequency

The optimisation procedure is based on a description of atmospheric turbulence in terms of its temporal power spectral density (PSD), while the action of control loops is expressed by means of transfer functions in the frequency domain. The description of atmospheric turbulence, based on both physical modelling and experimental data when available, is discussed in detail in Section 4.2.1. The general architecture of real-time control loops is illustrated in Figure 4.2. The three main components of the loop are the sensing unit (SU), which provides an estimation of the atmospheric perturbation to be corrected for (e.g., OPD difference for a fringe tracking loop), the controller (C), which computes the correction to be applied to cancel the perturbation, and the actuator (Act), which performs the correction (e.g., an optical delay line). Both sensor and actuator produce additional noise in the control process, modelled by their PSDs (S_{SU} and S_{act}), which is applied at the input of the associated block. Sensor noise depends on the number of available photons in each elementary measurement (shot noise and detector noise), while actuator noise depends on the particular design of the actuator. The input and residual atmospheric fluctuations are described by their PSDs (S_{atm} and S_{res}).

In our implementation of the control loops, we have used simple PIDs as controllers. Their transfer function is composed of a proportional term (P), an integrator (I/s) and a derivator (Ds), with s the Laplace variable. Following Figure 4.2, the closed-loop transfer function writes:

$$H(s) = \frac{1}{1 + H_{\mathrm{SU}}(s)(P + I/s + Ds)H_{\mathrm{act}}(s)} \tag{4.1}$$

where $H_{\mathrm{SU}}(s)$ and $H_{\mathrm{act}}(s)$ are the transfer functions of the sensor and the actuator respectively. The general expression for the transfer function of the sensor is given by $H_{\mathrm{SU}}(s) = (1 - e^{-sT_i})/sT_i$ with T_i the individual integration time (Ménardi & Gennai 2001), while $H_{\mathrm{act}}(s)$ depends on the actuator. The

action of the closed loop is different for the three noise sources. Typical closed loop transfer functions applicable to the various noise sources are displayed in the left-hand side of Figure 4.3, for a repetition frequency of 2 kHz. The transfer functions applicable to the input atmospheric noise and to the actuator noise are almost identical (solid and dotted lines). They both reduce the fluctuations at low frequencies while keeping almost unaffected the fluctuations at frequencies higher than the repetition frequency of the loop. On the other hand, the transfer function applicable to the sensor noise (pure white noise applied at the input of the sensor) produces an attenuation of the noise at frequencies above the cut-off frequency of the loop. The influence of these transfer functions on the input noises is illustrated in the right-hand side of Figure 4.3, where actuator noise has been neglected.

The main metric for the quality of the correction is the standard deviation of the atmospheric perturbation at the output of the control loop. It can be easily computed in the frequency domain as it is equal to the square root of the area under the PSD of the residual fluctuations (dotted line in the right-hand side of Figure 4.3). The optimisation procedure is then implemented as a minimisation of the standard deviation of the output fluctuation as a function of the loop repetition frequency, searching in a predefined range of frequencies. The minimum is generally reached when the contributions of sensor noise and residual atmospheric noise are balanced. The former increases with the repetition frequency (shorter integration times produce more noise for each measurement), while the latter decreases with the repetition frequency, as fluctuations at higher frequencies are compensated. The implementation of the minimisation is based on the standard parabolic minimisation routine `minf_parabolic.pro` available in the AstroLib IDL library. For each particular value of the repetition frequency tested by the minimisation routine, the parameters of the PID controller have to be optimised before the standard deviation of the residual perturbation is computed, since the optimum controller depends on the repetition frequency. Therefore, a second level of optimisation is implemented, where the PID parameters are tuned.

Optimisation of the PID controller

Because simultaneous optimisation of the three parameters *P*, *I* and *D* would be extremely CPU intensive (all the more so since it must be repeated a large number of time), a rule-of-thumb was applied to link the

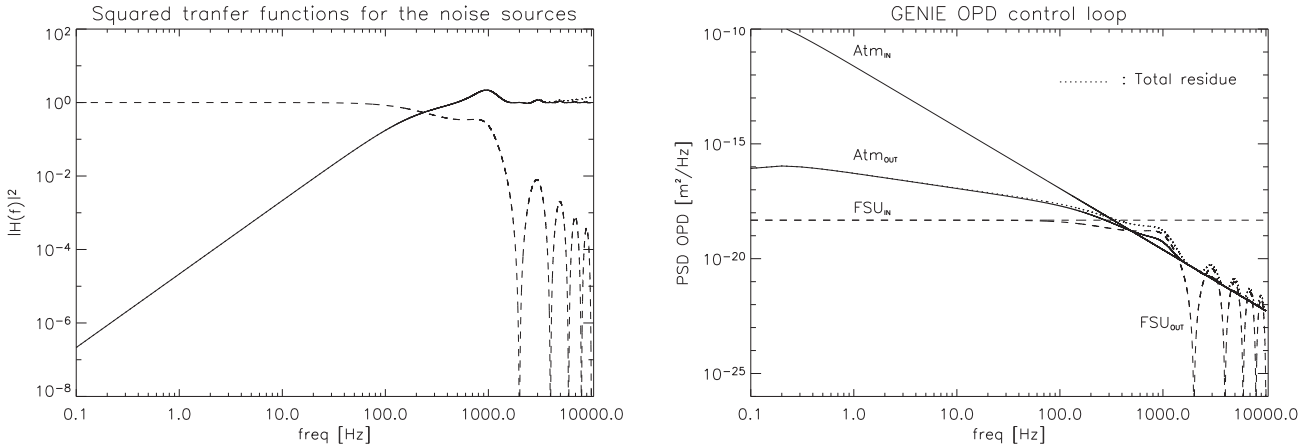

Figure 4.3: Left: Squared closed loop transfer functions applicable to the various sources of noise in the control process (case of the GENIE OPD loop, operated at 2 kHz). The solid line corresponds to the input (atmospheric) noise, the dashed line to the sensor noise and the dotted line to the actuator noise. Right: Simulated input and output PSDs of atmospheric and sensor noise in the case of the GENIE OPD control loop (operated at 2 kHz on a faint star). Delay line noise has been neglected in this simulation. The dotted line is the total residual, computed as the sum of the two output noise PSDs ($\mathrm{Atm_{OUT}}$ and $\mathrm{FSU_{OUT}}$).

three parameters and thus perform the optimisation on only one parameter. It has been shown in practical experiments on PID controllers (Ziegler & Nichols 1942) that the optimum parameters generally fulfill the following relations: $I = 2f_0P$ and $D = P/(8f_0)$, where f_0 is the oscillation frequency of the system pushed at its limit of stability. This frequency is related to the particular design of the actuator. When data was not available on the actuator, it was assumed to be a perfect transducer up to the repetition frequency of the loop, with its first resonance at about twice the repetition frequency. The actuator is thus optimised together with the controller, but within the possibilities offered by current technology (an upper limit is always imposed on the first resonance frequency). In this case, f_0 is simply given by twice the repetition frequency of the loop, and the optimisation of the global gain of the actuator (P) can be done as follows.

Increasing the global gain of the controller improves the rejection of the input perturbation, whatever its expression. However, control loops are subject to instabilities when the gain becomes too large. Two stability criteria are generally proposed to avoid such a behaviour:

- The phase of the open-loop transfer function $H_{\rm ol}(s) = H_{\rm SU}(s)(P + I/s + Ds)H_{\rm act}(s)$ at the location where its amplitude reaches 0 dB must be larger than $-180°$. A margin of $45°$ is recommended to be stable against the majority of phase excursions.
- The amplitude of $H_{\rm ol}(s)$ at the location where its phase reaches $-180°$ must be smaller than 0 dB. A margin of -12 dB is recommended.

The optimisation of the gain therefore boils down to increasing it as much as possible within the limitations imposed by the two stability criteria. We have implemented this optimisation by a combined minimisation of the two stability criteria within the allowed margins. In practice, the minimisation is performed on a weighted sum of $|\phi_{\rm 0dB} - 45°|$ and $|A_{-180°} + 12{\rm dB}|$, the gain-dependent departures from the optimum phase at 0 dB and from optimum amplitude at $-180°$. We make sure that the final values are on the safe side of the stability margins by artificially increasing by a factor 100 the weight of the above expressions if they are on the "unstable" side of the margin. The result of the global optimisation process is presented for various control loops in Section 4.2.1. Although these results make sense on the theoretical point of view, they still have to be demonstrated in practice on an optical breadboard.

Once the optimum repetition frequency and PID parameters are determined, the squared PSD obtained at the output of the control loop is used to generate the required time series for the associated atmospheric parameter. As we are only working on the amplitude of PSDs (not on their phase, which is random owing to the random character of the noise sources), we make use of the random-phase theorem for Gaussian random fields to generate a random phase and apply it to the PSDs before producing time series by fast Fourier transform.

4.1.3 Modal filtering and the fluctuations of coupling efficiency

The correction of wavefronts by single-mode fibres is a critical element of the GENIE instrument. The simulation of modal filtering begins with an adaptation of the fibre parameters to the chosen wavelength. The core radius a is chosen so that the condition for single-mode propagation is fulfilled across the whole spectral band, using the following equation (Shaklan & Roddier 1988):

$$V = \frac{2\pi a {\rm N.A.}}{\lambda}\ , \tag{4.2}$$

where N.A. is the numerical aperture of the fibre. The normalised frequency V must be smaller than 2.405 to ensure single-mode propagation, so that the optimum (i.e., largest allowed) core is given by $a = 2.405\lambda_{\rm min}/(2\pi{\rm N.A.})$. Under these conditions, the fundamental propagation mode (LP_{01}) of the single-mode waveguide can be approximated by a gaussian distribution with a $1/e$ width given by (Shaklan &

Roddier 1988):

$$w = a\left(0.65 + \frac{1.619}{V^{3/2}} + \frac{2.879}{V^6}\right) . \tag{4.3}$$

Before computing the efficiency of the injection into the waveguide (coupling efficiency), the effective focal length of the instrument is optimised. For that purpose, we use an approximate expression for the coupling efficiency in the presence of central obscuration, given by Equation 14 in Ruilier & Cassaing (2001), which we maximise with respect to the focal length. In the absence of central obscuration, the focal length f would simply be given by $w/f = 0.71\lambda/D$ (Ruilier & Cassaing 2001).

The coupling efficiency into a single-mode waveguide depends on how well the light distribution in the focal plane of the telescope matches the LP_{01} mode in the waveguide. The fraction of light injected into the waveguide is given by the squared overlap integral of the electric field distributions in the diffraction pattern and in the fibre LP_{01} mode. The optimal injection condition is for an on-axis source: off-axis sources have a less efficient coupling efficiency because their Airy pattern is offset with respect to the acceptance pattern of the fibre. In the simulator, we compute numerically the overlap integral for a regular grid of off-axis angles, taking into account the central obscuration in the computation of the telescope's diffraction pattern. This look-up table, illustrated in Figure 4.4, will be used for computing the real-time coupling efficiency as a function of tilt error without having to do a time-consuming integral at each time step.

The effect of atmospheric turbulence on the coupling efficiency is modelled by the separate contributions of tip-tilt errors and of higher order aberrations. Tip-tilt errors have the effect of shifting the telescope's diffraction pattern with respect to the fibre, which is accounted for by taking the equivalent off-axis position in the coupling look-up table. The effect of Strehl ratio, which contains the remaining part of wavefront errors, can be approximated as a simple multiplicative factor affecting the ideal coupling efficiency.

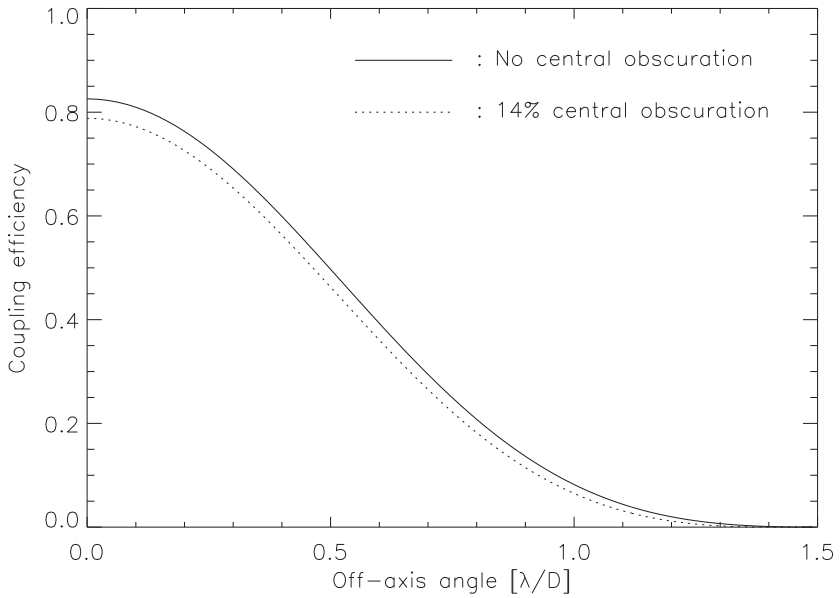

Figure 4.4: Coupling efficiency into a single-mode fibre as a function of the off-axis angle in units of λ/D. The solid line is without central obscuration, while the dotted line has been obtained with a 14% linear central obscuration as in the case of the UTs. The focal length of the instrument has been optimised and is almost the same in the two cases ($f/D \simeq 2.8$ for a numerical aperture of 0.21).

Modelling wavefront turbulence in the presence of adaptive optics

In the simulator, the turbulent wavefronts are described by a decomposition on individual Zernike modes, whose temporal power spectral densities are described by Roddier et al. (1993) and Conan et al. (1995). These individual PSDs are affected by the closed-loop transfer functions of the relevant adaptive optics systems, which are implemented in the simulator from their technical specifications. With its 60-actuator design, the MACAO adaptive optics system affects the first 60 Zernike modes by reducing their low-frequency fluctuations (the correction is significant for frequencies below about 50 Hz). On the ATs, STRAP corrects only for the tip-tilt errors at a slightly higher frequency. Finally, the influence of IRIS, the infrared tip-tilt sensor placed in the interferometric laboratory, is also taken into account. The simulated performances of these subsystems have been validated by comparison with on-sky measurements.

The limited computing power does not allow for a high number of Zernike modes to be computed individually. In the current version of the simulator, only the first 100 Zernike modes are actually simulated. The contribution of higher order Zernike modes is taken into account following Noll (1976), who proposed an approximate expression for the phase variance induced by turbulent Zernike modes above a given order $J > 10$. The actual PSD of this additional contribution is given by a weighted sum of all remaining Zernike modes. In the simulator, we approximate this PSD by an average over the first 10 modes above number $J = 100$. This approach has been validated by a comparison with both theoretical models and experimental data (in particular, the MACAO commissioning data).

We are now left with a number of PSDs for the individual Zernike modes, affected by closed-loop control whenever relevant. In order to produce the PSD of the global Strehl from these, we have to make some assumptions on the correlations between various modes. In our approach, we assume the Zernike modes to be fully uncorrelated. In that case, the PSD of the Strehl cannot be computed by simply adding the various individual PSDs. Instead, their randomness is simulated by producing time series for the phase variance of all Zernike modes across the pupil, using the random-phase theorem for Gaussian random fields as in Section 4.1.2. The respective contributions of all modes can then be added in the time domain in order to produce a random time series for the Strehl ratio. Its PSD can then be deduced by Fourier transforming this time series. With the PSD of Strehl in one hand and tip-tilt errors in the other hand, we are now in a position to compute the PSD of coupling efficiency into single-mode waveguides. Here again, a transit in the time domain is needed: we use the time series that we have already produced for the Strehl, and complement it with the random time series for tip-tilt errors, whose instantaneous values are related to an off-axis coupling efficiency stored in the look-up table. By multiplying the value of the off-axis coupling with the time series for the Strehl, we obtain a time series for the global coupling efficiency and the power spectrum is deduced. This PSD will then be used to feed the intensity control loop, which aims at matching the intensities propagated in the various single-mode fibres.

Additional phase shift at beam injection

Because it modifies the shape of the wavefront, modal filtering also has an influence on the average phase of the beam: besides piston, some other Zernike modes have a non-null average phase contribution when projected onto the fundamental mode of the fibre. This is in fact the case for all Zernike modes with azimuthal symmetry, such as defocus (Z_4) or spherical aberration (Z_{11}). For small aberrations, i.e., weights $a_i < 0.2$ for the related Zernike modes, the contribution of these modes to the total piston is proportional to their weights a_i, with coefficients computed by Ruilier (1999). For example, a defocus error a_4 has a contribution to the total phase equal to about $1/3$ of the contribution of a pure piston a_1 with the same weight ($a_1 = a_4$). In principle, this error could be compensated if the fringe sensor feeding the delay lines was measuring the same piston, i.e., using similar single-mode fibres. However, fringe tracking is generally done at shorter wavelengths (H or K band) than the scientific observations of

the nuller (L′ or N band), so that the coupled piston experienced by the fringe tracker will be different. Therefore, this contribution has also been implemented in the simulator.

4.2 A performance study of the GENIE instrument

Before discussing the performance of the GENIE instrument, let us briefly discuss one of the important decisions that had to be made early in the phase-A study: the choice of the observing wavelength. Four main criteria were involved in this trade-off:

- **Performance.** This criterion is discussed in detail in the paper presented in the following section. The two bands considered so far (L′ and N band) both have advantages and drawbacks, but the huge background emission experience in the N band oriented the choice towards the L′ band, where the requirements on leakage calibration and real-time control are however more stringent.
- **Technology.** Single-mode fibres are now becoming standard components in the near-infrared up to the L′ band, where integrated optics components should also soon be available. On the other hand, even though modal filters in the thermal infrared are currently being developed, further efforts are still required to apply this new technology on the sky.
- **Operation.** Because it can be operated with ATs on a large part of the Darwin/TPF-I targets, an L′ band instrument is preferred, all the more that this waveband is not yet offered at the VLTI.
- **Darwin preparation.** In order to obtain a deep null, the challenges are similar on the ground and in space: beam co-phasing and balancing on one hand, background subtraction on the other hand, are the two critical issues. Of course, the challenges are far more difficult on the ground due to the Earth's atmosphere. Because the two main issues have similar contributions to the noise budget in the L′ band, while the N band is essentially dominated by background issues, the former is preferred for a pertinent demonstration of nulling interferometry. From the scientific point of view, however, the preference goes to the N band which is most sensitive to dust at "habitable" temperature ($\sim$ 300 K).

Most criteria point towards the L′ band, so that both industrial teams arrived to the conclusion that this band was the most relevant for the GENIE instrument. The Bracewell configuration was also favoured by both teams, with a background subtraction technique based either on multiple fibres or on phase modulation between split pupils.

4.2.1 Article: *Performance study of ground-based infrared Bracewell interferometers*

The following article (Absil et al. 2006a) presents a thorough study of the performance of ground-based nulling interferometers and is illustrated in the particular case of the GENIE instrument. A simple Bracewell configuration is assumed throughout the paper, as it is the configuration chosen for all ground-based nullers so far. The various astrophysical sources and physical phenomena implemented in the simulator are described, followed by a description of the control loops, their design and expected performance. We identify the mains issues related to ground-based nulling and present some ways to mitigate them. The end-to-end simulation of the GENIE instrument finally provides realistic estimations of its sensitivity limit in terms of detectable exozodiacal level, taking into account calibration and data postprocessing techniques.

Astronomy & Astrophysics manuscript no. 3516 February 20, 2006
(DOI: will be inserted by hand later)

Performance study of ground-based infrared Bracewell interferometers

Application to the detection of exozodiacal dust disks with GENIE

O. Absil[1⋆], R. den Hartog[2], P. Gondoin[2], P. Fabry[2], R. Wilhelm[3], P. Gitton[3], and F. Puech[3]

[1] Institut d'Astrophysique et de Géophysique, Université de Liège, 17 Allée du Six Août, B-4000 Sart-Tilman, Belgium
e-mail: absil@astro.ulg.ac.be
[2] Science Payloads and Advanced Concepts Office, ESA/ESTEC, postbus 299, NL-2200 AG Noordwijk, The Netherlands
[3] European Southern Observatory, Karl-Schwarzschild-Str. 2, D-85748 Garching bei München, Germany

Received 25 May 2005 / Accepted 2 November 2005

Abstract. Nulling interferometry, a powerful technique for high-resolution imaging of the close neighbourhood of bright astrophysical objets, is currently considered for future space missions such as Darwin or the Terrestrial Planet Finder Interferometer (TPF-I), both aiming at Earth-like planet detection and characterization. Ground-based nulling interferometers are being studied for both technology demonstration and scientific preparation of the Darwin/TPF-I missions through a systematic survey of circumstellar dust disks around nearby stars. In this paper, we investigate the influence of atmospheric turbulence on the performance of ground-based nulling instruments, and deduce the major design guidelines for such instruments. End-to-end numerical simulations allow us to estimate the performance of the main subsystems and thereby the actual sensitivity of the nuller to faint exozodiacal disks. Particular attention is also given to the important question of stellar leakage calibration. This study is illustrated in the context of GENIE, the Ground-based European Nulling Interferometer Experiment, to be installed at the VLTI and working in the L' band. We estimate that this instrument will detect exozodiacal clouds as faint as about 50 times the Solar zodiacal cloud, thereby placing strong constraints on the acceptable targets for Darwin/TPF-I.

Key words. Instrumentation: high angular resolution – Instrumentation: interferometers – Techniques: interferometric – Circumstellar matter – Planetary systems

1. Introduction

The existence of extraterrestrial life in the Universe is a long-standing question of humankind. Future space missions such as Darwin (Fridlund 2000) or the Terrestrial Planet Finder Interferometer (Beichman et al. 1999; Lawson & Dooley 2005) are currently being studied respectively by ESA and NASA to search for evidence of life on Earth-like exoplanets by means of nulling interferometry (Bracewell 1978). These ambitious missions are particularly innovative from the technology point of view and demand several techniques to be first tested on ground. Both ESA and NASA have therefore initiated studies for ground-based infrared nulling interferometers (or "nullers"), to be installed respectively at the VLTI (Glindemann et al. 2004) or Keck Interferometer (Colavita et al. 2004). A cryogenic nulling beam-combiner is also under development for the LBT in the context of the NASA Origins Program (Herbst & Hinz 2004).

The principle of nulling interferometry, first proposed by Bracewell (1978) and generalized by several authors (Angel 1989; Léger et al. 1996; Angel & Woolf 1997; Karlsson & Mennesson 2000; Absil et al. 2003c), is to combine the light collected by two or more telescopes in a co-axial mode, adjusting their respective phases in order to produce a totally destructive interference on the optical axis. The interferometer is characterized by its transmission map $T_\lambda(\theta, \phi)$, displayed in Fig. 1 for a two-telescope interferometer, in one arm of which a phase shift of π radians has been introduced (*Bracewell interferometer*). Assuming that the field-of-view is limited by the diffraction pattern of a single telescope, its expression results from the fringe pattern produced by the interference between the beams, i.e., for a two-telescope interferometer:

$$T_\lambda(\theta,\phi) = \left(\frac{2J_1(\pi\theta D/\lambda)}{\pi\theta D/\lambda}\right)^2 \sin^2\left(\pi\frac{B\theta}{\lambda}\cos\phi\right), \quad (1)$$

where θ and ϕ are respectively the radial and polar angular coordinates with respect to the optical axis, B the interferometer baseline, D the telescope diameter and λ the wavelength. In the following study, we assume that recombination and detection

Send offprint requests to: O. Absil

⋆ O. A. acknowledges the financial support of the Belgian National Fund for Scientific Research (FNRS).

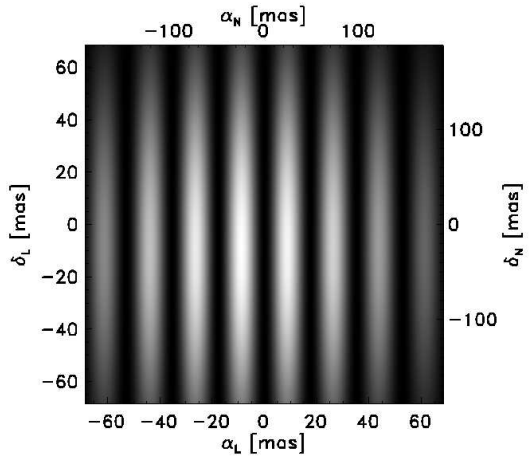

Fig. 1. Monochromatic transmission map for a 47 m Bracewell interferometer formed of two 8-m telescopes. The interferometric field-of-view, limited by the use of single-mode waveguides (see Sect. 3.3), is given by $\Omega = \lambda^2/S$ with S the telescope surface. Its diameter is respectively of 137 mas and 378 mas at the centers of the L' and N bands. The transmission map acts as a "photon sieve": it shows the parts of the field that are transmitted (white stripes) and those that are blocked (dark stripes, including the central dark fringe) by the interference process. The whole transmitted flux is integrated on a single pixel.

are both done in the pupil plane, so that no image is formed: the flux is integrated on the field-of-view and detected on a single pixel. Performing the detection in an image plane would not significantly change the conclusions of this study.

Besides pure technology demonstration, ground-based nullers have an important scientific goal in the context of the Darwin/TPF-I missions, through the detection of faint circumstellar dust disks ("exozodiacal dust disks") around nearby main sequence stars. Such dust clouds may present a severe limitation to Earth-like planet detection with Darwin/TPF-I if they are more than 20 times as dense as the Solar zodiacal cloud (Absil 2001). A systematic survey of nearby main-sequence stars is thus mandatory to select convenient targets for these future space missions. Photometric surveys with infrared space telescopes such as IRAS, ISO and Spitzer have detected cold dust around nearby stars at a level of $\sim$ 100 times our Kuiper Belt, but did not allow the characterization of warm dust emission at a better level than about 500 times the Solar zodiacal cloud (Beichman et al. 2005). Attempts to spatially resolve faint exozodiacal clouds with single dish telescopes in the mid-infrared (Kuchner et al. 1998) and near infrared (Kuchner & Brown 2000) have not yielded better detection limits. Even the MIRI instrument onboard the future James Webb Space Telescope, equipped with coronagraphic devices at 10.6 μm and other longer wavelengths, does not have a good enough angular resolution ($\sim$ 330 mas) to detect warm dust within the habitable zone of Darwin/TPF candidate targets.

Nulling interferometry, combining high dynamic range and high angular resolution, is particularly appropriate to carry out this systematic survey of the Darwin/TPF-I candidate targets. The Darwin target catalogue includes F, G, K and M-type main sequence stars up to 25 pc (Stankov et al. 2005), with median distances to these four stellar types of respectively 20, 20, 19 and 15 pc. Ideally, the survey should detect exozodiacal clouds about 20 times as dense as the Solar zodiacal cloud ("20-zodi" clouds hereafter). Based on the model of Kelsall et al. (1998), such clouds are typically 10^4 times fainter than the star in the L' band (centered around 3.8 μm) or 10^3 times fainter in the N band (centered around 10.5 μm). The M band will not be considered in this study, because is too much affected by water vapor to be useful for nulling interferometry (Young et al. 1994).

Besides this survey aspect, ground-based nullers have various interesting scientific applications. Any target requiring both high dynamic range and high angular resolution will benefit from their capabilities, including the detection and characterization of debris disks around Vega-type stars, proto-planetary disks around Young Stellar Objects, high-contrast binaries, bounded brown dwarfs and hot extrasolar giant planets. Extragalactic studies may also benefit from ground-based nulling through the characterization of dust tori around nearby AGNs. Ground-based nullers are extremely powerful at angular diameter measurements as well: thanks to their very high stability, they could, for instance, detect pulsations in unresolved stars that still produce a non negligible stellar leakage in the nulled data.

In this paper, we estimate the performance of ground-based infrared nulling interferometers for the detection of exozodiacal dust around typical Darwin/TPF-I targets. The structure of the paper follows the path of the light, beginning with the astrophysical sources and ending up after detection with the data analysis procedures. In section 2, we present the different contributors to the detected signals in ground-based nulling interferometry. Section 3 then focuses on a particularly important contributor (instrumental leakage), which strongly depends on the turbulent processes taking place in the Earth's atmosphere. We will show that this stochastic contributor needs to be compensated in real time at the hardware level in order to reach the required sensitivity. This has important consequences for the design of a ground-based nulling interferometer, as discussed in section 4, where real-time control loops are addressed. After passing though the instrument and being recorded by the detector, the signal still needs to be carefully analyzed in order to extract the useful exozodiacal contribution from the raw data. Section 5 describes the associated post-processing techniques. In all these sections, we will take a Sun-like G2V star at 20 pc as a typical target for illustrative purposes. Finally, these concepts are applied in section 6, where we derive the expected sensitivity of a specific instrument to the dust emission for different types of targets in the Darwin star catalogue.

2. Signals and noises in ground-based nulling interferometry

2.1. Exozodiacal dust disk

The Solar zodiacal cloud, a sparse disk of 10-100 μm diameter silicate grains, is the most luminous component of the solar system after the Sun. Its optical depth is only $\sim 10^{-7}$, but its integrated emission at 10 μm is about 300 times larger than the

flux of an Earth-sized planet. Very little is known about dust disks around main sequence stars. We will thus assume that exozodiacal clouds have the same density distribution as the Solar zodiacal cloud, as described by Kelsall et al. (1998), but with a different scaling factor. In the following study, we will also assume exozodiacal disks to be smooth (no clump or wake in the disk) and to be seen face-on. With such assumptions, the azimuth of the baseline has no influence on the observations: only the baseline length matters, which is convenient for illustrative purposes. Nevertheless, we should note the influence of the disk shape on the transmitted signal.

- The *disk inclination* has a strong influence on the transmitted amount of exozodiacal light. If the disk is seen edge-on and oriented perpendicularly to the fringe pattern (i.e., major axis of the disk parallel to the baseline), it will produce almost the same transmitted signal as a face-on disk. However, if it is oriented in the same direction as the fringe pattern, a large part of the disk emission will be cancelled out by the central dark fringe. The azimuth of the baseline thus has a large influence on the detection of inclined disks, which is an advantage: if one lets the projected baseline evolve as an effect of the Earth diurnal rotation, the exozodiacal disk signal will be modulated as the baseline orientation changes, making the identification of the disk signal easier. The effect will be all the larger when the disk inclination is close to edge-on (Absil et al. 2003b).
- *Inhomogeneities* in the disk could lead to unexpected modulation as the baseline changes. In fact, the exozodiacal dust emission is expected to be smooth (less than 1% random variations) except for rings and wakes due to gravitational trapping by planets or bands due to recent asteroid or comet collisions (Dermott et al. 1998). The detection of such features would be a direct signature of the presence of planets or planetesimals in the disk. This would however require a good signal-to-noise ratio since these structures will be much fainter than the integrated disk emission.

2.2. Geometric stellar leakage

Even when the star is perfectly centered on the optical axis, a part of the stellar light still leaks through the transmission map due to the finite extent of the stellar disk, an effect known as geometric stellar leakage. We define the *nulling ratio N* as the ratio between the transmitted stellar flux and the total stellar flux collected by the two telescopes. Assuming that the stellar angular radius θ_* is small as compared to the fringe spacing λ/B, and computing the transmitted flux as a two-dimension integral of the transmission map on the stellar disk, one gets the following expression for the nulling ratio:

$$N = 1/\rho = \frac{\pi^2}{4}\left(\frac{B\theta_*}{\lambda}\right)^2 , \quad (2)$$

assuming a uniform brightness across the stellar disk. The inverse of this quantity is called the *rejection rate* ρ, which is the fundamental figure of merit for a nulling interferometer. Typical values of the rejection rate for a Bracewell interferometer observing a Sun-like star at 20 pc are given in Table 1.

Table 1. Rejection rate for a Bracewell interferometer observing a Sun-like star at a distance of 20 pc in the L' and N bands, for typical interferometric baselines (14.4 m = LBT, 47 m = VLTI, 85 m = Keck). The star is assumed to be at zenith.

Baseline	14.4m	47m	85m
L' band (3.8 μm)	22197	2084	637
N band (10.5 μm)	169573	15897	4863

The rejection rate is quite sensitive to limb darkening, because it is precisely the outer parts of the stellar disk that mostly contribute to stellar leakage. Assuming a simple linear limb-darkening law $B_\lambda(\mu) = B_\lambda(1)[1 - u_\lambda(1-\mu)]$ for the stellar surface brightness B_λ, with μ the cosine of the angle between the normal to the surface and the line of sight, the nulling ratio would be the following:

$$N_{\rm LD} = 1/\rho_{\rm LD} = \frac{\pi^2}{4}\left(\frac{B\theta_*}{\lambda}\right)^2\left(1 - \frac{7u_\lambda}{15}\right) , \quad (3)$$

showing a linear dependance with respect to the limb-darkening parameter u_λ. For a typical K-band limb darkening $u_{\rm K} = 0.26$ applicable to a Sun-like star (Claret et al. 1995), the rejection rate would increase by a substantial 14% assuming the same physical diameter in the uniform and limb-darkened cases. Other potential contributors to the actual amount of stellar leakage are the asymmetry of the stellar disk, through stellar oblateness and/or spots. However, these are only second order effects for late-type main-sequence stars, which are generally close to spherical symmetry and are expected to have only small and scarce spots. These effects will be neglected in the discussion.

Due to the limited rejection rate, geometric leakage will often exceed the flux from the exozodiacal disk at the destructive output of the nuller, especially in the L' band. Fortunately, geometric leakage is mostly deterministic, allowing the prediction of its contribution. This calibration procedure is discussed in Sect. 5.2.

2.3. Instrumental stellar leakage

The expression (3) of the rejection rate is valid only for a perfect Bracewell interferometer. In practice, the rejection rate is degraded by atmospheric turbulence and various instrumental effects causing imperfect co-phasing of the light beams, intensity mismatches and polarization errors (Ollivier 1999). This contribution, called *instrumental leakage*, adds to the geometric leakage at the destructive output of the interferometer. It is dominated by non-linear, second order error terms and does not depend on the stellar diameter to the first order (Lay 2004).

Instrumental leakage has two effects on the performance of the nuller: first, it introduces a *bias*, the mean contribution of instrumental leakage, and second, it introduces an *additional stochastic noise* through its fluctuations. While the second contribution can be reduced by increasing the observation time (see Sect. 4.4), the first one does not improve with time and limits the global performance of the nuller. Unlike geometric leakage, an analytical expression of instrumental leakage cannot be

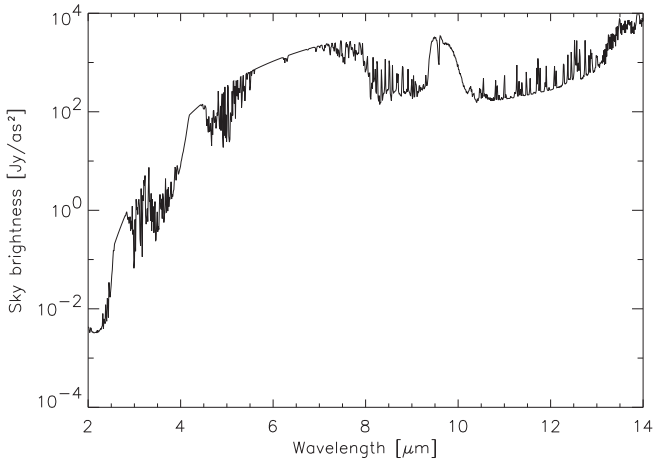

Fig. 2. Infrared sky brightness for typical Paranal atmospheric conditions.

obtained: it depends on the particular shape and amplitude of the power spectral densities of various atmospheric effects and instrumental errors such as piston, dispersion, wavefront errors, polarization errors, etc (Lay 2004). Its reduction can thus only be done through real-time control of these errors. In practice, instrumental leakage can be at least partially calibrated by observing "calibrator stars" with well-known diameters, a common method in stellar interferometry. This calibration, discussed in Sect. 5.3, will help remove the bias associated with the mean instrumental leakage and thereby relax the requirements on the performance of the real-time control loops.

2.4. The sky background

The thermal emission of the sky, which peaks in the mid-infrared, is obtained in good approximation by multiplying the Planck blackbody function by the wavelength-dependent sky emissivity. The infrared sky brightness is plotted in Fig. 2 for an atmosphere at a mean temperature of 284 K, which is typical for Cerro Paranal. The mean sky brightness in the relevant atmospheric wavebands is given in Table 4.

The fluctuation of the infrared background radiation produced by the atmosphere (or *sky noise*) has not been well modelled to date. Sky noise measurements have been carried out in the N band at Paranal with the VLTI mid-infrared instrument MIDI (Absil et al. 2004), while L'-band measurements have been carried out at Siding Springs, Australia (Allen & Barton 1981), showing that, at low frequencies, sky noise dominates over the shot noise associated with the mean background emission. Typical logarithmic slopes ranging from -1 to -2 have been recorded for the sky noise power spectral density (PSD).

2.5. The instrumental background

In order to conduct the light beams from the telescopes to the instrument, a large number of relay optics are used. All of them emit at infrared wavelengths. The wavelength-dependent emissivity of the optical train is theoretically equal to the complementary of its transmission. In order to evaluate this contribution, we have to make some assumptions about the interferometric facility and nulling instrument. We will take the case of the VLTI, which has a transmission ranging between 30% and 40% in the near- and mid-infrared[1], and we will assume that the nulling instrument is at ambient temperature, except for the detection unit (spectrograph and detector). The instrumental background is given in Table 4, separated into "VLTI brightness" for the interferometric infrastructure and "GENIE brightness" for the nulling instrument, assuming an emissivity of 30% for the latter. A full cryogenic instrument would reduce the background emission, and thus improve the global sensitivity. However, even at ambient temperature, the full potential of the instrument can still be achieved by increasing the integration time, thereby reducing the contribution of the shot noise associated with the background emission. Fluctuations of the instrumental background are also expected to happen (e.g. due to beam wandering, mirror vibrations, gain fluctuations, etc.), but at a much lower level than sky noise. They will be neglected in the following discussion.

2.6. Detection criterion

In addition to the classical sources of noise such as shot noise, read-out noise and background noise, whose effect can be reduced by increasing the integration time, nulling interferometry is faced with two types of biases that must be removed to ensure a secure detection of the exozodiacal cloud. These biases are associated with the mean contribution of geometric and instrumental stellar leakage. In order to detect circumstellar features as faint as 10^{-3} (N band) to 10^{-4} (L' band) of the stellar flux with a signal-to-noise ratio of 5, *one should reduce the contributions of both geometric and instrumental stellar leakage down to* 10^{-4} *(N band) or* 10^{-5} *(L' band) of the initial stellar flux*, so that the total stellar leakage does not exceed about one fifth of the exozodiacal disk signal. Real-time control systems at hardware level and calibration techniques at software level will be used to reach this level of performance. The requirements on phase and intensity control will be particularly tight for short operating wavelengths. In the next section, the discussion of atmospheric turbulence is thus mainly illustrated in the L' band where its effects are the largest.

3. Influence of atmospheric turbulence

In order to estimate the performance of a nulling interferometer in the presence of atmospheric turbulence, we have developed a software simulator called *GENIEsim*[2] (Absil et al. 2003a). This semi-analytical simulator computes in real-time the transmission map of the interferometer, taking into account phase and intensity fluctuations associated with atmospheric turbulence. It inherently takes into account the bilinear error terms discussed by Lay (2004) that are supposed to be the largest

[1] Due to the additional emission of dust particles located on the optics, the measured emissivity of the VLTI optical train is in fact closer to 100% than the expected 60-70%.

[2] GENIEsim, written in IDL, is open source and available on demand. Send request to R. den Hartog (`rdhartog@rssd.esa.int`).

contributors to the instrumental nulling. In the following paragraphs, we describe the various sources of phase, intensity and polarization errors that have been implemented in the simulator and discuss their effect on instrumental nulling.

3.1. The piston effect

The 0th-order term of atmospheric turbulence, the spatially averaged phase perturbation on the pupil, is known as the piston effect. Optical path difference (OPD) fluctuations are mainly due to differential piston between the two apertures of the interferometer. Under the Taylor hypothesis of frozen turbulence, where a frozen phase screen is blown at the wind speed above the telescopes (Roddier 1981), the classical description of atmospheric turbulence proposed by Kolmogorov (1941) states that the temporal PSD of phase fluctuations follows a $-8/3$ power-law. In practice, three physical phenomena induce a departure from the theoretical $-8/3$ logarithmic slope (Conan et al. 1995): correlations between the pupils and the finite outer scale of turbulence $\mathcal{L}_0$ both reduce the fluctuations at low frequencies, while pupil averaging reduces them at high frequencies (Fig. 3). The latter effect has in fact never been observed, so that we keep the $-8/3$ slope at high frequencies as a conservative scenario. This scenario also features additional instrumental contributions:

- Bimorph piston effect: this is the OPD induced by resonances of the adaptive optics deformable mirror (Vérinaud & Cassaing 2001). This contribution has been evaluated for the MACAO adaptive optics at VLTI, and turns out to be dominant above 100 Hz despite the use of a "piston-free" algorithm for the control of the deformable mirror.
- Coupled piston: this is the additional OPD created by high-order wavefront errors when injecting the beams into single-mode waveguides (Ruilier & Cassaing 2001).

The standard deviation of the OPD fluctuations, neglecting the effect of the outer scale, is given by (Roddier 1981):

$$\sigma_{\mathrm{OPD}} = 2.62 \frac{\lambda}{2\pi} \left(\frac{B}{r_0} \right)^{5/6} . \quad (4)$$

Since the Fried parameter r_0 is proportional to $\lambda^{6/5}$, σ_{OPD} does not depend on wavelength. For a typical baseline of 47 m and 1" seeing, the theoretical variance of piston is about 35 μm, i.e., about 9 fringes in the L' band. This variance, which is also the area under the dotted curve in Fig. 3, sets the level of the PSD.

The effect of phase errors on a Bracewell nulling interferometer is to shift the position of the fringes in the transmission map: the dark fringe is not centered any more on the optical axis. For a small phase error $\epsilon_\phi(\lambda)$ between the two beams, the shifting of the dark fringe produces a non-null on-axis transmission $T_\lambda(0,0) = \epsilon_\phi(\lambda)^2/4$ (Ollivier 1999). In order to keep the instrumental rejection rate above the required 10^5 in the L' band, the phase error should be smaller than 0.006 radian (i.e., 4 nm in the L' band), while atmospheric piston induces OPD errors of about 35 μm. A deep and stable null can thus only be achieved by stabilizing the dark fringe on the optical axis, by means of a fringe tracker (Sect. 4.1).

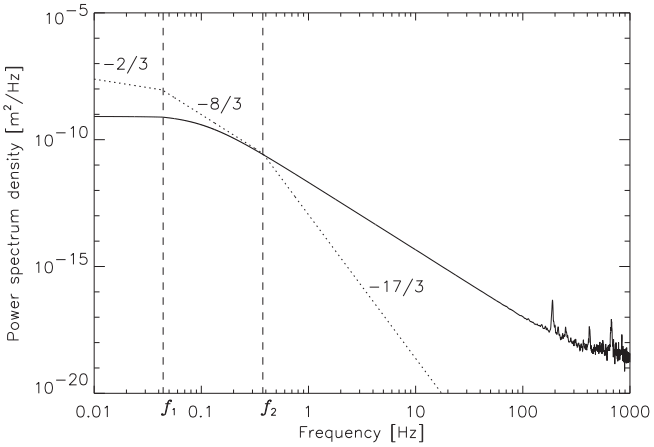

Fig. 3. Differential piston power spectrum, under the following conditions: B = 47 m, D = 8 m, v = 11 m/s and r_0 = 10 cm at 500 nm (equivalent to 1" seeing). The dotted line represents the theoretical Kolmogorov piston PSD, showing the effects of pupil correlations (below $f_1 \simeq 0.2v/B$) and pupil averaging (above $f_2 \simeq 0.3v/D$), but without the effect of the outer scale nor the instrumental contributions. The solid line is the representation of the piston PSD that we actually use in our simulations as a conservative scenario. It includes the effect of pupil correlations and of the outer scale of turbulence (flattening of the PSD for frequencies below $v/\mathcal{L}_0$), as well as the contributions of bimorph and coupled piston (high-frequency fluctuations), but excludes pupil averaging. A best-case scenario would correspond to the combination of the dotted line for $f > f_2$ and the solid line for $f < f_2$.

3.2. Longitudinal dispersion

In addition to the achromatic piston effect produced by the fluctuations of the air refractive index, another source of phase errors comes from the fluctuation of the water vapor column densities above the two telescopes. A useful concept to describe the column density fluctuations of water vapor is "Water-vapor Displacing Air" (WDA), introduced by Meisner & Le Poole (2003). The fluctuation of the WDA column density induces a chromatic OPD difference between the beams, because its refraction index n_{WDA} strongly depends on wavelength in the infrared as illustrated in Fig. 4. This effect, referred to as *longitudinal dispersion*, has the same kind of influence on the transmission map as the piston effect, except that the offset of the dark fringe is now wavelength-dependent. This has two deleterious consequences on the performance of a nulling instrument:

- *Inter-band dispersion* is the phase error measured at the center of the science waveband assuming that piston is perfectly corrected at another wavelength by means of a fringe tracker (this correction is generally done in the H and/or K band, e.g. at the Keck and VLT interferometers),
- *Intra-band dispersion* refers to the differential phase error within the science waveband: if one manages to co-phase the beams at the central wavelength of the science waveband, their phases will not be perfectly matched at the edges of the band.

Since longitudinal dispersion is produced by the same turbulent atmosphere as piston, it is expected to follow the same theoretical PSD. This has been confirmed experimen-

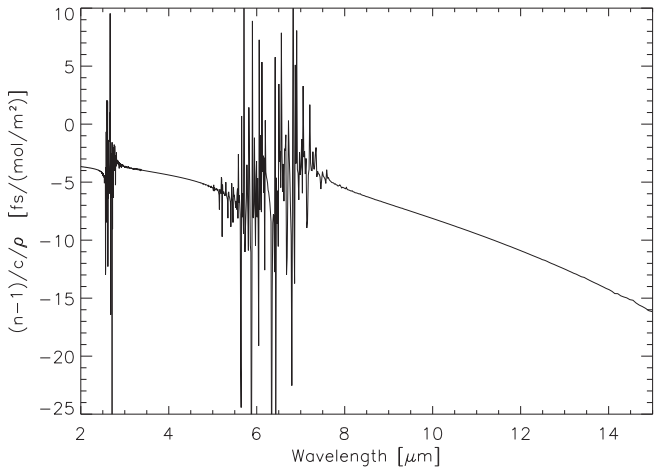

Fig. 4. Reduced refraction index of WDA ($\hat{n}_{\mathrm{WDA}} = \frac{n_{\mathrm{WDA}}-1}{c\rho}$, with c the speed of light and ρ the molar density) expressed in femtosecond per mole/m^2, plotted at infrared wavelengths.

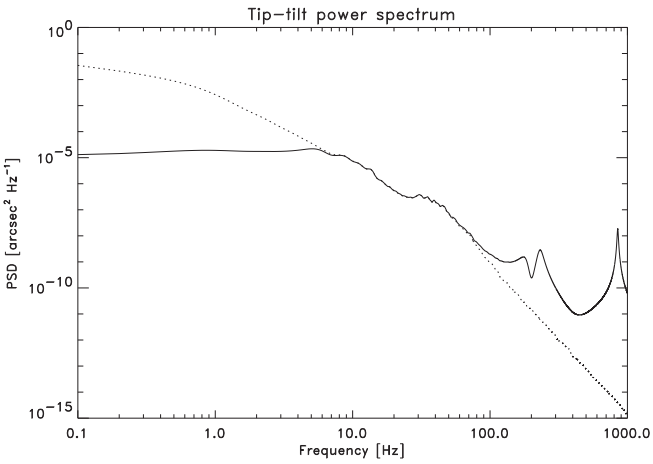

Fig. 5. PSD for tip-tilt before (dotted line) and after (solid line) close-loop control with MACAO. The peaks at high frequencies are induced by mechanical resonances in the deformable mirror.

tally by Lay (1997). An rms value of 1.5 mole/m^2 for the column density fluctuation of water vapor has been measured by Meisner & Le Poole (2003) at Paranal on an integration time of 100 sec (this value corresponds to 27 μm rms of differential precipitable water vapor). This translates into typical inter-band and intra-band OPD errors of 550 nm and 150 nm rms respectively in the L' band assuming that fringe tracking is performed in the H band. A control system must thus be devised to stabilize the dark fringe on the optical axis in order to meet the requirements on the instrumental rejection rate.

3.3. Wavefront errors

Propagation through the turbulent Earth atmosphere degrades the shape of the wavefronts, producing imperfect interference between the beams at recombination, and thus creates a halo of incoherent stellar light at the detector. Modal filtering by means of single-mode fibers, as proposed by Mennesson et al. (2002), eliminates wavefront corrugations by projection on the fundamental mode of the fiber, thereby ensuring perfect matching of the wavefronts over a broad bandpass. After injection into a single-mode fiber, the shape of the initial wavefront only affects the amount of energy coupled into the guide. *The modal filter thus converts phase defects into intensity errors*, which are less severe for a nulling interferometer (Ollivier 1999). It also induces a small coupled piston due to the non-null mean of $z > 1$ Zernike polynomials projected onto the Gaussian fundamental mode of the fiber (Ruilier & Cassaing 2001). The use of single-mode fibers to filter the beams at the focus of the telescopes strongly relaxes the constraints on pointing accuracy and low order aberrations, and thus improve the capability to achieve deep rejection ratios. We will assume that modal filtering, or at least spatial filtering using pinholes for the N band, is used in our nulling interferometer.

In the following study, we will also assume that the telescopes are equipped with adaptive optics, with performance similar to that of the MACAO systems on ESO's Very Large Telescopes (Arsenault et al. 2003). The power spectral densities of individual Zernike modes are taken from Conan et al. (1995), with typical high-frequency slopes of $-17/3$ and various slopes at low frequencies. These PSDs are corrected by the adaptive optics servo system for frequencies below about 10 Hz, thereby making their low-frequency content negligible. The case of tip-tilt is illustrated in Fig. 5, including the contribution of high order Zernike modes (ten Brummelaar 1995). The values for the rms tip-tilt and Strehl are given in Table 2.

The coupling efficiency η into a single-mode fiber is computed by taking into account two contributions: the tip-tilt error which induces an offset of the stellar Airy pattern with respect to the fiber core (assuming the on-sky tip-tilt to be perfectly translated into an on-fiber jitter), and the Strehl ratio which represents the coherent part of the beam and can be taken as a multiplicative factor in the computation of coupling efficiency (Ruilier & Cassaing 2001). The mean and rms coupling efficiencies after correction by adaptive optics are given in Table 2.

The effect of coupling efficiency fluctuations, which produce unequal intensities in the two arms of the interferometer, is to induce a non-null transmission on the optical axis. Letting ϵ_I be the relative intensity error between the two beams, the expression of the central transmission is $T_\lambda(0,0) = \epsilon_I^2/16$ (Ollivier 1999). In order to keep the instrumental rejection rate above the required 10^5, relative intensity errors should be smaller than 1%, while the AO-corrected atmospheric turbulence induces intensity fluctuations as high as 8% in the L' band. A servo loop for intensity matching is therefore necessary to obtain a deep and stable null in the L' band. Such a device is not needed in the N band, where relative fluctuations of 1% are expected.

3.4. Scintillation

Scintillation is the effect of rapid intensity fluctuations of a point-like source as a result of the interference of light rays diffracted by turbulent cells. The condition for scintillation to take place is that the Fresnel scale $r_{\mathrm{F}} = (\lambda\, h\, \mathrm{secz})^{1/2}$ is larger

Table 2. rms tip-tilt, mean and rms Strehl ratio for an 8-m telescope after correction by MACAO, as simulated by GENIEsim under typical atmospheric conditions at Cerro Paranal (1" seeing, 11 m/s wind speed). The mean and rms coupling efficiencies into a single-mode fiber are deduced (taking into account the effect of central obscuration).

	Average	Std deviation
Tip-tilt [mas]	0	14
Strehl L' band	0.80	0.050
Strehl N band	0.97	0.008
Coupling L' band	0.58	0.044
Coupling N band	0.77	0.008

than the Fried scale r_0, with h the height of the turbulent layer and z the zenith distance (Quirrenbach 1999). Even for high turbulent layers (20 km) and large zenith distances ($z = 45°$), we obtain $r_F \simeq 0.3$ m while $r_0 \simeq 1.1$ m in the L' band for 1" seeing, showing that the Fried parameter is always larger than the Fresnel scale. Numerical estimates obtained with GENIEsim confirm this statement: scintillation does not induce intensity fluctuations larger than 0.2% in the L' band. Since $r_0 \propto \lambda^{6/5}$ while $r_F \propto \lambda^{1/2}$, scintillation is also negligible for longer wavelengths, including the N band.

3.5. Polarization errors

The polarization errors encountered by a nulling interferometer are of three main types: differential phase shift, differential attenuation and differential rotation can occur between the two beams for each linear polarization component. These effects can be translated into phase and intensity errors, but unlike phase and intensity errors due to turbulence, they are only due to the instrument itself. Polarization errors are thus expected to be mainly static or slowly drifting, even if instrumental vibrations might induce some fluctuations. A highly symmetric design of the whole interferometer is required to reduce polarization issues as much as possible (Serabyn & Colavita 2001). In the following study, we will assume that the nulling instrument is designed so as to keep this contribution negligible in the instrumental leakage budget. This may not be the case in practice, because existing interferometers are not necessarily designed to meet the tight tolerances on polarization associated with nulling interferometry. This might force the nuller to operate in polarized light, by inserting polarizers at the beginning of the optical train[3] and just before recombination. The instrumental throughput would then be reduced by 50%, thereby increasing the required integration times.

4. Real-time control and instrumental design

We have seen that atmospheric turbulence causes additional stellar photons to leak through the null (*instrumental leakage*), and that this bias cannot be calibrated analytically as for geometric leakage. Moreover, the stochastic fluctuation of instrumental leakage is the source of an important noise contribution, called *systematic noise* (Lay 2004) or *variability noise* (Chazelas et al. 2005). This section describes the three major control systems that are needed to reduce instrumental leakage and variability noise down to an acceptable level by correcting the effects of atmospheric turbulence in real time. As discussed in Sect. 3 and summarized in Table 3, an instrumental rejection rate of 10^5 requires the residual phase and intensity errors to be smaller than 4 nm and 1% rms respectively. If this level of performance cannot be met, the use of calibrator stars will be further investigated to estimate and remove the contribution of instrumental leakage.

[3] In practice, a polarizer cannot be put in front of the primary or secondary mirror of a telescope, so that the first few mirrors of the optical train could still contribute to polarization errors.

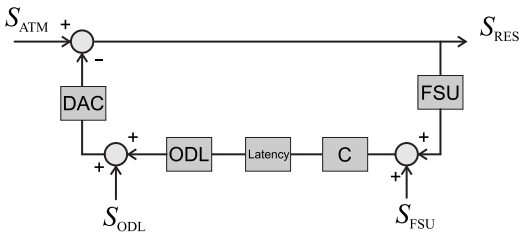

Fig. 6. Simplified block-diagram of a fringe tracking system: the OPD error between two beams, characterized by its PSD S_{ATM}, is sampled by a fringe sensing unit (FSU) feeding an OPD controller (C), which computes the correction to be applied by the optical delay line (ODL). The latency represents the effect of the finite CPU and electronics time required between fringe sensing and correction, while the digital-to-analogue converter (DAC) represents the conversion from a digital command to an analogue OPD correction by the delay line. The OPD power spectrum after closed-loop control is denoted S_{RES}, while the noise introduced by the FSU and the ODL are respectively S_{FSU} and S_{ODL}.

4.1. Fringe tracking

The purpose of a fringe tracker is to actively compensate for random phase fluctuations between the beams of the interferometer at a given wavelength. A fringe sensing unit (FSU) measures the phase difference at a given sampling frequency and transmits this information to a controller which computes the compensation to be applied to one of the beams by an optical delay line (ODL), as illustrated in Fig. 6. Both the FSU and the ODL introduce noise in the fringe tracking control loop, while the controller is (almost) noiseless. In order to be efficient, fringe tracking requires a high signal-to-noise ratio to be achieved on phase measurements on very short time scales (typically between 0.1 and 1 msec). It is therefore usually performed in the near-infrared ($\lambda < 2.4\,\mu$m) where stellar photons are numerous and the sky background rather low.

Large interferometric facilities such as the VLTI or Keck Interferometer are (or will soon be) equipped with fringe trackers. For instance, FINITO and PRIMA at VLTI will deliver a residual OPD of about 150 nm rms on bright stars, respectively in the H and K bands (Wilhelm & Gitton 2003). However, this is not sufficient to meet our goal on OPD stability, implying that a second stage of OPD control must be implemented inside the nulling instrument. In fact, the main limitation to the accu-

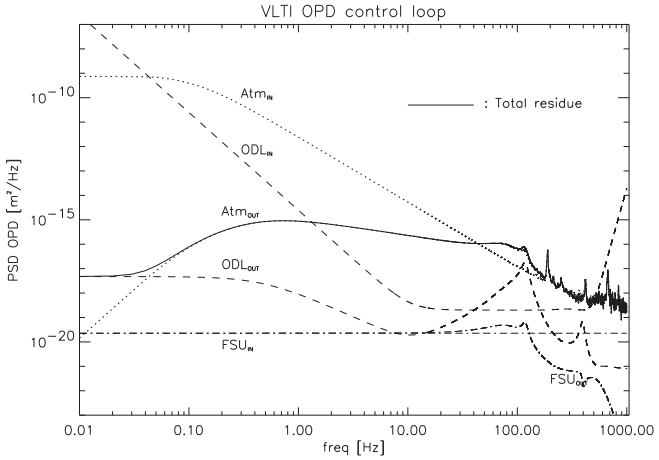

Fig. 7. Simulation of the VLTI OPD control loop. The plot gives the PSDs at the input (before actuation: subscript "IN") and output (after actuation: subscript "OUT") of the loop for the three noise sources in the VLTI fringe tracking loop, i.e., atmospheric fluctuations (Atm, dotted curves), fringe sensing (FSU, dashed-dotted curves) and optical delay line (ODL, dashed curves). The total closed-loop OPD jitter (area under the solid line) is 133 nm rms for a repetition frequency of 4 kHz.

racy of the VLTI fringe tracker comes from the ODL, which does not efficiently correct for OPD fluctuations at frequencies higher than 50 Hz (see Fig. 7). The main requirement for the additional fringe tracker is thus to be equipped with a low-noise ODL optimized for high repetition frequencies (up to 20 kHz).

We have simulated the performance of a fringe tracker optimized to achieve small residual OPD on bright stars. The fringe tracker features a fringe sensor working both in the H and K band and uses a short-stroke fast piezo or voice-coil delay line to compensate the remaining OPD fluctuations. The control loop parameters are computed through a simultaneous optimization of the repetition frequency and of the controller parameters (a simple PID[4]). The repetition frequency has been artificially limited to 20 kHz to comply with state-of-the-art back-end electronics. The delay line is assumed to have a perfect response up to this frequency (short-stroke piezo translators can achieve this kind of performance). The OPD control performance, summarized in Table 3, is computed in two cases:

- the *worst case* corresponds to a $-8/3$ slope for the turbulence PSD at high frequencies (see Fig. 3) and includes the bimorph piston effect;
- the *best case* takes into account the effect of pupil averaging on the PSD ($-17/3$ slope at high frequencies) and does not include the bimorph piston effect.

The predicted performance ranges between 6 nm and 17 nm rms. These figures could be improved by using a priori knowledge on the behaviour of atmospheric turbulence in the control process, e.g. through Kalman filtering. First estimates have shown an improvement of about 2 nm on the residual OPD with respect to the above numbers (C. Petit, personal communication). This performance, summarized in Table 3, is marginally compliant with the required 4 nm rms.

[4] PID stands for "Proportional, Integral and Differential" and is a basic controller for closed-loop control.

Table 3. Performance of an L' band nuller at VLTI as simulated with GENIEsim on a 100 sec observation block, taking into account all turbulence-induced errors. The performance of the control loops are summarized together with their repetition frequencies in pessimistic and optimistic cases (see text). The target performance discussed in Sect. 3 appears in the last column. The total null is the mean nulling ratio including both the geometric and instrumental leakage contributions, and is computed as the ratio between the total input and output stellar fluxes (from both telescopes). The last line gives the standard deviation of the instrumental nulling ratio for this 100 sec observation block.

	worst case	best case	goal
Piston	17nm @ 20kHz	6.2nm @ 13kHz	< 4nm
Inter-band	17nm @ 200Hz	4.4nm @ 300Hz	< 4nm
Intra-band	4.1nm @ 200Hz	1.0nm @ 300Hz	< 4nm
Intensity	4% @ 1kHz	4% @ 1kHz	< 1%
Total null	9.7×10^{-4}	6.2×10^{-4}	4.8×10^{-4}
Instr. null	5.0×10^{-4}	1.5×10^{-4}	10^{-5}
rms null	5.8×10^{-4}	1.6×10^{-4}	10^{-5}

4.2. Compensation of longitudinal dispersion

There are two different sources of dispersion to be corrected: the slowly varying differential phase due to unequal paths through wet air in the delay lines, and an additional rapid phase fluctuation due to column density fluctuations of dispersive components in the atmosphere. The first one is deterministic and easy to correct provided that the atmospheric conditions are monitored in the delay lines, while the second one is the real problem and is mainly associated with water vapour, as well as other molecular species such as ozone, carbon dioxide, etc, which are the main contributors below 2.5 μm (Mathar 2004).

In order to correct for both inter-band and intra-band dispersion (Sect. 3.2), one should measure the differential column density of water vapour experienced by the two beams in their paths through the atmosphere. This quantity can be inferred by measuring the phase difference between the beams at two different wavelengths, using the knowledge of the refractive index of wet air across the infrared. In practice, a blind phase correction in the science band, relying for instance on H- and K-band measurements, is dangerous because it is not sensitive to possible biases, e.g. related to the imperfect knowledge of the refraction index or to the presence of other dispersive gases (Meisner & Le Poole 2003). Phase measurements in the science band are thus necessary to ensure a good co-phasing, using a part of the scientifically useful signal. These measurements will be carried out at a slower rate, on one hand because of the lower signal-to-noise ratio on phase measurements at longer wavelengths and on the other hand because the possible biases related to the extrapolation of the phase delay from the H/K bands towards longer wavelengths are mainly affected by global atmospheric parameters (temperature, partial pressures of gases, etc.) which are not expected to evolve quickly

during the night. Another possibility would be to perform both fringe tracking and dispersion control by using science-band photons exclusively, in order to reduce the technical complexity of the instrument. This would however lead to slightly reduced performance, due to the worse signal-to-noise ratios on phase measurement at longer wavelengths, and would even become impractical in the N band.

Interferometric facilities are currently not equipped with an active dispersion compensation device, which should thus be integrated in the nuller itself. The required correction is two-fold: the inter-band phase error should be corrected with a dedicated short-stroke delay line (less than 1 μm rms to be compensated), while intra-band dispersion could be corrected by introducing a variable amount of dispersive material in the beams to correct for the slope of the phase inside the science waveband (Koresko et al. 2003). The performance of such a correction system is summarized in Table 3 in the L' band, once again in two cases:

- the *worst case* is obtained by assuming that phase measurements in the L' band are needed at each step of the control process, and assuming a $-8/3$ slope for the high-frequency asymptote of the atmospheric turbulence PSD.
- the *best case* is computed assuming that H/K band phase measurements are sufficient for dispersion control and that the input PSD has a $-17/3$ slope at high frequencies.

The closed-loop performance ranges between 4.4 nm and 17 nm rms for inter-band dispersion, between 1.0 nm and 4.1 nm rms for intra-band dispersion. It is marginally compliant with the requirement (4 nm rms).

4.3. Intensity matching

The third real-time control loop to be implemented in the nulling instrument is a device to correct for unequal intensities between the two beams. In fact, intensity fluctuations are not a problem per se: it is only the differential fluctuations between the beams that matter. The most straightforward way to compensate for this effect is to measure the intensities of the two beams, determine which one is the brightest and reduce its intensity down to the level of the other one by means of an actuator. This correction must take into account the effect of coupling into single-mode fibers, so that the intensity sensors must also be placed after the modal filters. Furthermore, it must be carried out in the science waveband, because coupling efficiency is wavelength-dependent. We will thus "waste" an additional part of the useful signal for intensity control. A possible actuator could consist in a piezo-driven adjustable iris, which would reduce the beam size in a pupil plane while keeping it (almost) circular to preserve injection properties as much as possible.

The closed-loop control performance is summarized in Table 3 for the L' band, with a typical residual intensity mismatch of 4% when the loop is running at 1 kHz. This performance does not meet the required 1% mismatch, which makes additional calibrations mandatory (see Sect. 5.3). Note that this control loop does not remove the fluctuations of the mean coupling efficiency (common to both beams), which has a typical standard deviation of 8%.

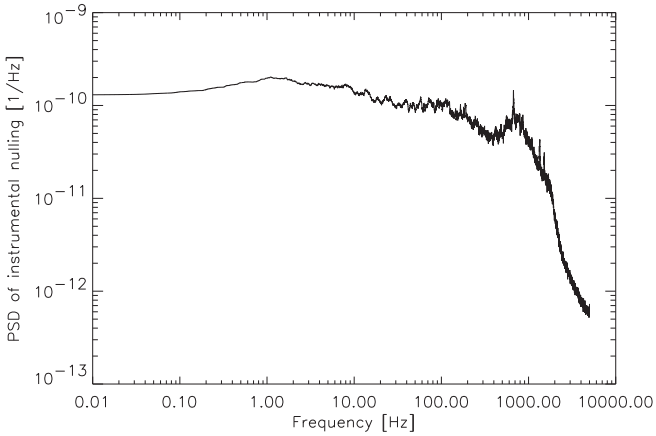

Fig. 8. Power spectrum of instrumental nulling due to phase and intensity errors after closed-loop control, obtained for a 100 sec simulation with GENIEsim in the L' band. The semi-analytical simulation takes into account the bilinear error terms discussed by Lay (2004), but not the possible $1/f$-type noises discussed by Chazelas et al. (2005). The power spectrum has been smoothed with a standard IDL routine to show its mean behaviour: almost flat at low frequencies, while the logarithmic slope at high frequencies is about -2.

4.4. Instrumental nulling performance

Table 3 shows the nulling performance associated with the residual phase and intensity errors after closed-loop control for a G2V star at 20 pc. The rms instrumental nulling ratio corresponds to the concept of variability noise (Chazelas et al. 2005). Its power spectrum is illustrated in Fig. 8, showing an almost flat spectrum for frequencies below 1 kHz and a rapid decrease of the power content above 1 kHz. Variability noise thus behaves as a white noise at typical read-out frequencies ($\sim$10 Hz), so that its cumulated contribution increases as the square root of integration time just as for shot noise. We do not take into account here the possible $1/f$-type noises (Chazelas et al. 2005), which might alter the slope of the PSD at low frequencies and thus change the behaviour of long-term variability noise by introducing more power at low frequencies. This assumption is supported by the use of real-time control loops, which will help remove possible drifts in the instrumental response.

5. Post-processing of nulling data

Because the expected performance of state-of-the-art real-time control loops is not sufficient to reduce instrumental leakage down to the required level (10^{-5} in the L' band), and because other sources such as geometric leakage and background also contribute to the detected signal after destructive beam combination, the exozodiacal disk signal can only be extracted from the raw data after a final and critical phase of correction: post-processing.

5.1. Background subtraction

The first step in the data analysis procedure is to remove the contribution of the background. In order to extract the useful data from the incoherent background in the nulled data, modulation techniques are required. The classical "chopping-nodding" technique consists in tilting the secondary mirror by a small quantity (a few arcseconds) in order to measure the background in an empty sky region close to the source and subtract it from the on-source measurement. The chopping sequence is repeated at a few Hertz. Nodding consists in repeating the whole chopping sequence off-source, by slightly tilting the telescope, in order to remove the possible gradient in the background emission.

Because of the large temporal fluctuations of the background emission, chopping at a few Hz is not sufficient to reduce sky noise below the level of the scientifically useful signal after background subtraction. Other techniques are therefore considered in order to measure the background emission simultaneously to the observations, e.g. by inserting additional fibers in the transmitted field-of-view of the interferometer. At VLTI for instance, the use of variable curvature mirrors in the delay lines provides a clean field-of-view 2" in diameter, which allows us to reduce the contribution of stellar light in the background fibers down to about 10^{-4} of the background contribution. Another solution for background subtraction is to use phase modulation techniques, which require the telescope pupils to be divided into two parts in order to modulate between two different nulled outputs (Serabyn et al. 2004). This is the only practical solution for an N-band nuller, for which the contrast between background and exozodiacal fluxes is huge (almost 10^7, see Table 4).

5.2. Geometric leakage calibration

An important step in the post-processing of nulling interferometry data is the calibration of geometric leakage. We have discussed in Sect. 2.6 that the residual contribution of geometric leakage after calibration should not exceed 10^{-5} of the initial stellar flux in the L' band, while typical rejection rates of 2000 are expected (Table 1). The calibration of geometric leakage, based on the analytical expression (3) of the rejection rate, should therefore reach a precision of about 2% in order to retrieve the useful exozodiacal disk signal with a good signal-to-noise ratio. Closer stars, for which the rejection rate is smaller, require even better calibration accuracies. *A typical precision of 1% for geometric leakage calibration is thus required in the L' band*, while such a calibration is marginally needed in the N band since the achievable rejection rate (∼16000) already matches the requirement on starlight rejection (10^{-4}).

Assuming that the baseline B and the effective wavelength λ are known with a good accuracy, a good knowledge of the stellar angular radius θ_* and limb-darkening coefficient u_λ is sufficient in order to compute the geometric leakage. The global optical transmission of the interferometer must also be known in order to convert this value into a number of photoelectrons measured at the detector. While the interferometric transmission can be straightforwardly measured with a high precision at the constructive output of the nuller where most of the stellar photons end up, the imperfect knowledge of stellar diameters has a large (and generally dominant) contribution to the calibration error budget. Differentiating equation (3), we obtain a required precision $\Delta\theta_*/\theta_* = 0.5\Delta N/N = 0.5\%$ on the stellar diameter knowledge.

The most precise way to determine stellar angular radii is currently based on stellar interferometry. Stellar diameter measurements with an accuracy as good as 0.2% have been demonstrated on resolved stars such as α Cen A and B (Kervella et al. 2003). However, the Darwin/TPF-I targets, with typical angular diameters of 1 mas and below, are only marginally resolved even with the longest baselines currently available: the AMBER instrument at VLTI provides at best an angular resolution of 1.6 mas in J band. A precision of a few 0.1% on diameter measurements with AMBER could thus only be achieved for the closest stars in the Darwin catalogue (< 10 pc). An additional difficulty comes from the extrapolation of the limb-darkening law from the J band to the L' band, since limb-darkening coefficients are currently modelled only up to the K band (Claret 2000). Lunar occultation measurements could also be used to determine the diameters of the brightest targets of the Darwin catalogue ($K \sim 3$) with a limiting resolution of ~ 1 mas, but with the restriction that only about 10% of the sky falls on the Moon's path (Fors et al. 2004).

For stars more distant than about 10 pc, for which interferometric diameter measurements will probably not reach a 0.5% precision, indirect measurements based on surface brightness relations might be used. Empirical laws make it possible to predict the limb-darkened angular diameters of dwarfs and subgiants using their dereddened Johnson magnitudes, or their effective temperature (Kervella et al. 2004). Intrinsic dispersions as small as 0.3% are obtained for the relations based on B−L magnitudes. However, the apparent magnitudes of the Darwin/TPF-I targets need to be accurately known (to better than 0.02 mag): this is usually not the case at infrared colours and might mandate a dedicated photometry programme.

All in all, it is expected that diameter measurements with a precision of 0.5% will be obtained on most of the Darwin/TPF-I targets. A 1% precision is still considered as a worst case scenario in the performance budget.

5.3. Instrumental leakage calibration

After calibration of geometric leakage, there is one remaining step of calibration to be carried out: the evaluation and subtraction of the mean instrumental leakage from the nulled data. Calibration of the instrumental response is a routine procedure in stellar interferometry, and is achieved by observing a well-know *calibrator star*, usually chosen as a late-type unresolved giant star (Mérand et al. 2005). These measurements are carried out just before and after the observation of the target star, and as close as possible to it in the sky, so that the atmospheric properties do not change significantly.

This method can be extended to measure instrumental leakage in nulling interferometry. In this case, calibrator stars must be carefully chosen: even if instrumental leakage does not de-

pend on the angular diameter of the star to the first order, the control loop performance strongly depends on the stellar flux and spectrum, so that the calibrator star should in fact have the same flux and spectrum as the target star in order to get the same instrumental leakage in both cases. Having the same flux and spectrum means that the angular diameters should also be the same, and consequently that the calibrator star will produce the same amount of geometric leakage as the target star. A precise knowledge of the calibrator's angular diameter is thus needed in order to remove the contribution of geometric leakage and obtain a good estimation of instrumental leakage.

The final estimation $Z(\lambda)$ of the exozodiacal signal after both geometric and instrumental leakage calibrations can be expressed as follows:

$$Z(\lambda) = S_{\rm t}(\lambda) - \frac{\pi^2 B^2 \theta_{\rm t}^2}{4\lambda^2} F_{\rm t}(\lambda) - \frac{F_t(\lambda)}{F_c(\lambda)} \left(S_{\rm c}(\lambda) - \frac{\pi^2 B^2 \theta_{\rm c}^2}{4\lambda^2} F_{\rm c}(\lambda) \right) \quad (5)$$

with $S_{\rm t}(\lambda)$ and $S_{\rm c}(\lambda)$ the background-subtracted nulled fluxes for the target and calibrator stars, θ_t and θ_c their angular radii, $F_{\rm t}(\lambda)$ and $F_{\rm c}(\lambda)$ their fluxes, measured at the constructive output of the interferometer. The first subtracted term represents the contribution of geometric leakage while the second one (between brackets) is the estimation of instrumental leakage obtained with the calibrator star.

Table 4. In the first part of the table, we compare the star and exozodiacal disk fluxes to the thermal background, computed from its individual contributors (Paranal night sky, VLTI optical train and GENIE instrument) by integration over the field-of-view defined by a single-mode fiber ($\Omega = \lambda^2/S$). The target is a Sun-like star at 20 pc surrounded by a 20-zodi disk. The values are given in Jy at the central wavelength of the infrared atmospheric windows and "at the entrance of the Earth's atmosphere" (an equivalent emission is given for the background contributors as if they originated from outside the Earth atmosphere). Second part: signals in electrons per second actually detected at the GENIE science detector. The total shot noise is deduced, and used to compute the time needed for a photometric signal-to-noise ratio of 5.

	L'	N
Total stellar signal [Jy]	3.1	0.51
Total disk signal [Jy]	3.0×10^{-4}	5.1×10^{-4}
Sky brightness [Jy/as^2]	5.0	690
VLTI brightness [Jy/as^2]	115	21300
GENIE brightness [Jy/as^2]	29	5320
Total bckg signal [Jy]	1.8	2550
Final stellar leakage [el/s]	1.0×10^4	1.5×10^3
Final disk signal [el/s]	3.6×10^2	4.1×10^3
Final bckg signal [el/s]	4.8×10^6	2.7×10^{10}
Shot Noise [el/s$^{1/2}$]	2.2×10^3	1.7×10^5
Time for SNR = 5 [sec]	950	40000

6. Detection of exozodiacal dust disks with GENIE

In the following paragraphs, we evaluate the sensitivity of GENIE, the Ground-based European Nulling Interferometer Experiment (Gondoin et al. 2004), to exozodiacal dust for typical Darwin/TPF-I targets.

6.1. Background-limited signal-to-noise ratio

Before computing the actual detection performance of the nuller, let us assess the required integration times in a non-turbulent environment, where the only source of noise is the shot noise from all sources inside the field-of-view. The photon budget of Table 4 includes the geometric and instrumental leakage contributions given in Table 3 (worst case scenario), the contribution of the dust disk itself[5] and the different sources of background emission (sky and instrument).

We assume an overall instrumental throughput (including VLTI, GENIE and detectors) of 1% both in the L' and N bands. Table 4 gives the time required to detect a 20-zodi disk around a G2V star at 20 pc with a signal-to-noise ratio of 5. While the integration time in the L' band is reasonable (15 minutes), it is very large in the N band (11 hours). In fact, the difficulty in the N band comes not only from the required integration time, but also from the huge contrast between the exozodiacal and background fluxes (almost 10^7) at the output of the nuller. These two background-related issues are the main reasons for the choice of the L' band in the context of GENIE (Gondoin et al. 2004). Note that, even in the L' band, the required background calibration accuracy is challenging: in order to reach a final signal-to-noise ratio larger than 5, the background must be removed with an accuracy of 10^{-5}, which is within reach using the advanced background subtraction methods discussed in Sect. 5.1.

[5] The part of the exozodiacal emission transmitted by the interference fringe pattern shown in Fig. 1 typically ranges between 30% and 40%.

6.2. Final signal-to-noise ratio

In this section, we evaluate the global sensitivity of the GENIE instrument by simulating a 30-minute observation of a Sun-like star at 20 pc surrounded by a 20-zodi disk. In Table 5, we first give the raw sensitivity of the nuller, i.e., without calibration of instrumental leakage (very conservative approach assuming that no convenient calibrator star can be found). In this case, the mean instrumental leakage fully contributes as a bias which adds to the exozodiacal disk signal that we want to detect. This implies that the mean instrumental leakage should be at least five times smaller than the disk contribution to ensure a safe detection. Table 5 shows that, depending on the model for atmospheric turbulence, the raw sensitivity ranges between 530 and 1800 zodis for a signal-to-noise ratio of 5 across the whole L' band. Instrumental leakage is the main contributor to the noise budget in that case. Note that shot noise, detector noise and variability noise are almost negligible after only 30 min of integration. This would not be the case if spectral dispersion was used: in order to keep the same sensitivity, the integration time should then be increased by a factor equal to the square root of the number of spectral channels.

In a second step, we compute the performance assuming that an appropriate calibrator star can be found, i.e., with simi-

Table 5. Expected sensitivity of the GENIE instrument at VLTI, given in number of zodis that can be detected around a Sun-like at 20 pc in 30 min in the full L' band using the UT2-UT3 baseline (47 m). The worst case corresponds to conservative control loop performance and 1% precision on diameter measurements, while the best case relies on optimistic control loop performance and 0.5% precision on angular diameters. Each individual contribution is given in photo-electrons detected at the nulled output. The raw sensitivity is given without any calibration of instrumental leakage, while the calibrated sensitivity assumes that a calibrator star with similar characteristics as the target star is used to perform instrumental leakage calibration.

	worst case	best case
20-zodi signal [e-]	6.5×10^5	8.7×10^5
Shot noise [e-]	1.3×10^5	1.5×10^5
Detector noise [e-]	3.4×10^3	4.0×10^3
Variablility noise [e-]	1.9×10^4	5.9×10^3
Calibrated geom. leakage [e-]	2.2×10^5	1.5×10^5
Raw instr. leakage [e-]	1.2×10^7	4.6×10^6
Calibrated instr. leakage [e-]	3.8×10^5	2.1×10^5
Zodis for SNR=5 (raw)	1800	530
Zodis for SNR=5 (calibrated)	56	34

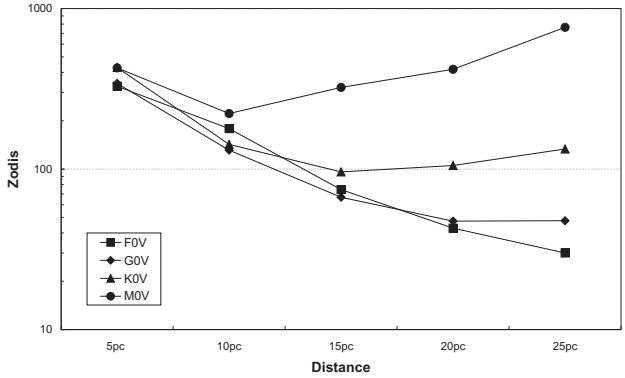

Fig. 9. Sensitivity of GENIE to dust disks around nearby main-sequence stars, expressed in units relative to the Solar zodiacal cloud. The simulations have been obtained with optimized UT-UT baselines for 30 minute exposures. The smallest baseline (47 m on UT2-UT3) is used in most cases because the dominant noise source generally comes from the calibration of geometric leakage for both the target and calibrator stars.

lar flux, spectrum and angular diameter than the target star but without circumstellar dust. In this case, the calibration precision for instrumental leakage is mainly limited by the imperfect knowledge of the calibrator angular diameter, assumed to be the same than for the target star. This contribution is dominant in the noise budget, so that the GENIE sensitivity could benefit from improvements in the precision of stellar diameter measurements. In practice, the calibrator star will not be perfectly identical to the target, inducing a bias in the calibration process due to the different behaviour of the control loops for different stellar magnitudes and/or spectra. This bias is not dominant in the calibration process as long as the H, K and L' magnitudes of the target and calibrator do not differ by more than about 0.2 magnitudes. A convenient calibrator will probably not be available in all cases, so that the actual performance of the nuller could be somewhat degraded with respect to the final values of Table 5 (Absil et al., in preparation).

6.3. Influence of stellar type and distance

In order to assess the scientific pertinence of GENIE in the context of the Darwin/TPF-I programmes, we have evaluated the detection performance for exozodiacal dust clouds around typical Darwin/TPF-I targets, i.e. late-type dwarfs with distances ranging between 5 and 25 pc. In Fig. 9 are plotted the expected detection levels for the GENIE instrument with 30 minutes of integration on the 8-m UTs, while Fig. 10 gives the performance on the 1.8-m ATs for an integration time of 2 hours. The baseline lengths have been optimized in order to reach an optimum sensitivity to exozodiacal dust, within the limitations imposed by the VLT interferometer (UT-UT baselines comprised between 47 and 130 m, AT-AT baselines ranging from 8 to 202 m). Here again, we have assumed that a calibrator star similar to the target star can be found for the evaluation of instrumental leakage. This optimistic assumption is at least partially compensated by the fact that we use conservative assumptions on atmospheric turbulence properties and on stellar diameter knowledge (cf. the "worst case" of Table 5).

The performance estimates in the case of UTs show a maximum efficiency for exozodiacal dust detection at 25 pc for F0V, 20 pc for G0V, 15 pc for K0V and 10 pc for M0V stars. This maximum is reached when the two main sources of noise are well balanced: for nearby targets, which are partially resolved, the contribution of geometric leakage is dominant, while for more distant and thus fainter targets the main contribution comes from shot noise. The strong limitation on the sensitivity for close targets can be overcome by using smaller baselines, which are available only for AT pairs at the VLTI. This is illustrated in Fig. 10: with the shortest baselines, one can achieve exozodiacal dust detection down to the 20-zodi level for bright and close targets (especially F-type stars), which are however scarce in the Darwin star catalogue.

These simulations indicate that exozodi detection down to a density level of about 50 times our local zodiacal cloud is a realistic goal for most F and G stars in the Darwin catalogue, while exozodiacal densities of about 100 zodis could be detected around K-type stars. In the case of M stars, only the closer stars could lead to a pertinent detection level, of about 200 zodis.

7. Conclusions and perspectives

In this paper, we have demonstrated the exceptional capabilities of ground-based nulling interferometers to detect faint circumstellar features such as exozodiacal disks. Ground-based nulling interferometry requires high-performance closed-loop control of atmospheric turbulence in the L' band, and extremely precise background subtraction in the N band. In this paper, we have computed the expected performance of state-of-the-art servo loops for piston, dispersion and intensity control, allowing the stabilization of the instrumental nulling ra-

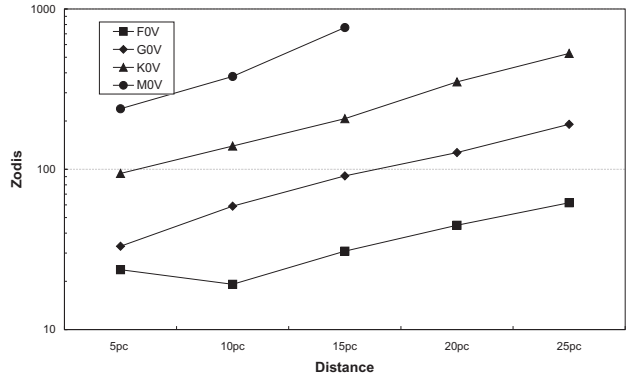

Fig. 10. Sensitivity of GENIE to dust disks around nearby main-sequence stars, expressed in units relative to the Solar zodiacal cloud. The simulations have been obtained with optimized AT-AT baselines in 2 hours of integration. The availability of very small baselines (down to 8 m) allows us to reduce the contribution of geometric leakage and thus improves the detection levels of Fig. 9 at short distances.

tio. Calibration procedures have been discussed to further remove stellar light from the nulled output of the instrument. This comprehensive study shows that an L'-band nuller such as GENIE at VLTI could detect exozodiacal disks about 50 to 100 times as dense as the Solar zodiacal cloud. This instrument will thus significantly improve the detection performance of current infrared and sub-millimetric facilities, and above all will peer into the currently inaccessible warm region of dust disks located within a few AU of nearby late-type dwarfs (typical Darwin/TPF-I targets).

The simulated performance of the nulling instrument critically depends on a number of noise contributions which could be improved in different ways. Geometrical leakage could be reduced by using short baselines, typically ranging between 8 and 40 m, while its calibration would be improved by obtaining accurate stellar diameter measurements at long baselines (> 300 m) and/or precise photometry to derive diameters from surface-brightness relationships, and by extending the limb-darkening models towards the mid-IR wavelengths used by the nulling instruments. Instrumental leakage depends strongly on the ability to correct the effects of atmospheric turbulence, and would therefore benefit from advances in real-time control algorithms and compensation devices. Polarization errors, which have been discussed only briefly in this paper, could also be critical and need to be carefully addressed at the design level. Finally, advanced background subtraction methods such as the phase modulations techniques foreseen for the Darwin/TPF-I missions might further improve the overall performance of a ground-based nuller.

Acknowledgements. The authors wish to thank their ESA and ESO colleagues, the two industrial partners (Alcatel Space and EADS-Astrium) and the GENIE scientific team for their support and contributions. The authors are also grateful to the anonymous referee and to Jean Surdej for their precious help in improving the quality and readability of the paper.

References

Absil, O. 2001, Diploma thesis, University of Liège, http://vela.astro.ulg.ac.be/themes/telins/harigs/

Absil, O., Bakker, E., Schöller, M., & Gondoin, P. 2004, in Proc. SPIE, Vol. 5491, New Frontiers in Stellar Interferometry, ed. W. Traub, 1320

Absil, O., den Hartog, R., Erd, C., et al. 2003a, in Toward Other Earths: Darwin/TPF and the Search for Extrasolar Terrestrial Planets, Vol. SP-539 (ESA's Publication Division), 317

Absil, O., Kaltenegger, L., Eiroa, C., et al. 2003b, in Toward Other Earths: Darwin/TPF and the Search for Extrasolar Terrestrial Planets, Vol. SP-539 (ESA's Publication Division), 323

Absil, O., Karlsson, A., & Kaltenegger, L. 2003c, in Proc. SPIE, Vol. 4852, Interferometry in Space, ed. M. Shao, 431

Allen, D. & Barton, J. 1981, PASP, 93, 381

Angel, J. 1989, in The Next Generation Space Telescope, ed. P. Bély, C. Burrows, & G. Illingworth (HST Sc. I., Baltimore), 81

Angel, J. & Woolf, N. 1997, ApJ, 475, 373

Arsenault, R., Alonso, J., Bonnet, H., et al. 2003, in Proc. SPIE, Vol. 4839, Adaptive Optical System Technologies, ed. P. Wizinowich & D. Bonaccini, 174

Beichman, C., Bryden, G., Rieke, G., et al. 2005, ApJ, 622, 1160

Beichman, C., Woolf, N., & Lindensmith, C. 1999, TPF: A NASA Origins Program to Search for Habitable Planets (Jet Propulsion Laboratory: Pasadena, CA), JPL 99-3

Bracewell, R. 1978, Nature, 274, 780

Chazelas, B., Brachet, F., Bordé, P., et al. 2005, Applied Optics, accepted

Claret, A. 2000, A&A, 363, 1081

Claret, A., Díaz Cordovés, J., & Giménez, A. 1995, A&AS, 114, 247

Colavita, M., Wizinovich, P., & Akeson, R. 2004, in Proc. SPIE, Vol. 5491, New Frontiers in Stellar Interferometry, ed. W. Traub, 454–463

Conan, J.-M., Rousset, G., & Madec, P.-Y. 1995, J. Opt. Soc. Am. A, 12, 1559

Dermott, S., Grogan, K., Holmes, E., & Wyatt, M. 1998, in Proceedings of the Exo-zodiacal Dust Workshop, ed. D. Backman, L. Caroff, S. Sanford, & D. Wooden, Vol. 1998-10155 (NASA/CP), 59–63

Fors, O., Richichi, A., Núñez, J., & Prades, A. 2004, A&A, 419, 285

Fridlund, M. 2000, ESA bulletin, 103, 20

Glindemann, A., Albertsen, M., Andolfato, L., et al. 2004, in Proc. SPIE, Vol. 5491, New Frontiers in Stellar Interferometry, ed. W. Traub, 447–453

Gondoin, P., Absil, O., den Hartog, R., et al. 2004, in Proc. SPIE, Vol. 5491, New Frontiers in Stellar Interferometry, ed. W. Traub, 775–786

Herbst, T. & Hinz, P. 2004, in Proc. SPIE, Vol. 5491, New Frontiers in Stellar Interferometry, ed. W. Traub, 383–390

Karlsson, A. & Mennesson, B. 2000, in Proc. SPIE, Vol. 4006, Interferometry in Optical Astronomy, ed. P. Léna & A. Quirrenbach, 871

Kelsall, T., Weiland, J., Franz, B., et al. 1998, ApJ, 508, 44
Kervella, P., Thévenin, F., di Folco, E., & Ségransan, D. 2004, A&A, 426, 297
Kervella, P., Thévenin, F., Ségransan, D., et al. 2003, A&A, 404, 1087
Kolmogorov, A. 1941, Doklady Akad. Nauk. S.S.S.R., 30, 229
Koresko, C., Mennesson, B., Serbyn, E., et al. 2003, in Proc SPIE, Vol. 4838, Interferometry for Optical Astronomy II, ed. W. Traub, 625
Kuchner, M. & Brown, M. 2000, PASP, 112, 827
Kuchner, M., Brown, M., & Koresko, C. 1998, PASP, 110, 1336
Lawson, P. & Dooley, J. 2005, Technology Plan for the Terrestrial Planet Finder Interferometer (Jet Propulsion Laboratory: Pasadena, CA), JPL 05-5
Lay, O. 1997, A&AS, 122, 535
Lay, O. 2004, Applied Optics, 43, 6100
Léger, A., Mariotti, J., Mennesson, B., et al. 1996, Icarus, 123, 149
Mathar, R. 2004, Applied Optics, 43, 928
Meisner, J. & Le Poole, R. 2003, in Proc. SPIE, Vol. 4838, Interferometry in Optical Astronomy II, ed. W. Traub, 609
Mennesson, B., Ollivier, M., & Ruilier, C. 2002, J. Opt. Soc. Am. A, 19, 596
Mérand, A., Bordé, P., & Coudé du Foresto, V. 2005, A&A, 433, 1155
Ollivier, M. 1999, PhD thesis, Université de Paris XI
Quirrenbach, A. 1999, in Principles of Long Baseline Stellar Interferometry, ed. P. Lawson (JPL publ.), 71
Roddier, F. 1981, in Progress in optics, ed. E. Wolf, Vol. XIX (North-Holland, Amsterdam), 281
Ruilier, C. & Cassaing, F. 2001, J. Opt. Soc. Am. A., 18, 143
Serabyn, E., Booth, A., Colavita, M., et al. 2004, in Proc. SPIE, Vol. 5491, New Frontiers in Stellar Interferometry, ed. W. Traub, 806
Serabyn, E. & Colavita, M. 2001, Applied Optics, 40, 1668
Stankov, A., Kaltenegger, L., & Eiroa, C. 2005, ESA/ESTEC internal publication DMS/SCI-A/DARWIN/289
ten Brummelaar, T. 1995, Optics Communications, 115, 417
Vérinaud, C. & Cassaing, F. 2001, A&A, 365, 314
Wilhelm, R. & Gitton, P. 2003, in Toward Other Earths: Darwin/TPF and the Search for Extrasolar Terrestrial Planets, Vol. SP-539 (ESA's Publication Division), 659
Young, A., Milone, E., & Stagg, C. 1994, A&AS, 105, 259

5

Selected scientific applications of the GENIE instrument

Contents

5.1 Characterisation of debris disks around Vega-type stars 99
5.1.1 The debris disk around ζ Lep 100
5.1.2 Observing procedure 102
5.1.3 Influence of the disk morphology 104
5.1.4 Influence of the grain size and composition 107
5.1.5 Conclusions 109
5.2 Spectroscopy of hot Extrasolar Giant Planets 110
5.2.1 Classical detection method and calibration issues 111
5.2.2 Perspectives: OPD modulation and colour-differential techniques 112

We have demonstrated in the previous chapter that GENIE will provide useful information on the presence of dust at the 50-zodi level around nearby stars. Besides this main goal, GENIE will be exploited for many other exciting scientific programmes. In fact, any target requiring both high dynamic range and high angular resolution would benefit from its capabilities. Among the prime science goals of GENIE are therefore the detection and characterisation of proto-planetary disks around Young Stellar Objects (YSO), debris disks around Vega-type stars, high-contrast binaries, bounded brown dwarfs and hot Extrasolar Giant Planets (EGP). In this chapter, we discuss the potential contribution of GENIE in the characterisation of Vega-type stars, around which large amounts of dust are present. We show that it could largely improve our knowledge of these disks and thereby our understanding of the evolution of planetary systems. The perspectives for EGP detection and spectroscopy are also briefly discussed. In both cases, the GENIE simulator has been extensively used to simulate realistic observations with the future instrument.

5.1 Characterisation of debris disks around Vega-type stars

With only a handful of systems resolved so far, the high-resolution study of debris disks is still in its infancy. The current accuracy of interferometric instruments such as FLUOR at the CHARA array or AMBER at the VLTI should allow for a better understanding of the inner regions of these circumstellar

disks in the coming years, as discussed in Chapter 2. However, these instruments will be limited to contrast ratios of a few 0.1%, so that low density debris disks are still out of reach with these "classical" interferometers and therefore a real gold mine for future nulling instruments.

In this section, we evaluate the capabilities of the GENIE instrument to characterise the morphology and composition of inner debris disks, where small quantities of hot dust are expected to be found. Zeta Leporis (ζ Lep hereafter), a prototypical Vega-type star, will be used throughout the discussion for illustrative purposes. The following sections summarise the content of two posters presented respectively at Heidelberg (Absil et al. 2003a) and Garching (Absil et al. 2005). The results originally presented in the former have been updated with the latest version of the GENIE simulator (version 8.4.4), taking into account the noise sources in a more realistic way.

5.1.1 The debris disk around ζ Lep

The choice of a suitable target to illustrate this discussion is mainly based on the availability of a model for the inner dust distribution around a sufficiently bright Vega-type star. Fajardo-Acosta et al. (1998) have identified and studied a few targets around which warm dust is suspected to be present (see Table 2.2). Among them, ζ Lep (A2V, 22 pc) is a good candidate, as it exhibits the largest 10 μm excess in their survey. It is also one of the two targets around which an IRAS 12 μm excess was confirmed with ground-based photometry at 10 μm in the study of Aumann & Probst (1991). Moreover, it has been marginally resolved in the mid-infrared at the Keck Observatory by Chen & Jura (2001), suggesting the presence of dust within 6 AU from the star. Barrado y Navascués (1998) estimated its age to be 200 ± 100 Myr from its belonging to the Castor moving group and, more recently, Song et al. (2001) derived an age between 50 and 350 Myr from Stromgren photometry.

By modelling the Spectral Energy Distribution (SED) of the star-disk system (Figure 5.1), Fajardo-Acosta et al. (1998) have deduced a morphological model for the dust distribution, arranged in a shell bounded by an inner radius $r_{\rm in} \sim 0.5$ AU and an outer radius $r_{\rm out} \sim 7$ AU. With an expected integrated flux of about 200 mJy for the circumstellar disk in the L′ band, the star/disk contrast amounts to ~ 100, making ζ Lep an easy target since GENIE should detect exozodiacal features as faint as a few 10^{-4} of the stellar contribution in the L′ band (see Section 4.2.1).

Morphology of the debris disk

Because debris disks are more generally assumed to be arranged in flat optically thin disks, we have adapted this shell model to a flat disk model by decreasing the unsigned exponent α of the radial density power-law, as proposed by Fajardo-Acosta et al. (1998). Our disk model is then described by the following density and temperature power-laws:

$$\rho(r_c) = \rho_0 \left(\frac{r_c}{r_{\rm in}} \right)^{-\alpha} , \tag{5.1}$$

$$T(r_c) = T_{\rm in} \left(\frac{r_c}{r_{\rm in}} \right)^{-\delta} , \tag{5.2}$$

where r_c represents the distance to the star projected on the ecliptic plane of the system, and where ρ_0, $T_{\rm in}$ are respectively the number density and temperature of dust grains at the inner edge $r_{\rm in}$ of the disk. The exponent δ for the radial temperature power-law equals 0.5 if the dust grains are blackbodies in radiative equilibrium, as assumed by Fajardo-Acosta et al. (1998). Although this is a crude approximation, as dust grains actually have a wavelength-dependent emissivity, the exponent actually measured by Kelsall et al. (1998) in the solar zodiacal disk ($\delta = 0.467$) shows that it is not far from reality.

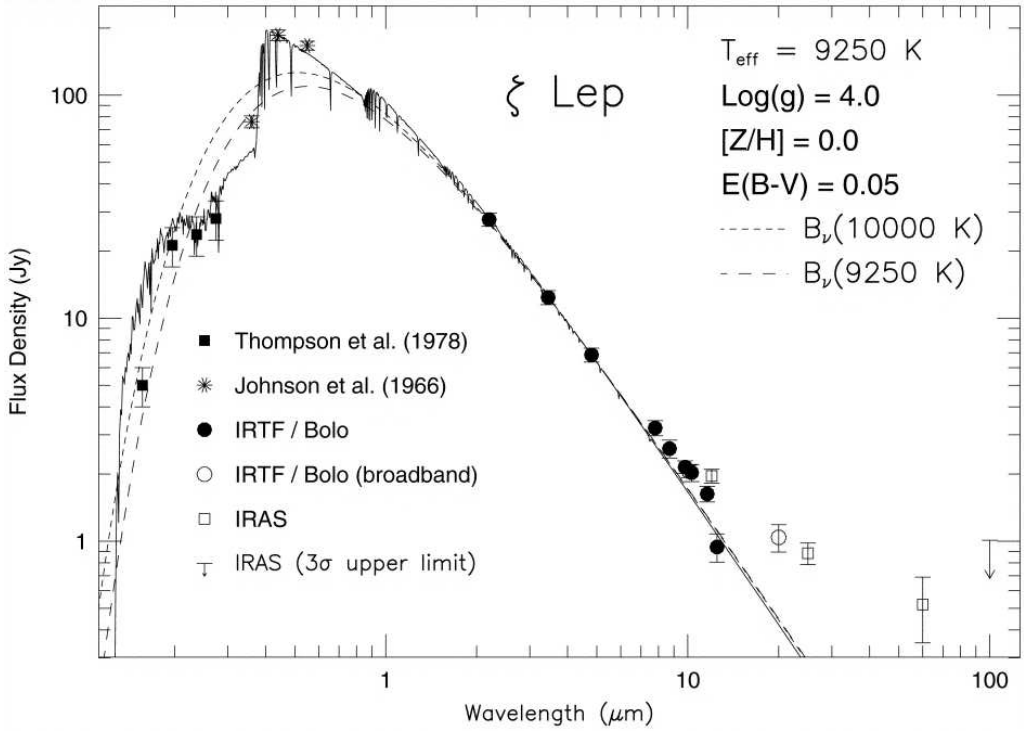

Figure 5.1: Spectral Energy Distribution of the ζ Lep star-disk system in the UV, visible and infrared domains. The photospheric flux (solid line) is modelled with a synthetic spectrum from the Kurucz (1992) model atmospheres, normalised to the near-infrared K and L fluxes. Blackbody distributions are given for comparison, showing weak deviations in the infrared domain. Excess emission is detected in the mid- and far-infrared, starting at $\sim 8\,\mu$m. The presence of warm dust close to the star is proposed as an explanation to this excess.

In the two above expressions, the vertical dependence of the dust properties has been neglected, which is an acceptable approximation assuming that the disk is geometrically thin. The parameters of the model for ζ Lep and its debris disk, derived from Fajardo-Acosta et al. (1998), are summarised in Table 5.1. This model, truncated at 7 AU, reproduces 90% of the observed flux at 10.3 μm and even more at shorter wavelengths, for which the thermal emission is more concentrated in the first AUs around the star. Of particular interest is the fractional dust luminosity ($L_{\rm dust}/L_\star$), the ratio of the integrated excess flux emitted by the dust to the integrated flux emitted by the star alone. This ratio is equivalent to the mean optical depth of circumstellar dust grains and is therefore an indicator of the quantity of dust around the star.

Stellar parameters		Disk parameters	
Distance [pc]	21.5	$r_{\rm in}$ [AU]	0.5
V mag.	3.55	$r_{\rm out}$ [AU]	7
K mag.	3.31	$T_{\rm in}$ [K]	960
Type	A2V	$T_{\rm out}$ [K]	250
$R_\star$ [$R_\odot$]	1.749	α	0.6
$T_{\rm eff}$ [K]	9000	δ	0.5
$L_\star$ [$L_\odot$]	16.36	$L_{\rm dust}/L_\star$	1.7e-4

Table 5.1: Star and disk parameters for the Vega-type star ζ Lep, adapted from Fajardo-Acosta et al. (1998). The stellar radius, effective temperature and luminosity have been revised by fitting the photospheric SED of ζ Lep with a NextGen atmosphere model spectrum (Hauschildt et al. 1999).

We have used the DISKPIC package, developed by Absil (2003), to simulate the image of the ζ Lep system as seen by GENIE. DISKPIC is based on a simple morphological description of optically thin debris disks, using the parameters listed in Table 5.1. In this model, the dust properties are assumed to be independent of vertical position (thin disk approximation) and of azimuth. Only the thermal emission is taken into account, an approximation valid for wavelengths longer than 3 μm.

Size and nature of the dust grains

In addition to investigating the morphology of the dust disk with the DISKPIC package, we have used the 3D debris disk model developed by Augereau et al. (1999) to investigate the physical parameters of the dust grains (composition and size distribution). The model provides synthetic images and SEDs of optically thin dust disks, including both thermal emission of the dust particles in thermal equilibrium with the central star and scattered light by the grains. The photospheric SED of ζ Lep has been fitted with a NextGen atmosphere model spectrum (Hauschildt et al. 1999) with $T_{\rm eff}$ = 9000 K and $\log(g)$ = 4.0, giving $L_\star = 16.36\,L_\odot$ at 21.5 pc. The optical properties of the dust grains are given by the Mie theory. Two grain types have been considered:

- the smooth astronomical silicate grains discussed by Weingartner & Draine (2001),
- cold-coagulation type grains as proposed by Li & Lunine (2003), with a porosity of 73% when the grains are icy and up to 90% when the H_2O-dominated ices are sublimated, which is our case (< 6 AU).

The grain size distribution is assumed to follow a power law $dn(a) \propto a^{-3.5}da$ between minimum and maximum grain sizes $a_{\rm min}$ and $a_{\rm max}$. An exponential vertical profile $Z(r,z) = \exp\left(-(|z|/H(r))^\gamma\right)$ is used, with the vertical scale height $H(r) = 0.1r$. In this model, grains with temperatures above 1700 K are assumed to be sublimated and are eliminated. The sublimation distance depends on the grain composition and size. Because of the size distribution, this results in a smooth inner disk radius extending over a few tenths of AU typically (see Figure 5.2). The other parameters of the disk follow the prescriptions of Table 5.1, except for the exponent δ of the radial temperature power-law, which is deduced from the optical properties of the grains. It is generally comprised between 0.46 and 0.51 as a function of grain size and composition.

Once we have chosen the dust composition and the grain size distribution through $a_{\rm min}$ and $a_{\rm max}$, the SED of the dust disk is computed and the surface density of the disk is adjusted so that the SED gives the best possible fit to the observed mid-infrared excesses. Synthetic images of the disk are then calculated for different inclination angles of the system with respect to the line sight. A sample image, obtained for an inclination of 40°, is given is Figure 5.2.

5.1.2 Observing procedure

The essential steps in the observing procedure of a nulling interferometer have already been presented in Section 4.2.1. The first step is to remove the background emission, which is estimated by off-source measurements. In the following discussion, we will assume that background subtraction is performed with multiple fibres arranged in the field-of-view (see Section 3.4.3). The background is supposed to be spatially uniform, so that the only calibration error comes from the presence of stellar light in the background fibre. During the phase-A study, it was estimated that, in the L′ band, a fraction equal to 2×10^{-4} of the stellar flux ends up in the background fibres. We do not take into account here the possible calibration of the stellar point spread function to reduce this contribution.

After background calibration, one obtains the raw nulling ratio, defined as the ratio between the

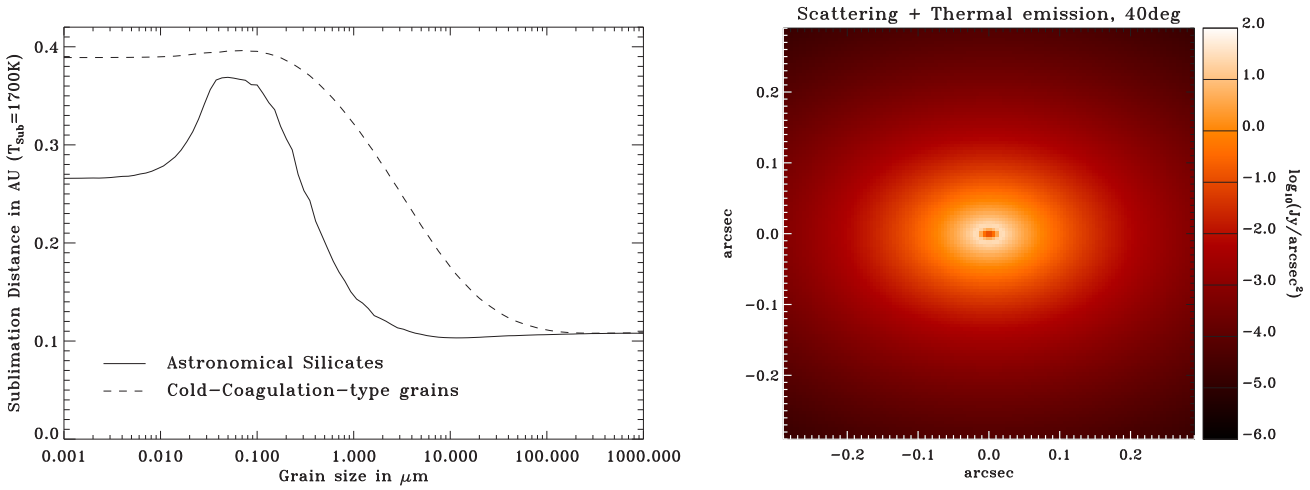

Figure 5.2: Left: sublimation distance of dust grains as a function of their size, for two types of grains. The temperature of the dust grains at a given distance is maximal when their size equals $\lambda_{\max}/2\pi$, where $\lambda_{\max}$ is the wavelength at which the stellar spectrum peaks. Smaller grains do not absorb stellar light efficiently, while larger grains radiate more efficiently (in a larger wavelength domain) the absorbed energy. Right: sample image of the dust disk around ζ Lep for an inclination of 40°, displayed on the interferometric field-of-view of a 1.8-m AT in L′ band (logarithmic scale). Courtesy of J.-C. Augereau.

background-subtracted destructive and constructive outputs. The second step of postprocessing is the removal of the geometric stellar leakage, based on its analytical expression (Equation 3.11). This step requires a good knowledge of the stellar angular diameter. An alternative, which will be used here, is to fit both the stellar diameter and disk parameters at the same time. We will see in the next sections that this procedure gives excellent results when a good (u, v) plane coverage is available.

Finally, the last critical step is the estimation and subtraction of instrumental leakage from the scientific observations. For that purpose, a calibration star is observed before and after the target star. In order to provide a good estimation of the instrumental leakage, the calibration star should be similar to the target star in terms of magnitude and colour, except for the absence of circumstellar dust. Proximity in the sky is another important criterion in order to have the same turbulence conditions for the three observations. Under these conditions, the control loops should produce the same quality of correction for the target and calibration stars, which is mandatory for an accurate removal of instrumental leakage. The calibration of instrumental leakage is done as follows:

1. Compute analytically the geometric leakage associated with the calibrator, knowing its angular diameter;
2. Subtract the geometric leakage from the mean leakage to retrieve the instrumental leakage in the case of the calibrator measurements;
3. Perform an interpolation between the two measurements of instrumental leakage (before and after the target star) and scale the result to the observed total flux of the target star;
4. Subtract the estimated instrumental leakage from the scientific data to retrieve the actual nulling ratio.

A convenient calibrator for ζ Lep is its neighbour η Lep, an F1 main sequence star located at 15 pc having similar infrared magnitudes and colour: $H = 2.94$, $K = 2.91$ and $L = 2.87$ for η Lep, while $H = 3.32$, $K = 3.31$ and $L = 3.24$ for ζ Lep. Although this star was identified as a possible Vega-type star by Mannings & Barlow (1998) using the IRAS database, the small excess in the mid-infrared suggests that the quantity of hot dust is much smaller than around ζ Lep. The angular diameter of η Lep can be

estimated by surface brightness relations. Assuming a standard error of 0.02 on visible magnitudes and a conservative 3% error on the infrared magnitudes, the approach of Kervella et al. (2004d) provides an angular diameter of 0.993 ± 0.013 mas for a Hipparcos parallax of 66.47 ± 0.74 mas. This result is close to the conservative 1% precision on angular diameters assumed in Section 4.2.1. Precise photometric measurements would be required to improve the quality of the model.

Preliminary simulations show that, even with a good calibrator such as η Lep, the optimum control loop performances are quite different between the target and calibration stars. The lower magnitudes of the calibrator allow for a higher repetition frequency in the control loops, resulting in an instrumental leakage decreased by about 40% with respect to the target star. For this reason, the same repetition frequencies will be used for the control loops during the whole calibration sequence. Even better, it is foreseen that the GENIE control loops will be capable of artificially reducing the amount of photons feeding them so as to give precisely the same performance for both target and calibration stars. If such a system is not available, significant biases will inevitably arise in the instrumental leakage calibration process, as the calibrator is never perfectly identical to the target star in terms of infrared magnitudes.

In the following simulations, the observations are performed for the moment when ζ Lep crosses the local meridian, at a zenithal distance of $9°48'$ for Cerro Paranal. Such a small zenithal distance ensures optimum atmospheric transmission. In this situation, the projected baseline on the plane of the sky has approximately the same length as the ground baseline.

5.1.3 Influence of the disk morphology

In this section, we use the DISKPIC package to investigate the influence of inclination, inner radius and radial density power-law on the output of GENIE. Purely theoretical considerations will be first presented, in absence of noise, in order to show the influence of each parameter separately. In the second part of this section, we simulate realistic observations with GENIEsim and try to retrieve the disk parameters from the output of the simulation. This study was performed at a time when the choice of wavelength was not already made for the GENIE instrument (Absil et al. 2003a), so that both the L′ and N bands have been investigated. The L′ band simulations have been updated by taking into account the instrumental concepts proposed during the phase-A studies.

Trends in a noiseless environment

These simulations are performed in the N band for illustration purpose. The L′ band would give the same qualitative results. The only major difference between the two bands is that the geometric leakage is negligible in the N band while not in the L′ band where the angular resolution is higher. The influence of the disk morphology is therefore easier to isolate in the N band.

We have generated images of the dust disk with various inclinations, ranging from 0° (face-on) to 90° (edge-on), using the DISKPIC package. The nulling ratio has then been computed for the star-disk system on a baseline of 46.7 m (corresponding to the UT2-UT3 baseline at VLTI). Figure 5.3 shows the evolution of the nulling ratio as a function of the baseline orientation for four different inclinations of the disk. The baseline angle is counted positively east of north. A position angle of 0° was assumed for the dust disk (i.e., major axis along the N-S direction). For low inclinations, the nulling ratio is not affected by the baseline orientation, because the disk image has nearly circular symmetry. For high inclinations, the flux in the destructive output drops dramatically when the dark fringe and the major axis of the disk are superposed (baseline angle of 90°).

In Figure 5.4, we have used different values of the density power-law exponent α and of the inner radius $r_{\rm in}$ to generate the disk images. The nulling ratio has been computed for different baseline lengths

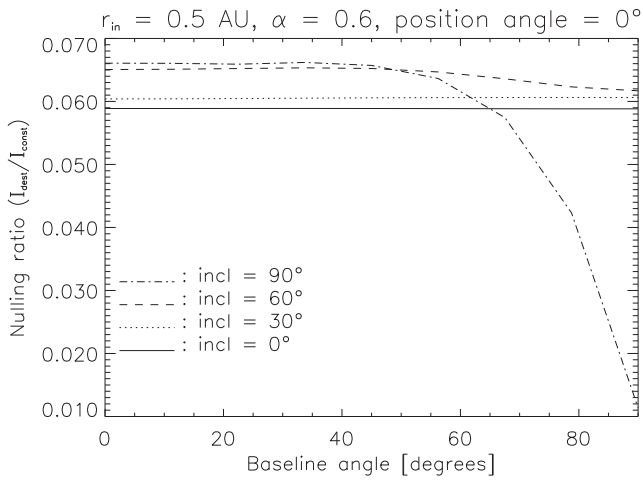

Figure 5.3: The evolution of the nulling ratio for different baseline orientations is remarkable for high inclinations: edge-on disks are strongly cancelled by the central dark fringe when they are aligned perpendicularly to the baseline (baseline angle of 90° in the plot).

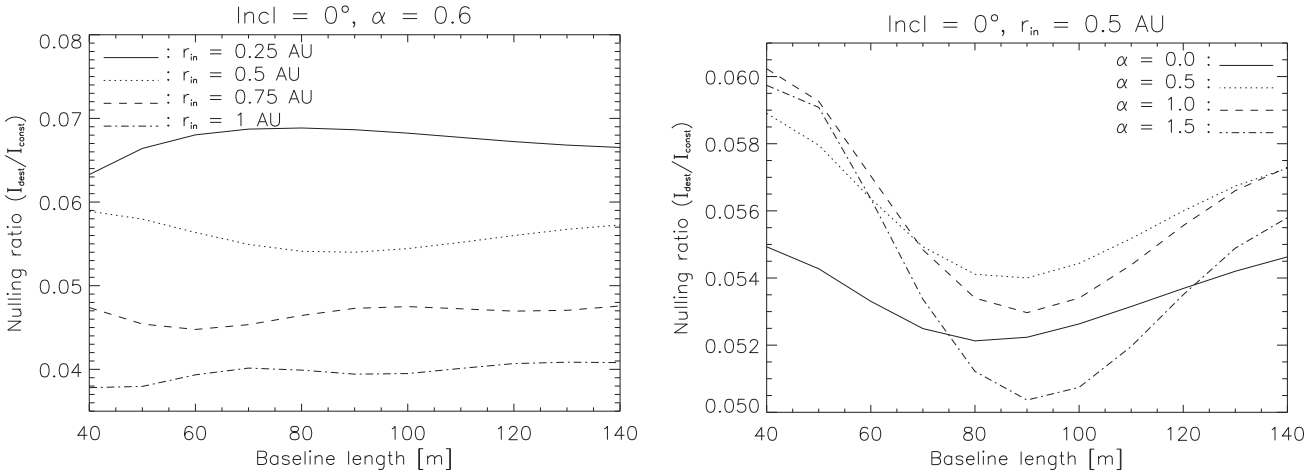

Figure 5.4: Left: The influence of the dust inner radius is remarkable: the nulling ratio is maximum when a bright fringe transmits the large flux produced by the hot dust located at the inner cut-off. Right: The behaviour of the nulling ratio for different density power-laws does not differ much. The difference would be more visible if the inner radius was not resolved (i.e., for baselines < 40 m in the N band, or baselines < 15 m in the L′ band).

ranging from 40 m to 140 m. The influence of the inner radius on the nulling ratio is remarkable: the maxima of the curves in the left-hand side of Figure 5.4 correspond to the baselines at which a bright fringe is superposed on the inner component of the dust disk (brightest part of the disk). On the other hand, the density power-law exponent has a smaller influence on the nulling ratio: the position of the maximum does not change any more, and the behaviour of the nulling ratio with increasing baselines is similar for all values of α. Retrieving this parameter from nulling measurements will be more difficult.

Simulated observations in the L′ band

Now that we have investigated the influence of each parameter on the nulling ratio, the GENIEsim software will be used to simulate realistic observations of the ζ Lep system, from which we will try to retrieve the disk parameters. We follow the observing procedure described in Section 5.1.2. In these simulations, we have assumed a face-on disk, so that the baseline orientation does not matter. Ten

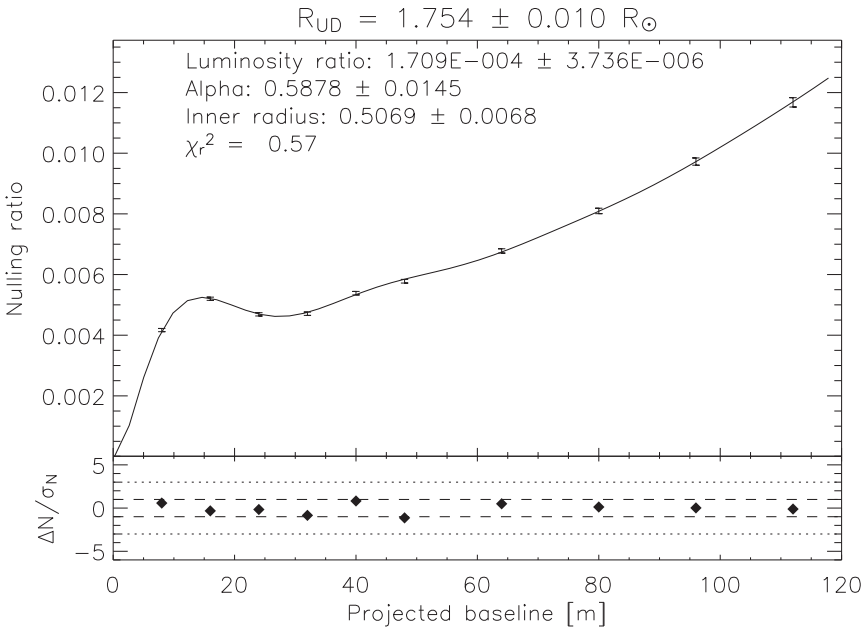

Figure 5.5: Simulated L′ band observations of ζ Lep with GENIE using the VLTI Auxiliary Telescopes. The solid line shows the best-fit model to the simulated data set represented by its error bars. Each observation, obtained in 1000 sec with a pair of ATs, has an SNR of about 90. The stellar radius has been fitted together with the disk parameters, yielding a final value of $1.754 \pm 0.010\,R_\odot$. The values used in the initial model are listed in Table 5.1. The residuals of the fit are displayed at the bottom of the plot, showing a very good agreement between the data and the best-fit model.

observations of 1000 sec have been carried out in the L′ band with ten different AT baselines, ranging from 8 m to 112 m, on successive nights at the moment when ζ Lep crosses the local meridian. After calibration of the instrumental leakage, a signal-to-noise ratio (SNR) of $\sim$ 90 on the dust emission is reached for each observation.

Three disk parameters (luminosity ratio, inner radius and density power-law) have been fitted to the observations, together with the stellar diameter. The result of the fit is displayed in Figure 5.5, together with the simulated data and related 1-σ error bars. The quality of the fit is quite good, as demonstrated by the reduced χ^2 of 0.57 and the low residuals, shown at the bottom of the figure. The best-fit parameters are very close to the theoretical ones, with relative errors comprised between 0.5 and 2.5% (compare Figure 5.5 with the input parameters of Table 5.1).

Simulated observations in the N band

Because background subtraction techniques have not been thoroughly investigated in the N band, we do not have a realistic model for the residuals after background subtraction. In the following discussion, we have thus assumed that the residuals are negligible with respect to other noise sources, which is obviously a strong limitation to the validity of the results. Realistic simulations will only be possible when the advanced subtraction techniques discussed in Section 3.4.3 have been tested and validated on the sky. The results presented here must therefore be regarded as optimistic.

Six observations of 1000 s have been carried out in the N band with the six different UT-UT baselines on successive nights at the moment when ζ Lep crosses the local meridian. Even with only 10% accuracy on the calibration of the instrumental leakage, a signal-to-noise ratio of 450 on the dust emission is reached for each observation, thanks to the influence of instrumental errors in the N band and to reduce

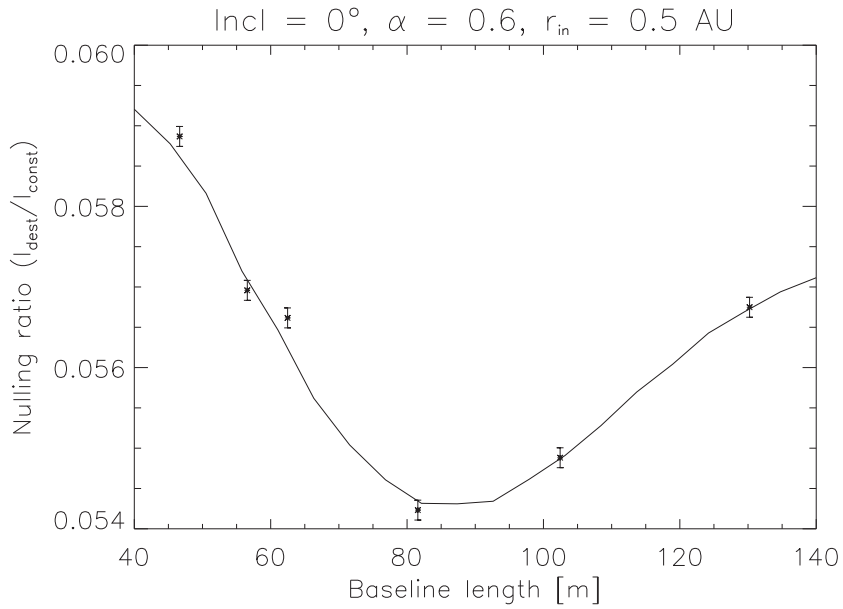

Figure 5.6: Simulated N band observations of ζ Lep with GENIE, using the six available UT-UT baselines at the VLTI. Each observation of 1000 sec gives an SNR of 450 (in the whole N band). The solid line represents the best-fit model, whose parameters are listed in Table 5.2.

	Model	Best fit	Error (1σ)
$L_{\rm dust}/L_\star$	1.7e-4	1.7022e-4	0.0017e-4
α	0.6	0.645	0.025
$r_{\rm in}$ [AU]	0.5	0.5025	0.003

Table 5.2: Parameters of the best-fit model adjusted to the observed nulling ratios for ζ Lep in the N band (see Figure 5.6).

the large collecting area of the 8-m UTs. Figure 5.6 shows the observed nulling ratios together with their 1-σ error bars.

Three disk parameters (luminosity ratio, inner radius and density power-law) have been fitted to the observations. Because the contribution of the star to the total nulling ratio is quite small (about 7×10^{-4}), we were not able to fit the stellar diameter together with the disk parameters, and simply subtracted geometric leakage from the data using a model for the stellar diameter. The best-fit parameters for the disk are listed in Table 5.2, together with the theoretical ones, showing weak deviations. Note that, even with our optimistic assumption, the errors on the morphology parameters α and $r_{\rm in}$ are of the same order as in the L′ band. This is due in part to the smaller range of baselines and to the lower angular resolution in the N band.

5.1.4 Influence of the grain size and composition

In this section, we investigate the influence of grain size and composition, using the 3D disk model of Augereau et al. (1999). Realistic observations have been simulated, but here we have not tried to retrieve the input parameters by a fitting procedure, because the 3D model is very slow and therefore not appropriate for such a task. Each individual observation consists of a 1000 s exposure on the science target when its crosses the local meridian, followed by the observation of the calibration star (η Lep) to evaluate and subtract the contribution of instrumental leakage. The simulations have been obtained in the L′ band, and the final nulling ratios take into account both the contributions of the disk and the star

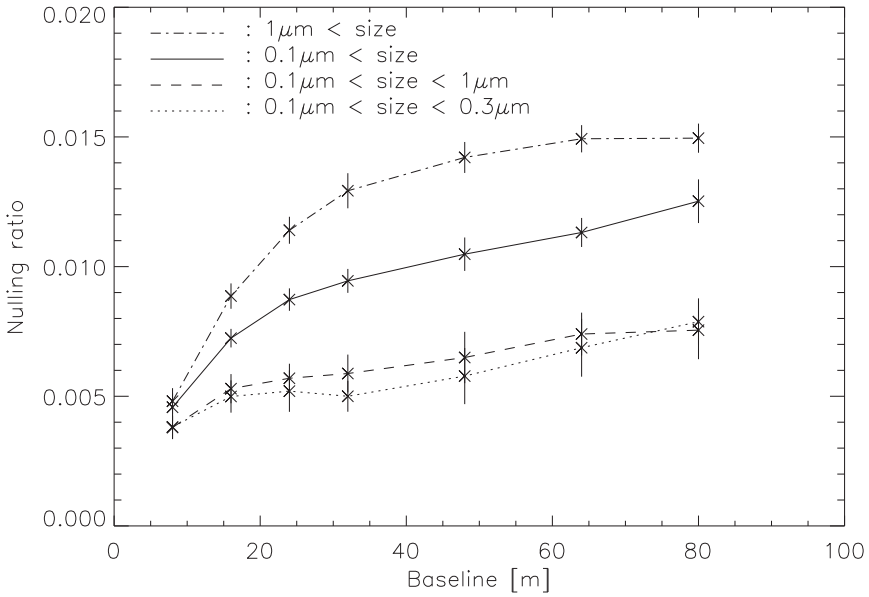

Figure 5.7: Influence of the size distribution of dust grains on the observed nulling ratio with GENIE, using different AT-AT baselines. Error bars take into account all noise sources including calibration processes. The disk is supposed to be face-on.

(geometric leakage).

We have first investigated the influence of the size distribution of the dust grains, taking four possible ranges for their sizes: 1 μm – 1 cm, 0.1 μm – 1 cm, 0.1 μm – 1 μm and 0.1 μm – 0.3 μm, using the same power law for all distributions ($dn(a) \propto a^{-3.5}da$). The evolution of the sublimation radius as a function of grain size has already been shown in Figure 5.2: small grains are more susceptible to sublimation, inducing larger inner radii for the last two cases. The result of the simulation, displayed in Figure 5.7, shows a great sensitivity of the nulling data to the grain size distribution when varying the baseline. We first remark that the larger the grains, the larger the nulling ratio. In fact, it is the total L′ band flux of the disk which is larger for larger grains. This is due to the fact that we have fitted the disk SED to the observed mid-infrared excess, while grains of different sizes do not have the same infrared colours for their thermal emission. In particular, small grains have a prominent silicate emission feature around 10 μm. Such an effect can therefore only be detected by multi-wavelength studies, and is not directly related to the influence of the nulling instrument.

A more interesting effect is the high sensitivity of the nulling ratio to the baseline length for large grains. This is related to the fact that the thermal emission from large grains is more concentrated in the stellar neighbourhood so that, at short baselines, the central dark fringe partially cancels the thermal emission from these grains. We also see that the nulling ratio reaches a local maximum when the baseline becomes large enough so that the first bright fringe coincides with the bright inner rim of the disk. This happens at a 80 m baseline for the largest grains and at a 24 m baseline for the smallest grains. After the local maximum, the nulling ratio continues to increase as the fringe pattern shrinks and reaches a second local maximum at $3\lambda/2b = r_{\rm in}$ (second bright fringe on the inner rim, i.e., around 70 m for the smallest grains). The simulations show that the different size distributions can easily be discriminated thanks to the small error bars, except for the last two models which have in fact very similar distributions.

Secondly, we have studied the influence of the grain type, using either astronomical silicate or cold coagulation grains. For an equivalent geometric cross section, porous grains are less effective than silicate grains to re-emit their thermal radiation, because their optical constants are closer to those of

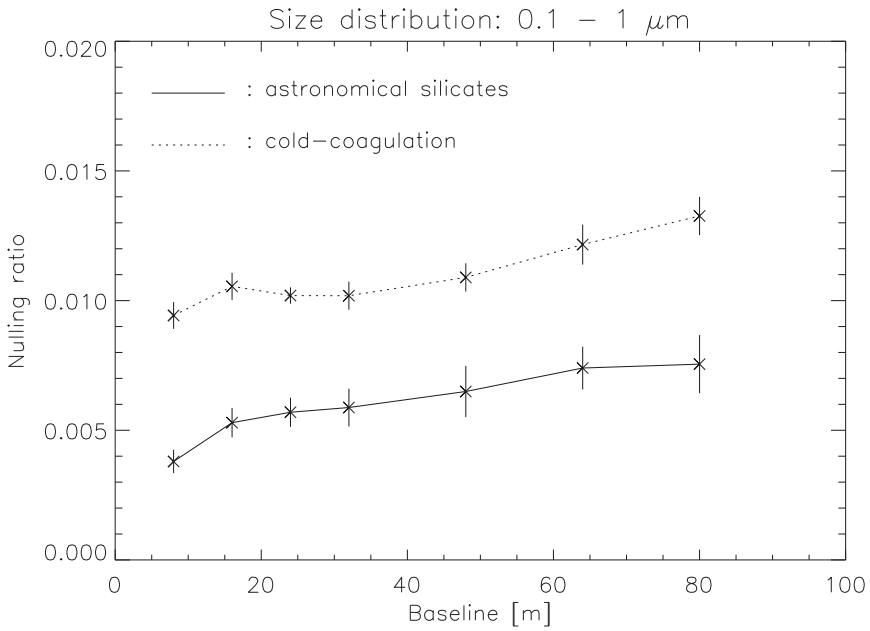

Figure 5.8: Influence of the physical composition of the dust grains on the observed nulling ratio. Cold-coagulation grains are highly porous and thus more efficiently heated. The inner rim is therefore shifted outwards in this case.

vacuum. For this reason, and due to their different compositions, the two types of grains produce thermal emissions with different colours. In the particular case illustrated in Figure 5.8 (size distribution ranging between 0.1 μm and 1 μm), this leads to an increased L′-band flux for coagulation grains with respect to the pure silicate grains. The nulling curve is thus translated upwards. A second effect comes from the better resistance of silicate grains to sublimation than coagulated grains due to their compact nature. The thermal emission is therefore more concentrated close to the star in the case of silicate grains, with possibly a smaller inner radius (depending on the actual size distribution). This effect can be clearly seen in the case of small grains (Figure 5.8), for which the first maximum in the nulling ratio is obtained for a smaller baseline in the case of porous grains than silicate grains. This means that the first bright fringe reaches more rapidly the inner rim of the disk as the baseline is increased, revealing a larger inner rim in the case of porous grains.

We have finally studied the influence of the scattered emission on the observed nulling ratio, in order to assess the error that would be made if only the thermal emission was taken into account. The actual contribution of the scattered emission is indeed of only a few percent, so that its expected contribution to the nulling ratio is quite small. However, its spatial distribution is significantly more extended than the thermal emission. This is illustrated in Figure 5.9, for an almost edge-on disk (10° from edge-on). For this reason, the scattered component can have a significant effect on the nulling ratio for edge-on disks: the nulling ratio presented in Figure 5.3 would show a weaker dependence to the baseline angle in the case of the edge-on disk ($i = 90°$) if scattered emission was taken into account. The magnitude of the effect strongly depends on the scattering efficiency of the dust grain, i.e., on their size and composition.

5.1.5 Conclusions

Future observations of inner debris disks around Vega-type stars with a nulling interferometer such as GENIE will allow basic morphology parameters such as inclination, inner radius, surface density distribution, etc., to be retrieved with a very high precision. This precision is in fact a few orders of magnitudes

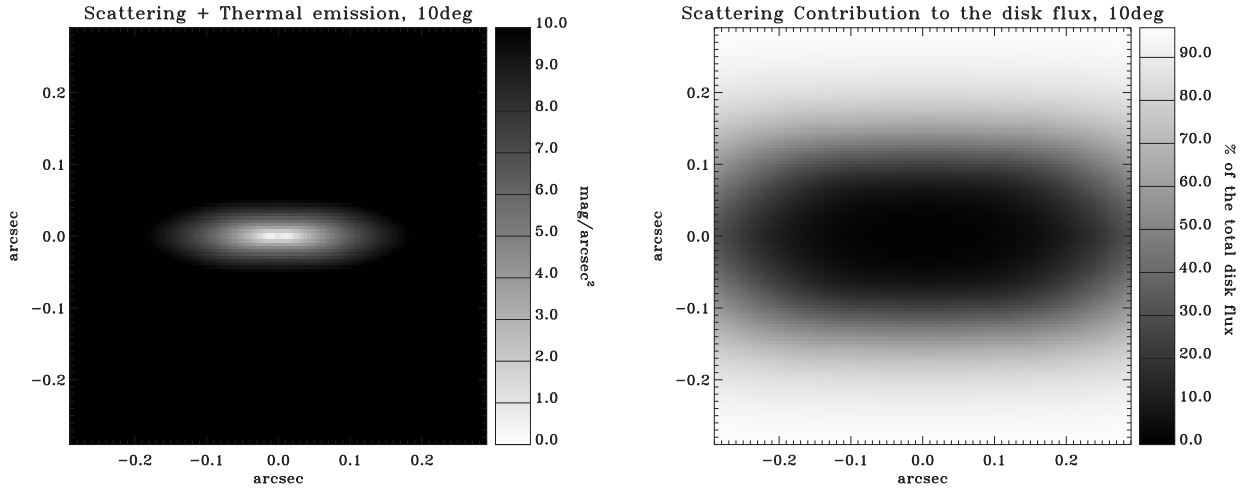

Figure 5.9: Left: spatial distribution of the total emission from the disk, assumed to be inclined by 10° with respect to edge-on (logarithmic scale). Right: distribution of the scattered emission only, showing that it mostly arises from the outer regions of the disk. Courtesy of J.-C. Augereau.

better than what is achievable with current instruments, which have been mostly unsuccessful in determining the infrared luminosity and morphology of the inner part of the debris disk. Nulling instruments will thus largely improve our understanding of the dynamical processes at play in planetary systems, both in their early and late formation phases. The possible presence of gaps due to the formation of planets could probably be inferred. Moreover, the nulling data are also sensitive to the size distribution of the dust grains, which will give critical information on the replenishment processes happening in these second-generation dust disks. In particular, one could infer to origin of the dust grains (cometary, asteroidal or interstellar medium) based on this piece of information.

It must also be noted that the spectral resolution capabilities foreseen in an instrument like GENIE ($R \leq 1000$) will be another significant source of information, which has not been investigated here. The wavelength-dependence of the dust emission will provide further information on the dust size and composition.

5.2 Spectroscopy of hot Extrasolar Giant Planets

The study of hot Extrasolar Giant Planets (EGPs) has been early identified as one of the most compelling scientific applications of GENIE, yet one of the most challenging. The angular resolution of GENIE in the L′ band ($\lambda/2b \sim 2$ mas) makes it appropriate for studying the thermal emission emanating from short period planets heated up to about 1000 K due to the proximity to their parent star (see Table 5.3). From the detection of the thermal emission of hot EGPs with low-resolution spectroscopy, their surface temperature will be deduced, allowing for their evolutionary state and the energy redistribution mechanisms to be investigated. Moreover, the detection of spectral bands associated with molecular species such as water, methane or carbon monoxide (see Figure 7.1) will provide crucial information on the atmospheric photochemistry and further improve our understanding of these bodies (cloud condensation, temperature profile, etc). The rationale for performing low-resolution spectroscopy on hot EGPs is further discussed in Section 7.1.1.

The capability of GENIE to detect and characterise hot EGPs as been evaluated by den Hartog et al. (2004, 2006) using the GENIE simulation software. In this section, we summarise the main outcome of these studies.

5.2.1 Classical detection method and calibration issues

The basic EGP detection method follows the steps presented in Section 5.1.2. Geometric stellar leakage is removed based on its analytical expression, while instrumental leakage is estimated through the observation of calibration stars. In both cases, a critical parameter influencing the quality of the subtraction is the stellar angular diameter, which must be accurately known for both the target and calibration stars.

To illustrate the potential of the "classical" detection method, we have chosen seven relatively nearby stars known to host hot EGPs with estimated temperatures comprised between about 750 K and 1600 K (see Table 5.3). The effective temperature of the planets is computed on the basis of a radiative balance with the star, assuming a Bond albedo of 0.1 as proposed by Baraffe et al. (2003) in the case of HD 209458b (see Section 7.2.1 for more information on the EGP models). In the following discussion, we will take a planetary radius of $1.2\,R_{\rm Jup}$ for all the hot EGPs listed in Table 5.3, which represents the mean radius for seven planets studied by photometric transits (Burrows et al. 2004). The knowledge of the ephemeris of the extrasolar planetary systems allows for an optimised observation, when the star-planet system is aligned with the baseline and as close a possible to its maximum angular separation. Even at maximum angular separation, the longest available baseline (130 m) is generally necessary to resolve the star-planet system.

Table 5.3 summarises the expected SNR on the seven targets for 4 hours of observation with two 8-m UTs under standard Paranal atmospheric conditions, assuming various accuracies on the knowledge of the target star angular diameter. Based on surface brightness relationships, it is expected that a typical accuracy of 0.5 to 1% can be achieved on the determination of stellar diameters for nearby solar-type main sequence star. The table demonstrates that GENIE can generally detect EGPs with an SNR better than 3. If a series of observations during consecutive nights are combined as illustrated in Figure 5.10, the SNR per observation may in fact be lower while still providing sufficient confidence in the planetary detection. Qualitatively, the SNRs are maximum for planetary systems located at about 30 pc. This results from the competing actions of shot noise and geometric leakage calibration noise: the relative contribution of shot noise increases linearly with the distance of the system, while the relative contribution of calibration noise decreases as the square of the distance (assuming that the same accuracy can be obtained on stellar angular diameters at all distances).

The SNRs presented in Table 5.3 have been obtained by integrating the signal over the whole L′ band. However, the penalty from dispersing the signal into a few spectral channels is not large in most

	Star		Planet			$b_\perp$	SNR vs. diameter accuracy			
Name	Type	d [pc]	a [AU]	a [mas]	$T_{\rm eff}$ [K]	[m]	0.25%	0.5%	1%	1.5%
HD 73256b	G8V	36.5	0.037	1.01	1224	129	12.9	10.4	6.7	4.8
HD 83443b	K0V	43.5	0.040	0.92	1137	128	6.3	6.0	5.3	4.4
HD 179949b	F8V	27.0	0.040	1.48	1580	102	17.5	9.0	4.5	3.0
τ Boo b	F7V	15.0	0.046	2.95	1518	61	13.7	6.8	3.4	2.3
HD 75289b	G0V	28.9	0.046	1.59	1385	127	20.8	10.8	5.5	3.7
HD 162020b	K2V	31.3	0.072	2.30	765	129	12.1	9.8	6.4	4.5
HD 130322b	K0V	29.8	0.088	2.95	767	124	13.0	9.2	5.3	3.6

Table 5.3: Stellar and planetary parameters for the seven chosen planetary systems. The semi-major axis a of the orbit is given in AU and in mas. The latter defines the angular separation between the two bodies at maximum elongation. The SNR levels obtainable after 4 hours of integration time with two UTs is then given for different levels of stellar diameter accuracy. The UT-UT baseline has been optimised for each target. The longest baseline (UT1-UT4) is required in most cases, so that the projected baseline $b_\perp$ is generally close to 130 m.

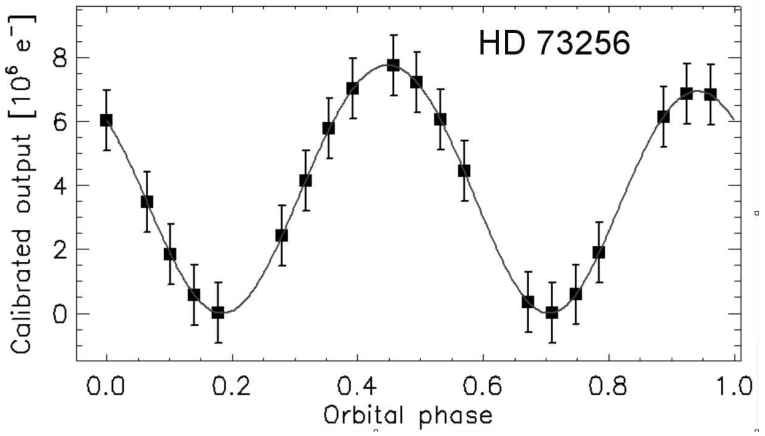

Figure 5.10: Illustration of the expected results after 20 consecutive nights of observation on HD 73256b, assuming a sub-optimal estimate of the stellar diameter ($\Delta\theta_\star/\theta_\star = 1\%$).

cases, because the dominant source of noise generally comes from the calibration of stellar leakage, which is proportional to the detected signal and therefore independent of the spectral resolution. As long as calibration noise is dominant, dispersing the signal over several channels does not significantly reduce the SNR. However, the ratio of signal to shot noise increases as the square root of the number of spectral channels, so that spectral resolution cannot be increased indefinitely. From Table 5.4, it appears that low resolution spectroscopy ($R \simeq 20$) will be feasible on most systems.

According to our estimates, the capability of GENIE to characterise EGPs looks promising, and should open up the spectroscopic survey of hot EGPs with temperatures down to about 700 K. The main limitation of GENIE regarding EGP detection does not really come from the faintness of the planetary signal, but rather from the imperfect suppression of stellar light. This is not surprising, as the distance between the star and its planet is so small (typically ten stellar radii) that the fringe spacing cannot be chosen wide enough to efficiently dim the star. The estimation and subsequent subtraction of stellar residuals is therefore a critical issue, which can potentially be mitigated by using more advanced observation methods as discussed below.

5.2.2 Perspectives: OPD modulation and colour-differential techniques

The first method that was investigated to mitigate the calibration issues is based on OPD modulation. This technique, proposed by D'Arcio et al. (2004), consists in applying a variable optical path difference

	Number of spectral channels					
Name	4	8	16	32	64	128
HD 73256	5.2	4.2	3.2	2.3	1.4	0.7
HD 83443	3.0	2.2	1.5	1.1	0.6	0.3
HD 179949	4.5	4.4	4.3	4.2	3.7	2.6
τ Boo	3.4	3.4	3.4	3.4	3.4	3.4
HD 75289	5.4	5.3	5.2	4.9	4.2	2.8
HD 162020	4.9	3.9	3.0	2.1	1.3	0.7
HD 130322	4.6	4.0	3.2	2.4	1.5	0.8

Table 5.4: Average SNR level per spectral channel for the detection of planetary emission in 4 hours of integration time, using various levels of spectral dispersion. The stellar diameter accuracy assumed here is 1%.

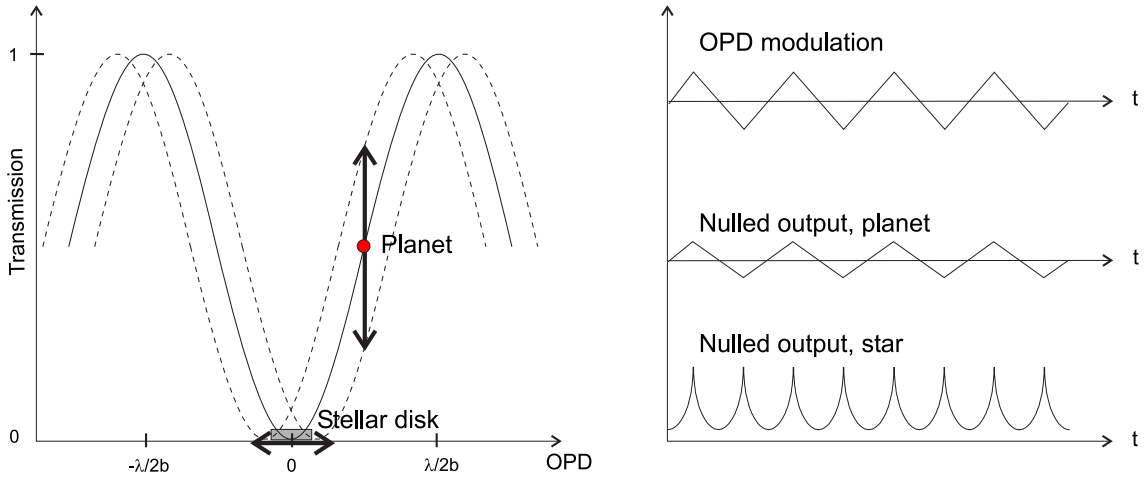

Figure 5.11: Planet detection with an OPD-modulated Bracewell nulling interferometer. The transmission pattern sweeps back and forth around its rest position (zero OPD). At the planet location, the transmission varies synchronously with the applied modulation while at the star location, the transmission varies quadratically with the applied modulation.

between the beams of the nulling interferometer in order to modulate the output signals at various frequencies. A small OPD dither at frequency f will modulate the stellar leakage at frequency $2f$, since leakage does not depend from the sign of the OPD. On the other hand, a planet transiting a quasi-linear portion of the transmission map (i.e., half-way between a crest and a trough) will induce a signal at frequency f at the nulled output, which can be extracted by coherent detection techniques (see Figure 5.11). This technique is particularly attractive for two-telescope nulling interferometers, for which other modulation techniques cannot be implemented.

At first, OPD modulation seems to be an attractive way to mitigate the problem of calibration for EGP detection by ground-based nulling interferometers. Its potential has therefore been assessed in the context of the GENIE instrument by den Hartog et al. (2004), suggesting that an SNR $\sim$ 100 could be achieved on a bright EGP such as τ Boo b. However, a major drawback to this detection method was soon discovered: the presence of a planet close to the star in the field of view will offset the phase of the fringes detected by the fringe sensor by an amount equivalent to the ratio of the total flux of the planet to that of the star. The photocentre of the star-planet system is slightly offset in the direction of the planet with respect to the centre of the stellar disk, in such a manner that if at one excursion in OPD an extra amount of planetary light is detected, the opposite excursion will cause an extra amount of stellar light to arise. It can be shown that, if fringe sensing is performed at the same wavelength as the scientific observation, the effects will exactly compensate and no modulation will be obtained at all.

Even though fringe tracking is performed in the H and K band in the case of GENIE, additional phase sensing will be performed in the L′ band to monitor phase fluctuations due to water vapour (see Section 4.2.1) and to ensure a good co-phasing at the wavelength where the observations are actually carried out. As a result, OPD modulation will be essentially inefficient in the case of GENIE, and other techniques have to be investigated.

One of the most promising techniques currently considered for the detection of EGPs with stellar interferometers is based on the wavelength dependence of the stellar and planetary spectra. This technique, called colour-differential interferometry (Chelli & Petrov 1995), is already implemented in classical interferometers such as AMBER or MIDI at VLTI where it relies on the wavelength variation of the visibility and/or the phase of the interferometric fringes. One of its main advantages is that the chromatic differences in visibility and phase are much less sensitive to instrumental and atmospheric instabilities, and therefore easier to calibrate. It should allow both AMBER and MIDI to detect the thermal

emission from a few hot EGPs (Millour et al. 2006; Schuller et al. 2003).

In the context of nulling interferometry, the attractiveness of colour-differential observations lies in the avoidance of the calibration of physical and instrumental leakage, which provides a strong limitation as discussed in detail in the previous section. Removing the calibration terms also implies that the SNR can be further improved by longer integration. In practice, the method will consist in fitting the destructive output signal with a model based on the constructive output plus a planetary spectrum. The stronger the planetary spectrum differs from the stellar spectrum, the easier it will be to exploit the spectral differences between destructive and constructive outputs to fit a planetary spectral model. The advantage of GENIE with respect to AMBER and MIDI is twofold. First, the reduction of the stellar light enhances the contribution of the planetary spectrum in the final output and also reduces the shot noise associated with stellar light. Second, GENIE will control in real time the chromatic OPD errors, one of the major sources of noise in colour-differential interferometry. The high instrumental stability of GENIE should be another improvement with respect to current instruments. Differential techniques should thus allow GENIE to achieve its full potential, and reach a shot-noise limited SNR of a few tens on bright EGPs. Further investigations are needed to evaluate the actual performance of this technique.

6

Potential of nulling interferometry in Antarctica

Contents

6.1 The Antarctic plateau as an astronomical site 116

6.1.1 Atmospheric turbulence at Dome C 117

6.1.2 Water vapour, sky transparency and sky brightness 119

6.1.3 The potential gain for interferometry 121

6.2 ALADDIN: an optimised nulling interferometer 121

6.2.1 The interferometric infrastructure 121

6.2.2 The nulling instrument 122

6.3 Preliminary performance study at Dome C 123

6.3.1 Expected performance for the baseline design 123

6.3.2 Influence of the accuracy on stellar angular diameters 127

6.3.3 Influence of integration time 127

6.3.4 Influence of pupil diameter 129

One of the main limitations of ground-based nulling interferometers is related to the influence of atmospheric turbulence, as demonstrated in Section 4.2.1. Active compensation of the harmful effects of turbulence requires real-time control systems to be designed with challenging performance. The choice of a good astronomical site with (s)low turbulence is therefore of critical importance. In this respect, recent studies suggest that the high Antarctic plateau might be the best place on Earth to perform high-resolution observations in the infrared domain, thanks to its very stable atmospheric conditions. In this chapter, we investigate the performance of a nulling interferometer optimised for the detection of exozodiacal disks at Dome C, on the high Antarctic plateau. We show that an optimised nulling interferometer operating on a pair of 1-m class telescopes located about 40 m above the ground could achieve better detection performance than a similar instrument working with two 8-m telescopes at a temperate site such as Cerro Paranal. Dome C can thus be considered as "halfway to space".

6.1 The Antarctic plateau as an astronomical site

The Antarctic plateau has long been recognised as a high-quality site for observational astronomy. In fact, the South Pole has already been exploited as an astronomical site for more than ten years, mainly in the sub-millimetric and infrared domains where the low temperature and low water vapour content bring a substantial gain in sensitivity. For instance, the polarisation and anisotropy of the Cosmic Microwave Background have been studied with great detail (Kovac et al. 2002; Kuo et al. 2004). However, the high velocity winds experienced at South Pole do not provide good enough turbulence conditions to perform high-resolution observations in the infrared. The construction of a French-Italian station at Dome Concordia (75°S, 123°E), located on a local maximum of the Antarctic plateau (3250 m), has recently opened the path to new and exciting astronomical studies (Candidi & Lori 2003). Dome C was originally selected for glaciological reasons: more than 3000 metres of layered ice have a great potential for long time paleoclimatic reconstruction. But it was soon discovered that this location was also among the best regarding atmospheric conditions. Its main peculiarity with respect to South Pole is that it resides on top of the plateau, where katabatic winds have not yet acquired a significant velocity nor a large thickness by flowing down the slope of the plateau (Figure 6.1).

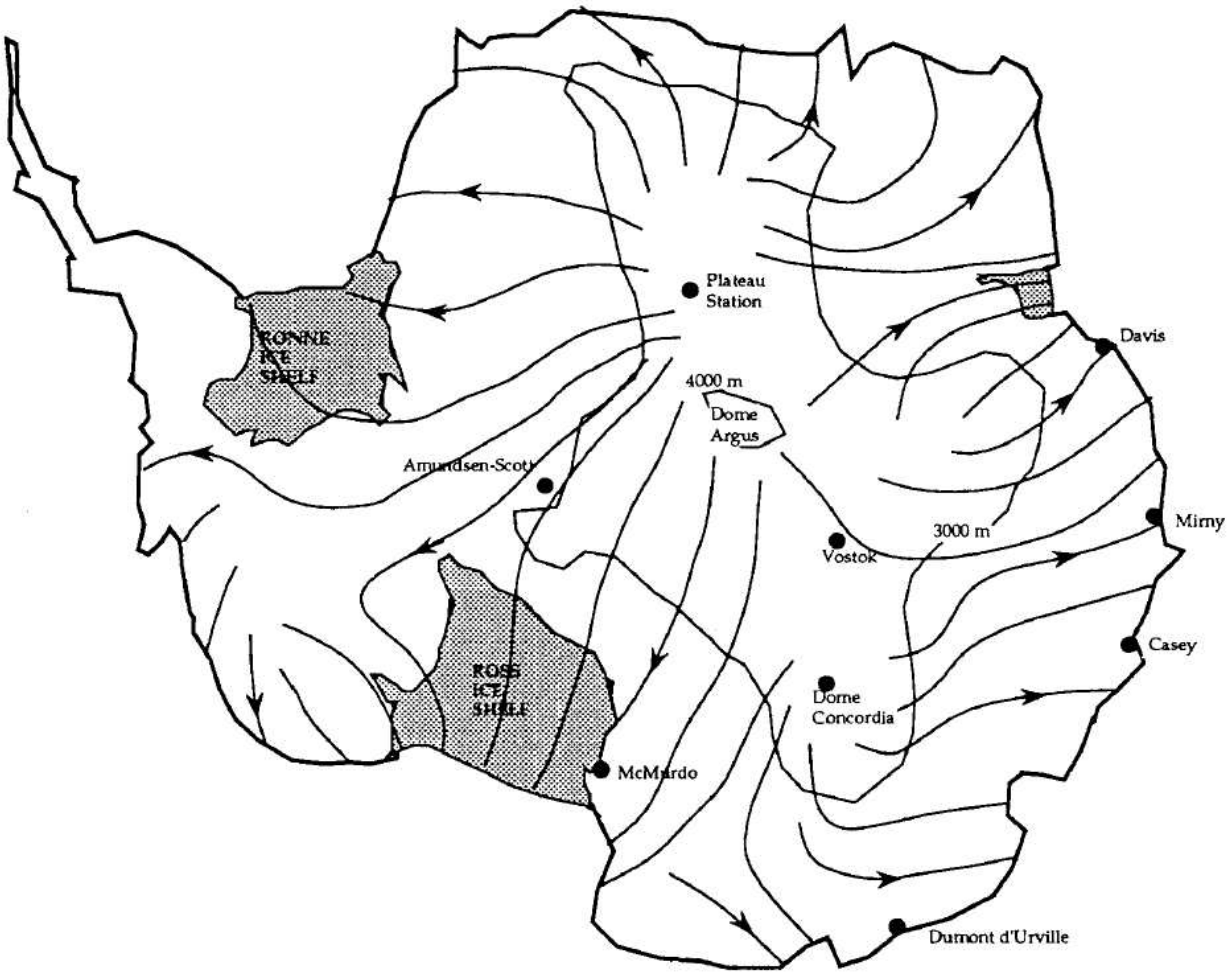

Figure 6.1: General topography of the Antarctic continent and direction of the katabatic winds, adapted from Marks et al. (1999). Wind speed is very low at the peaks of the plateau where the wind originates (2.9 m/s in average at Dome C) and increases as the cold air flows down the hill (5.5 m/s in average at the Amundsen-Scott South Pole station).

6.1.1 Atmospheric turbulence at Dome C

Intensive site characterisation at Dome C has begun during the austral summer 2002–03, with the installation of a Differential Image Motion Monitor (DIMM, Vernin & Munoz-Tunon 1995) for seeing measurements. Thanks to the darkness of the Antarctic sky, DIMM observations have been performed during daytime for the first time by Aristidi et al. (2003), giving a first estimate of the seeing conditions. A median seeing of 1.20 arcsec was then measured, not as good as expected. It was soon discovered that the black coating of the telescope produced strong local turbulence due to the heating by the Sun. Similar measurements with a white telescope provided better results during the following summer campaigns (Aristidi et al. 2005a), with a median seeing of 0.55 arcsec (better than the seeing at Cerro Paranal and Mauna Kea during nighttime). Additionally, an interesting behaviour has been discovered: the best seeing conditions (0.4 arcsec or better) generally happen in the mid local afternoon (Figure 6.2). At this moment, the discontinuity of the temperature gradient observed around 200 m disappears and is replaced by a standard surface inversion layer of about 30 m. An isothermal temperature profile is thus observed in the mid-afternoon, resulting in low turbulence in the boundary layer. The excellent seeing obtained during this transition indicates that the atmosphere above is producing very little turbulence.

During the summer 2004–05 campaign, the presence of two DIMMs observing simultaneously at two different heights (3 m and 8 m above the snow surface) allowed the investigation of the surface layer contribution to the seeing (Aristidi et al. 2005a). Figure 6.2 shows the behaviour of the seeing measured at the two heights as a function of local time. Almost half of the ground turbulence is concentrated into the first 5 m above the surface, confirming that the free air seeing (above the ground layer) must be exceptionally low. The measurement of a very large isoplanatic angle (6.8 arcsec) further confirms this statement, as this parameter is almost insensitive to ground-layer turbulence.

In parallel with the DIMM experiment, the Automated Astrophysical Site Testing International Observatory (AASTINO, Lawrence et al. 2003) was deployed at the Concordia station in January 2003. In its first version, AASTINO could only evaluate the atmospheric turbulence by means of a SODAR, an acoustic radar that measures the distribution of turbulence in the atmospheric layer comprised between 30 and 900 m above the ground. This instrument had already been used to measure the turbulence profile at South Pole (Travouillon et al. 2003), showing that turbulence was mostly confined to a boundary layer sitting below 270 m. This behaviour could be explained by the horizontal katabatic wind whose

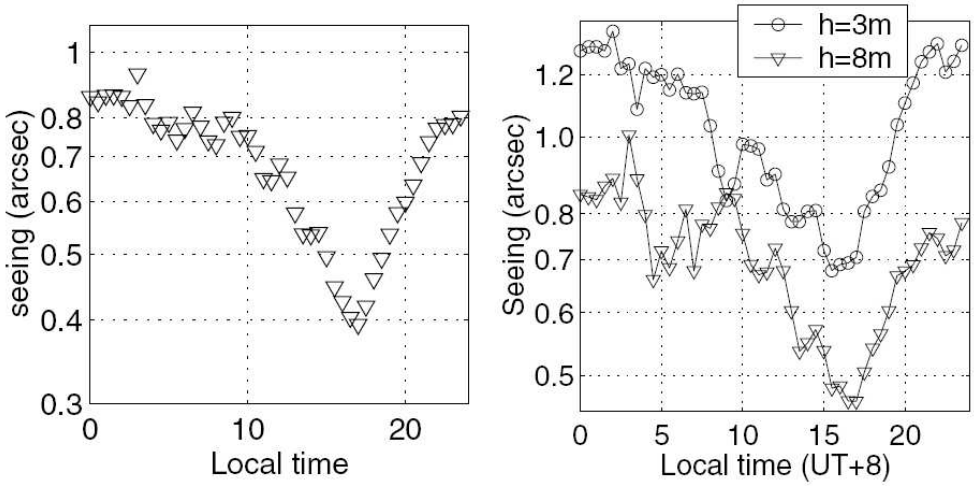

Figure 6.2: Left: seeing versus local time (hours), averaged over the 2003–04 and 2004–05 campaigns. Seeing values, obtained from the DIMM at elevation $h = 8$ m, were binned into 30-min intervals. Right: seeing versus time in 2004–2005 for the two DIMMs. Taken from Aristidi et al. (2005a).

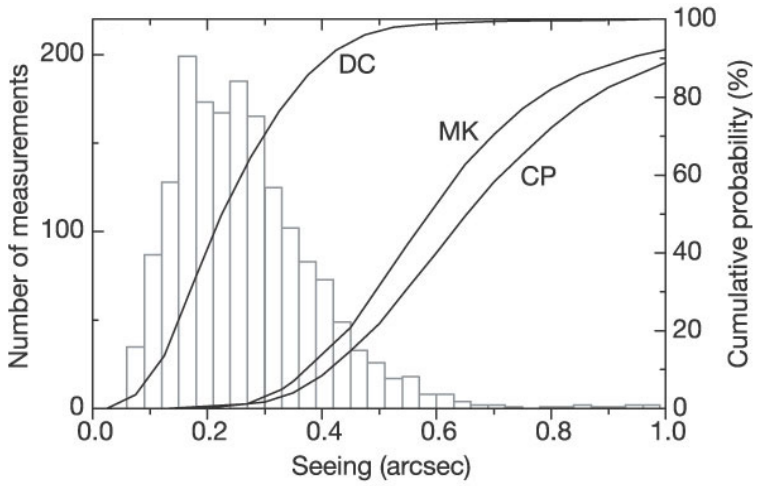

Figure 6.3: Histogram of Dome C seeing above 30 m from MASS combined with SODAR, and cumulative distributions of seeing at Dome C (DC), Mauna Kea (MK) and Cerro Paranal (CP). Adapted from Lawrence et al. (2004).

altitude profile closely matches the turbulence profile. Since January 2004, AASTINO also features a Multi-Aperture Scintillation Sensor (MASS, Kornilov et al. 2003) to evaluate vertical refractive index fluctuation profiles from the spatial/temporal structure of single star scintillation. It must be noted that the MASS is insensitive to seeing below about 500 m. The use of both instruments in automated mode during wintertime in 2003 and 2004 has confirmed the exceptional quality of the atmospheric conditions at Dome C. Lawrence et al. (2004) report a median seeing of 0.27 arcsec above 30 m (Figure 6.3), with a best seeing of 0.07 arsec (lowest value ever recorded on Earth). The isoplanatic angle θ_0 and coherence time τ_0 were also derived from MASS measurements, with average values of 5.7 arcsec and 7.9 msec respectively.[14] However, it must be noted that the derivation of the coherence time from MASS measurements is not yet fully validated. In any case, both isoplanatic angle and coherence time are largely better than in any other ground-based site.

In 2005, the first winter-over mission at Dome C has allowed DIMM measurements and balloon-borne thermal measurements to be obtained for the first time during the long Antarctic night. Preliminary results are reported by Agabi et al. (2006), and further confirm the two-layered structure of atmospheric turbulence at Dome C. A 36 m high surface layer is responsible for 87% of the turbulence, while the very stable free atmosphere has a median seeing of 0.36 ± 0.19 arcsec above 30 m. The ground seeing is quite large, resulting in a total seeing of 1.9 ± 0.5 arcsec. In addition to the two DIMMs located 3 m and 8 m above the ground, a third seeing monitor has recently been placed onto the roof of the calm building of Concordia, at an elevation of 20 m. Micro-thermal sensors have also been placed at various altitudes on a 32-m tower. The results from these new experiments should soon provide a better characterisation of the turbulent ground layer. Future improvements of the AASTINO will also focus on the ground layer with sonic anemometers and lunar scintillation measurements (Storey et al. 2005).

In addition to direct measurements of turbulence, wind speed measurements have been performed at Dome C for two decades by an automated weather station, while balloon-borne weather sondes have been used to characterise the wind profile in summertime starting 2000. Wind speed is a crucial parameter determining the rate at which the turbulence pattern is blown across the aperture of a telescope. Aristidi et al. (2005b) report a median ground speed of 2.9 m/s for the wind at Dome C, the lowest wind speed recorded at any major astronomical site with the exception of Maidanak (Uzbekistan). Wind speed profiles taken by balloon-borne sondes also show that the whole atmosphere is exceptionally calm with

[14] For comparison, the corresponding values at Cerro Paranal are $\theta_0 = 2.5$ arcsec and $\tau_0 = 3.3$ msec.

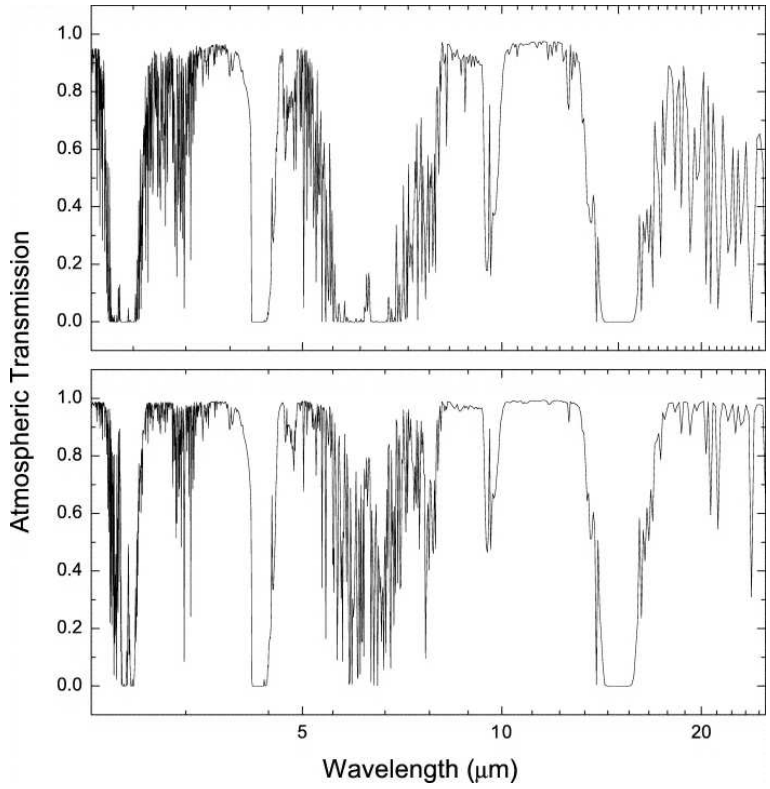

Figure 6.4: Atmospheric transmission in the near- and mid-infrared at Mauna Kea (top) and on top of the high Antarctic plateau (bottom), as estimated by Lawrence (2004).

respect to temperate sites. The presence of the circumpolar vortex above Dome C during particular periods of the year might could however be a significant source of turbulence at an altitude of 20 km. Thanks to the low wind speed above Dome C, the atmospheric turbulence is quite slow, as confirmed by the large coherence time of 7.9 msec (Lawrence et al. 2004).

6.1.2 Water vapour, sky transparency and sky brightness

Another critical parameter for infrared observations is the water vapour content of the atmosphere. On one hand, it strongly influences the sky transparency as a function of wavelength, and on the other hand, its temporal fluctuation is an important source of noise for infrared observations. The water vapour content of the Antarctic atmosphere has been measured at South Pole by radiosonde, giving an exceptionally low average value of 250 μm during austral winter (Chamberlin et al. 1997; Bussmann et al. 2005), where temperate sites have typically a few millimetres of precipitable water vapour (PWV). This is mainly due to the extreme coldness of the air, with a ground-level temperature of about $-61°$C (212 K) at the South Pole during winter,[15] which induces a low saturation pressure for water vapour. An even lower PWV content is expected at Dome C, with an estimation of 160 μm by Lawrence (2004). The first benefit from such a low water vapour content is to widen and improve the overall transmission the infrared atmospheric windows. Based on a line-by-line radiative transfer model, Lawrence (2004) has estimated the infrared transmission on top of the Antarctic plateau (Figure 6.4), showing in particular an extension of the K band up to 2.5 μm and of the L band from 2.9 to 4.2 μm. The transmission of the M band around 5 μm is also significantly improved.

The brightness of the infrared sky is also partially determined by the water vapour content, which

[15] Dome C is even colder during winter, with an average ground temperature of $-65°$C (208 K).

affects its wavelength-dependent emissivity factor. The other parameter determining the sky emission is its effective temperature, which depends on the altitude of the main opacity layer at a given wavelength. The effective temperature above South Pole has been measured by Chamberlain et al. (2000) in the mid-infrared, with values ranging from 210 K to 239 K depending on wavelength. Most of the winter sky background emission is in fact supposed to emanate from an atmospheric layer just above the temperature inversion layer, which it located between 50 and 200 m at Dome C (Chamberlain et al. 2000; Lawrence 2004). The atmospheric temperature at this altitude is about 230 K in wintertime (Agabi et al. 2006). As a result of both low temperature and low emissivity, the sky background is exceptionally low in Antarctica. The measurements obtained at South Pole show that is it reduced by a factor ranging between 10 and 100 in the infrared domain with respect to temperate sites. The largest gain is expected to happen in the K, L and M bands. It is estimated that a 1-m class telescope at Dome C would reach almost the same sensitivity as a 10-m class telescope at a temperate site at these wavelengths.

The very low water vapour content of the Dome C atmosphere has another important advantage in the context of high-precision infrared interferometry: longitudinal dispersion, created by the fluctuations of water vapour column density above the telescopes (see Section 4.2.1), is also greatly reduced. The standard deviation of PWV (σ_{PWV}) can be estimated at Dome C assuming that water vapour seeing follows the same statistics as piston, as suggested by Lay (1997). In that case, the standard deviation of PWV fluctuation depends on the Fried parameter r_0 viz. $\sigma_{\mathrm{PWV}} \propto r_0^{-5/6}$ according to Roddier (1981). Assuming that σ_{PWV} is also proportional to $\langle \mathrm{PWV} \rangle$, the average PWV content, the standard deviation of PWV at Dome C can then be obtained by relating it to the data obtained at temperate sites:

$$\sigma_{\mathrm{PWV}}(\mathrm{DC}) = \sigma_{\mathrm{PWV}}(i) \frac{\langle \mathrm{PWV} \rangle_{\mathrm{DC}}}{\langle \mathrm{PWV} \rangle_i} \frac{r_{0,i}^{5/6}}{r_{0,\mathrm{DC}}^{5/6}} \,, \tag{6.1}$$

where i represents a temperate site. The applications of this relation with the data of Cerro Paranal (Chile) or Mauna Kea (Hawaii) taken as a reference give very similar estimates of 1.00 and 0.91 μm for σ_{PWV} at Dome C (see Table 6.1), using a conservative average PWV content of 250 μm for Dome C by analogy to the South Pole measurements. For this calculation, we assumed a seeing of 0.27 arcsec, which is valid only above 30 m (Lawrence et al. 2004). Using this value is recommended in the present case for two reasons: on one hand, it is expected that the telescopes will be placed on top of towers, above the turbulent ground layer, and on the other hand, the study of Bussmann et al. (2005) shows that most of the PWV is concentrated between 200 m and 2 km above the ground, so that water vapour seeing should hardly be affected by the ground layer.

In addition to low water vapour content, the Antarctic atmosphere is also characterised by a low aerosol/dust content, a rare presence of clouds or snowfall, moderate auroral activity, and no light pollution. All these characteristics further confirm the high quality of Dome C as an astronomical site.

Site	r_0	$\langle \mathrm{PWV} \rangle$	σ_{PWV}	References
Cerro Paranal	14.5 cm	3 mm	27 μm	Meisner & Le Poole (2003)
Mauna Kea	17.8 cm	1.6 mm	11 μm	Colavita et al. (2004)
Dome C	38.2 cm	250 μm	1.0 μm	Bussmann et al. (2005)

Table 6.1: Water vapour seeing at three astronomical sites. The Fried parameters r_0 are given at 500 nm, adapted from the values of Racine (2005). References for the PWV data are given in the last column. The standard deviation of water vapour seeing at Dome C is deduced from the data at Cerro Paranal and Mauna Kea following Equation 6.1.

6.1.3 The potential gain for interferometry

The appropriate parameter to characterise a site in the context of interferometry is the coherence volume, which defines the quantity of photons that can be added during a "coherent" fringe detection. This volume is defined as a cylinder with a base $\propto r_0^2$ related by the Fried parameter and a height $c\tau_0$ equal to the product of the coherence time and the speed of light. Using the values reported by Lawrence et al. (2004) for these parameters ($r_0 = 38.2$ cm in the visible and $\tau_0 = 7.9$ msec), the coherence volume $c\tau_0 r_0^2$ at Dome C is estimated to be 17 times larger than at Cerro Paranal. This result, which is valid at all wavelengths, means that 17 times more photons are available at Dome C to perform interferometric measurements!

The total gain in sensitivity for a nulling infrared interferometer should also take into account the significant reduction of the background emission, which is generally the major source of shot noise as stellar light is largely reduced by the nulling process. All in all, the estimated gain in sensitivity for an L-band nulling interferometer is about 400 with respect to a temperate site such as Cerro Paranal.

If the ability to cover the whole sky plane using natural guide stars was included in the computation of the gain, the coherence volume should also take into account the isoplanatic angle, thereby defining the coherence hypervolume $c\tau_0 r_0^2 \theta_0^2$. The total gain in the efficiency of interferometric studies would then reach about 2000 in the L band.

6.2 ALADDIN: an optimised nulling interferometer

Based on the quality of Dome C as an astronomical site and on the potential gain for interferometry, several interferometric projects have been proposed in the last few years for an implementation at Dome C, such as the Antarctic Planet Interferometer (API, Swain et al. 2004) or the Kiloparsec Explorer for Optical Planet Search (KEOPS, Vakili et al. 2005). Another concept is the Antarctic L-band Astrophysics Discovery Demonstrator for Interferometric Nulling (ALADDIN, Coudé du Foresto et al. 2006), a recent proposal emanating from a consortium of French, German and Belgian laboratories, which has been studied during the present thesis. This project can be seen as an adaptation of the GENIE project to the Antarctic conditions, as ALADDIN is based on the same concept (a Bracewell interferometer working in the L band) and focuses on the same objectives (demonstration of nulling interferometry and detection of exozodiacal disks). The ALADDIN project has recently been submitted to ESA as a possible alternative to the GENIE instrument, which could potentially outperform GENIE thanks to the favourable atmospheric conditions at Dome C and thanks to the optimised design of the interferometric facility.

6.2.1 The interferometric infrastructure

One of the main difficulty with the ALADDIN interferometer is that it should be placed about 40 m above the ice surface in order to benefit from the exceptionally low turbulence of the free air above the boundary layer. The concept proposed here consists in a 40 m long rotating truss installed on top of a 40 m tower and on which are placed two moveable off-axis siderostats (Figure 6.5). Such a design has two main advantages: thanks to the rotating truss, the baseline can always be chosen perpendicular to the line of sight so that long delay lines are not needed, and thanks to the moveable siderostats, the baseline length can be optimised to the observed target. The available baseline lengths range from 4.3 to 30 m and provide a maximum angular resolution of 10 mas in the L band, which is largely sufficient to study the habitable zone around typical Darwin/TPF-I target stars (see Figure 8.11).

In this preliminary version of the ALADDIN design, the diameter of the siderostats has been set

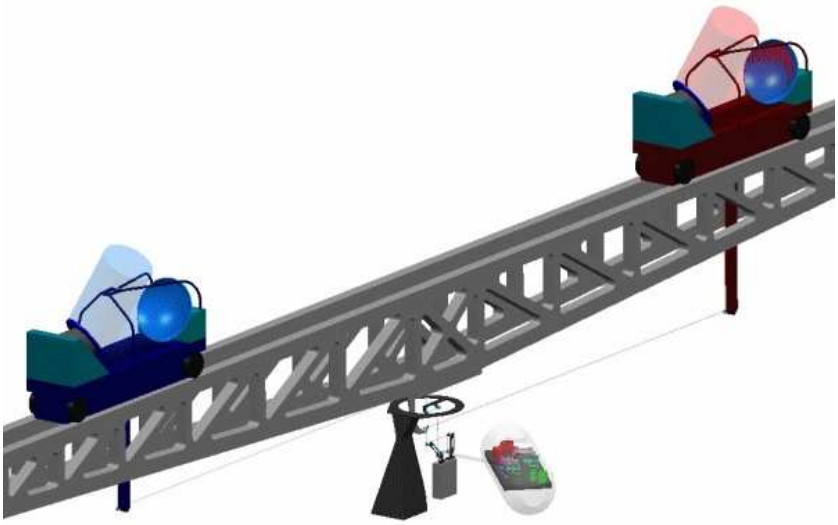

Figure 6.5: Overview of the ALADDIN infrastructure as proposed by Alcatel Alenia Space (M. Barillot, P. Courteau) in collaboration with Observatoire de Paris (V. Coudé du Foresto), Max-Planck Institut für Astronomie (M. Swain) and Université de Liège (O. Absil). The light beams collected by the two off-axis siderostats are derorated and sent towards the on-ground nulling instrument via an optical train composed of 10 mirrors (including siderostats).

to 1 m, which is expected to provide similar performance to 8-m telescopes at a temperate site. Only ten reflections are required to lead the light from the sky down to the instrument, which is placed on the ground and does not need to be rotated with the truss thanks to the optical train which derotates the beams. All relay mirrors are at ambient temperature, i.e., about 210 K during wintertime. The harmful influence of ground-layer seeing is mitigated by propagating compressed beams about 18 mm in diameter, i.e., smaller than the typical Fried parameter.

Building the ALADDIN infrastructure requires additional effort with respect to installing the nulling instrument at the ESO VLTI, but this effort is largely compensated by the many simplifications at the level of the instrument, as described below.

6.2.2 The nulling instrument

The design of the nulling instrument is directly inherited from the GENIE phase-A study as ALADDIN is foreseen to operate in the same wavelength regime (the extended L band). It comprises the same basic functionalities as described in Sections 3.4 and 4.2.1, except for two critical control loops that are not needed any more as we will demonstrate in the performance study. On the one hand, ALADDIN can be operated without dispersion correction thanks to the very low water vapour seeing, provided that the observing waveband is restricted to the $3.1 - 4.1\ \mu$m region; on the other hand, intensity control is not required any more since the size of the collectors is significantly smaller than the Fried parameter in the L band, which is about 4 m. Only the fringe tracking system and two fast tip-tilt servo loops are required to co-phase and balance the beams. They are expected to be operated at lower repetition frequencies thanks to the slowness of atmospheric turbulence. This represents a very significant simplification with respect to the GENIE instrument.

The whole instrument, which is fixed on the ground, is supposed to be enclosed in a cryostat, in order to improve its overall stability and to mitigate the influence of temperature variations at the ground level (the mean temperature during austral summer is about 40°C higher than during winter, while the instrument is supposed to be operated during the whole year). The lower temperature of the optics

Atmospheric parameters		Instrumental parameters	
Fried parameter r_0 at 500 nm	38 cm	Baseline	4.3 – 30 m
Equivalent seeing	0.27″	Diameter	1 m
Coherence time τ_0	7.9 msec	Waveband	3.1 – 4.1 μm
Equivalent wind speed	15 m/s	Ambient temperature	210 K
Outer scale L_{out}	100 m	Cryogenic temperature	77 K
Sky temperature	230 K	Total warm throughput	80%
Mean PWV content	250 μm	Total warm emissivity	20%
Standard deviation of PWV	1 μm rms	Total cold throughput	10%
Pressure	640 mbar	Fringe sensing	K band
		Tip-tilt sensing	J band

Table 6.2: Atmospheric and instrumental parameters for the performance simulation of ALADDIN. The atmospheric parameters assume the instrument to be located 40 m above the ground level. Note that the equivalent wind speed is integrated over the whole turbulence profile above 40 m.

inside the cryostat (77 K) also further decreases the background emission produced by the instrument. Enclosing the nulling instrument in a cryostat is facilitated by its smaller size as compared to GENIE.

6.3 Preliminary performance study at Dome C

In this section, we use the GENIEsim software to estimate the performance of ALADDIN at Dome C. Thanks to the versatility of the simulator, only a few input parameters had to be changed with respect to the GENIE instrument. These changes include the atmospheric transmission (Lawrence 2004), the removal of the dispersion and intensity control loops, as well as the atmospheric and instrumental parameters listed in Table 6.2. It must be noted that the performance of ALADDIN can be modelled with greater confidence than for GENIE as it does not rely on the nominal performance of an external system such as the VLTI.

6.3.1 Expected performance for the baseline design

Before discussing the global sensitivity of the instrument, let us investigate the performance of individual control loops and check whether they are required or not.

Control loop performance

Because dispersion and intensity control are not expected to be required in the case of ALADDIN, we have disabled these two control loops in the GENIEsim software when simulating the residual atmospheric turbulence experienced at beam combination. The simulation results are presented in Table 6.3, where the absence of dispersion and intensity control is represented by a 0 Hz repetition frequency. For these simulations, we have used either the “worst case scenario” or the “best case scenario” for atmospheric turbulence. The former does not take into account pupil averaging for piston and dispersion and thus assumes a logarithmic slope of $-8/3$ at high frequencies for the power spectral densities of these two quantities, while the latter takes into account pupil averaging and thus has a $-17/3$ logarithmic slope at high frequency (see Section 4.2.1). The rationale for introducing the worst-case scenario is that the $-17/3$ has never been observed to our best knowledge (most probably due to instrumental limitations), while spurious instrumental effects might potentially increase the high-frequency content of

	Worst case	Best case	Goal
Piston	13 nm @ 4 kHz	9.5 nm @ 2 kHz	< 4 nm
Inter-band dispersion	7.5 nm @ 0 Hz	7.5 nm @ 0 Hz	< 4 nm
Intra-band dispersion	7.9 nm @ 0 Hz	7.9 nm @ 0 Hz	< 4 nm
Tip-tilt	6.4 mas @ 1 kHz	6.4 mas @ 1 kHz	(see mismatch)
Intensity mismatch	1.2% @ 0 Hz	1.2% @ 0 Hz	< 1%
Total null	3.5×10^{-4}	2.8×10^{-4}	1.7×10^{-4}
Instrumental null	1.8×10^{-4}	1.1×10^{-4}	10^{-5}
rms null	1.3×10^{-4}	1.2×10^{-4}	10^{-5}

Table 6.3: Control loop performances and optimum repetition frequencies (0 Hz means that no control loop is used) as simulated on a 100 sec Observation Block (OB). The observations are carried out in the extended L band for a G0V star located at 20 pc using the basic design of ALADDIN and a baseline of 24 m. The target performance discussed in Section 4.2.1 appears in the last column. The total null is the mean nulling ratio including both the geometric and instrumental leakage contributions. The last line gives the standard deviation of the instrumental nulling ratio for this 100 sec OB.

piston. It must be noted that the power spectrum of higher order Zernike modes (tilt and above) remains the same in both scenarios and takes into account pupil averaging.

The results listed in Table 6.3 confirm that two critical control loops (dispersion and intensity) are not required any more: the input atmospheric perturbations for these two quantities are in fact already marginally compliant with the requirements. A second important conclusion is that fringe tracking can be carried out at a much lower frequency than in the case of GENIE, where a typical frequency of 20 kHz was required. Finally, it must be noted that the two models for atmospheric turbulence provide similar results. This comes from the fact that the actual shape of the power spectral density does not have any influence on the global fluctuation of the quantities that are not subject to real-time control, and also from the fact that the cut-off frequency $f_2 \simeq 0.3v/D$ at which pupil averaging becomes dominant (see Section 4.2.1) is significantly higher than in the case of GENIE due to the reduced pupil diameter D.

It must be emphasised that the big advantage of ALADDIN with respect to GENIE mainly comes from the improved feasibility of the concept, which avoids two critical control loops and reduces the repetition frequency of the remaining ones. The overall nulling performance, on the other hand, is only improved by a factor ranging between 1 and 4 depending on the assumptions on atmospheric turbulence (compare with Table 3 in Section 4.2.1), so that the global nulling performance of ALADDIN is still a factor ∼10 above the requirement. This shows that the calibration of instrumental stellar leakage is still required to reach our goal in terms of sensitivity (20-zodi level).

Estimated sensitivity

Using the parameters of Table 6.2, we have simulated the detection performance of ALADDIN in the case of exozodiacal disks, using the zodiacal disk model of Kelsall et al. (1998) as usual. The simulations take into account the same calibration procedures as presented in Section 4.2.1 in the context of GENIE. Four hypothetic targets, representative of the Darwin star catalogue, have been chosen for this performance study: a K0V at 5 pc, a G5V at 10 pc, a G0V at 20 pc and a G0V at 30 pc. The integration time has been fixed to 30 min as in the case of GENIE. Unless specified, we have assumed the diameters of the target stars to be known with an accuracy of 1% (conservative assumption) and we have used the "worst case scenario" for atmospheric turbulence with the $-8/3$ logarithmic PSD slope at high frequencies. As demonstrated in Table 6.3, using the "best case scenario" would not significantly change the final results.

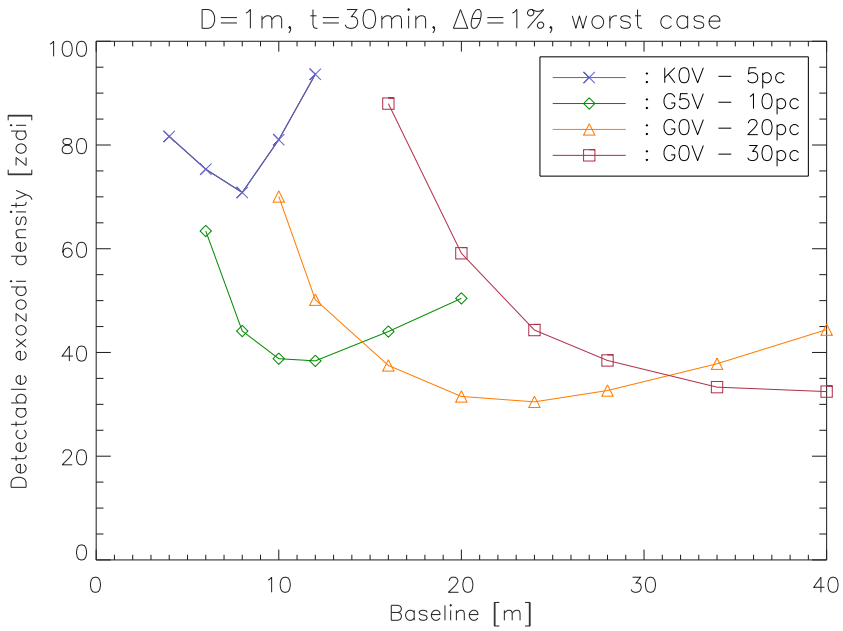

Figure 6.6: Simulated performance of ALADDIN in terms of exozodiacal disk detection for four typical Darwin targets. The basic design for ALADDIN was used here (see Table 6.2), assuming an integration time of 30 min, an accuracy of 1% on the knowledge of the stellar angular diameter, and using the worst-case scenario for atmospheric turbulence (see text).

In Figure 6.6, we present the results of the simulation in terms of detectable exozodiacal level as a function of baseline length. As in Section 4.2.1, the threshold for detection is set at a global signal-to-noise of 5, including calibration residuals for background and for geometric and instrumental stellar leakage. This figure shows that the optimum baseline for studying typical Darwin target stars is comprised between about 8 and 40 m, which closely matches the baseline range offered by ALADDIN.

It must be noted that, with its 1 m class telescopes, ALADDIN significantly outperforms GENIE for the same integration time (see Table 6.5 for a thorough comparison). This fact is not only due to the exceptional atmospheric conditions, but also to the optimisation of ALADDIN both regarding the available baselines and the instrumental design. It must be acknowledged that if the 8 m Unit Telescopes of the VLTI were movable, placed some 40 m above the ground and connected to the nulling instrument by only 10 optical reflections, and if the GENIE instrument was entirely enclosed in a cryostat, the performance improvement of ALADDIN with respect to GENIE would significantly shrink and probably disappear.

Choice of the optimum baseline

From our simulations, a general rule-of-thumb can be inferred for the choice of the optimum baseline. This choice is directly related to the size of the habitable zone around the target stars, where Darwin will search for Earth-like planets. According to Kasting et al. (1993), the position of the habitable zone expressed in AU is given in good approximation by the following formula:

$$r_{\mathrm{HZ}} = \left(\frac{T_\star}{T_\odot}\right)^2 \frac{R_\star}{R_\odot} \,, \tag{6.2}$$

which gives a position of 0.68, 0.85 and 1.16 AU for a K0V, a G5V and a G0V star respectively. The angular size of the habitable zone is compared to the angular resolution provided by the optimum baseline

	K0V 5 pc	G5V 10 pc	G0V 20 pc	G0V 30 pc
Optimum baseline	8 m	12 m	24 m	40 m
Angular resolution $\lambda/2b$	46 mas	31 mas	15 mas	9 mas
Habitable zone θ_{HZ}	135 mas	85 mas	58 mas	39 mas
Radius for $T = 800\ K$	17 mas	10 mas	7 mas	4.8 mas

Table 6.4: Comparison of the angular resolution of the optimum baseline to the characteristic size of the habitable zone of the target systems. The angular position for which the thermal emission of blackbody dust grains would peak at the observing wavelength is also given.

in Table 6.4. We also give the angular distance from the star at which blackbody dust grains would reach a temperature of 800 K and would thus have their thermal emission peaking at the centre of the extended L band (around 3.6 μm). The table shows that the first bright fringe of the optimised nulling interferometer is always located between these two reference locations. The ratio between the optimum angular resolution and the size of the habitable zone is typically around 0.3. The second bright fringe of the transmission pattern will thus generally coincide with the location of the habitable zone.

Ground-level performance

Before further investigating the performance of ALADDIN as a function of various parameters, let us estimate the gain that is obtained from placing the instrument above the boundary layer. For that purpose, we use the ground-level wintertime seeing conditions recently reported by Agabi et al. (2006): a median seeing of 1.9 arcsec (i.e., a Fried parameter of 5.4 cm at 500 nm) and a coherence time of about 2.9 msec. It must be noted that the latter is very poorly constrained, and that the value measured above the boundary layer by Lawrence et al. (2004) should also be regarded as possible (7.9 msec).

One of the main limitation of ground-level observations comes from the fact that the Fried parameter in the L band (~57 cm) is now smaller than the size of the apertures, so that multiple speckles are formed in the image plane. The use of adaptive optics would thus be recommended to ensure a good injection efficiency into the waveguides. Using only tip-tilt control at 1 kHz, which provides a residual tip-tilt ranging between 30 and 70 mas depending on the assumption on the coherence time, the typical fluctuations of the relative intensity mismatch between the two beams would be about 20%, which is much too large to ensure a good instrumental nulling ratio. Another important limitation comes from the increased piston effect experienced by the interferometer. Assuming fringe tracking to be performed at a maximum frequency of 10 kHz, the residual OPD would range between 35 and 60 nm rms. Here again, a stable nulling ratio cannot be obtained under such conditions. On the other hand, longitudinal dispersion is not expected to increase so significantly since the precipitable water vapour content of the first 40 m of the atmosphere is relatively small due to the very low temperature right above the ice.

As a result, variability noise would become the main source of noise in the budget of a ground-level ALADDIN. The simulations performed with GENIEsim show that the sensitivity in the case of a G0V star located at 20 pc would only be about 100 zodi, instead of 30 zodi for the basic concept of ALADDIN installed on a 40-m tower. In order to match such performance at the ground level, unrealistically high repetition frequencies would be required for piston and tip-tilt control, as well as low-order adaptive optics (or intensity control) to stabilise the injection efficiency into the waveguides. Dispersion control might also be required. The conclusion is that placing the instrument above the ground layer is mandatory to obtain a significant gain on both the performance and feasibility aspects with respect to a instrument installed at a temperate site such as Cerro Paranal.

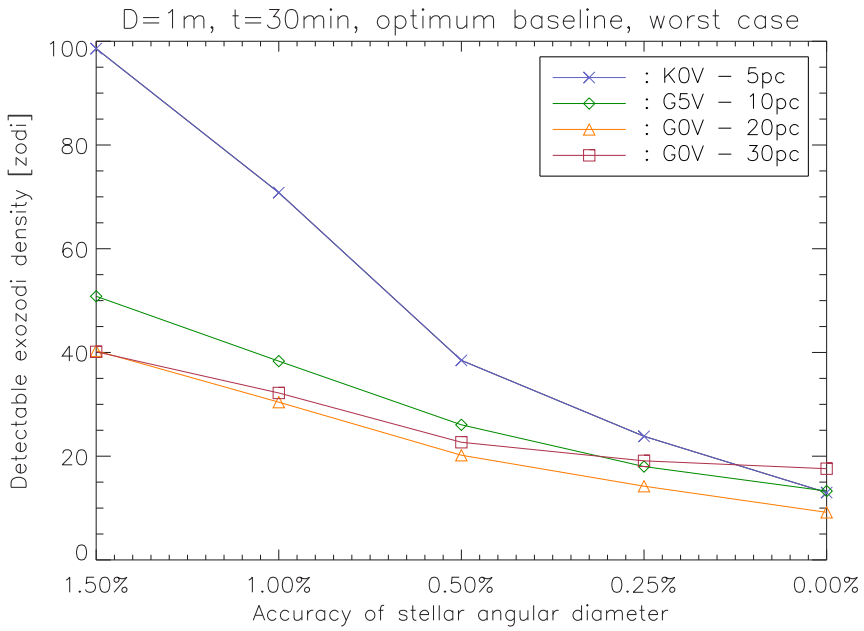

Figure 6.7: Simulated performance of ALADDIN in terms of exozodiacal disk detection for various assumptions on the accuracy with which the stellar angular diameter is known.

6.3.2 Influence of the accuracy on stellar angular diameters

An important parameter influencing the performance of a nulling interferometer is the accuracy with which the angular diameter of the target star is known ($\Delta\theta_\star$), as it is the main factor influencing the quality of calibration not only for geometric stellar leakage but also for instrumental stellar leakage, which relies on the estimation of the instrumental nulling ratio on a well-known calibration star. In Figure 6.7, we investigate the influence of this $\Delta\theta_\star$ parameter for the basic ALADDIN concept. This simulation shows that, similarly to GENIE, an improved accuracy on stellar diameters would largely improve the detection capabilities of ALADDIN.

The very good sensitivity obtained for a perfect accuracy on the stellar diameter gives an idea of the gain that could be achieved be using more complex nulling configurations, such as a Degenerate Angel Cross, which provides a θ^4 central transmission (see Section 3.4.2). The use of phase chopping with multi-telescope configurations would also have the same effect, as geometric stellar leakage would then be removed by the chopping process (see Section 8.1). Figure 6.7 shows that an advanced nulling interferometer at Dome C should be capable of reaching a sensitivity well below the 20-zodi level. Multi-telescope configurations are however not foreseen in the context of ALADDIN, for which simplicity is strongly advocated.

Table 6.5 compares the expected sensitivity of ALADDIN, operated on 1-m telescopes, with that of GENIE, using either 8-m Unit Telescopes or 1.8-m Auxiliary Telescopes. A significant gain, typically ranging between 2 and 3, is obtained with ALADDIN. The gain is all the larger when the target star is close, because the use of short baselines is very important for stars with relatively large angular diameters (~1 mas).

6.3.3 Influence of integration time

Another advantage of the ALADDIN concept is the ability to perform very long on-source integrations. The interferometer is assumed to be operated both during winter and summer, even though the summer-

Star	0.25%	0.5%	1%	1.5%	Instrument
K0V – 5pc	83	110	185	266	GENIE – AT
	107	215	430	645	GENIE – UT
	24	38	71	99	ALADDIN
G5V – 10pc	140	147	174	212	GENIE – AT
	29	56	112	167	GENIE – UT
	18	26	38	51	ALADDIN
G0V – 20pc	338	339	344	351	GENIE – AT
	23	37	69	102	GENIE – UT
	14	20	30	40	ALADDIN
G0V – 30pc	714	714	717	721	GENIE – AT
	38	48	77	109	GENIE – UT
	19	23	32	40	ALADDIN

Table 6.5: Comparison of the GENIE and ALADDIN performance expressed in detectable exozodiacal disk densities as compared to the solar zodiacal disk. Four different accuracies have been assumed for the knowledge of the target stars' angular diameter. The simulations are performed in the L band, which extends from 3.5 to 4.1 μm in the case of GENIE and from 3.1 to 4.1 μm in the case of ALADDIN. An integration time of 30 min is assumed in all cases.

time performance will be somewhat degraded due to the higher temperature of the sky and of the optical train, which produces a larger background emission. Long integrations are also enabled by the fact that ALADDIN is dedicated to the survey of exozodiacal disks, while GENIE would have to compete with other instruments at the VLTI (especially when using the Unit Telescopes). Therefore, we have investigated the gain in sensitivity that can be achieved by longer integrations. The computation of this gain is not trivial, as all the noise sources do not have the same time behaviour. For instance, shot noise, detector noise and variability noise have the classical $\sqrt{t}$ dependence, while the contributions of geometric and instrumental stellar leakage are proportional to time.

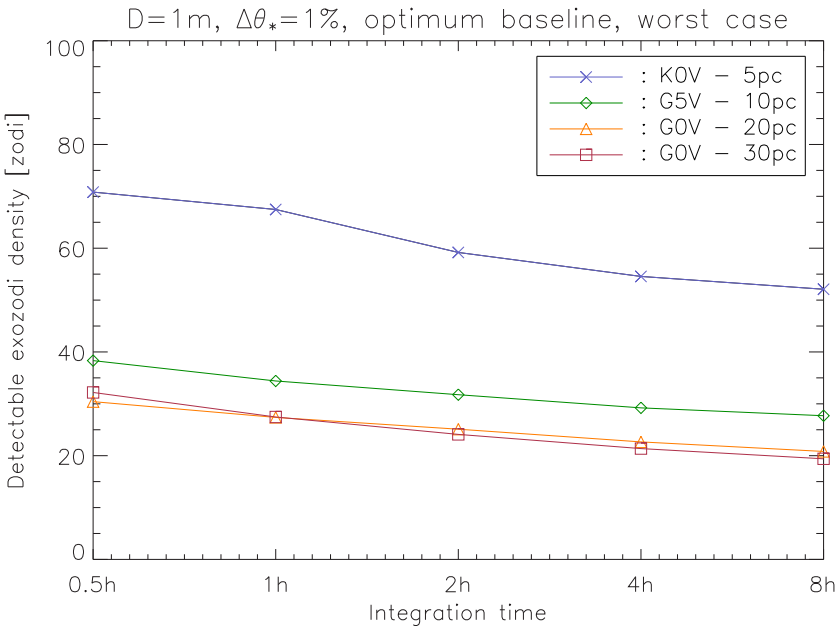

Figure 6.8: Simulated performance of ALADDIN in terms of exozodiacal disk detection for increasing integration times.

In Figure 6.8, we have simulated the sensitivity of ALADDIN as a function of integration time. Because increasing the integration time does not improve the accuracy of both geometric and instrumental stellar leakage calibration, which are among of the main contributors to the noise budget, the overall performance does not largely improve for long exposures. It must still be noted that the goal sensitivity of 20 zodi is reach after 8h for G0V stars at 20 and 30 pc.

A side effect of increasing the integration time is that the optimum baseline is decreased. For instance, the optimum baseline in the case of a G0V star at 20 pc is of 12 m for an 8h integration instead of 24 m for a 30 min integration. Shorter baselines allow for less exozodiacal light to make it through the transmission pattern, but also for a better cancellation of the stellar light. The result is an improved signal-to-noise ratio regarding stellar leakage calibration, while the relative increase of the shot noise contribution is compensated by the longer integration time. Reducing the optimum baseline is favourable to the overall feasibility of the concept, as it reduces the required size of the truss bearing the siderostats.

6.3.4 Influence of pupil diameter

Finally, in order to chose the most appropriate diameter for the ALADDIN siderostats, we study the influence of the collecting area on the sensitivity of the instrument. In order to keep the same design for the instrument, we restrict the pupil diameter to 2 m at most, as larger pupils would become comparable to the size of turbulent cells (about 4 m in the L band) and would therefore require either adaptive optics or additional intensity control to be implemented.

In Figure 6.9, we have simulated the performance of ALADDIN for three different sizes of the siderostats. By increasing the diameter from 0.5 m to 1 m, the performance is typically increased by 33%, while the gain in performance is about 25% when increasing the diameter from 1 m to 2 m. It must be noted that the performance of ALADDIN with 50-cm collectors is still better than that of GENIE at the VLTI. Reducing the size of the siderostats would thus make sense if the feasibility of the interferometer was found to be jeopardised by the requirement to put 1-m siderostats on a 40-m truss located 40 m above the ground. Increasing the integration times by a factor about 4 would then be required to achieve

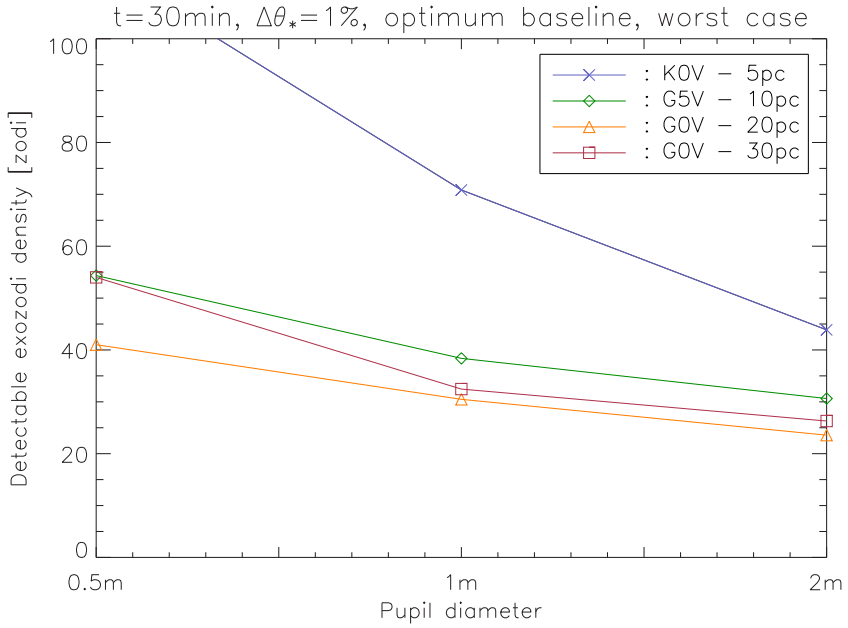

Figure 6.9: Simulated performance of ALADDIN in terms of exozodiacal disk detection for three different pupil diameters (50 cm, 1 m and 2 m).

similar performance with 50-cm collectors as with 1-m collectors. A longer integration time is in fact also required to decrease the optimum baseline down to an acceptable length, as 50-cm siderostats are associated with optimum baselines typically twice as large as for the original 1-m ones. In practice, the final choice of the collectors' diameter will result from a trade-off between feasibility, performance, integration time and available baselines.

Part III

The quest for extrasolar planets from space

7

Pegase: a space-based precursor to Darwin

Contents

7.1 Context and objectives of the Pegase space mission 134

7.1.1 Scientific objectives of Pegase 134

7.1.2 Overview of the Pegase design 137

7.2 The prime targets: hot Extrasolar Giant Planets 139

7.2.1 Modelling the infrared emission of EGPs 139

7.2.2 Observing scenario 143

7.3 Simulated performance of Pegase 146

7.3.1 Geometric stellar leakage and calibration issues 146

7.3.2 Instrumental stellar leakage and real-time control 147

7.3.3 The thermal background and its fluctuations 149

7.3.4 Total signal-to-noise ratio and target selection 151

7.3.5 Wavelength dependence of the signal-to-noise ratio 154

Pegase is an answer to the call for ideas from Centre National d'Etudes Spatiales (CNES) for a scientific payload onboard its formation flying demonstrator mission. It proposes a Bracewell interferometer focusing on the high-angular resolution study of low-mass companions and circumstellar disks in the near-infrared regime (2.5 – 5 μm). In this chapter, we investigate the detection capabilities of Pegase in the case of hot Extrasolar Giant Planets (EGPs). After a brief presentation of the overall design of the interferometer, we discuss the general properties of hot EGPs, estimate their thermal and reflected fluxes in the near-infrared and propose a general observing scenario for these targets. Based on this model, we compute the signal-to-noise ratio that can be achieved with Pegase on the currently known hot EGPs. We describe in detail the various contributors to the total noise budget and their preponderance as a function of instrumental performance and wavelength. We show that Pegase will be capable of characterising about 20 hot extrasolar planets with masses similar or larger than that of Uranus thanks to its high angular resolution, high dynamic range and low-resolution spectroscopy capabilities.

7.1 Context and objectives of the Pegase space mission

The French Space Agency (CNES) is currently considering the implementation of a space mission dedicated to the demonstration of formation flying with a foreseen launch between 2010 and 2012. The mission should include two or three free-flying spacecrafts based on the Proteus or Myriade buses (respectively mini- and micro-satellites). This mission aims at demonstrating the necessary technology for future major space missions based on formation flying such as Darwin, but should also include a scientific objective. In this frame, CNES has issued at the beginning of 2004 a call for ideas for a scientific payload on board this technology demonstration mission. In answer to the call for ideas, a consortium of European laboratories[16] lead by Institut d'Astrophysique Spatiale (IAS) has proposed a concept of an infrared space interferometer called Pegase, dedicated to the high angular resolution spectroscopic analysis of hot EGPs, brown dwarfs and circumstellar disks (Absil et al. 2004b). Pegase has been selected along with three other concepts for a phase-0 study which was performed at CNES during 2005. In this chapter, we focus on the studies that have been carried out by our consortium in answer to the call for ideas, and in particular on the demonstration that low-resolution spectroscopy of hot EGPs with Pegase is within reach.

7.1.1 Scientific objectives of Pegase

There are three main types of targets for the Pegase interferometer: hot Extrasolar Giant Planets (EGPs), brown dwarfs and circumstellar disks. The most compelling science goal, which is also the highest priority and the main design driver, is the spectroscopic study of extrasolar planets.

Hot extrasolar giant planets

By hot EGPs, we designate the giant extrasolar planets of Jupiter-type mass orbiting close to their parent stars (0.02 to 0.1 AU, i.e., orbital periods shorter than 10 days). About 37 such planets have been detected so far in our neighbourhood ($\lesssim$ 150 pc), generally by means of radial velocity surveys, which allow the characterisation of orbital parameters of the companion planet and the estimation of its mass through the product $M_p \sin i$. Four of these planets (HD 209456b, HD 189733b, HD 149026b and TrES-1) have also been characterised by the observation of the photometric drop as the planet transits in front of the stellar photosphere, giving an unambiguous access to the mass and radius of these planets. From this additional piece of information, one can constrain their nature, their evolution and some of their atmospheric properties (see e.g. Vidal-Madjar et al. 2003; Burrows et al. 2004; Charbonneau et al. 2006). The detection of the secondary eclipse can even provide some limited information on the thermal emission of these planets (Charbonneau et al. 2005; Deming et al. 2005). Similar results have been obtained on five giant planets detected by photometric transits farther out in the galaxy, at about 1500 pc from our solar system by the OGLE survey (Udalski et al. 2004). However, in order to improve our understanding of the physics of hot EGPs and to test atmospheric models, a spectroscopic study of their thermal and/or reflected radiation is mandatory.

There is a particular interest in studying the physics of hot EGPs because they have no equivalent in the solar system and because none of the planet formation theories had initially predicted their existence. These hot, highly irradiated objects are nowadays thought to have formed far from their central star and then to have migrated inwards, where they now have their rotation synchronously locked with their

[16] Namely: Institut d'Astrophysique Spatiale (Orsay), Observatoire de Paris, Observatoire de la Côte d'Azur (Nice), ONERA (Châtillon), Université de Liège, Alcatel Alenia Space (Cannes), Ecole Nationale Supérieure de Lyon, Observatoire de Grenoble, Observatoire de Genève and Instituto des Astrofisica de Canarias (Teneriffe).

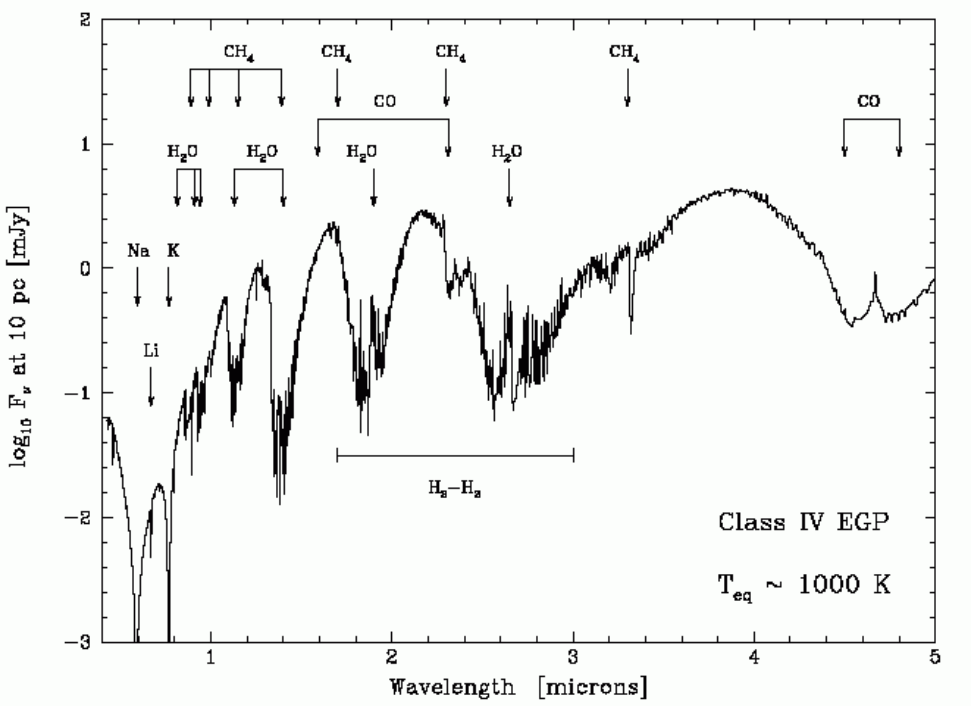

Figure 7.1: A first example of a synthetic spectrum for a hot EGPs, as simulated by Sudarsky et al. (2003) for an irradiated giant planet located at about 0.1 AU from its parent star and heated up to 1000 K. The high temperature does not allow for large methane absorption bands to form: most of the carbon resides in carbon monoxide.

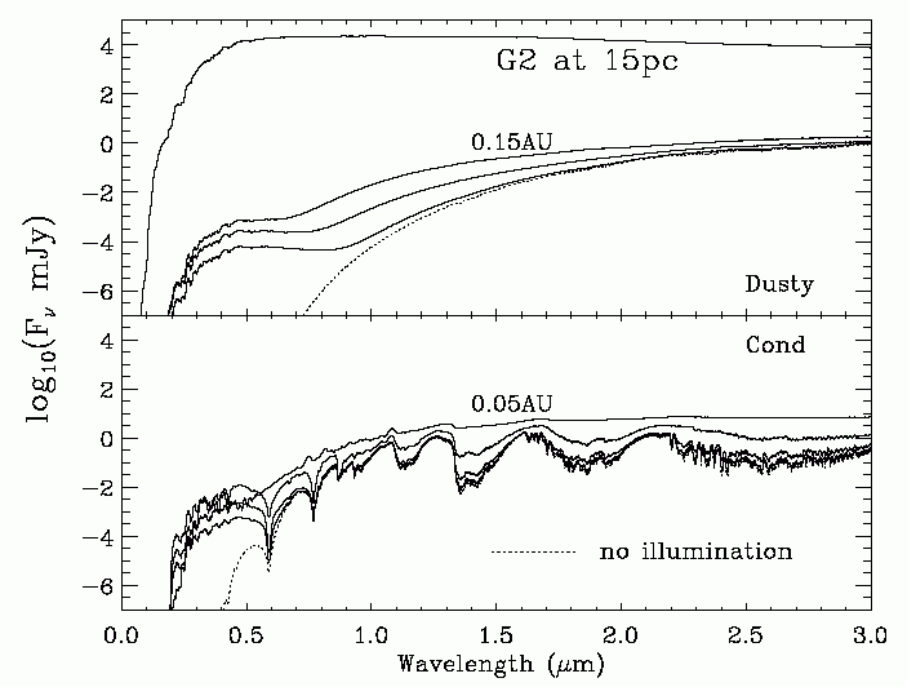

Figure 7.2: A second example of synthetic spectra for hot EGPs, as simulated by Barman et al. (2001) for two different atmospheric models. At the top of the plot, dust is supposed to have entirely settled, leaving "clear skies", while at the bottom of the plot settling is ignored so that dust contributes to the opacity. The planets have been placed respectively at 0.15, 0.25 and 0.5 AU from the star at the top, and at 0.05, 0.1 and 0.25 AU at the bottom of the plot.

revolution period. Most models predict them to be gaseous giants, but they usually diverge on many important aspects of atmospheric modelling, such as the presence of aerosols and dust, the condensation of clouds, the thermalisation between the irradiated and night hemispheres or the presence of high speed zonal winds. Figure 7.1 shows two examples of synthetic spectra for hot EGPs, predicting very different spectral features. The detection of spectral features associated with molecular species such as methane, carbon monoxide or water vapour would provide a considerable observational input to constrain these models.

Infrared spectroscopy in the 1−5 μm region is particularly interesting for hot EGPs because the contrast (typically ranging between 10^5 and 10^3) is lower than in the visible and above all because of the presence of important molecular species such as CH_4, CO and especially H_2O, which is impossible to detect from the ground because of atmospheric absorption. We will see in Section 7.1.2 that the Pegase waveband will actually be restricted to the 2.5 – 5 μm region mainly for technical reasons, but also because future ground-based projects will focus on the wavelengths below 2.5 μm. This domain does still allow the identification of the most important molecular species: H_2O around 2.6 μm, NH_3 around 3.0 and 4.0 μm, CH_4 around 3.3 μm and CO around 4.5 and 4.8 μm. Collision-induced absorption by H_2 can also potentially be detected between 2.5 and 3.0 μm. Moreover, this wavelength regime gives access to an almost unperturbed part of the continuum in the thermal emission, between roughly 3.5 and 4.3 μm, which allows for a good estimation of the planet equilibrium temperature.

Brown dwarfs

Although the mass distribution of stellar and sub-stellar objects is continuous, stars differ from planets by their formation process. In the standard model, stars form by gravitational collapse of a gas cloud, while planets form by accretion of a cloud of planetesimals. The limit between the two regimes is thought to be indicated by the very small number of bound objects with masses between 12 and 80 M_{Jup}, referred to as the brown dwarf desert (Forveille et al. 2004).

Provided that a large enough part of the infrared spectrum is accessible, the spectroscopic studies of brown dwarfs provide many constraints on their surface temperature, their radius, and the composition and structure of their atmosphere. Observing the scarce bounded brown dwarfs would have the advantage of giving an accurate estimation of the mass of the companion (thanks to the observation of the companion trajectory and the three Kepler's laws) and its age (thanks to the spectroscopic study of the parent star), compared to free flying objects where these parameters have to be estimated using theoretical models. However, the spectroscopy of these bounded low-mass objects is hampered by the generally large contrast with their parent stars. Pegase aims at providing the required angular resolution and dynamic range to study bounded brown dwarfs: the contrast between a Sun-like star and a brown dwarf typically ranges between 10^3 and 10^5 for a 1 Gyr-old system, which makes this kind of target well suited to Pegase. In addition, the study of brown dwarfs of various ages will help in constraining the evolution models of these objects.

Circumstellar disks

Protoplanetary disks belong to another group of objects for which high angular resolution combined with high dynamic range is needed. Their study directly relates to the planet formation processes. Pegase will bring precious information on such objects thanks to its high angular resolution and good spectral coverage in the near-infrared, in which both the reflected and thermally emitted radiations are accessible. Three main programmes will be carried out in the frame of circumstellar disks: the detection of gaps created by the formation of planets, the measurement of stellar winds and the study of accretion in the

stellar magnetosphere. Instead of classical visibility measurements as a function of the baseline, it is suggested to measure the visibility in spectroscopic mode (as a function of the wavelength). In that observing mode, inhomogeneities in the disks (gaps for instance) appear more distinctly compared to a classical homogeneous disk (Herwats 2005).

Additional goals

The expected performance of Pegase (see Section 7.3) will allow for a number of complementary programmes to be carried out, such as:

- the study of dust tori in active galactic nuclei,
- the extension of the programme on circumstellar disks to gas envelopes and debris disks, including the detection of exozodiacal light,
- the detection of coronal emission lines in active stars.

7.1.2 Overview of the Pegase design

The baseline concept for the mission consists in a simple two-telescope interferometer formed of three free flying satellites orbiting at the Lagrange point L2. Two Myriade micro-satellites are used as siderostats and one Proteus mini-satellite serves as a beam combining facility (see Figure 7.3). The central Proteus bus holds the whole optical payload, consisting in two 40-cm telescopes, a fringe sensor operating in the visible for fine optical path control as well as visibility measurements, its associated small delay line (stroke of about 1 cm), a star tracker for precise pointing, a chromatism compensator and a flux matching device, a beam-combiner for nulling interferometry, an infrared spectrometre with typical resolution of 60 and associated detection unit, the required metrology and sub-systems for configuration control, and finally an on-board CPU for data pre-processing (see Figure 7.4). The interferometric baseline ranges between 2×25 m and 2×500 m.

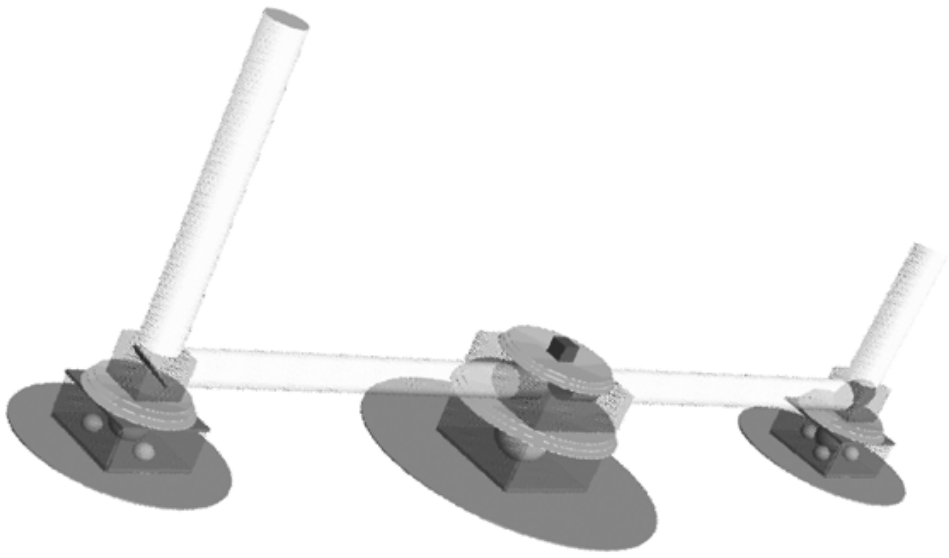

Figure 7.3: Flying configuration of the Pegase mission. The two siderostats bring both beams to the central platform where calibration, combination and detection of the interferometric signal take place.

The interferometer comprises a simple visibility measurement mode which scans the fringes with an OPD dither mirror (analogue to the FLUOR beam combiner, see Section 2.1.2) in addition to the main nulling mode. The latter requires an achromatic phase shifter to be introduced in one of the two arms, for instance by means of dispersive plates. Modal filtering is implemented at beam combination, using a fibre coupler or an integrated optics device. This provides the required accuracy on wavefront quality, converting phase defects in the input beams into (less serious) intensity errors in the output beams (see Section 3.1.3). The spectral band of Pegase was first proposed to range from 1.5 to 6 μm in order to include as many spectral features as possible in the hot EGP spectra, but the band was finally restricted to the 2.5 – 5 μm region for two main reasons: first, it allows the beam combination to be performed with a single instrument (the original band would have had to be divided into two sub-bands to carry out modal filtering) and second, the signal-to-noise ratio achieved on hot EGPs is optimal in this range (see Section 7.3). The detection unit features a HgCdTe focal plane array, passively cooled down to 55 K, with a cut-off frequency of 5 μm. Thanks to the low spectral resolution, a simple prism spectrograph is sufficient.

The fringe sensor works in the 0.5 – 1.5 μm regime, using a concept already proposed by ONERA in the context of the PRIMA fringe sensor (Cassaing et al. 2000): the four outputs of the so-called ABCD algorithm are formed simultaneously with an advanced beam-combining scheme that could well be implemented with an integrated optics component. This scheme also allows classical visibility measurements to be obtained with the fringe sensor itself, so that additional science can be carried out in the visible. Precise diameter measurements with the visible beam combiner will be very useful for the calibration of the nulled output, where geometric stellar leakage depends on the angular size of the stellar photosphere. Advanced methods for hot EGP characterisation in the visible are also considered, for instance using differential spectroscopy between the constructive and nulled outputs of the visible beam combiner.

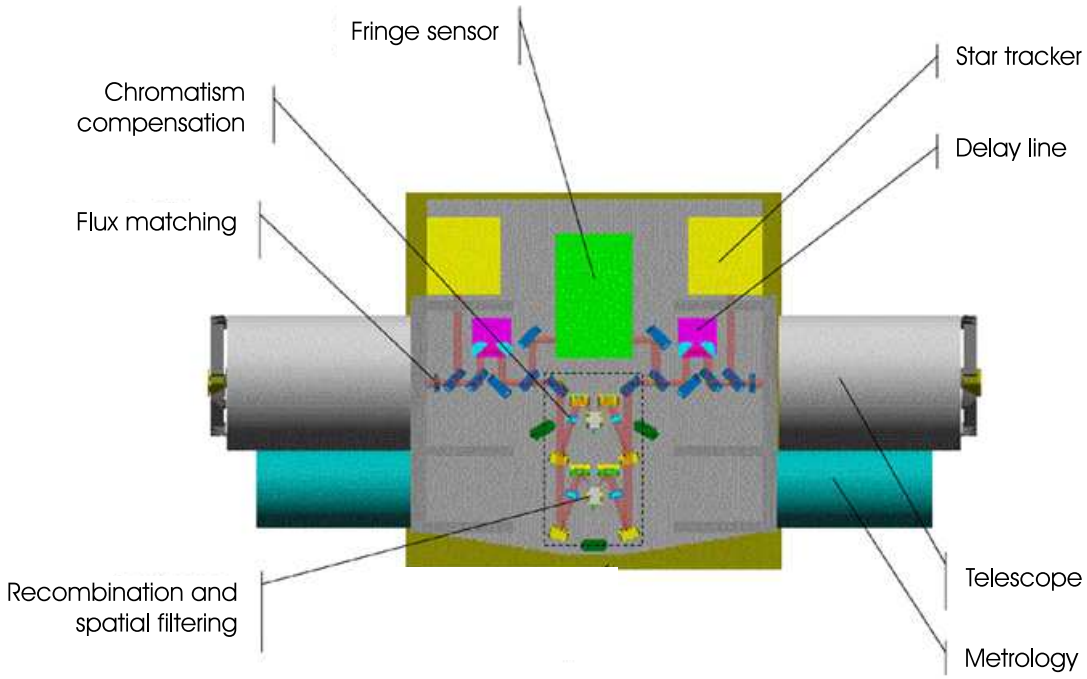

Figure 7.4: The Pegase payload located in the central beam combining satellite. The detection and spectroscopy unit is located on a second stage (not represented), which is fibre-linked to this stage.

During the 2 – 3 years of mission lifetime, about 50 targets are expected to be surveyed, with a duty cycle of about 50% as half of the time is expected to be spent in reconfiguring the array (baseline changes and rotations) and in sending data towards the Earth with a high gain antenna.

7.2 The prime targets: hot Extrasolar Giant Planets

The 37 stars known to host hot extrasolar planets within a distance of 150 pc from our solar system are listed in Table 7.1 and represented with their masses and semimajor axes in Figure 7.5. Because the Pegase interferometer, located at the Lagrange point L2 of the Sun-Earth system, must constantly be pointed in the anti-solar direction within ±30° in order to avoid stray light and heating due to the solar radiation, only the targets located in this band of the sky around the ecliptic can be observed. The ecliptic latitude β must therefore be comprised between $-30°$ and $30°$ for the source to be observable, which is the case for only 22 of the 37 candidate targets (see Table 7.1).

7.2.1 Modelling the infrared emission of EGPs

Among the 37 planets listed in Table 7.1, most are supposed to be gaseous giants as they have masses equal or larger to that of Uranus ($M_{\rm Uranus} = 0.045\,M_{\rm Jup} = 14.5\,M_\oplus$). Only Gl 876b, which has a mass smaller than 10 $M_\oplus$, is assumed to have a rocky surface. In the following paragraphs, we describe the models that we have used to compute the thermal flux from both the giant and the rocky planets.

Equilibrium temperature

The estimation of the surface temperature of extrasolar planets results from the thermal equilibrium between the heating due to the stellar flux, the cooling by their own thermal emission and the contribution

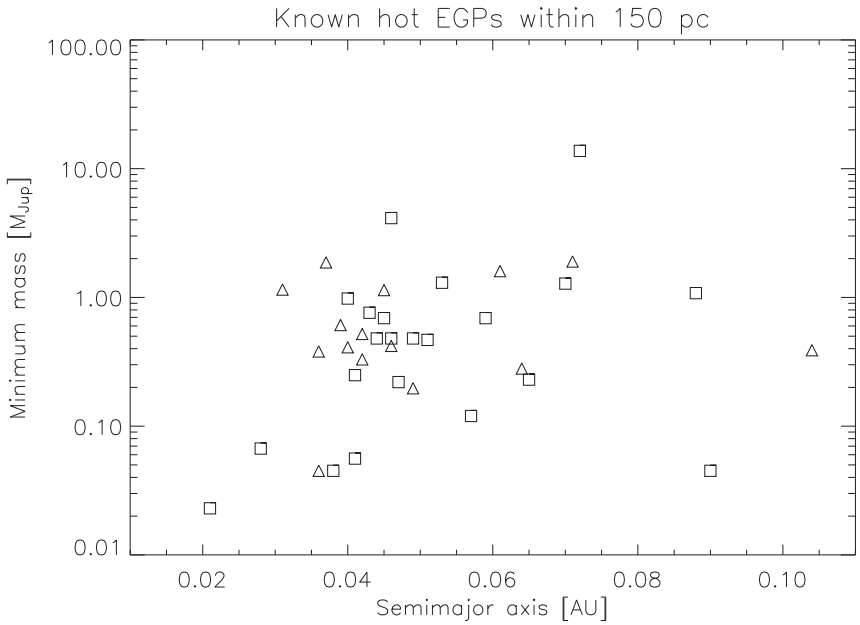

Figure 7.5: Semimajor axis and minimum mass of the 37 hot extrasolar planets currently known within 150 pc from our solar system. Targets represented by squares are observable with Pegase, while the triangles are located outside the Pegase observation cone.

	Stellar parameters			Planetary parameters					
	Spectral type	Dist. (pc)	Eclip. latitude	Semimajor axis (AU)	θ_{max} (mas)	Mass (M_{Jup})	Radius (R_{Jup})	T_{eq} (K)	Contrast at 3.3 μm
HD 63454b	K4 V	35.8	−76.3°	0.036	1.006	0.380	0.88	969	3686
HD 76700b	G6 V	59.7	−73.1°	0.049	0.821	0.197	0.70	1145	5894
HD 212301b	F8 V	52.7	−59.7°	0.036	0.683	0.045	0.43	1666	8729
HD 75289b	G0 V	28.9	−56.3°	0.046	1.589	0.420	0.91	1385	2896
HD 108147b	F8/G0 V	38.6	−53.6°	0.104	2.694	0.389	0.88	934	14733
HD 83443b	K0 V	43.5	−52.0°	0.040	0.919	0.410	0.90	1137	2916
HD 73256b	G8/K0	36.5	−46.6°	0.037	1.014	1.870	1.49	1224	879
HD 109749b	G3 IV	59	−33.4°	0.064	1.076	0.280	0.79	1178	8477
HD 330075b	G5	50.2	−29.1°	0.043	0.857	0.760	1.10	1254	1804
HD 160691d	G3 IV-V	15.3	−28.4°	0.090	5.882	0.045	0.43	990	58771
HD 46375b	K1 IV	33.4	−17.7°	0.041	1.228	0.249	0.76	1176	4678
HD 162020b	K2 V	31.3	−16.9°	0.072	2.300	13.75	2.00	765	3042
BD-103166b	G4 V	100	−16.0°	0.046	0.460	0.480	0.95	1247	2735
HD 2638b	G5 V	53.7	−8.3°	0.044	0.819	0.480	0.95	1239	2554
Gl 876d	M4 V	4.7	−6.6°	0.021	4.408	0.023	0.14	585	204757
HD 179949b	F8 V	27	−1.9°	0.040	1.481	0.980	1.20	1580	1304
HD 102195b	K0V	29	+1.2°	0.049	1.690	0.480	0.95	1027	3982
HD 217107b	G8 IV	37	+3.9°	0.070	1.892	1.280	1.31	969	3930
HD 88133b	G5 IV	74.5	+6.4°	0.047	0.631	0.220	0.73	1737	6508
Gl 581b	M3	6.26	+10.3°	0.041	6.550	0.056	0.46	529	109446
55 CnC e	G8V	13	+10.4°	0.038	2.923	0.045	0.43	1232	10601
HD 168746b	G5	43.1	+11.4°	0.065	1.507	0.230	0.74	1020	9046
HD 130322b	K0 V	29.8	+15.1°	0.088	2.953	1.080	1.24	767	9877
HD 49674b	G5 V	40.7	+17.9°	0.057	1.396	0.120	0.60	1091	10516
Gj 436b	M2.5	10	+22.6°	0.028	2.800	0.067	0.49	652	22152
HD 149143b	G0 IV	63	+23.7°	0.053	0.841	1.300	1.32	1291	1735
51 Peg b	G2 IV	14.7	+25.2°	0.051	3.483	0.468	0.94	1366	3699
τ Boo b	F7 V	15.6	+26.5°	0.046	2.949	4.130	1.94	1518	614
HD 209458b	G0 V	47	+28.7°	0.045	0.957	0.690*	1.43	1401	1121
υ And b	F8 V	13.5	+29.0°	0.059	4.380	0.690	1.07	1341	3022
HD 68988b	G0	58	+40.5°	0.071	1.224	1.900	1.50	1115	2327
HD 189733b	K1−2 V	19.3	+42.2°	0.031	1.606	1.150*	1.26	1175	985
HD 187123b	G5	50	+54.3°	0.042	0.840	0.520	0.97	1269	2227
HD 118203b	K0	88.6	+56.5°	0.061	0.688	1.600	1.42	921	2930
TrES - 1	K0 V	157	+58.7°	0.039	0.250	0.610*	1.08	1147	1951
HD 149026b	G0 IV	78.9	+59.1°	0.042	0.532	0.330	0.73	1697	4351
HD 188753b	K0	44.8	+60.7°	0.045	0.995	1.140	1.26	1077	1835

Table 7.1: Properties of the 37 hot extrasolar planets detected so far within 150 pc from our solar system. The host stars are generally late-type main sequence stars. Their ecliptic latitude β defines whether they are observable with Pegase or not (see text). The maximum angular separation θ_{max} between the star and the planet is computed at maximum elongation. The mass of the planet is generally the minimum mass except for the values followed by an asterisk, which are real masses as the inclination of the orbital plane of these planets was determined by the observation of transits. Radii, equilibrium temperatures and contrasts are computed as described in Section 7.2.1.

of internal heat sources. In the absence of external irradiation, the photosphere of a gaseous planet would cool down to an intrinsic temperature of about 100 K in a few Gyr (Baraffe et al. 2003). Since the planets listed in Table 7.1 orbit around (old) main sequence stars, most of them are suspected to have already reached such a low intrinsic temperature. The equilibrium temperature of hot EGPs is therefore much higher than their intrinsic temperature (Chabrier et al. 2004), so that internal heat sources can be neglected in the following discussions. Under such conditions, their surface temperature is simply equal to their equilibrium temperature.

Approximating the thermal emissions from the star and the planet by the equivalent blackbody emissions at effective temperatures $T_\star$ and $T_{\rm eq}$ respectively, the equilibrium temperature $T_{\rm eq}$ of an irradiated planet results from the balance between the received and the emitted fluxes (Paczyński 1980):

$$4\pi R_\star^2 \sigma T_\star^4 \frac{f(1-A_b)\pi R_p^2}{4\pi a^2} = 4\pi R_p^2 \sigma T_{\rm eq}^4 \,, \tag{7.1}$$

where A_b is the Bond albedo of the planet, a the semimajor axis of its orbit and f the proxy for atmospheric circulation (Seager et al. 2005), which is derived by considering whether the incident stellar radiation is re-emitted into 4π steradian ($f = 1$) or into 2π steradian ($f = 2$). The former is the case if the absorbed stellar radiation is redistributed evenly throughout the planetary atmosphere, while the latter applies if only the heated day side re-radiates the energy ($T_{\rm eq}$ is computed for the day side only in this case). In the following discussion, we will assume that the planetary atmosphere is perfectly thermalised (e.g. due to strong winds rapidly redistributing the heat), so that the day and night hemispheres have the same equilibrium temperature and $f = 1$. In practice, the day hemisphere, which is always oriented towards the star due to synchronous rotation, could be warmer than the night hemisphere by up to 500 K (Showman & Guillot 2002). In such conditions, the flux detected by Pegase would depend on the orbital phase of the planet. However, as Pegase will most often observe the star-planet system at maximum elongation (see Section 7.2.2), both day and night hemispheres will contribute to the detected flux so that using a mean temperature to characterise the total emission is a valid (but rather pessimistic) approximation. Under such assumptions, the equilibrium temperature of the irradiated planet writes:

$$T_{\rm eq} = T_\star (1-A_b)^{1/4} \left(\frac{R_\star}{2a}\right)^{1/2} \,. \tag{7.2}$$

Depending on the proximity of giant planets to their parent stars, the Bond albedo, defined as the ratio between the total reflected and total incident powers, can take very different values ranging from 0.02 to 0.8 (Sudarsky et al. 2000). For instance, in class IV roasters (with $900 \leq T_{\rm eq} \leq 1500$ K), a silicate cloud exists at moderate depths ($\sim 5-10$ bars), but the large absorption cross sections of the sodium and potassium gases above it likely preclude the cloud from having a significant effect on the albedo. The near-infrared albedo is therefore expected to remain close to zero (typically around 0.02). On the other hand, class V roasters (with $T_{\rm eq} \geq 1500$ K) have a silicate layer located much higher in the atmosphere, which is expected to reflect much of the incident radiation before it is absorbed by neutral sodium and potassium and molecular species. Hence, class V EGPs have much higher albedos than those of class IV, typically about 0.5.

For the computation of the equilibrium temperatures of Table 7.1, we have used a Bond albedo of 0.1 for all planets, as derived by Baraffe et al. (2003) for HD 209458b, except for Gl 876d which is suspected to have a rocky surface. For the latter, a Bond albedo equal to 0.306 has been assumed in analogy to the Earth's albedo, although the composition of the surface and of the potential atmosphere of this extrasolar planet is probably not the same as for the Earth.

Effective radius

The estimation of the radii of extrasolar planets has been based on theoretical models until the first measurement of a planetary transit on HD 209458b (Charbonneau et al. 2000). The unexpectedly large radius inferred for this planet was not consistent with theoretical models, so that an energy source appeared to be missing in order to explain the measured radius. Guillot & Showman (2002) proposed that a small fraction of the stellar flux might be transformed into kinetic energy in the planetary atmosphere and subsequently converted into thermal energy by dynamical processes at pressures of tens of bars. As an alternative source of energy, Bodenheimer et al. (2001) propose the dissipation of energy arising from ongoing tidal circularisation of the planetary orbit. This scenario is however not supported by the negligible eccentricity recently inferred from radial velocity measurements (Laughlin et al. 2005).

Another possible explanation comes from the fact that the measured radius is not the classical planetary radius at 1 bar, but rather the radius at which the optical depth to the primary's light along a chord parallel to the star-planet line of centres is about 1. Taking this effect into account, Burrows et al. (2003) find that, if HD 209458b's true transit radius is at the lower end of the measured range, an extra source of core heating power is not necessary to explain the transit observations. This model also reproduces the more recently measured radii of the OGLE planets (Burrows et al. 2004). The planetary radii predicted by this model might however be inappropriate for evaluating the thermal emission from hot EGPs, which arises from the location where the vertical optical depth reaches ~ 1. For this reason, in order to compute the thermal flux of the planets, we will use a more conventional model for planetary radii, which only makes use of the global density to relate mass and radius (see Figure 7.6). A density of 0.7 g/cm^3 will be assumed, as it represents an average for the EGPs characterised by transit measurements so far. Such a density might lead to an overestimation of the actual radius of massive planets, which are expected to have a higher density (at least in the non-irradiated case, see Burrows et al. 1997). In all cases, the EGP radii have artificially been limited to $2R_{\rm Jup}$ because at the planet - brown dwarf interface ($\sim 13M_{\rm Jup}$), the density is expected to reach about 1.8 g/cm^3 for a non-irradiated planet (Burrows et al. 1997), which gives a radius of about $2R_{\rm Jup}$. When available, the radii actually measured by planetary transits have been used.

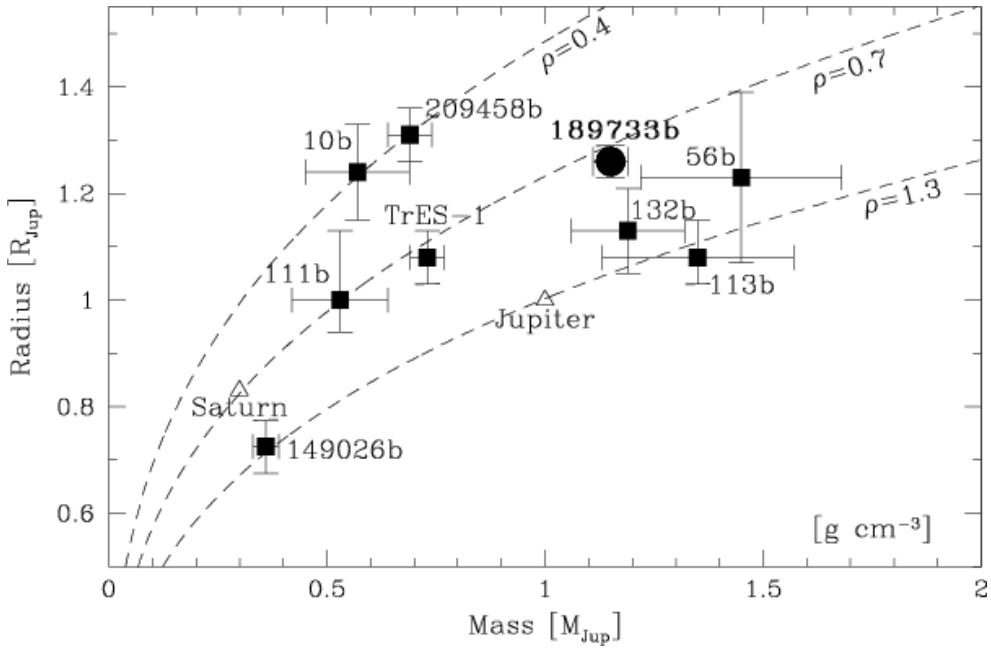

Figure 7.6: Mass-radius diagram for the 9 transiting planets detected so far (from Bouchy et al. 2005). Jupiter and Saturn are indicated for comparison, as well as the loci of isodensities at 0.4, 0.7 and 1.3 g/cm^3.

It must be noted that, in the case of Neptune-mass planets ($\sim 0.05\,M_{\rm Jup}$), our model predicts a radius around $0.5\,R_{\rm Jup}$ which might be largely underestimated, as Baraffe et al. (2005) suggest significantly larger radii ($\geq 0.8\,R_{\rm Jup}$) for such planets if they originate from the evaporation of massive Jupiter-like gas giants. On the other hand, it might well be that some of these planets are mainly composed of solid material, like Uranus and Neptune, and would therefore have a smaller radius around $0.35\,R_{\rm Jup}$. Therefore, a large uncertainty remains on the actual radius of such planets.

Finally, for the expectedly rocky planet Gl 876b, a radius of about $1.73\,R_\oplus \simeq 0.14 R_{\rm Jup}$ has been inferred by Rivera et al. (2005), based on the model developed by Léger et al. (2004).

Thermal flux and expected contrast

The total luminosity L_p of an irradiated planet writes (Chabrier et al. 2004):

$$L_p = A_b L_\star \frac{\pi R_p^2}{4\pi a^2} + 4\pi R_p^2 \sigma (T_{\rm eq}^4 + T_{\rm int}^4)\ , \tag{7.3}$$

where the first term is the contribution of the reflected part of the stellar spectrum, with A_b the Bond albedo of the planet, and where the last two terms represent the thermal emission of the planet with $T_{\rm eq}$ its equilibrium temperature and $T_{\rm int}$ its intrinsic effective temperature. As already discussed, the intrinsic heat production is generally negligible in the case of hot extrasolar planets. Based on the above expression and on our estimations of $T_{\rm eq}$ and R_p, and approximating the stellar emission by the equivalent blackbody radiation at an effective temperature $T_\star$, we can now deduce the wavelength-dependent infrared flux emitted by the planet that would actually be detected by an Earth-based observer:

$$F_p(\lambda) = A_b \frac{\pi R_\star^2}{d^2} B_\lambda(T_\star) \Phi(\Theta) \frac{R_p^2}{4a^2} + \frac{\pi R_p^2}{d^2} B_\lambda(T_p)\ , \tag{7.4}$$

where $B_\lambda(T)$ represents the surface brightness per wavelength unit for a blackbody at temperature T, d the distance to the target star and $\Phi(\Theta)$ a phase function affecting the reflected emission only. Assuming that the extrasolar planet is observed at maximum elongation, a phase function $\Phi(\Theta) = 0.5$ is adopted. In the above expression, we have neglected the wavelength dependence of the albedo and used the Bond albedo A_b instead, so that our model does not include the spectral features shown in Figure 7.1. Our model for the thermal flux only represents an estimation of the "mean flux", which is useful to assess the detection capability of Pegase in the case of extrasolar planets disregarding the influence of the particular shape of molecular bands.

From our estimation of the infrared flux of the extrasolar planets listed in Table 7.1, we also deduce the expected contrast between the stellar and planetary flux at 3.3 μm. This contrast typically ranges between 10^3 and 10^5 depending on the size and orbital distance of the planet and on the temperature of the parent star. In Figure 7.7, we represent the star planet contrast for the extrasolar planets listed in Table 7.1 as a function of their maximal angular distance. These are the two critical parameters that will determine the feasibility of their detection.

7.2.2 Observing scenario

The basic principle for the detection of an extrasolar planet with a nulling interferometer is to choose the baseline so as to obtain a perfectly constructive interference at the location of the planet. The most appropriate moment to observe EGPs happens when the angular distance with respect to their host star is maximum, so that a minimum baseline can be used to reduce the geometric stellar leakage as much as possible. Since the ephemeris of the planetary systems are known from radial velocity or photometric

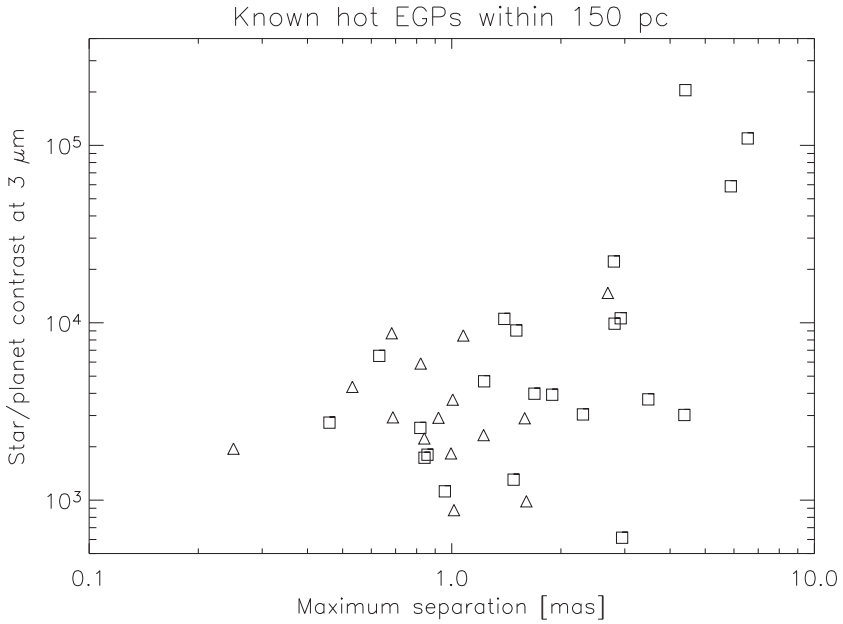

Figure 7.7: Angular separation at maximum elongation and expected star/planet contrast at 3.3 μm for the hot EGPs listed in Table 7.1. The planets represented by triangles are not observable with Pegase.

transit measurements, one can always make sure that the observations are carried out at maximum elongation. Assuming a circular orbit, which is the case for most hot EGPs, and a typical orbital period of 4 days, the angular separation between the star and the planet remains at 90% at least of its maximum value during about 13 hours, as illustrated in Figure 7.8. During this period, the interferometric transmission associated with the fringe pattern does not change by more than 3%. Long integration times can therefore be considered for these planets. Moreover, the continuous observation of the target EGP on this portion of its orbit should allow the detection of potential phase effects in its thermal emission due to the nonuniform distribution of temperature on the day-side and night-side hemispheres.

Even though the ephemeris of the planet is generally known with a good accuracy, the inclination and

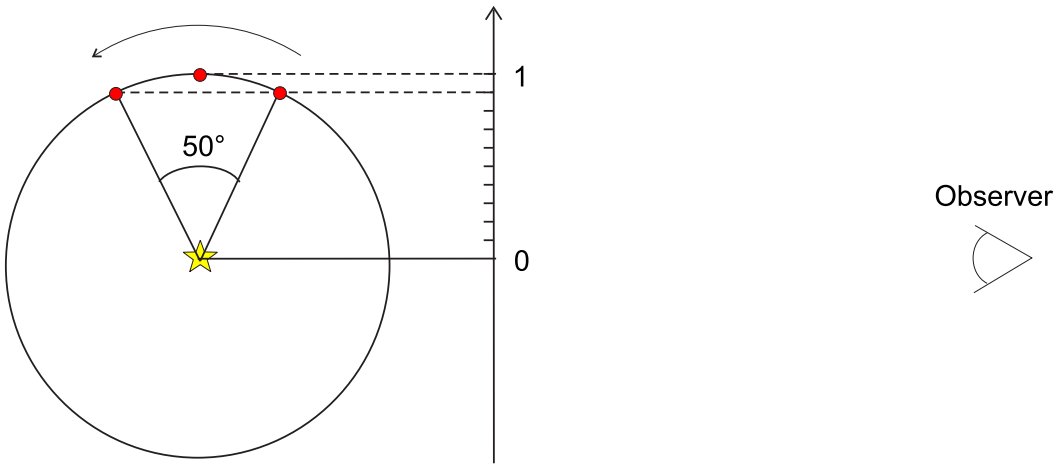

Figure 7.8: Assuming a circular orbit, the angular separation between the planet and its parent star remains above 90% of its maximum value during a significant time representing 50° out of 360°, i.e., 14% of the total orbital period. For a typiccal orbital period of 4 days, the planet can thus be observed during 13.3 hours around each of the two maximal separations. Note that the side on which the planet resides does not matter for the interferometer due to its symmetric transmission map.

the position angle of its orbit with respect to the plane of the sky are generally unknown. For this reason, at least three observations are planned for each planetary system with three different orientations of the baseline separated by 60° with respect to each other. In this way, the orientation of the most appropriate baseline among the three will be at most 30° from the actual position angle of the planet at maximum elongation, so that the first bright fringe will not fall too far from the actual position of the planet. The efficiency of the detection process will be reduced by 5% at most. In addition, this observing procedure will provide an estimation of the position angle of the orbit.

It must also be noted that the baseline b chosen for the observation can only be optimised for a given wavelength, at which the resolution $\lambda/2b$ is equal to the angular separation $\theta_{\rm max}$ of the system. However, we show in Figure 7.9 that if the baseline is optimised at 3.3 μm, the transmission of the planetary signal due to the interference process is comprised between 75% and 100% for the whole wavelength range from 2.5 to 5 μm. Therefore, three observations with one single baseline length are sufficient for each system.

In conclusion, each of the 22 planetary systems observable with Pegase (Table 7.1) will be visited three times, with an average integration time of about 13 hours for each visit. Disregarding the additional time needed to reconfigure the baseline of the array, the study of extrasolar planetary systems would require about 35 days. In practice, baseline modifications should only happen once a day, when Pegase is visible from the ground station, so that it is more reasonable to allocate 24 hours for each individual observation (including overheads), and thus a total of 66 days for the EGP programme.

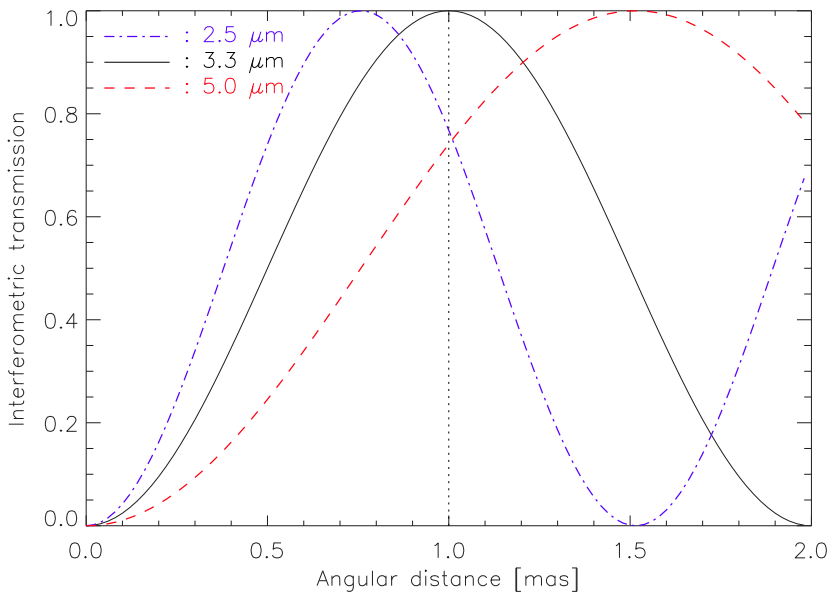

Figure 7.9: Interferometric transmission along the direction of the baseline at 3.3 μm and at the two edges of the observational band (2.5 – 5 μm). If the baseline length is optimised at 3.3 μm, e.g. b = 340 m for an angular separation of 1 mas in the present case, the interferometric transmission over the wavelength band does not fall below 75%. One single baseline is therefore sufficient to cover the whole band.

7.3 Simulated performance of Pegase

7.3.1 Geometric stellar leakage and calibration issues

An important source of noise in nulling interferometry comes from the residual stellar flux in the nulled output. The deterministic part of this residual, related to the finite size of the stellar photosphere, is referred to as geometric leakage and is given by the geometric nulling ratio (Equation 3.10):

$$N = \frac{\pi^2}{4}\left(\frac{b\theta_\star}{\lambda}\right)^2 , \tag{7.5}$$

with b the baseline length and $\theta_\star$ the stellar angular radius. Because the baseline is chosen so as to place the first bright fringe at the location of the planet ($\lambda/2b = \theta_{\max}$) at $\lambda = 3.3\ \mu$m, the geometric nulling ratio can be expressed as follows:

$$N = \frac{\pi^2}{16}\left(\frac{3.3\,\mu\text{m}}{\lambda}\right)^2\left(\frac{\theta_\star}{\theta_{\max}}\right)^2 . \tag{7.6}$$

The hot EGPs studied here are typically orbiting at 0.05 AU from their parent star, which has a typical radius of 4.6×10^{-3} AU assuming a Sun-like star. Therefore, the nulling ratio can be expressed as a function of wavelength by the approximate formula:

$$N \simeq 5 \times 10^{-3}\left(\frac{3.3\,\mu\text{m}}{\lambda}\right)^2 . \tag{7.7}$$

This equation shows that the geometric rejection ratio ($\rho = 1/N$) is generally about 200, i.e., at least a factor 10 smaller than the expected contrast between the star and the planet, which ranges between 10^3 and 10^5 (see Table 7.1). The contribution of geometric stellar leakage is therefore larger than the flux of the planet in the nulled output of the interferometer, so that it must be subtracted in order to reveal the planetary companion.

The general method for geometric leakage subtraction relies on the knowledge of the target star's angular radius, which is the only unknown parameter in Equation 7.5. Following the discussion in Section 4.2.1, we will assume that angular radii are known with a typical accuracy of 0.5% for the target stars, so that a precision of 1% can be achieved on the estimation of geometric stellar leakage. The effective rejection ratio, including calibration, will therefore reach about 2×10^4, which is sufficient to study the brightest targets listed in Table 7.1.

The subtraction of geometric stellar leakage can be further improved by using the fact that each extrasolar planetary system will be visited three times during the mission lifetime with different baseline orientations. While the transmission of the planetary signal depends on the orientation of the baseline, stellar leakage does not, assuming that the stellar photosphere is perfectly symmetric and that the interferometer is sufficiently stable to provide a good repeatability. The former is usually true for Sun-like stars, which are not expected to be elongated by more than a few 10^{-6} (Kuhn et al. 1998). The latter is expected to be the main source of variability in geometric stellar leakage from one measurement to another, due to potential variations in the baseline length for instance. This parameter has not been evaluated yet, so that we allocate a conservative accuracy of 10% on the repeatability of the interferometric observations.

All in all, the total accuracy with which geometric stellar leakage can be subtracted is expected to be of the order of 0.1%, taking into account both the knowledge of the stellar angular diameter and the repetition of the observations with three different baseline orientations.

7.3.2 Instrumental stellar leakage and real-time control

In addition to geometric stellar leakage, another contribution to the transmitted stellar flux comes from the influence of instrumental imperfections such as co-phasing errors, wavefront errors or mismatches in the intensities of the beams (see Section 3.1.2). This contribution, called instrumental stellar leakage, acts both as a bias, by introducing an additional amount of unwanted signal in the destructive output, and as a noise through its variability. Assuming that the interferometer behaves in the same way during the three visits of a target system, the average instrumental leakage should be the same in all three measurements so that the bias can be subtracted by comparing the results of the three observations. Only variability noise would thus contribute to the final noise budget, similarly to what is expected with the internal modulation techniques devised for the Darwin mission (see Chazelas et al. 2006, and Section 8.1).

However, because we do not have access to the actual power spectral densities of instrumental perturbations, a thorough study of variability noise cannot be carried out in the case of Pegase as was done in the case of GENIE or ALADDIN (Sections 4.2.1 and 6.3.1). Instead, we will assume that the variability of instrumental leakage is approximately given by its average value. This assumption is supported by the results obtained on the GENIE and ALADDIN instruments, for which the standard deviation of instrumental leakage is generally similar to its mean (see Table 3 in Section 4.2.1 and Table 6.3). In order to ensure a good signal-to-noise ratio on most hot EGPs, an average instrumental nulling ratio of 10^{-5} is required. In the following paragraphs, we discuss the two main sources of instrumental leakage (co-phasing errors and tip-tilt errors) and deduce the expected nulling performance of Pegase.

Fringe tracking

The principle of beam co-phasing with a fringe tracking device has already been extensively described in Section 4.2.1. In order to ensure an instrumental nulling ratio $N_i = 10^{-5}$, we deduce form Equation 3.12 that the standard deviation σ_{OPD} of the residual OPD error should fulfil the following relationship:

$$\sigma_{\mathrm{OPD}} \leq \frac{\lambda}{\pi} \sqrt{N_i} \,, \tag{7.8}$$

i.e., $\sigma_{\mathrm{OPD}} \lesssim 3$ nm at an observing wavelength of 3.3 μm. In the frame of the answer to the CNES call for ideas, the fringe tracking instrument onboard the Pegase mission has been investigated by F. Cassaing at ONERA (Châtillon). The performance of the fringe tracking system depends on the wavelength band at which it operates. The visible regime is preferred because the same OPD errors produce larger phase errors at shorter wavelengths, wich are therefore easier to measure. In any case, wavelengths shorter than 2.5 μm are required in order not to waste the photons useful to the science instrument. However, in order to keep a good SNR on the interference fringes, the increased angular resolution of the interferometer at shorter wavelengths should not result in a too low visibility for the target star. Using the same assumptions on the target system as in Equation 7.7, one can easily check that the expected stellar visibility (Equation 1.2) remains larger than 60% down to $\lambda \simeq 500$ nm if the baseline is optimised for planet detection at 3.3 μm.

In order to evaluate the performance of the fringe tracking system, F. Cassaing has assumed that the measurement error of the fringe sensor is the dominant source of noise in the control loop when the repetition frequency is set to 10 Hz at least. This means that the input OPD perturbations at frequencies higher than 10 Hz cannot reach a standard deviation of more than about 1 nm.[17] A total transmission of 3% was assumed for the whole fringe tracking system (including the upstream optical train), together with 30 cm telescopes (pessimistic assumption) and a spectral resolution of 5. It must be noted that,

[17] Such performance has already been demonstrated on a ground-based breadboard (Vink et al. 2003).

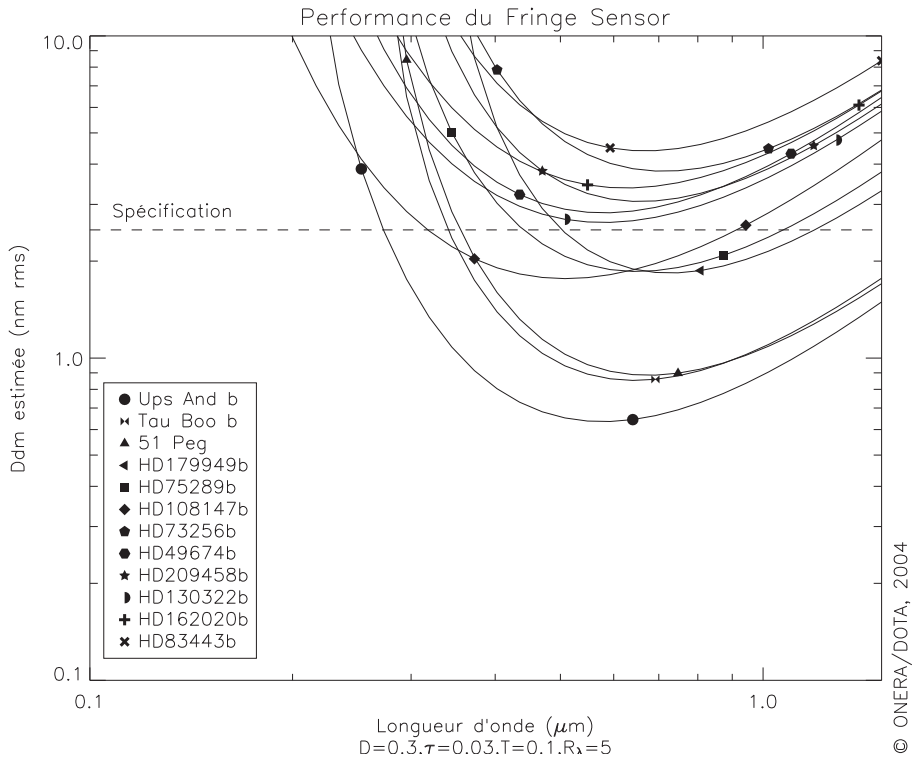

Figure 7.10: Simulated performance of the fringe tracking system onboard Pegase as a function of wavelength. Only sensor noise was considered in these simulations. Courtesy of F. Cassaing.

thanks to the low noise of the detectors available at visible and near-infrared wavelengths, the spectral dispersion of the fringes does not largely degrade the fringe tracking performance while allowing for an easier identification of the central "white" fringe located at zero OPD. The result of the simulations is displayed in Figure 7.10: a residual OPD error smaller than 3 nm is achieved for about half of the chosen targets. In the following discussion, we will therefore assume a mean performance of 3 nm rms for all targets.

Tip-tilt control

Because modal filtering is to be used in the Pegase nulling interferometer, wavefront errors will be traded against intensity errors, which are a less severe source of instrumental leakage (see Section 3.1.3). In the following discussion, we will assume that tip-tilt errors due to imperfect control of the spacecraft attitude is the main source of fluctuation for the coupling efficiency into the single-mode waveguides. Higher-order wavefront errors are supposed to be much smaller thanks to the high-quality polishing of the optics and to the limited thermal deformations of the optical elements thanks to the passive thermal control of the payload. True intensity errors, i.e., not related to the injection process into the single-mode waveguides, are not expected to be a significant source of intensity mismatch.

A tip-tilt control device, represented by the "Star tracker" box in Figure 7.4, will be implemented in the Pegase payload in order to provide a good stability of the injection process into the waveguides. The performance of the fine pointing device has been evaluated at ONERA during the preliminary study of the Pegase mission, showing that a typical tip-tilt residue of 30 mas rms can be achieved on most of the Pegase targets. The instrumental nulling ratio N_i can be directly deduced from the residual tip-tilt error σ_θ by an analytical formula taking into account the modal filtering process (Mennesson et al. 2002):

$$N_i = \frac{(\pi D \sigma_\theta)^4}{64\lambda^4} \,, \tag{7.9}$$

with D the telescope diameter. Assuming a typical tip-tilt error of 30 mas, the associated nulling ratio is about 1.5×10^{-7} at $\lambda = 3.3\ \mu$m, which is far better than the requirement of 10^{-5}. The main contribution to instrumental nulling will therefore come from residual OPD errors.

7.3.3 The thermal background and its fluctuations

There are three contributors to the background: the thermal emission from the warm zodiacal dust located along the line-of-sight of the Pegase interferometer, the thermal emission from the warm dust grains potentially surrounding the target star and the thermal emission from the instrument itself.

Zodiacal dust emission

Because the Pegase interferometer will be operated at 1 AU from the Sun, its field-of-view will be filled with the emission of the surrounding zodiacal dust, which has a typical temperature of 265 K. In this discussion, we will assume that the interferometer is pointed in the anti-solar direction in the ecliptic plane (typical observing configuration). The total near-infrared thermal emission produced by the zodiacal dust located in the line-of-sight is mainly dominated by the warm dust located close to the spacecraft: cooler dust located farther away produces significantly less flux in the $2.5 - 5\ \mu$m domain as the blackbody brightness is very sensitive to temperature in the Wien regime.

We have used the zodiacal disk model of Kelsall et al. (1998) to estimate the thermal emission of warm dust at 1 AU from the Sun. The result is displayed in Figure 7.11, expressed in Jy per steradian. In order to obtain the actual background emission experienced by the interferometer, this value must be multiplied by the size of the field-of-view, which is limited by the use of single-mode fibres (see Section 4.1.3). The effective area of the field-of-view can be computed by integrating the two-dimensional expression of the coupling efficiency (represented in Figure 4.4) up to $1.5\lambda/D$, where the coupling efficiency becomes null. This integration gives a final value of $0.772(\lambda/D)^2$ for the effective field-of-view area, which therefore ranges between 1.3 arcsec^2 and 5.1 arcsec^2 for wavelengths between 2.5 and 5 μm and a telescope diameter of 40 cm. The total background emission associated with the local zodiacal disk is therefore comprised between 3.5×10^{-6} Jy and 4.2×10^{-5} Jy depending on wavelength. When performing the final signal budget, these values will be affected by the total transmission of the interferometer excluding the on-axis coupling efficiency of 82% (see Figure 4.4), which is already taken into account in the size of the field-of-view.

The variability of the local zodiacal dust emission could be a significant source of noise, as it would produce different amounts of thermal emission in the three measurements of the target system and would therefore lead to an imperfect subtraction of the background emission. Thanks to the high thermal stability of the environment at the Lagrange point L2, background fluctuations are however not expected to be very large. Moreover, we will see that the planetary flux generally exceeds the local zodiacal background by at least an order of magnitude, so that even a 10% fluctuation of the zodiacal emission would not be a significant source of noise. The fluctuations of the zodiacal background emission will therefore be neglected in the following discussion.

Exozodiacal dust emission

Because it does not fill the field-of-view of the interferometer, the exozodiacal dust disk generally has a smaller contribution to the total background than the local zodiacal dust disk. The main problem with the exozodiacal disk rather resides in the fact that, if the system is seen close to edge-on, it can mimic the signature of an extrasolar planet as it would have different contributions in the three measurements

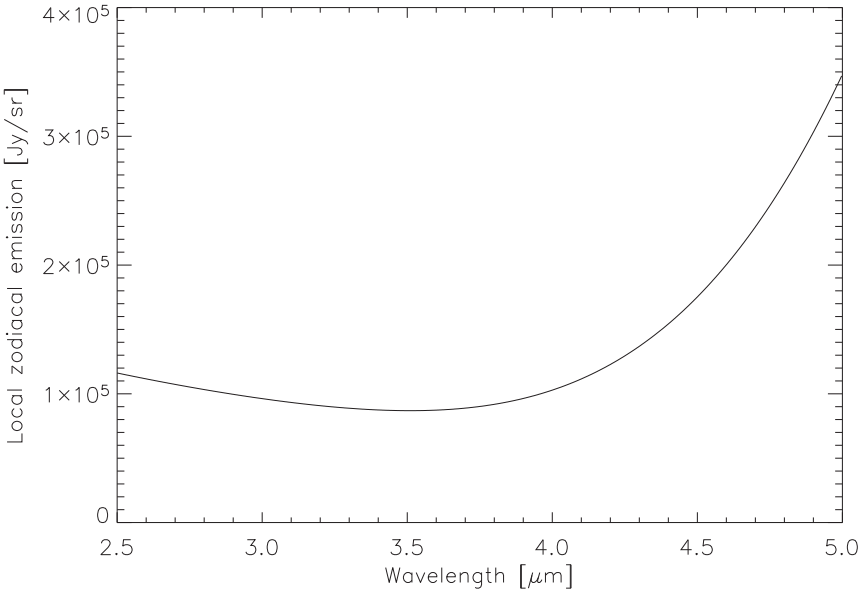

Figure 7.11: Surface brightness of the background emission produced by zodiacal dust at 1 AU from the Sun, based on the model of Kelsall et al. (1998).

performed with different orientations of the baseline. A thorough comparison of the actual signatures of extrasolar planets and exozodiacal disks in a nulling interferometer is currently being performed by C. Hanot at ESA/ESTEC.

However, it is not expected that large quantities of hot dust could persist in a planetary system where a giant planet has migrated as close as a few 0.01 AU from its parent star: gravitational scattering is thought to be responsible for the depletion of dust inside the orbit of the planet (Moro-Martín & Malhotra 2005). In the following discussion, we will therefore assume that the contribution of the exozodiacal disk to the total flux at the destructive output of the interferometer is negligible. It must however be noted that dust particles produced farther out in the disk and drifting inwards due to Poynting-Robertson drag can be trapped in mean motion resonance with the planet, and therefore produce asymmetric dust structures (clumps) which can mimic the presence of a planet even better than a symmetric exozodiacal disk (Moro-Martín & Malhotra 2005). This is not a real problem as these dust structures are not expected to be as bright as the hot giant planets; their detection would anyway be an important result in the context of the dynamical study of planetary systems.

Instrumental background

The design details of the Pegase interferometer have not been determined yet. However, the global transmission and emissivity of the Pegase nulling instrument can be deduced from the ALADDIN study, as both interferometers are foreseen to have very similar designs: about 13 reflections between the siderostats and the beam combiner, including two dichroic mirrors for deriving part of the light towards the fringe sensor and the tip-tilt sensor, followed by injection into the fibres and beam combination (or the other way around if the beam combiner is made of bulk optics instead of integrated optics), and finally spectral dispersion and detection. The only major difference comes from the fact that the whole optical train is at cryogenic temperature in the case of Pegase, for which the whole payload is passively cooled down to about 100 K to reduce the background emission as much as possible. Following the preliminary design of ALADDIN proposed by Alcatel Alenia Space (M. Barillot, private communication

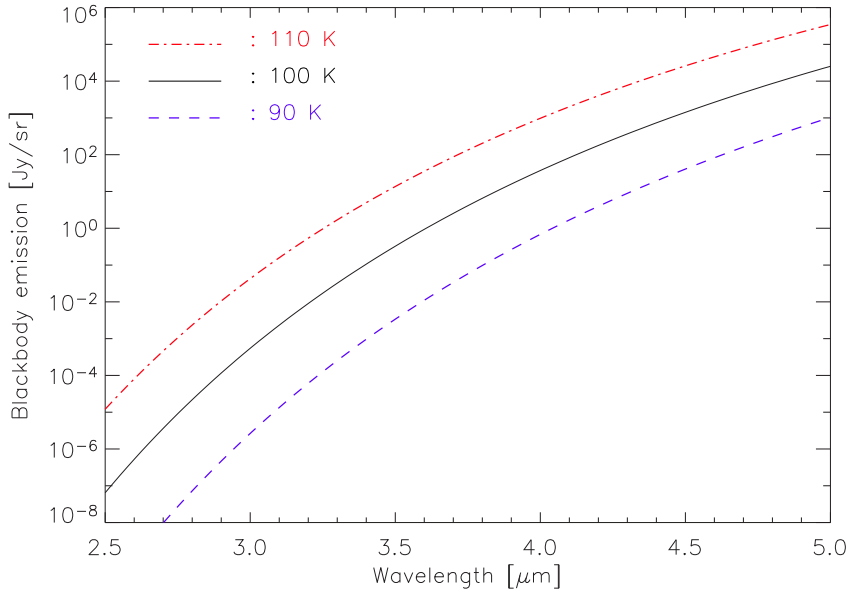

Figure 7.12: Surface brightness of the background emission produced by the whole optical train of Pegase, including the estimated grey emissivity factor of 25%, for three different instrumental temperatures.

– see Section 6.3), the total transmission and emissivity of Pegase are estimated to be respectively about 8% and 25%, including the quantum efficiency of the detector (about 65%).

The thermal emission produced by the instrument is modelled as a grey body emission, i.e., a blackbody emission multiplied by a constant emissivity factor related to the optical train. It is represented in Figure 7.12 for three possible temperatures of the Pegase payload. This figure shows two important features of the background emission, which are characteristic of the Wien regime: it rises very steeply as the wavelength increases and is very sensitive to the actual temperature of the payload (a 10% variation of temperature around 100 K modifies the total emission by a factor larger than 10). In order not to induce significant variations of the background emission between different measurements, a high thermal stability is therefore required. We will see that, assuming a mean temperature of 100 K, the standard deviation of temperature should not exceed 1 K in order to obtain a good SNR for the detection of hot extrasolar planets.

7.3.4 Total signal-to-noise ratio and target selection

In addition to the three aforementioned noise contributions, we have taken into account detection noise to compute the final SNR on the planetary signal. Detection noise includes the contributions of shot noise, associated with all sources within the field-of-view including background emission, and read-out noise, which is supposed to amount to 10 electrons per pixel. Thanks to the quantum well depth of about 250000 electrons for standard HgCdTe near-infrared detectors, single exposures can last as long as a few 100 sec while remaining in the linear regime of the detector (see typical signals in Table 7.2). In the following computations, we will therefore assume that the read-out frequency is set to 0.01 Hz. The effective read-out noise can thus be expressed as 10 electrons per 100 sec, or 1 electron/s$^{0.5}$ as read-out noise adds quadratically. Dark current is supposed to be made negligible by cooling down the detector to an appropriate temperature (about 55 K for the wavelength range considered here).

In Table 7.2 is summarised the computation of the final SNR for 6 of the 22 targets that can be observed with Pegase. We have chosen three representative hot Jupiter-type planets (τ Boo b, HD 209458b

and 51 Peg b), two hot Uranus-type planets (55 CnC e and Gj 436b) and one planet suspected to have a rocky surface (Gl 876b). In the following paragraphs, we give some details on the contents of Table 7.2. Each group of lines is related to one specific aspect of the SNR computation.

- **Instrument.** The interferometer is described by its fundamental parameters such as aperture size, baseline length, observing wavelength, spectral resolution, etc. The baseline is always optimised so as to provide an optimum SNR at 3.3 μm. Note that the actual optimum baseline is somewhat smaller than discussed in Section 7.2.2. This is due to the fact that the planetary transmission does not significantly decrease when increasing the baseline, while stellar leakage is much more sensitive to the baseline length. The interferometric transmission of the planetary signal generally ranges between 0.90 and 0.98 when using the optimum baseline. The total throughput and total emissivity both take into account the detector quantum efficiency. The instrumental rejection ratio is deduced from the contributions of OPD and tip-tilt errors, characterised by their standard deviation.
- **Star.** The stellar radii, masses and temperatures are taken from the literature when available, and otherwise adapted from the spectral classification of Cox (1999). The flux is based on a blackbody model. The geometric rejection rate is the inverse of the nulling ratio expressed in Equation 7.5. The total stellar rejection includes both the geometric and the instrumental rejection ratios, and is used to compute the output stellar flux.
- **Planet.** The planetary parameters have already been discussed in Table 7.1, and the computation of the thermal and reflected emission is described in Section 7.2.1. The interferometric transmission is close to unity, as the baseline is chosen so as to provide an optimum final SNR. As expected, the final planetary signal is generally 10 to 100 times weaker than the output stellar signal.
- **Background.** The local zodiacal dust and instrumental background emissions are computed as presented in Section 7.3.3. The instrumental background given in the table takes into account the instrumental emissivity. The background fluctuation is the standard deviation of the instrumental background and is only related to the temperature fluctuations of the payload. The output flux is computed by multiplying these contributions by the effective field-of-view area, i.e., $0.772(\lambda/D)^2$.
- **Individual noises.** The contribution of individual noise sources is expressed as a function of time in this section of the table. The time evolution of the various noise sources requires some explanations. Shot noise increases as the square root of time due to its Poisson statistics. Read-out noise shows the same time behaviour because the individual noise realisations experienced in successive read-outs add quadratically. The three other sources of noise are all proportional to time. These contributions are in fact biases, i.e., the residues of imperfect calibration or subtraction processes. Instrumental nulling noise and stellar leakage calibration noise are both proportional to the stellar signal, while background fluctuation noise is proportional to the background signal, hence the linear time dependence. The calibration accuracy for geometric stellar leakage is assumed to be equal to 0.1%, as discussed in Section 7.3.1.
- **Individual SNRs.** Using the integration time specified in the first line of this section, the individual signal-to-noise ratios are computed for the four noise sources. Shot noise and read-out noise are taken into account jointly in the detection SNR. While the detection SNR increases as the square root of time, the three others remain the same whatever the integration time. It must be noted that, with an integration time of 10 hours, the detection SNR is already comfortably larger than the instrumental SNR for most targets. Longer integration times would thus only marginally improve the final SNR. This result supports the proposed observing scenario, which is based on a typical integration time of 13 hours for each visit of the target systems.
- **Final SNR.** In order to compute the final SNR, we have used the pessimistic assumption that the three biases, respectively related to calibration, instrumental errors and background fluctua-

	τ Boo b	HD 209458b	51 Peg b	55 CnC e	Gj 436b	Gl 876d
Instrument						
Telescope diameter (m)	0.40	0.40	0.40	0.40	0.40	0.40
Baseline (m)	92	290	80	100	110	70
Wavelength (μm)	3.30	3.30	3.30	3.30	3.30	3.30
Spectral resolution	60	60	60	60	60	60
Total throughput	0.08	0.08	0.08	0.08	0.08	0.08
Total emissivity	0.25	0.25	0.25	0.25	0.25	0.25
Instrument temperature (K)	100	100	100	100	100	100
rms temperature fluct. (K)	1	1	1	1	1	1
rms OPD error (nm)	3	3	3	3	3	3
rms pointing error (mas)	30	30	30	30	30	30
Instrumental rejection	120428	120428	120428	120428	120428	120428
Star						
Distance (pc)	15.6	47	14.7	13	10	4.72
Spectral type	F7 V	G0 V	G2 IV	G8V	M2.5	M4 V
Radius ($R_\odot$)	1.220	1.100	1.300	0.878	0.430	0.300
Angular radius (mas)	0.364	0.109	0.411	0.314	0.200	0.296
Effective temperature (K)	6276	6030	5770	5458	3540	3500
Flux (Jy)	10.77	0.91	12.24	6.59	1.35	2.88
Geometric rejection	167.58	188.32	173.32	190.18	387.75	438.25
Total stellar rejection	167.35	188.02	173.07	189.88	386.50	436.66
Output flux (Jy)	5.15e-3	3.88e-4	5.66e-3	2.78e-3	2.79e-4	5.28e-4
Output flux (ph-el/s)	325.58	24.54	357.71	175.54	17.62	33.40
Planet						
Semimajor axis (AU)	0.046	0.045	0.051	0.038	0.028	0.021
Max. angular sep. (mas)	2.949	0.957	3.483	2.923	2.800	4.408
Mass ($M_{\rm Jup}$)	4.130	0.690	0.468	0.045	0.067	0.023
Radius ($R_{\rm Jup}$)	1.94	1.43	0.94	0.43	0.49	0.14
Bond albedo	0.10	0.10	0.10	0.10	0.10	0.31
Equilibrium temperature (K)	1518	1401	1366	1232	652	585
Thermal flux (Jy)	1.73e-2	8.03e-4	3.26e-3	6.12e-4	5.60e-5	9.52e-6
Reflected flux (Jy)	2.19e-4	1.05e-5	4.71e-5	9.65e-6	4.74e-6	4.56e-6
Star/planet contrast	614	1121	3699	10601	22152	204757
Interferometric transmission	0.902	0.919	0.921	0.952	0.978	0.979
Output flux (Jy)	1.27e-3	5.98e-5	2.44e-4	4.73e-5	4.75e-6	1.10e-6
Output flux (ph-el/s)	80.01	3.78	15.41	2.99	0.30	0.07
Background						
Local zodi (Jy/sr)	8.88e4	8.88e4	8.88e4	8.88e4	8.88e4	8.88e4
Instr. brightness (Jy/sr)	3.21e-2	3.21e-2	3.21e-2	3.21e-2	3.21e-2	3.21e-2
Rms bckg fluctuations (Jy/sr)	1.41e-2	1.41e-2	1.41e-2	1.41e-2	1.41e-2	1.41e-2
Output flux (Jy)	5.80e-7	5.80e-7	5.80e-7	5.80e-7	5.80e-7	5.80e-7
Output flux (ph-el/s)	3.66e-2	3.66e-2	3.66e-2	3.66e-2	3.66e-2	3.66e-2
Individual noises						
Shot noise (ph-el/s$^{1/2}$)	20.14	5.32	19.32	13.36	4.24	5.79
Read-out noise (ph-el/s$^{1/2}$)	1.00	1.00	1.00	1.00	1.00	1.00
Instr. leakage noise (ph-el/s)	0.452	0.038	0.514	0.277	0.057	0.121
Leakage calib. noise (ph-el/s)	0.326	0.025	0.358	0.176	0.018	0.033
Bckg fluct. noise (ph-el/s)	5.67e-8	5.67e-8	5.67e-8	5.67e-8	5.67e-8	5.67e-8
Individual SNRs						
Integration time (sec)	3.60e4	3.60e4	3.60e4	3.60e4	3.60e4	3.60e4
Detection SNR	752.85	132.38	151.20	42.37	13.10	2.25
Instrumental SNR	176.85	98.64	29.98	10.81	5.32	0.58
Calibration SNR	245.75	154.00	43.09	17.04	17.06	2.09
Bckg fluctuation SNR	1.41e9	6.66e7	2.72e8	5.27e7	5.30e6	1.23e6
Final SNR	90.48	41.35	15.83	5.72	3.10	0.38

Table 7.2: Details of the computation of the final signal-to-noise ratio for six representative hot extrasolar planets. See text for a thorough description of this table.

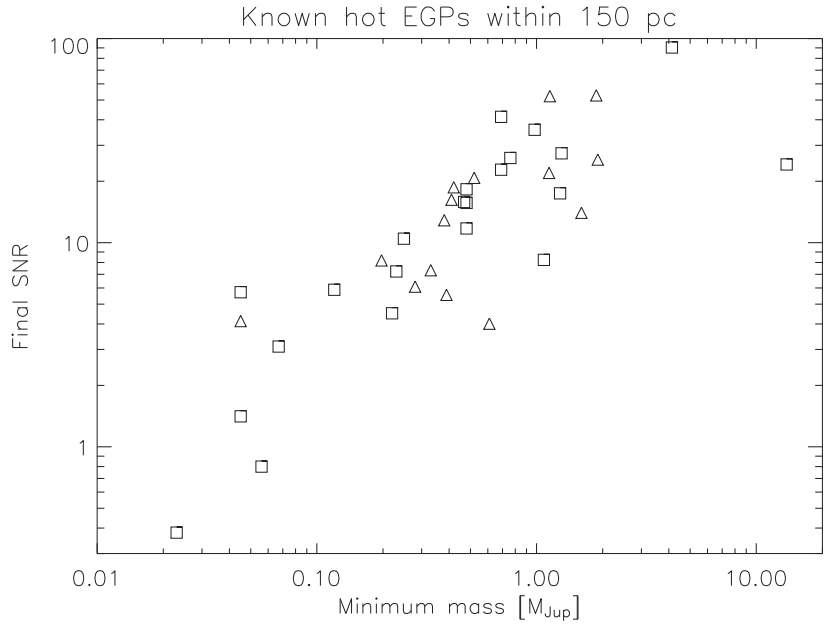

Figure 7.13: Expected signal-to-noise ratios at 3.3 μm for the hot EGPs in the solar neighbourhood, displayed as a function of their minimum mass. The planets represented by triangles are not observable with Pegase.

tions, add linearly. Adding them quadratically as totally uncorrelated noise sources would be too optimistic because stellar calibration noise is expected to be correlated with instrumental leakage noise, which is itself correlated with background subtraction noise through the instrumental temperature fluctuations (which also produce OPD and tip-tilt errors). The final SNR should thus be regarded as a minimum SNR.

The expected final SNR for the 37 known hot extrasolar planets within 150 pc is illustrated in Figure 7.13. Together with Table 7.2, this figure shows that a good SNR (higher than 5) can be achieved on most hot Jupiter-type planets ($M \gtrsim 0.2 M_{\rm Jup}$). Hot Uranus-type planets ($0.04 M_{\rm Jup} \lesssim M \lesssim 0.2 M_{\rm Jup}$) are also within reach, with a final SNR ranging between 1 and 6 depending on the proximity to the parent star. Rocky planets, on the other hand, are too faint to be detected with Pegase. It is expected that many more Uranus-type planets will be detected in the coming years by high-precision radial velocity surveys applied to main sequence stars in the solar neighbourhood. Such surveys will also be extended to earlier stellar types, around which they should discover many new Jupiter-type planets (Galland et al. 2005).

It must be noted that the major noise contribution comes in most cases from the variability of the instrumental stellar leakage. When the power spectral densities of the instrumental errors (OPD and tip-tilt) will be characterised, a more precise estimation of this noise contribution will be possible. It must be noted that a small improvement of the OPD control performance would largely improve the detection capability in the case of Uranus-type planets: a residual OPD error of 2 nm rms would produce a mean instrumental rejection ratio of 265000, and thereby improve the instrumental SNR by a factor slightly larger than two.

7.3.5 Wavelength dependence of the signal-to-noise ratio

In Figure 7.14, we have computed the SNR for HD 209548b as a function of wavelength in the $1.5-6\,\mu$m wavelength range. The four contributors to the final SNR are plotted separately in order to study their wavelength dependence.

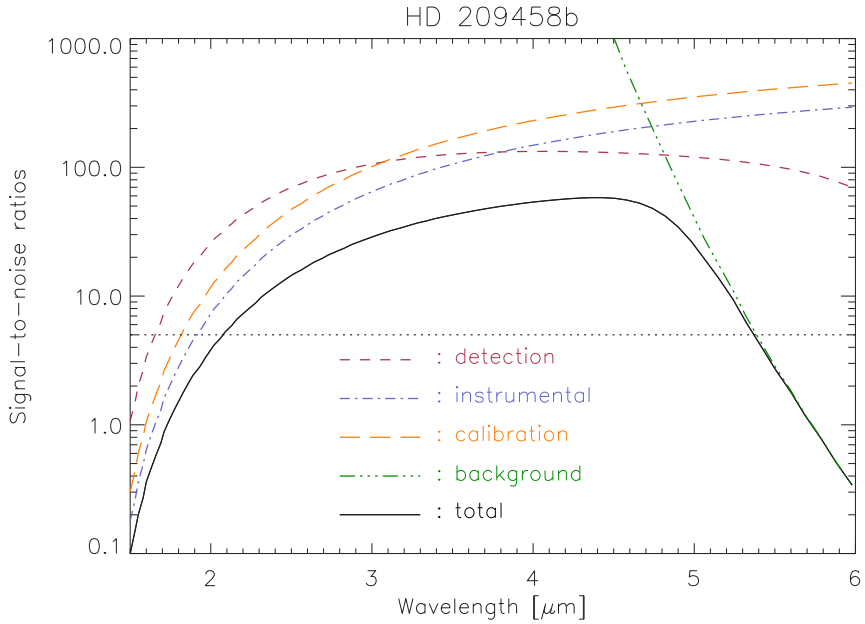

Figure 7.14: Simulated signal-to-noise ratio as a function of wavelength for the observation of the hot giant planet around HD 209458 with a total integration time of 10 hours and a spectral resolution of 60. Individual contributors to the total SNR are displayed separately (see text). The detection threshold is set at SNR = 5.

At short wavelengths, the main problem comes from the high contrast between the star and the planet, as well as from the poor instrumental rejection rate. The latter becomes as low as 23298 at $\lambda = 1.5$ μm. The total SNR reaches the detection threshold of 5 at $\lambda = 2.1$ μm. On the other hand, at long wavelengths, stellar leakage is not crucial any longer and the background fluctuation noise becomes the main contributor. The steepness of the background-related SNR curve is related to the sensitivity of the blackbody emission versus wavelength in the Wien regime. The total SNR falls below the detection threshold of 5 at $\lambda = 5.35$ μm in the case presented here (HD 209458b). The high level of the SNR in the $2.5 - 5$ μm band justifies *a posteriori* the choice of the observing waveband. Thanks to this high SNR (> 10) and to the spectral resolution of 60, spectral bands associated with molecular species will be easily identified in the spectra of hot EGPs.

The size of the observing waveband could potentially be extended towards shorter wavelengths by improving the co-phasing of the beams and the geometric leakage calibration, or towards longer wavelengths either by improving the thermal stability of the payload or by further decreasing its average temperature. However, it must be noted that the wavelength regime considered here is well appropriate to the use of single-mode fibres, which generally provide a good quality of modal filtering at up to twice their cut-off wavelength. Finally, it must be noted the total SNR on HD 209458b would only slightly improve if the integration time was increased, as only detection noise improves with time. This further confirms that an individual integration time of ~ 10 hours is a good choice.

8

Aperture configurations for the Darwin mission

Contents

8.1 A study of phase chopping techniques 158

8.1.1 The need for high-frequency chopping techniques 158

8.1.2 Principle of internal modulation 160

8.1.3 High-rejection configurations with internal modulation 162

8.1.4 Principle of inherent modulation 165

8.1.5 High-rejection configurations with inherent modulation 166

8.2 The resurgence of low-rejection configurations 167

8.2.1 The trade-off between low- and high-rejection configurations 168

8.2.2 A new concept: the Three Telescope Nuller (TTN) 171

The main objectives of the Darwin ESA mission are to detect Earth-like planets orbiting late-type main sequence stars up to 25 pc and to characterise their atmospheres by means of low resolution spectroscopy (Fridlund 2004b). Darwin will operate in the mid-infrared regime (from 6 to 18 μm), where the star/planet contrast ($\sim 10^7$) is more favourable than in the visible ($\sim 10^{10}$), and where suitable atmospheric signatures (CO_2, H_2O, O_3) can be found to assess the presence of biological activity on the detected planets. The technique of nulling interferometry has been selected by ESA as a baseline concept for the Darwin mission in order to reach the required angular resolution (< 50 mas) and dynamic range ($\sim 10^7$) for Earth-like planet detection. With a foreseen launch around 2015, Darwin is currently still in its definition phase, where the top-level architecture and design options are investigated. At the time when the present work begun, phase chopping techniques had only recently been proposed, and a configuration composed of six 1.5-m telescopes installed on free flying spacecrafts was considered as a model mission (Karlsson & Mennesson 2000). In this chapter, we further investigate phase chopping techniques and propose new configurations for the Darwin interferometer. We then summarise recent advances in the study of interferometric architectures and briefly discuss the new model mission. All the developments described in this chapter also apply to the NASA Terrestrial Planet Finder Interferometer (TPF-I), which has the same objectives as the Darwin mission and a similar overall design (Fridlund 2004a).

8.1 A study of phase chopping techniques

8.1.1 The need for high-frequency chopping techniques

A nulling interferometer composed of n telescopes with polar coordinates (L_k, δ_k) is characterised by its intensity response $R_\lambda(\theta, \alpha)$, the square modulus of the complex electrical field response $\mathbf{E}(\theta, \alpha)$, where (θ, α) are the polar coordinates in the plane of the sky with respect to the optical axis (Figure 8.1). Its expression, derived by Mennesson (1999), is a generalisation of Equation 3.5:

$$R_\lambda(\theta, \alpha) = |\mathbf{E}(\theta, \alpha)|^2 = \left| \sum_{k=1}^{n} A_k e^{i2\pi(L_k\theta/\lambda)\cos(\delta_k - \alpha)} e^{i\phi_k} \right|^2 , \tag{8.1}$$

where A_k and ϕ_k are the amplitude modulus and phase shift for telescope k. The amplitude coefficients are normalised so that $A_i = 1$ for the larger telescope its beam is entirely used in the beam combination scheme, taking into account the possible losses due to unused beam combiner outputs. The intensity response projected on the plane of the sky forms the so-called transmission map of the interferometer (see Section 3.1.1). Detection is assumed to be performed in the pupil plane, so that no image is formed: the total flux transmitted by the interference pattern is integrated on a single pixel. Therefore, there is *a priori* no distinction between the planetary signal and other sources located in the field-of-view, such as dust, residual stellar light or thermal background. As discussed in Section 3.1.4, this problem can be solved either by reducing the amount of spurious signals well below the planetary signal or by extracting the planetary signal with an appropriate technique.

The first requirement for a nulling interferometer is to achieve a deep central null, in order to extinguish the stellar light by a factor $\sim 10^7$. Mennesson & Mariotti (1997) have shown that, for the target stars and interferometric baselines considered here, this condition can only be achieved if the central transmission of the interferometer is proportional to θ^4 (or to a higher power of θ), where θ is the off-axis angle when pointing towards the star. According to Absil (2001), a θ^{2p} central transmission is obtained if and only if:

$$\sum_{k=1}^{n} A_k \left(L_k \cos(\delta_k - \alpha)\right)^q e^{j\phi_k} = 0 \ , \ \forall\, q \ (0 \le q \le p-1) \text{ and } \forall\, \alpha \ , \tag{8.2}$$

which is in fact equivalent to $4p-2$ independent real conditions. Based on these conditions, Absil (2001) deduced in his diploma thesis that four telescopes are required for a circular configuration to provide a

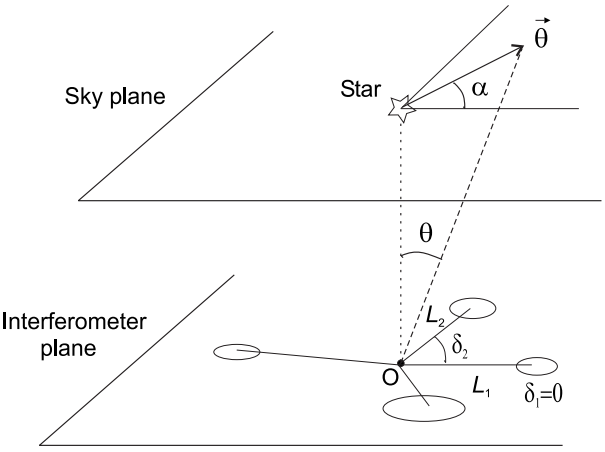

Figure 8.1: Geometrical configuration of the interferometric array. Planetary coordinates are given by the off-axis angular direction $\vec{\theta} = (\theta, \alpha)$. Each telescope of index k is located by means of the vector $\vec{L_k} = (L_k, \delta_k)$ in a reference frame with arbitrary origin O, used as a common phase reference.

θ^4 central transmission, while three telescopes are sufficient on a linear array. An additional telescope is required in both cases if one wants to use phase shifts different from 0 or π in the beam combination scheme. Such configurations are called *high-rejection configurations* in the following discussion, in opposition to *low-rejection configurations* which have a θ^2 central transmission.

Once the stellar light has been properly cancelled, there are other spurious signals to suppress. These come from the thermal emission of the zodiacal and exozodiacal dust, and from the interferometer itself. This is the reason why Bracewell (1978) proposed to rotate the interferometer around its line-of-sight with a period of about one hour. The planetary flux is then modulated as the planet crosses bright and dark fringes in the transmission map, so that it can be retrieved by synchronous demodulation. However, a low-frequency rotation of the interferometer is not sufficient to completely cancel these spurious signals, as proven below.

- **Zodiacal dust disk.** The zodiacal disk is a tenuous disk that surrounds the Sun, composed of dust released from active comets and colliding asteroids. It is heated to about 265 K at 1 AU from the Sun, and is a major contributor to the infrared background seen by Darwin: the total zodiacal flux collected by 1-m class telescopes is about 1000 times larger than the flux from an Earth-like extrasolar planet at 10 μm. This signal is not modulated by rotation of the array, so that it can be suppressed by signal processing. The problem rather comes from its associated shot noise and from the potential long-term fluctuations of its brightness. These fluctuations could be confused with the slowly modulated flux of the planet unless fast signal chopping is used.
- **Exozodiacal dust disk.** Another major source of noise is the exozodiacal dust disk potentially surrounding the target star. Considering it to be similar the solar zodiacal disk, its integrated flux is about 300 times larger than an Earth-like planet emission at 10 μm. The main problem with the exozodiacal disk is that its emission is also modulated by rotation of the array (unless it is seen face-on), so that it can be confused with the signature of a planet.
- **Instrumental background.** In order to keep the temperature of the optical train of Darwin as low as possible, a planar interferometer concept is highly preferred. This avoids thermal coupling between the different telescopes. The optical elements will be passively cooled down to 40 K, while the mid-infrared detectors require active cooling at 6 K. The thermal emission of the instrument would generate troublesome levels of background signal if its temperature was above 40 K. Moreover, fluctuations of temperature and emissivity in the optical train can induce fluctuations of the thermal background level, which have to be monitored at a sufficiently high frequency.

In addition to a high rejection rate, there are thus two other major requirements for a nulling interferometer: first, to sample the background fluctuations at a high enough frequency and second, to discriminate the planetary signal with respect to the exozodiacal dust disk. The first array configurations designed to separate the planetary signal from the exozodiacal emission have been proposed by Angel & Woolf (1997) and by Mennesson & Mariotti (1997). The former relied on the strong modulation of the exozodiacal emission at twice the interferometer rotation frequency (due to its symmetry), while the latter suggested to break the central symmetry of the interferometer, for example by using five telescopes regularly located on a circle or on an ellipse. But still, these configurations did not provide the required high frequency modulation, and were therefore still sensitive to background fluctuations and to other $1/f^{\alpha}$ type noises.

In the following sections, we investigate phase chopping techniques to mitigate the two aforementioned critical issues. Unlike the rotation of the array, phase chopping only relies on the beam combining scheme and in particular on the values of the phase shifts applied to individual beams. The first proposal for an implementation of phase chopping in a nulling interferometer, due to J.-M. Mariotti in 1997 (Mennesson et al. 2005), was therefore referred to as *internal modulation*. A similar concept was independently developed by Woolf & Angel (1997).

8.1.2 Principle of internal modulation

The principle of internal modulation is to divide a telescope array into two (or more) nulling interferometers and to combine their outputs with a time-varying phase shift in order to achieve a fast modulation of the planetary signal. The sub-interferometers are formed by dividing the amplitudes of the light beams collected by each telescope (Figure 8.2a-b). Both have a real entrance pupil, which means that the phase shifts applied to their light beams are restricted to 0 or π. Their transmission maps have different shapes (Figure 8.2c), but both achieve a θ^4 central transmission to efficiently suppress the star light.

The outputs of the two sub-interferometers are combined on a loss-less beam combiner, which induces a $\pi/2$ phase shift between the input beams in the first output, and a $-\pi/2$ phase shift in the second output. The new transmission maps associated with these outputs are asymmetric and conjugated to each other by point-symmetry with respect to their centre (Figure 8.2d). Denoting $R_{12}(\theta,\alpha)$ and $R_{21}(\theta,\alpha)$ the intensity responses associated with the two new outputs, this property writes $R_{12}(\theta,\alpha+\pi) = R_{21}(\theta,\alpha)$ and can easily be proven by developing the expression of the two intensity responses:

$$R_{12}(\theta,\alpha) = \frac{1}{2}|\mathbf{E}_1(\theta,\alpha) + e^{i\pi/2}\mathbf{E}_2(\theta,\alpha)|^2 \ , \tag{8.3}$$

$$R_{21}(\theta,\alpha) = \frac{1}{2}|\mathbf{E}_1(\theta,\alpha) + e^{-i\pi/2}\mathbf{E}_2(\theta,\alpha)|^2 \ . \tag{8.4}$$

By developing the square moduli, we get:

$$R_{12}(\theta,\alpha) = \frac{1}{2}|\mathbf{E}_1(\theta,\alpha)|^2 + \frac{1}{2}|\mathbf{E}_2(\theta,\alpha)|^2 + |\mathbf{E}_1(\theta,\alpha)||\mathbf{E}_2(\theta,\alpha)|\sin(\arg\mathbf{E}_1(\theta,\alpha) - \arg\mathbf{E}_2(\theta,\alpha)) \ ,$$

$$R_{21}(\theta,\alpha) = \frac{1}{2}|\mathbf{E}_1(\theta,\alpha)|^2 + \frac{1}{2}|\mathbf{E}_2(\theta,\alpha)|^2 - |\mathbf{E}_1(\theta,\alpha)||\mathbf{E}_2(\theta,\alpha)|\sin(\arg\mathbf{E}_1(\theta,\alpha) - \arg\mathbf{E}_2(\theta,\alpha)) \ ,$$

where "arg" is the argument of a complex quantity. Now, if the entrance pupil of the two sub-interferometers are real, it follows from Equation 8.1 that $\mathbf{E}_i(\theta,\alpha+\pi) = \overline{\mathbf{E}}_i(\theta,\alpha)$, where the bar denotes complex conjugation. Their arguments are thus related by $\arg\mathbf{E}_i(\theta,\alpha+\pi) = -\arg\mathbf{E}_i(\theta,\alpha)$, so that $R_{12}(\theta,\alpha+\pi) = R_{21}(\theta,\alpha)$. Therefore, an extended source with point symmetry such as the exozodiacal disk will have the same contribution in both outputs. For the same reason, the mean leakage of stellar light through the two

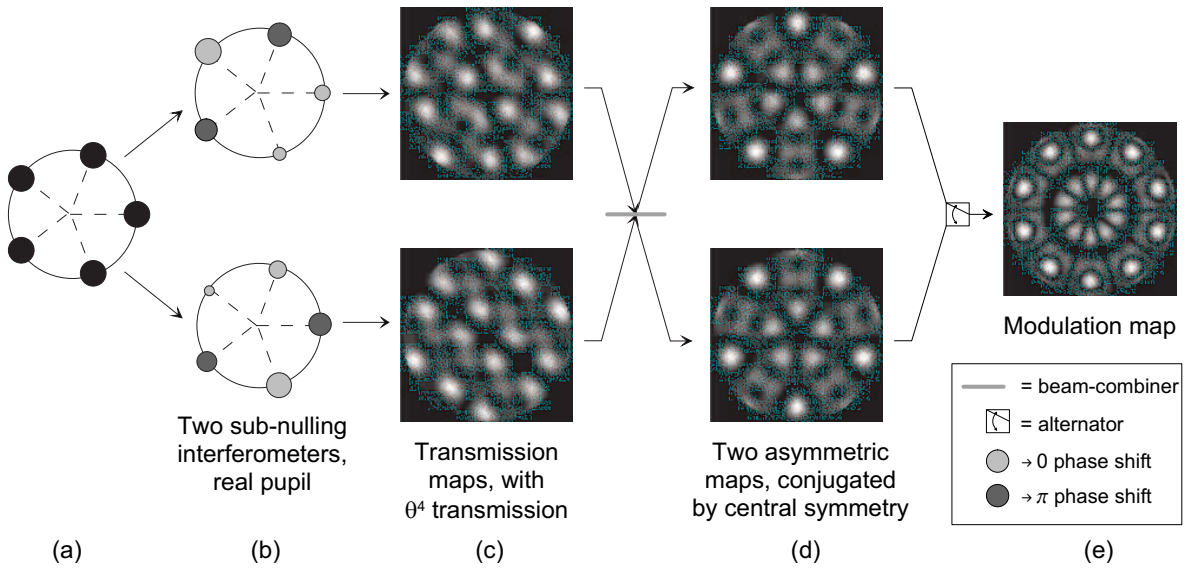

Figure 8.2: Principle of internal modulation. The outputs of two sub-interferometers are mixed on a lossless beam combiner to produce the two output signals.

transmission maps is also equal in both outputs. On the other hand, a planet would have two different contributions because when it lies on a bright zone in the first transmission map, it is located on a dark zone in the second map. By alternately detecting the two outputs on a common detector, a final signal is obtained where only the planetary part is modulated. The modulation map (Figure 8.2e) shows the regions of the sky which are strongly modulated (bright zones) and those where there is no modulation at all (dark zones).

A key advantage of internal modulation is that the switching between the two outputs can be done at a high frequency, so that there is now a clear distinction between the rapid modulation of the planetary signal and the slow fluctuations of the background. Note that in practice the two outputs will be continuously monitored by two single-pixel detectors to reach a maximum efficiency, so that the modulation frequency will actually be infinite. Another advantage of internal modulation is that, in principle, the array need not be rotated any more. In practice, a slow rotation of the array will still be used in order to get better image quality (Lay 2005).

In order to assess the efficiency of nulling configurations with internal modulation, the modulation efficiency is defined as the part of the incoming signal which is actually modulated and thus retrievable by synchronous demodulation. The expression of modulation efficiency reads:

$$\eta(\theta,\alpha) = \frac{|R_{12}(\theta,\alpha) - R_{21}(\theta,\alpha)|}{\sum_{k=1}^{n} D_k^2} = \frac{2\,|\mathbf{E}_1(\theta,\alpha)|\,|\mathbf{E}_2(\theta,\alpha)|}{\sum_{k=1}^{n} D_k^2}\ \sin(|\arg\mathbf{E}_1(\theta,\alpha) - \arg\mathbf{E}_2(\theta,\alpha)|)\ , \qquad (8.5)$$

where D_k is the normalised diameter of telescope k (normalisation to 1 for the larger telescope). This definition of modulation efficiency provides an easy comparison between different configurations because it is independent of the number and size of telescopes, since the amplitude responses $\mathbf{E}_i(\theta,\alpha)$ are normalised to the size of the larger telescope of the array.

Configurations with internal modulation have been proposed by various authors (Karlsson & Mennesson 2000; Absil et al. 2003b; Lay 2005; Mennesson et al. 2005). They include the so-called Robin Laurance configurations, which satisfy the following conditions:

- all telescopes are at equal distance from the beam-combining spacecraft to equalise the optical paths (and thereby avoid long delay lines);
- all telescopes are located in a common plane (perpendicular to the line-of-sight) to reduce thermal coupling, with a minimum separation of 20 m to avoid collisions;
- the central transmission is proportional to θ^4 (or θ^6) to cancel the star light efficiently;
- the only permitted phase shift in each sub-interferometer is π (real entrance pupils);
- all telescopes have the same diameter to reduce the manufacturing costs.

The Robin Laurance configurations are referred to as RLx(m_1,m_2,...,m_n), where x is the number of sub-interferometers, n the number of telescopes and m_i the relative telescope sizes, starting with the largest one. Before the present work, the mission model for Darwin was the RL3(3,2,0,1,0,2) configuration with six telescopes arranged in a regular hexagonal configuration (Karlsson & Mennesson 2000). This configuration achieves internal modulation between three Generalised Angel Crosses (GAC, Absil 2001). It has a maximum modulation efficiency of 0.29, which means that, in the case where the planet is located on a modulation maximum, only 29% of the planetary signal is actually modulated and can be retrieved by signal processing. The mean modulation efficiency on a field-of-view of 300×300 mas is 12% for a circular array 25 meters in radius and a wavelength of 10 μm. This is the relevant figure during the detection phase where the planet position is not known and the whole field-of-view has to be investigated.

The main problem associated with this configuration, in addition to its rather low modulation efficiency, is the complexity of the optical beam combination scheme: it needs no less than nine beam

splitters with ratios of 5:4, 4:1 and 1:1, as well as nine beam combiners and associated achromatic phase shifters to produce the three GAC outputs (Karlsson & Mennesson 2000). Three more beam combiners are needed to produce the six final outputs. Moreover, six detectors are needed for an optimum efficiency. Therefore, new configurations had to be designed to provide higher modulation efficiencies with simpler beam combination schemes, and thereby to improve the feasibility and reliability of the mission while reducing its cost.

8.1.3 High-rejection configurations with internal modulation

Two main types of configurations have been considered in our search for an optimum architecture: circular Robin Laurance configurations and linear configurations. In order to achieve both a θ^4 central transmission and internal modulation, circular configurations need at least five telescopes, while linear configurations can work with four telescopes (Absil 2001). Circular configurations are very convenient for space interferometry: if the beam-combining spacecraft is located at the centre of the circle and the plane of the array perpendicular to the line-of-sight, the optical paths travelled by each light beam are equal, so that long delay lines are not required. A difficulty associated with linear configurations is that optical paths generally cannot be equalised by geometric constructions. In some cases, reflections of the light beams on neighbouring telescopes can be used to equalise the external optical delays (see Figure 8.3). This could however exaggeratedly constrain the control requirements on their positions and attitudes.

In the following paragraphs, we present a new circular configuration combining a high modulation efficiency and a rather simple beam combination scheme. It is then compared with a promising linear configuration.

Circular configurations

Circular configurations with five and six telescopes have been comprehensively studied by Absil (2001). The best of them seems to be the so-called *bow-tie* configuration, with six telescopes in an irregular hexagonal arrangement (Figure 8.4). This Robin Laurance configuration—RL2(1,1,0.707,0,0,0.707)—performs internal modulation between two Generalised Angel Crosses. Its maximum modulation ef-

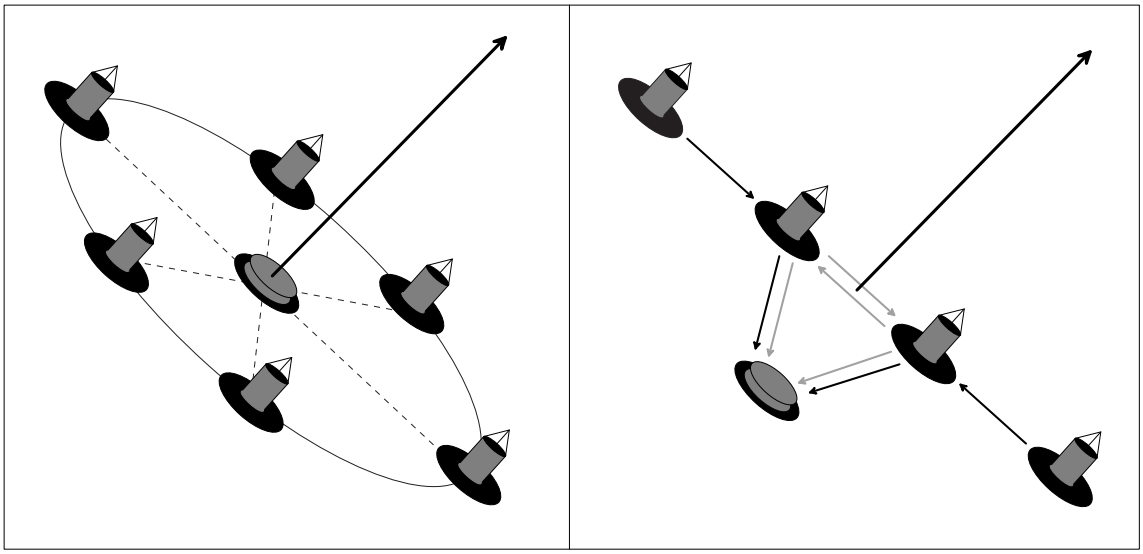

Figure 8.3: Optical path equalisation in the cases of circular and linear configurations.

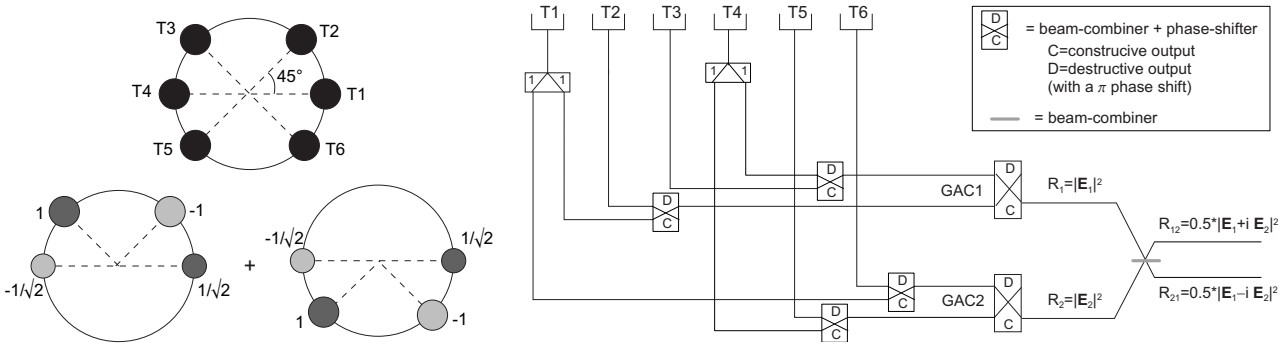

Figure 8.4: Left: The bow-tie configuration with its two sub-interferometers (Generalised Angel Crosses) and the relative signed amplitudes for each beam. Right: Beam combination scheme for the bow-tie interferometer. The final outputs are characterised by their transmission maps R_{12} and R_{21}. Note that one half of the intensity is lost at each beam combination because only one output is used.

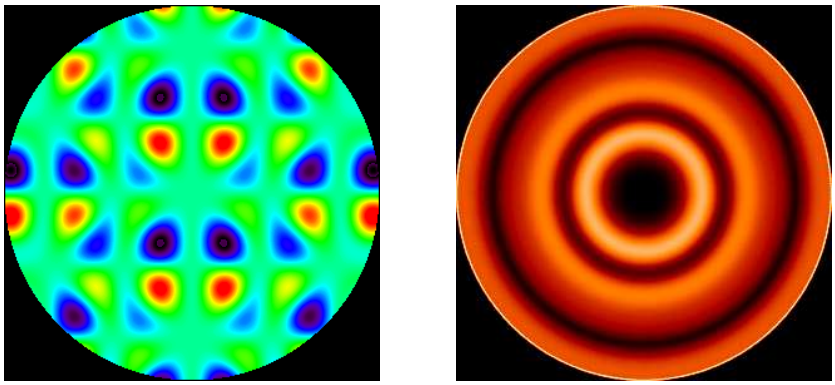

Figure 8.5: Left: Modulation map of the bow-tie interferometer over a 300 × 300 mas field-of-view for an array radius of 26 m (see text) and an observing wavelength of 10 μm. The sign of the modulation efficiency has been kept in order to distinguish the contributions from the two chopped states (see Equation 8.5). Red colours correspond to positive modulation efficiencies, blue colours to negative ones, and green colour to a modulation efficiency close to 0. Right: Standard deviation of the modulation efficiency computed on each point of the field-of-view while rotating the interferometer around its line-of-sight.

ficiency reaches 65%, i.e., more than twice that of the original RL3(3,2,0,1,0,2) hexagon. Its mean modulation efficiency is still rather low (13%) on a 300 × 300 mas field-of-view, but the interferometer baseline can be tuned so as to provide a high efficiency over the whole habitable zone of the target star (Figure 8.5). The beam combination scheme of the bow-tie (Figure 8.4) is much easier to implement than the RL3(3,2,0,1,0,2) configuration, in that it involves only two 50/50 beam splitters, six beam combiners with associated achromatic phase shifters, and an additional beam combiner to form the two final outputs. Two detectors are needed to ensure a maximum efficiency.

The modulation map of this new configuration is presented in Figure 8.5. It shows eight bright modulation maxima, each with a peak modulation efficiency of 65%. With an array radius of 26 m[18] and an observing wavelength of 10 μm, these maxima are located at 50 mas and 80 mas from the optical axis. This is also the typical angular separation between an Earth-like planet and its host star for G-types stars between 10 and 20 pc. The right-hand side of Figure 8.5 shows the result of a continuous rotation of the interferometer around its line-of-sight: two annuli are obtained where the standard deviation of modulation efficiency is maximum. The coverage of the habitable zone is quite good, provided that the array radius is tuned to the desired target. A slow continuous rotation of the telescope array is not

[18] A array radius of at least 26 m is required to fulfil the requirement on spacecraft separation (≥ 20 m).

expected to increase the complexity of the mission nor to require an important quantity of fuel.

Thanks to the improved maximum modulation efficiency, the bow-tie is expected to perform low-resolution spectroscopy of Earth-like planets four times faster than with the original RL3(3,2,1,0,1,0) configuration. This advantage adds to the relative simplicity of the beam combination scheme, making the bow-tie the most promising Robin Laurance configuration. Consequently, this configuration was chosen in 2002 as a new baseline architecture for the Darwin interferometer.

Linear configurations

Linear configurations achieving internal modulation have been reviewed by Lawson et al. (1999) and have been further investigated by Absil (2001). The most promising of them is presented in Figure 8.6. This configuration is dubbed *LinEqual* because of its four equal-size telescopes. It achieves internal modulation between two irregular Degenerate Angel Crosses (DAC), whose shapes have been chosen so that all telescopes have the same diameter. The beam combination scheme of LinEqual uses only four beam combiners and associated achromatic phase shifters instead of six for the bow-tie (Figure 8.6). Note that the beam coming from the central telescope of each DAC undergoes only one beam combination, so that it is less attenuated than the others.

The modulation map of LinEqual is displayed in Figure 8.7. The line-shaped map is characteristic

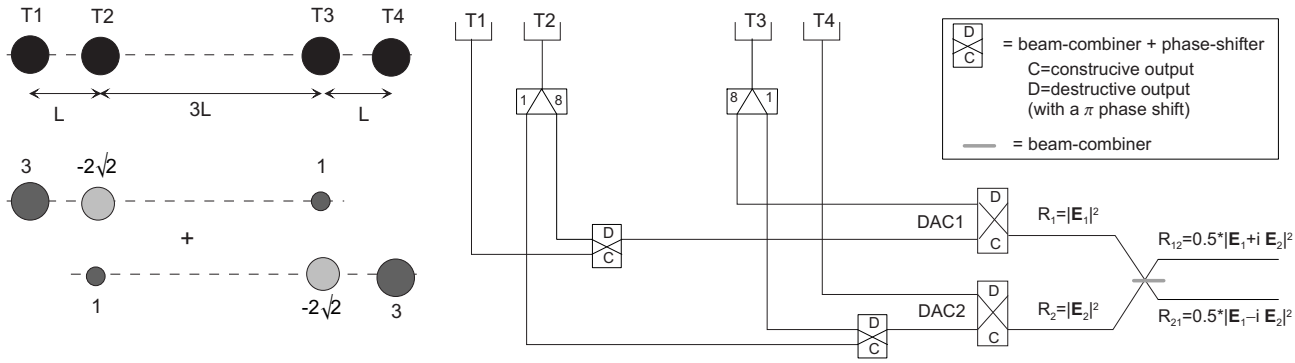

Figure 8.6: Left: The LinEqual configuration with its two sub-interferometers (Degenerated Angel Crosses) and the relative signed amplitudes for each beam. Right: Beam combination scheme for the LinEqual interferometer. The final outputs are characterised by their transmission maps R_{12} and R_{21}.

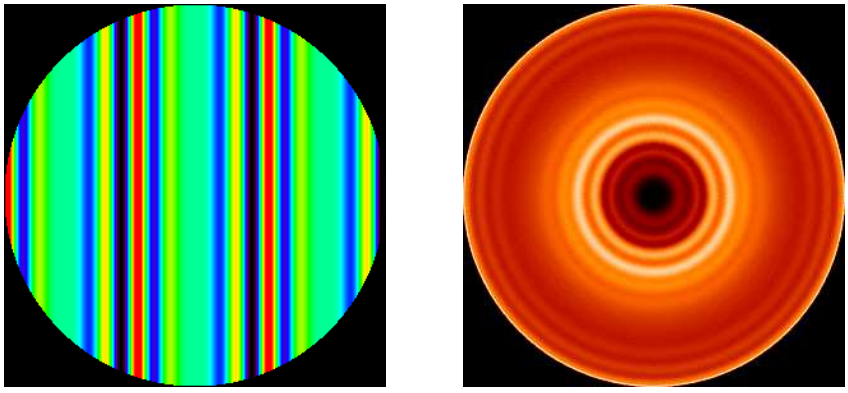

Figure 8.7: Left: Modulation map of the LinEqual interferometer over a 300 × 300 mas field-of-view for an array length of 100 m and an observing wavelength of 10 μm (same colour code as in Figure 8.5). Right: Standard deviation of the modulation efficiency computed on each point of the field-of-view while rotating the interferometer around its line-of-sight.

of linear configurations. The maximum modulation efficiency of LinEqual is 67%, almost the same as for the bow-tie. Its mean modulation efficiency across the 300×300 mas field-of-view reaches 19%, making LinEqual somewhat more efficient than the bow-tie during the detection phase, where the planet position is unknown and the whole field-of-view has to be investigated. A continuous rotation of the interferometer around its line of-sight is used to get a uniform sky coverage, as shown on the right-hand side of Figure 8.7. In order to keep the separation between free-flying spacecrafts larger than 20 meters, an array length of 100 meters is needed. Assuming a working wavelength of 10 μm as usual, the maximum modulation efficiency is reached at about 60 mas from the optical axis, which makes this configuration appropriate for habitable planet detection around Sun-like stars at 10 pc and farther.

8.1.4 Principle of inherent modulation

We have seen how internal modulation uses two asymmetric transmission maps conjugated to each other to modulate the planetary signal without modulating the other sources (star, exozodiacal disk and background). Keeping this basic principle, a new way to produce the conjugated maps is proposed here. The principle of this technique, called *inherent modulation*, is to combine a number of beams using two opposite sets of phase shifts to produce the two output signals (Figure 8.8). The final beam combiner, which was used to produce the two conjugated maps, is not required any more. With inherent modulation, the two outputs are not formed simultaneously, but one after another: all the light is alternately sent to a set of phase shifting devices or to the other (Figure 8.9). Alternately, all the beams can be divided into two equal parts and combined with two different schemes producing the two outputs simultaneously. In any case, this property restricts the modulation efficiency of inherent modulation to a maximum of only 50%, as the planetary signal will be detected only half of the time (or alternately, with only half of the collected beams). A way to mitigate this limitation will be discussed in Section 8.2.2.

It is noteworthy that some of the achromatic phase shifts are different from 0 or π and that they are generally not fractions of π. The entrance pupil of the interferometer is thus complex, which means that the amplitudes of the telescopes are multiplied by a set of complex coefficients $e^{i\phi_k}$ before beam combination. A complex entrance pupil is a necessary—and almost sufficient—condition to get an asymmetric transmission map (Absil 2001). As in the case of internal modulation the two transmission

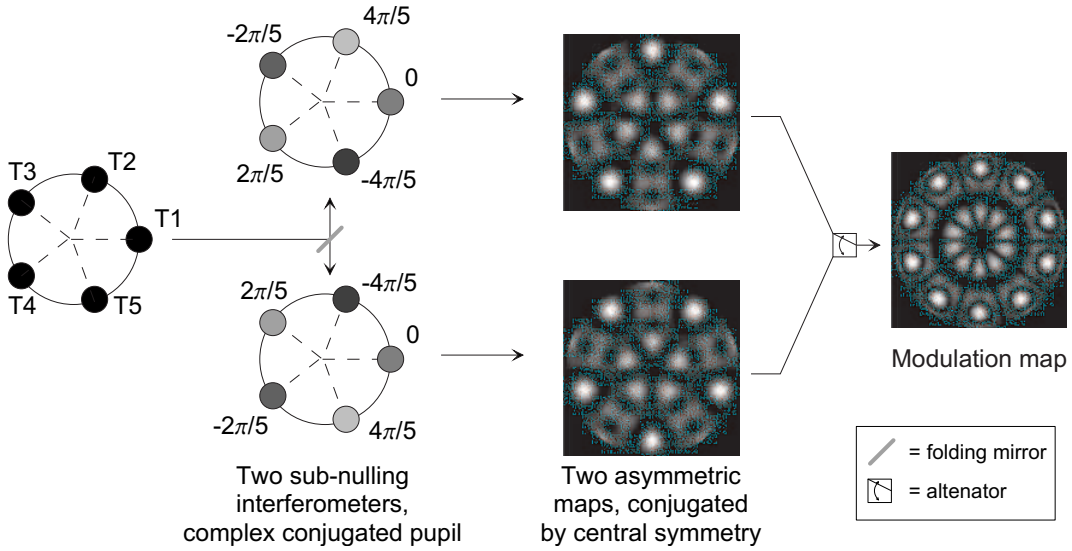

Figure 8.8: Principle of inherent modulation. Only one interferometer is used at a time.

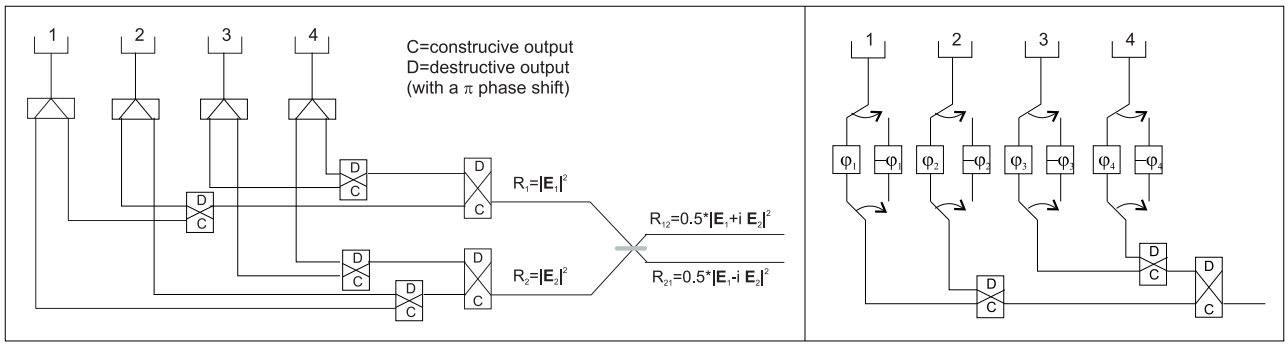

Figure 8.9: Beam combination schemes for internal (left) and inherent (right) modulations in the case of a four-telescope linear array. The number of beam combinations is reduced from seven to three by using inherent modulation.

maps are conjugated to each other by point symmetry, as proven by means of Equation 8.1:

$$\begin{aligned} R_1(\theta, \alpha+\pi) &= \left| \sum_{k=1}^{n} A_k e^{-i2\pi(L_k\theta/\lambda)\cos(\delta_k-\alpha)}\, e^{i\phi_k} \right|^2 \\ &= \left| \sum_{k=1}^{n} A_k e^{i2\pi(L_k\theta/\lambda)\cos(\delta_k-\alpha)}\, e^{-i\phi_k} \right|^2 \\ &= |\overline{\mathbf{E}}_2(\theta,\alpha)|^2 = R_2(\theta,\alpha) \end{aligned}$$

A major advantage of inherent modulation is the relative simplicity of its beam combination scheme. This is illustrated in Figure 8.9, where two similar linear arrays using internal and inherent modulations are compared. With inherent modulation, the beam splitters are replaced by folding mirrors. Eight phase-shifting devices and three beam combiners are used instead of six beam combiners and associated phase shifters followed by another beam combiner. The number of phase-shifting devices can sometimes be reduced if some of the ϕ_i are equal to some of the $-\phi_j$, which is the case in the example of Figure 8.8.

8.1.5 High-rejection configurations with inherent modulation

It can be demonstrated that all configurations based on internal modulation can also be implemented with inherent modulation. In order to derive the sets of phase shifts and amplitudes for inherent modulation, starting from a known configuration with internal modulation, the contributions from each telescope in the two final outputs have to be computed in terms of amplitude and phase. These amplitudes and phases must then be directly applied to the inherent modulation beam combination scheme.

For instance, all Robin Laurance configurations can be implemented with inherent modulation. However, a major difference comes from the beam combination scheme: circular arrays with a complex entrance pupil can achieve the necessary θ^4 central transmission only if five telescopes or more are used (Absil 2001). Combining five telescopes at the same time forces to use a third order beam combination scheme (Mennesson & Mariotti 1997). This type of configurations have a *beam combination efficiency*[19] of only 5/8 while it is equal to 1 for a four-telescope array. Therefore, the modulation efficiency of circular arrays with inherent modulation is generally low.

If a θ^4 central transmission is required to achieve a high rejection rate, linear configurations will therefore be preferred to circular ones in the case of inherent modulation. In order to achieve a θ^4

[19]The beam combination efficiency is the maximum constructive interference one can expect from a given beam combination scheme, disregarding the geometric arrangement of the telescopes (Mennesson & Mariotti 1997).

	T1	T2	T3	T4
Relative diameter	$D_1 = 0.65$	$D_2 = 1$	$D_3 = 1$	$D_4 = 0.65$
Position	$L_1 = 0$ m	$L_2 = 20$ m	$L_3 = 40$ m	$L_4 = 60$ m
Phase shift	$\phi_1 = -0.511$	$\phi_2 = 3.142$	$\phi_3 = 1.267$	$\phi_4 = 4.920$

Table 8.1: Description of the LinOpt configuration, based on four aligned and equally spaced telescopes.

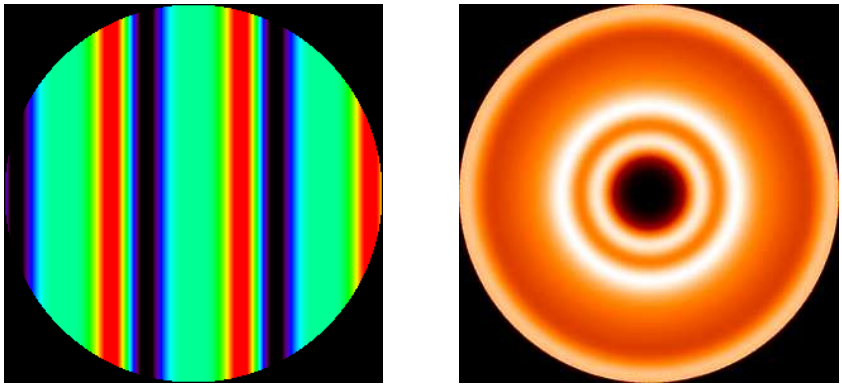

Figure 8.10: Left: Modulation map of the LinOpt interferometer over a 300×300 mas field-of-view for an array length of 60 m and an observing wavelength of 10 μm (same colour code as in Figure 8.5). Right: Standard deviation of the modulation efficiency computed on each point of the field-of-view while rotating the interferometer around its line-of-sight.

transmission with a complex-pupil linear array, only four telescopes are required (Absil 2001). The second order beam combination scheme used for four-telescope arrays make them very attractive because the amount of light lost during the beam combination process is much lower than for five-telescope arrays. Their efficiency is thus expected to be higher than for circular arrays. Our systematic search for high-efficiency configurations has resulted in the linear configuration described in Table 8.1, which we have called *LinOpt*. It is composed of two big and two small telescopes (diameter ratio of 0.65), placed at equal distances from each other as represented in Figure 8.3. It must be noted that, in order to reduce the manufacturing costs and to match the diffraction-limited fields-of-view, the four telescopes will most probably have the same diameter and the relative amplitudes of the beams will be obtained by using 65/35 beam splitters in the beam combination scheme.

The maximum modulation efficiency of the LinOpt configuration is 46% and its mean efficiency 14% on a 300×300 mas field-of-view. Its modulation map is presented in Figure 8.10, showing two maxima located at 40 and 70 mas from the centre for an array length of 60 m. The beam combination scheme of LinOpt is presented on the right-hand side of Figure 8.9. Eight phase-shifting devices and three beam combiners are needed to produce the final output. The LinOpt configuration is not as competitive as the bow-tie, but its much more simple implementation and its reduced number of telescopes also makes it a good candidate for the Darwin mission.

8.2 The resurgence of low-rejection configurations

The rationale for using high-rejection configurations for the Darwin mission, with central transmissions proportional to θ^4 or higher powers of the off-axis angle, was based on the fact that the mission was originally designed to give optimum performance on the closest targets. The inability to use very short baselines due to collision hazard prevents from tuning the baseline to these targets. Obtaining sufficiently deep stellar nulling ratios with θ^2 configurations is therefore not possible in these cases. In the past few

years, the general approach for the Darwin and TPF-I missions has changed. The main criterion for the choice of an interferometric architecture is now clearly identified as the capability to survey as many stars as possible for the presence of planets and to characterise as many of the detected planets within the mission lifetime. The redefinition of the criterion for an optimal architecture has lead to the resurgence of θ^2 configurations, as explained below.

8.2.1 The trade-off between low- and high-rejection configurations

In this section, we discuss the various criteria that come into play in the choice of an optimal architecture for the Darwin mission. The number of stars that can be surveyed during the mission lifetime is of course of utmost importance in this context.

Influence of stellar leakage on the survey capabilities

The basic principle of extrasolar planet detection with a nulling interferometer is to tune the baseline so as to place a bright fringe at the location of the planet while efficiently cancelling the stellar light. The deepest nulling ratios are reached when the planet is located on the first bright fringe of the transmission map. The achievable stellar rejection rate is therefore fixed by the geometry of the target system and the interferometer architecture.

For instance, considering a Sun-Earth system, the ratio between the star-planet angular separation at maximum elongation $\theta_{\max}$ and the stellar angular radius $\theta_\star$ is about 215. Using the simple Bracewell architecture described in Section 3.1.1, the baseline is therefore chosen as follows: $b = \lambda/2\theta_{\max} \simeq \lambda/430\theta_\star$. From Equation 3.11, we deduce that the stellar rejection rate will be about 5×10^5 for the Bracewell interferometer, provided that the baseline can be tuned as desired. On the other hand, the rejection rate achieved by a θ^4 configuration such as the Degenerate Angel Cross (Equation 3.16) is about 10^{11}. High-rejection configurations therefore make geometric stellar leakage completely negligible in the final noise budget, while low-rejection configurations do not achieve the required rejection rate of 10^7 to reveal the planetary signal. This is not a real problem as phase chopping will remove the mean contribution of stellar leakage, provided that the star is symmetric. The problem rather comes from the associated shot noise, which can be the dominant source of noise in the detection process.

The above discussion does not take into account the fact that the baseline cannot be safely set to lower values than 20 m due to collision hazard. For instance, when observing a Sun-Earth system at 10 pc, the angular separation of 100 mas at maximum elongation would require a baseline of 10 m for observations at 10 μm. Using the minimum baseline of 20 m, the stellar rejection rate would only reach about 10^5. However, as can be seen in Figure 8.11, the average angular separation between habitable Earth-like planets and their parent stars in the Darwin catalogue is smaller than 50 mas, so that baselines shorter than 20 m are not frequently requested.

The question that we have now to address is whether geometric stellar leakage becomes the main contributor to the shot noise when θ^2 configurations are used, and if yes, whether this significantly increases the total integration time. The answer is in Figure 8.12, where we have plotted the geometric stellar leakage as a function of wavelength together with the contribution of the local zodiacal dust emission, based on the model of Kelsall et al. (1998). The stellar leakage is computed for a Bracewell interferometer with a 20 m baseline for the two cases (G2V star at 10 pc and 20 pc). The figure shows that, for a typical Darwin target (G2V at 20 pc), the additional shot noise coming from imperfectly cancelled stellar light is not dominant for most of the waveband. On the other hand, for the closest and brightest targets, θ^2 configurations would produce significantly more shot noise and thereby require longer integration times.

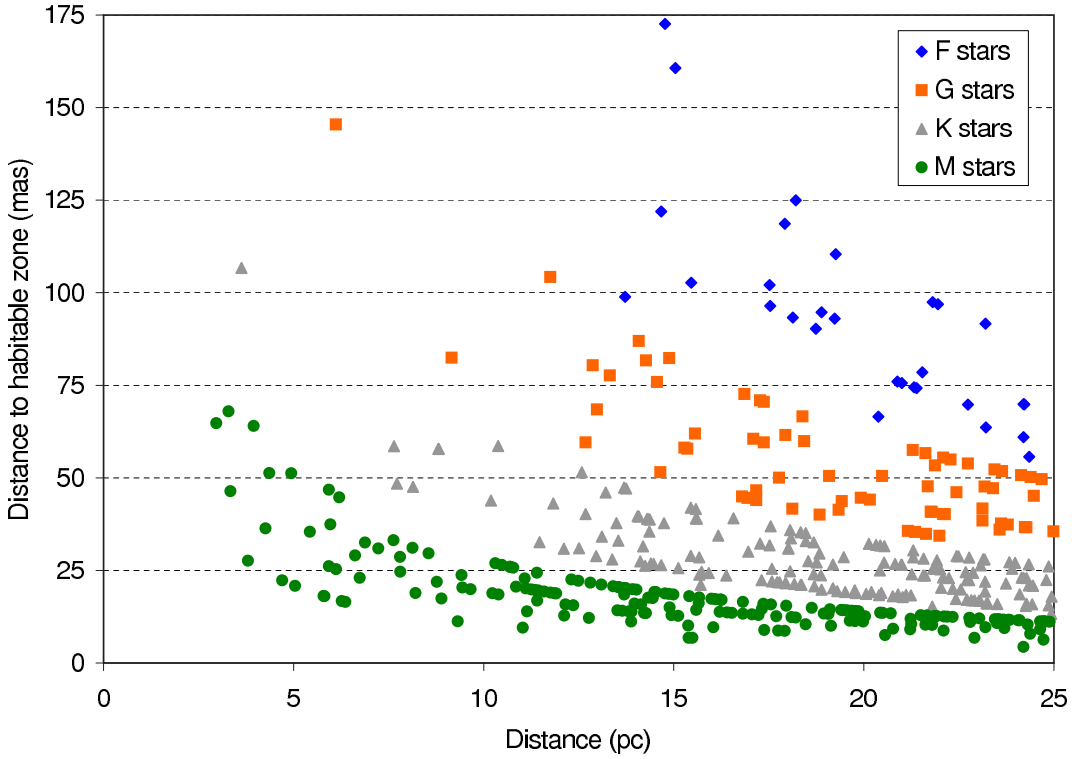

Figure 8.11: Angular distance between an habitable Earth-like planet and its parent star at maximum elongation for the stars of the extended Darwin catalogue. Adapted from Kaltenegger et al. (2006).

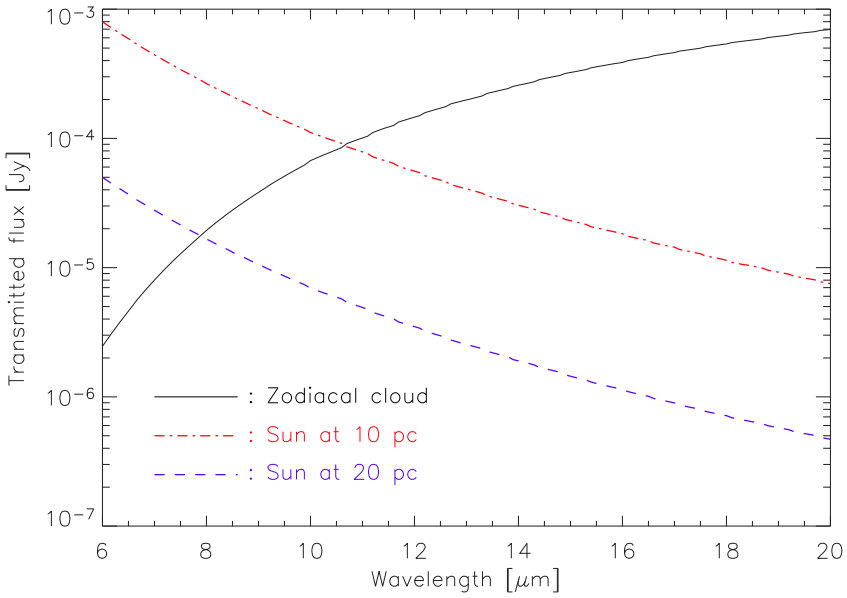

Figure 8.12: Transmitted fluxes for two potential target stars and the local zodiacal dust emission, assuming a Bracewell interferometer with a 20 m baseline in all cases.

A thorough study of the number of stars that can be surveyed during the mission lifetime with various architectures has been carried out by Dubovitsky & Lay (2004) and has lead to a seemingly unexpected conclusion: θ^2 configurations generally perform better than θ^4 configurations. The reason for this fact is double:

- Low-rejection configurations produce a significant amount of additional shot noise only for the closest stars, which are scarce and are also those for which the integration times are the shortest. Therefore, the penalty in total integration time is rather small.
- Low-rejection configurations generally have higher modulation efficiencies. The factors responsible for the lower modulation efficiency of the θ^4 configurations are lower fringe maxima and/or narrower bright fringes (Dubovitsky & Lay 2004).

In conclusion, low-rejection configurations are proven to be more efficient than the architectures with a central transmission proportional to θ^4 or higher. For instance, Dubovitsky & Lay (2004) show in their analysis that a Dual Chopped Bracewell architecture can survey up to twice as many stars as the bow-tie configuration. A possible drawback of the θ^2 configurations is that they are more sensitive to potential asymmetries in the stellar emission, which would lead to an imperfect subtraction of geometric stellar leakage by phase chopping. It is however not expected that stellar spots or oblateness might produce a significant contribution to residual stellar leakage after subtraction by phase chopping, because late-type main sequence stars are not expected to be very active nor distorted by rapid rotation.

Variability noise

In the above discussion, we have neglected another important source of noise in nulling interferometry: instrumental stellar leakage, which contributes both as a bias (referred to as *null floor* leakage), by introducing a non-null average amount of additional stellar light in the destructive output, and as a noise, which relates to its variability. Phase chopping techniques allow for the subtraction of the null-floor leakage, which is the same in the two chopped states provided that there is no systematic difference between them. The bias will therefore contribute only as an additional source of shot noise. On the other hand, most of the instrumental noise is not suppressed by phase chopping, as proven by Lay (2004). This contribution, referred to as *systematic noise* (Lay 2004) or *variability noise* (Chazelas et al. 2006), is dominated by nonlinear, second order terms related to the perturbations in the amplitudes, phases and polarisation angles of the electric fields from each telescope. The disturbance power spectra mix with each other so that perturbations at all frequencies, including DC, have an effect. Although a simple binary phase chop removes a number of these systematic errors, it has no effect on the dominant amplitude-phase cross terms and on the co-phasing errors. There is no phase chopping scheme that can remove the systematic errors without also removing the planet signal (Lay 2004).

Two independent studies (Lay 2004; Chazelas et al. 2006) have recently revisited the instrumental requirements on the Darwin and TPF-I missions in order to reduce instrumental stellar leakage down to a sufficiently low level for Earth-like planet detection. Both showed that the requirements on amplitude and phase control do not come from the null-floor leakage, but from variability noise. According to Lay (2004), the phase of the signal from each collector should be controlled to about 1 millirad ($\sim$ 1.5 nm at 10 μm) and the amplitude to about 0.1%. It must be noted that it is in fact impossible to obtain a stable null floor without also having a deep instrumental null, because instrumental perturbations are expected to have a significant dynamic component.

A major property of variability noise is that is does not depend on the actual architecture of the interferometer to the first order: θ^2 and θ^4 configurations produce similar amounts of variability noise if they are subject to the same amplitude and phase perturbations. Another major property is that variability noise significantly increases at short wavelengths. It is in fact expected that variability noise could exceed

shot noise at short wavelengths and become the dominant source of noise. This behaviour was already suggested in our study of the Pegase interferometer (see Figure 7.14). In that case, the advantage of θ^4 configurations with respect to θ^2 configurations would almost disappear.

Technical aspects

From the technical point of view, there are significant advantages in using low-rejection configurations. On one hand, they only require from three to four telescopes for the implementation of phase chopping techniques, while high-rejection configurations need at least four telescopes (five for circular architectures). This reduces not only the complexity and cost of the flight configuration, but also the amount of real-time control systems for the amplitude and phases of all beams. On the other hand, the advantage also comes from the simpler beam combination schemes of low-rejection configurations. For instance, a Double Chopped Bracewell only requires three pair-wise beam combinations with phase shifts restricted to 0 or π. The reduced amount of optical elements required to combine the beams should also lead to a sightly enhanced overall transmission. All these aspects improve the global feasibility of the mission while reducing its cost.

8.2.2 A new concept: the Three Telescope Nuller (TTN)

Following the resurgence of θ^2 configurations, an important effort has been undertaken to further study interferometric architectures with a reduced number of telescopes. On the NASA side, the investigations have mainly focused on Dual Bracewell architectures, such as the X-array (Lay & Dubovitsky 2004). On the European side, a new configuration based on inherent modulation with three telescopes has been proposed by Karlsson et al. (2004), and is now used as a mission model for Darwin. In this section, we briefly describe the design and performance of this configuration, the Three Telescope Nuller (TTN).

General design of the TTN

The TTN is based on the principle of inherent modulation. Three telescopes can be combined in a destructive way by adjusting their respective phases to 0°, 120° and 240° respectively, whatever their geometric arrangement. The second chopped state is obtained by taking the opposite phase shifts, i.e., 0°, 240° and 120° respectively. In principle, any geometric arrangement can be used for the three telescopes. However, in order to avoid the use of long delay lines, two configurations are preferred: the linear architecture with equally spaced telescopes and the equilateral triangle. They are illustrated in Figure 8.13, together with possible beam relay schemes for each arrangement. The linear configuration requires an additional beam combining spacecraft in order to avoid long delay lines, while the equilateral triangle can be implemented on three spacecrafts. Nevertheless, the right-most implementation of the triangular architecture (with a central beam combiner) is expected to be less complex than the three-spacecraft version.

The modulation map for the two versions of the TTN are illustrated in Figure 8.14 (linear version) and in Figure 8.15 (triangular version). It must be noted that the angular resolution of the triangular TTN is larger than that of the linear TTN for the same minimum separation of 20 m between individual collectors. This will be beneficial for the closest targets. On the other hand, the linear configuration has better imaging capabilities than the triangular one (Lay 2005). In particular, the threefold symmetry of the modulation map of the triangular TTN renders it unable to separate the contributions of planets lying at similar angular radii with 120° azimuthal offsets.

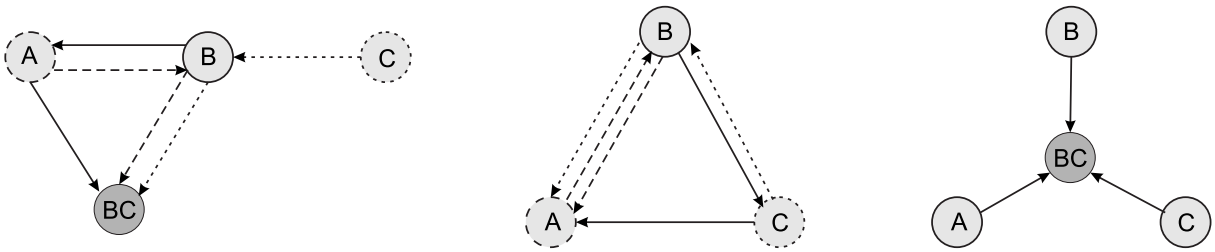

Figure 8.13: The three preferred geometric configurations for the TTN with their respective beam relay schemes. Reflections of the beam on neighbouring telescopes are necessary to equalise the optical paths before beam combination for the first two. An additional spacecraft, containing the beam combination optics (BC), is necessary in the case of the linear array in order to avoid the use of long delay lines. The right-most version of the triangular TTN with a central beam combiner spacecraft is currently considered as the Darwin mission model.

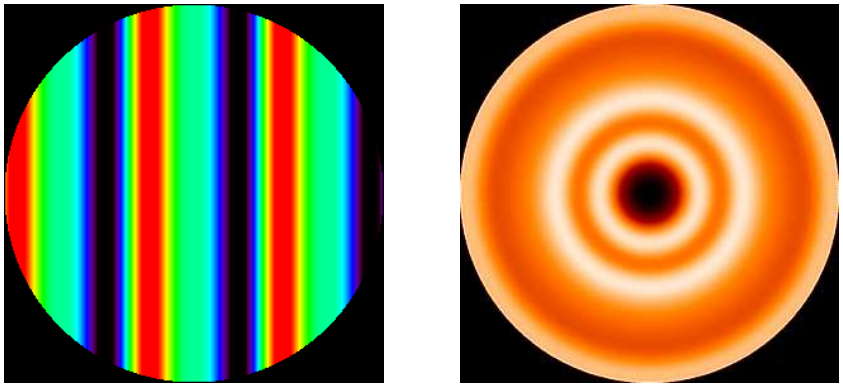

Figure 8.14: Left: Modulation map of the linear TTN interferometer over a 300×300 mas field-of-view for an array length of 40 m and an observing wavelength of 10 μm (same colour code as in Figure 8.5). Right: Standard deviation of the modulation efficiency computed on each point of the field-of-view while rotating the interferometer around its line-of-sight.

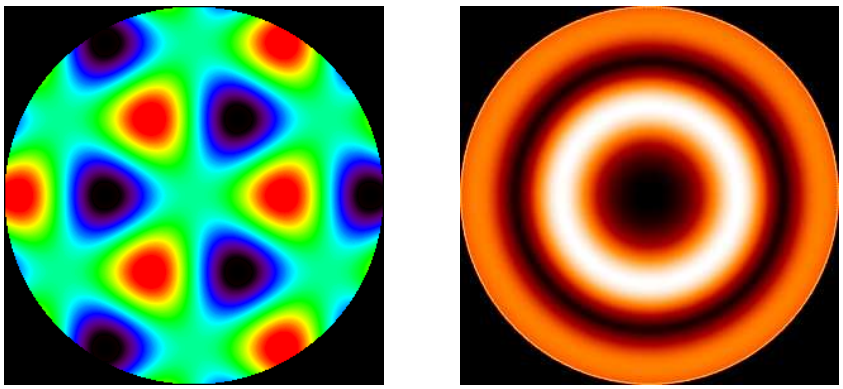

Figure 8.15: Left: Modulation map of the triangular TTN interferometer over a 300×300 mas field-of-view for a telescope separation of 20 m and an observing wavelength of 10 μm (same colour code as in Figure 8.5). Right: Standard deviation of the modulation efficiency on each point obtained by continuous rotation of the interferometer around its line-of-sight.

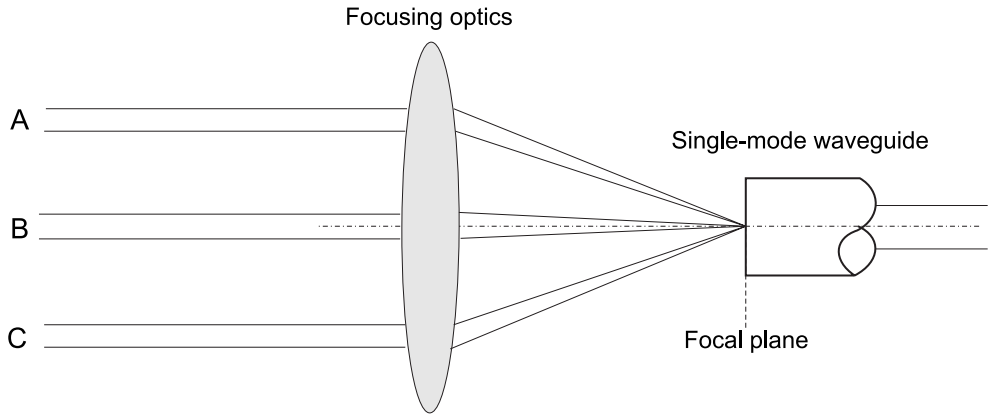

Figure 8.16: Principle of multi-axial single-mode beam combination (adapted from Wallner et al. 2004b).

Unfortunately, there is a limitation to the efficiency of three telescope configurations, which relates to the beam combination scheme. Ideally, the three telescopes should be combined at the same time, while only pair-wise beam combination is permitted when the combination has to be performed in a co-axial manner. A second order beam combination scheme is therefore necessary for the TTN. Since half of the beam intensity is lost at each pair-wise beam combination, the intensity of the third beam will have to be reduced by a factor 2 before being mixed with the output of the first beam combiner. In fact, it can be shown that if a number n of telescopes have to be combined with a pair-wise scheme, the global beam combination efficiency is given by $n/2^m$, where m is the order of the beam combination scheme (Mennesson & Mariotti 1997). A three telescope beam combination scheme has therefore an efficiency of 75% only, while configurations with two or four telescopes have an efficiency of 100%.

Multi-beam injection into single-mode fibres

In order to circumvent the low efficiency of classical pair-wise beam combination schemes in the case of three telescopes, a new beam combination technique has been proposed by Wallner et al. (2004b), which incorporates the functionalities of beam combination and modal filtering in a single device. It relies on the multi-axial injection of the three beams in the same single-mode waveguide, by focusing them onto the input face of, e.g., a single-mode optical fibre (see Figure 8.16). Because the amplitudes of each beam are projected on the same fundamental mode of the fibre, co-axial beam combination[20] is obtained inside the fibre, by overlapping the complex amplitudes of the three beams. If all the beams have the same spacing from the optical axis, they couple into the fibre with the same coupling efficiency because the fibre mode is symmetric with respect to the fibre axis. Similarly, the effect of phase front tilt cancels out by symmetry. This original beam combination technique has recently been validated in the laboratory by Haguenauer & Serabyn (2006), showing deep nulling of monochromatic light close to the 10^{-6} level.

The efficiency of this beam combination scheme mainly depends on the arrangement of the input beams and on the injection efficiency as a function of the off-axis angle. Wallner et al. (2004b) have shown that the insertion loss is minimum for a three-beam arrangement where the beams are jointed (see Figure 8.17) and equals 33% in that case. This loss has to be compared with the classical 20% loss experienced when injecting a single beam into a single-mode waveguide. The actual loss is therefore only about 13%. This loss can even be cancelled by cutting the input pupils into several equal segments and by arranging them to synthesise a single circular pupil (Figure 8.17).

[20] Remember that multi-axial beam combination cannot be used in nulling interferometry, because it would result in a fringe pattern where stellar light would alternately interfere constructively and destructively (Section 3.1.1).

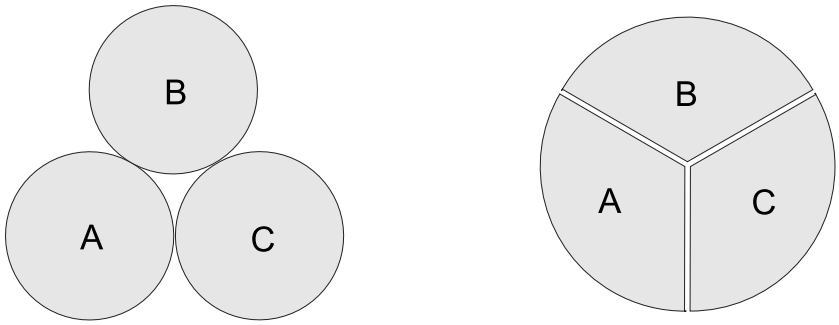

Figure 8.17: Two possible layouts of the input pupil applied at the entrance of the single-mode waveguide. In the case of the right-hand side configuration, two other pupils are constructed in the same way with the two other thirds of each beam (Karlsson et al. 2004).

In the context of Darwin, mid-infrared single-mode waveguides are required for the implementation of this new technique. It must be noted that the manufacturing of such components is still very challenging nowadays, even though the results obtained by several teams around the world are very encouraging (see e.g. Bordé et al. 2003a; Wallner et al. 2004a; Drouet D'Aubigny et al. 2004; Labadie et al. 2006).

Modulation efficiency

Even with multi-beam injection, the modulation efficiency of the TTN is still rather low (maximum efficiency of 50%) due to the limitation of inherent modulation discussed in Section 8.1.4. In order to circumvent the fact that the planetary signal is only detected half of the time in the classical inherent modulation scheme, an original beam combination scheme has been proposed for the TTN (Karlsson et al. 2004). Instead of dividing the amplitudes of each beam into two equal parts before producing the two complementary outputs, which does not improve the global efficiency of the modulation scheme, the idea is to combine the beams pair-wise before combining them by multi-beam injection using the appropriate phase shifts (0°, 120° and −120°). The pair-wise beam combiners placed at the first stage of the beam combination process produce complementary outputs with a ±90° phase shift between the input beams.

Following the beam combination scheme proposed in Figure 8.18, let us work out the final expression of the electric field in the right-hand side output:

$$\begin{aligned}\mathbf{E}_2 &= \frac{1}{2}\left(\mathbf{E}_\mathrm{C}(-120^\circ)+\mathbf{E}_\mathrm{A}(-30^\circ)\right)+\frac{1}{2}\left(\mathbf{E}_\mathrm{A}(0^\circ)+\mathbf{E}_\mathrm{B}(90^\circ)\right)+\frac{1}{2}\left(\mathbf{E}_\mathrm{B}(120^\circ)+\mathbf{E}_\mathrm{C}(-30^\circ)\right)\\ &= 0.966\left(\mathbf{E}_\mathrm{A}(-15^\circ)+\mathbf{E}_\mathrm{B}(105^\circ)+\mathbf{E}_\mathrm{C}(-135^\circ)\right)\end{aligned}$$

In this expression, only the relative phases of the beams matter (their absolute phase is arbitrary). Computing the expression of the left-hand side output in the same way, one ends up with the following intensities in the two chopped states:

$$\begin{aligned}I_1 &= 0.933\left|\mathbf{E}_\mathrm{A}(0^\circ)+\mathbf{E}_\mathrm{B}(-120^\circ)+\mathbf{E}_\mathrm{C}(120^\circ)\right|\\ I_2 &= 0.933\left|\mathbf{E}_\mathrm{A}(0^\circ)+\mathbf{E}_\mathrm{B}(120^\circ)+\mathbf{E}_\mathrm{C}(-120^\circ)\right|\end{aligned}$$

The two complementary outputs of the inherent modulation scheme have thus been produced simultaneously thanks to this original beam combination scheme, with a beam combination efficiency of 93.3% instead of 50% for the classical implementation of inherent modulation. The maximum modulation efficiency, both in the linear and equilateral architectures, is then equal to 93.3%. The mean modulation efficiency is about 45% for the linear architecture and about 33% for the equilateral one. If the beams

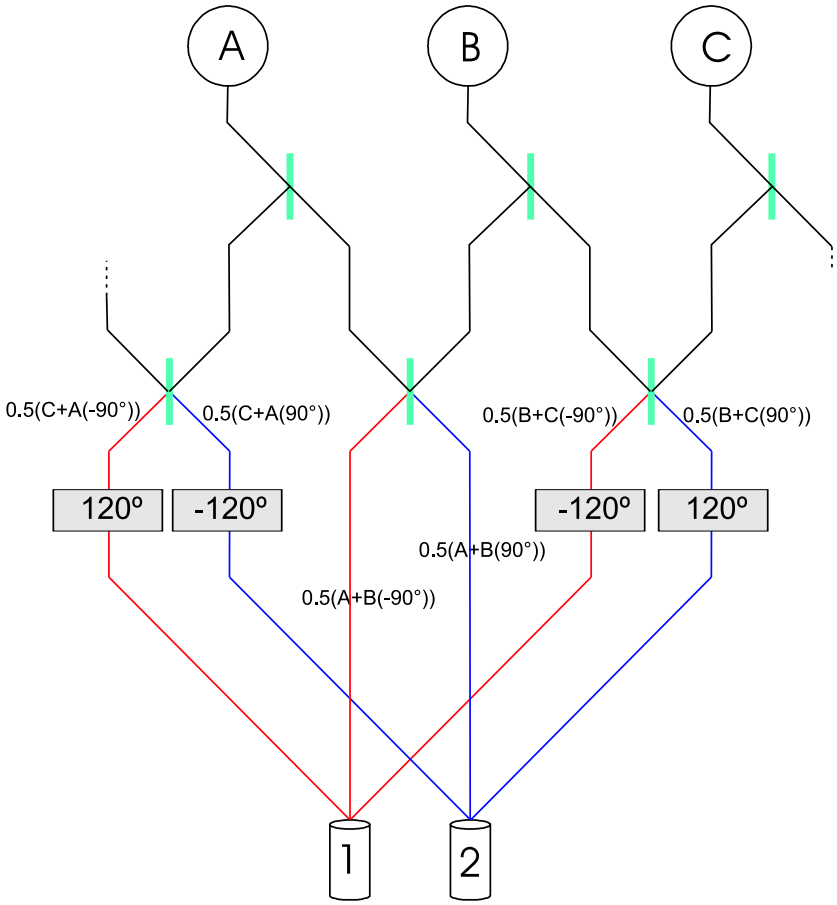

Figure 8.18: Modified beam combination scheme for the TTN, adapted from Karlsson et al. (2004). Each beam is divided into two equal parts before being combined pair-wise with each of its neighbours. The six outputs beam are then phase shifted and injected three by three into single-mode waveguides to produce the final outputs.

are combined as shown on the left-hand side of Figure 8.17, these figures have to be reduced by 13% to account for the injection loss, but they still remain amongst the highest for the architectures investigated so far. The high modulation efficiency however comes at the expense of increased technical complexity with respect to the original implementation of inherent modulation.

The only known configurations giving better modulation efficiencies are the Dual Chopped Bracewell interferometers (Lay 2005), which provide maximum efficiencies up to 100%. The TTN may still outperform these four-telescope configurations due to the fact that fewer spacecraft are used, thereby allowing a larger mass allocation to the telescopes and thus potentially a larger overall collecting area. The overall performance and design of the TTN makes it very appropriate in the context of Earth-like planet detection and characterisation, so that this configuration is now taken as a mission model for Darwin.

Conclusion

Objectives and results

The past 30 years have seen tremendous advances in stellar interferometry, from the deployment of two 25-cm telescopes separated by 12 m in the original experiment of Labeyrie (1975), to the recent advent of large interferometric facilities such as the Very Large Telescope Interferometer, comprising four 8-m telescopes arranged on hectometric baselines. The scientific outcome of stellar interferometers has also increased dramatically during the last decade, with e.g. more than 30 observation-based refereed papers published in 2005 on topics such as stellar modelling, circumstellar envelopes around evolved stars, accretion disks around young stars, multiple stellar systems, and even active galactic nuclei. Still, the full potential of stellar interferometry has yet to be exploited. One of the major improvements of interferometric facilities for the years to come will be the development of their high dynamic range capabilities. An improved dynamic range would be beneficial to the numerous scientific applications where faint structures are to be detected in the vicinity of bright objects, such as dust disks and extrasolar planets around nearby stars for instance. It was the purpose of this work to contribute to this development, in both its technical and astrophysical aspects.

As a first contribution, we have demonstrated the capabilities of existing interferometric instruments to achieve high-contrast imaging. Using the FLUOR near-infrared beam combiner installed at the CHARA Array, we have detected the presence of warm dust in the first few astronomical units (AU) around Vega, which was already known to harbour significant amounts of cold dust located at about 85 AU (Chapter 2). This discovery has not only proven that circumstellar dust can be present in the inner part of debris disks, where terrestrial planets are thought to have formed, but also has demonstrated that a dynamic range of 1:100 can be achieved by state-of-the-art single-mode infrared interferometers. The precision on the inferred contrast between the disk and the star ($1.29 \pm 0.19\%$) further indicates that a dynamic range up to 1:500 is within reach.

Because the expected contrast between stars and planets is generally much larger than 10^3, current interferometers however will not provide the required performance level to characterise a large sample of planetary systems. The rest of our work thus focused on the development of nulling interferometry, a technique providing both high dynamic range and high angular resolution in the visible and infrared regimes. The bulk of the work concerns the future Ground-based European Nulling Interferometer Experiment (GENIE), to be installed at the VLTI (Cerro Paranal, Chile). We have contributed both to the design (Chapters 3 and 4) and the science case (Chapter 5) of this instrument, with a particular emphasis on a thorough study of its expected performance. An end-to-end simulation software has been developed for that specific purpose, taking into account in a realistic way all environmental aspects, including atmospheric turbulence, background emission and instrumental effects. With the help of this simulator, we have demonstrated that GENIE will be capable of detecting circumstellar features as faint as a few 10^{-4} of the stellar flux. Such performance will not only allow for a detailed study of debris disks around main sequence stars, but will also open the way to spectroscopy of hot extrasolar planets (Chapter 5). The same simulator has then been adapted to the particular atmospheric conditions on the high Antarc-

tic plateau (Dome C) to assess the performance of an optimised nulling interferometer dedicated to the detection of faint circumstellar disks (Chapter 6).

Finally, in the last two chapters of this dissertation, we have discussed the implementation of nulling interferometry in the context of two space-based missions: Pegase and Darwin. Concerning the former, we have strongly contributed to the study of the science case, which mainly focuses on hot extrasolar giant planets (Chapter 7). Our performance analysis demonstrates that low-resolution spectroscopy will be possible for about 20 known extrasolar planets with masses similar to or larger than that of Uranus. As for the latter, we have proposed new interferometric architectures which significantly improve the efficiency and feasibility of the Darwin mission (Chapter 8).

Perspectives

The direct detection of Earth-like extrasolar planets orbiting nearby stars and the search for key tracers of biological activity in their atmospheres are high-priority objectives in the long-term science plan of ESA as well as of NASA. By demonstrating the high dynamic range capabilities of infrared (nulling) interferometers, we contribute to the road map towards future space missions dedicated to the detection and characterisation of Earth-like planets. The proven capability of interferometry to detect faint structures in the vicinity of bright objects also opens the path towards major advances in various fields of astrophysics. In particular, two prominent aspects of extrasolar planetary systems have been considered in this dissertation.

- **Characterisation of warm debris disks.** The study of warm dust in the inner regions of debris disks is important for two main reasons. On the one hand, the prevalence of dust in the habitable zones around nearby main sequence stars is a crucial parameter for the design of future life-finding missions such as Darwin. On the other hand, the ongoing observing efforts will provide significant insights on the formation and evolution of planetary systems. Our first result on Vega has already allowed for the composition and size of warm dust grains to be evaluated. By complementing our observations in various ways (interferometry at other infrared wavelengths, mid-infrared imaging and spectroscopy), we will be able to better constrain the production and dynamics of dust grains around Vega. Furthermore, the survey of nearby debris disks that we plan to carry out in the coming years will not only bring much-needed statistical information on the presence of warm dust in suspected planetary systems, but will also identify suitable targets for detailed studies.
- **Spectroscopy of hot extrasolar planets.** According to our performance assessments in the case of GENIE and Pegase, the prospects are very good for obtaining in the near-term future low-resolution near-infrared spectra of hot extrasolar giant planets. This breakthrough will open a new field of science, viz. comparative exo-planetology, by giving access to the composition of extrasolar planetary atmospheres. In this context, the combination of nulling interferometry with colour differential techniques should be further investigated in order to mitigate the calibration issues faced by nulling interferometry.

The present work also offers a glimpse of the future of interferometry. It provides the required material and tools to compare the performance of infrared interferometric instruments installed at ground-based sites (temperate or Antarctic) with respect to their space-borne counterparts. Such a comparison is a crucial element in the perspective for next generation interferometers (Absil & Mawet 2006).

Bibliography

Absil, O., 2001, *Nulling Interferometry with IRSI-Darwin: Detection and Characterization of Earth-like Exoplanets*, Diploma thesis, University of Liège, http://vela.astro.ulg.ac.be/themes/telins/harigs/.

Absil, O., 2003, *GENIEsim: the GENIE Science Simulator*, Master thesis, University of Liège, http://vela.astro.ulg.ac.be/themes/telins/harigs/.

Absil, O., Augereau, J.-C., den Hartog, R. et al., 2005, GENIE: high-resolution study of debris disks, in *The Power of Optical/IR Interferometry: Recent Scientific results and Second Generation VLTI Instrumentation*, in press.

Absil, O., Bakker, E. J., Schöller, M. & Gondoin, P., 2004a, Thermal background fluctuations at 10 micron measured with VLTI/MIDI, in *New Frontiers in Stellar Interferometry* (W. Traub, ed.), *Proc. SPIE*, vol. 5491, 1320–1332.

Absil, O., den Hartog, R., Gondoin, P. et al., 2006a, Performance study of ground-based infrared Bracewell interferometers – Application to the detection of exozodiacal dust disks with GENIE, *Astron. & Astrophys.* in press.

Absil, O., di Folco, E., Mérand, A. et al., 2006b, Circumstellar material in the Vega inner system revealed by CHARA/FLUOR, *Astron. & Astrophys.* in press.

Absil, O., Kaltenegger, L., Eiroa, C. et al., 2003a, Can GENIE characterize debris disks around nearby stars?, in *Toward Other Earths: Darwin/TPF and the Search for Extrasolar Terrestrial Planets*, vol. SP-539, 323–328, ESA's Publication Division.

Absil, O., Karlsson, A. & Kaltenegger, L., 2003b, Inherent modulation: a fast chopping method for nulling interferometry, in *Interferometry in Space* (M. Shao, ed.), *Proc. SPIE*, vol. 4852, 431–442.

Absil, O., Léger, A., Ollivier, M. et al., 2004b, Pegase: a space interferometer for the spectro-photometry of Pegasides, in *The 37th Liège International Astrophysical Colloquium* (J. Surdej, D. Caro & A. Detal, eds.), 184–190.

Absil, O. & Mawet, D., 2006, Perspectives for next generation ground- and space-based interferometers, in *Towards Other Worlds*, Proc. JENAM, in press.

Agabi, A., Aristidi, E., Azouit, M. et al., 2006, First whole atmosphere night-time seeing measurements at Dome C, Antarctica, *Publ. of the Astron. Soc. Pac.* in press.

Akeson, R. L., Boden, A. F., Monnier, J. D. et al., 2005a, Keck Interferometer observations of classical and weak line T Tauri stars, *Astrophysical Journal* **635**, 1173–1181.

Akeson, R. L., Ciardi, D. R., van Belle, G. T. & Creech-Eakman, M. J., 2002, Constraints on Circumstellar Disk Parameters from Multiwavelength Observations: T Tauri and SU Aurigae, *Astrophysical Journal* **566**, 1124–1131.

Akeson, R. L., Ciardi, D. R., van Belle, G. T. et al., 2000, Infrared Interferometric Observations of Young Stellar Objects, *Astrophysical Journal* **543**, 313–317.

Akeson, R. L., Walker, C. H., Wood, K. et al., 2005b, Observations and Modeling of the Inner Disk Region of T Tauri Stars, *Astrophysical Journal* **622**, 440–450.

Angel, J. R. P., 1990, Use of a 16-m Telescope to Detect Earthlike Planets, in *The Next Generation Space Telescope* (P.-Y. Bely, C. Burrows & G. Illingworth, eds.), 81–88, Space Telescope Science Institute, Baltimore.

Angel, J. R. P. & Woolf, N. J., 1997, An Imaging Nulling Interferometer to Study Extrasolar Planets, *Astrophysical Journal* **475**, 373–379.

Aristidi, E., Agabi, A., Fossat, E. et al., 2005a, Site testing in summer at Dome C, Antarctica, *Astron. & Astrophys.* **444**, 651–659.

Aristidi, E., Agabi, A., Vernin, J. et al., 2003, Antarctic site testing: First daytime seeing monitoring at Dome C, *Astron. & Astrophys.* **406**, L19–L22.

Aristidi, E., Agabi, K., Azouit, M. et al., 2005b, An analysis of temperatures and wind speeds above Dome C, Antarctica, *Astron. & Astrophys.* **430**, 739–746.

Arsenault, R., Donaldson, R., Dupuy, C. et al., 2004, MACAO-VLTI adaptive optics systems performance, in *Advancements in Adaptive Optics* (D. B. Calia, B. L. Ellerbroek & R. Ragazzoni, eds.), *Proc. SPIE*, vol. 5490, 47–58.

Aufdenberg, J. A., Mérand, A., Coudé du Foresto, V. et al., 2006, First Results from the CHARA Array VII: Limb-Darkening Observations of Vega Consistent with a Pole-on, Rapidly Rotating Star, *Astrophysical Journal* submitted.

Augereau, J. C., Lagrange, A. M., Mouillet, D. et al., 1999, On the HR 4796 A circumstellar disk, *Astron. & Astrophys.* **348**, 557–569.

Aumann, H., Beichman, C., Gillett, F. et al., 1984, Discovery of a shell around Alpha Lyrae, *Astrophysical Journal, Letters* **278**, L23–L27.

Aumann, H. H., 1988, Spectral class distribution of circumstellar material in main-sequence stars, *Astronomical Journal* **96**, 1415–1419.

Aumann, H. H. & Probst, R. G., 1991, Search for Vega-like nearby stars with 12 micron excess, *Astrophysical Journal* **368**, 264–271.

Backman, D. E. & Paresce, F., 1993, Main-sequence stars with circumstellar solid material - The VEGA phenomenon, in *Protostars and Planets III*, 1253–1304.

Backman, D. E., Witteborn, F. C. & Gillett, F. C., 1992, Infrared observations and thermal models of the Beta Pictoris disk, *Astrophysical Journal* **385**, 670–679.

Baraffe, I., Chabrier, G., Barman, T. S. et al., 2003, Evolutionary models for cool brown dwarfs and extrasolar giant planets. The case of HD 209458, *Astron. & Astrophys.* **402**, 701–712.

Baraffe, I., Chabrier, G., Barman, T. S. et al., 2005, Hot-Jupiters and hot-Neptunes: A common origin?, *Astron. & Astrophys.* **436**, L47–L51.

Barillot, M., 2004a, Performance and Specifications – Acceptance and Tests plan, *Tech. Rep. GENIE-ASP-RP-007*, Alcatel Space, Darwin-GENIE Definition Phase.

Barillot, M., 2004b, Trade-off, Optical Layout, Design and Performance description of GENIE Candidate Concepts, *Tech. Rep. GENIE-ASP-RP-023*, Alcatel Space, Darwin-GENIE Definition Phase.

Barman, T. S., Hauschildt, P. H. & Allard, F., 2001, Irradiated Planets, *Astrophysical Journal* **556**, 885–895.

Barman, T. S., Hauschildt, P. H. & Allard, F., 2005, Phase-Dependent Properties of Extrasolar Planet Atmospheres, *Astrophysical Journal* **632**, 1132–1139.

Barrado y Navascués, D., 1998, The Castor moving group. The age of Fomalhaut and Vega, *Astron. & Astrophys.* **339**, 831–839.

Beaulieu, J.-P., Bennett, D. P., Fouqué, P. et al., 2006, Discovery of a cool planet of 5.5 Earth masses through gravitational microlensing, *Nature* **439**, 437–440.

Beichman, C. A., Bryden, G., Gautier, T. N. et al., 2005a, An Excess Due to Small Grains around the Nearby K0 V Star HD 69830: Asteroid or Cometary Debris?, *Astrophysical Journal* **626**, 1061–1069.

Beichman, C. A., Bryden, G., Rieke, G. H. et al., 2005b, Planets and Infrared Excesses: Preliminary Results from a Spitzer MIPS Survey of Solar-Type Stars, *Astrophysical Journal* **622**, 1160–1170.

Beichman, C. A., Woolf, N. J. & Lindensmith, C. A. (eds.) , 1999, *The Terrestrial Planet Finder (TPF): a NASA Origins Program to search for habitable planets*, JPL Publication 99-3, Pasadena.

Berger, J.-P., Haguenauer, P., Kern, P. Y. et al., 2003, An integrated-optics 3-way beam combiner for IOTA, in *Interferometry in Optical Astronomy II* (W. Traub, ed.), *Proc. SPIE*, vol. 4838, 1099–1106.

Boden, A. F., 2000, Elementary Theroy of Interferometry, in *Principles of Long Baseline Stellar Interferometry* (P. R. Lawson, ed.), 9–29, JPL Publications, Pasadena.

Bodenheimer, P., Lin, D. N. C. & Mardling, R. A., 2001, On the Tidal Inflation of Short-Period Extrasolar Planets, *Astrophysical Journal* **548**, 466–472.

Bordé, P., Perrin, G., Amy-Klein, A. et al., 2003a, Updated results on prototype chalcogenide fibers for 10 μm wavefront spatial filtering, in *Toward Other Earths: Darwin/TPF and the Search for Extrasolar Terrestrial Planets*, vol. SP-539, 371–374, ESA's Publication Division.

Bordé, P., Rouan, D. & Léger, A., 2003b, Exoplanet detection capability of the COROT space mission, *Astron. & Astrophys.* **405**, 1137–1144.

Boss, A. P., 1998, Evolution of the Solar Nebula. IV. Giant Gaseous Protoplanet Formation, *Astrophysical Journal* **503**, 923–937.

Bouchy, F., Udry, S., Mayor, M. et al., 2005, ELODIE metallicity-biased search for transiting Hot Jupiters. II. A very hot Jupiter transiting the bright K star HD 189733, *Astron. & Astrophys.* **444**, L15–L19.

Bracewell, R. N., 1978, Detecting nonsolar planets by spinning infrared interferometer, *Nature* **274**, 780.

Burrows, A., Hubeny, I., Hubbard, W. B. et al., 2004, Theoretical Radii of Transiting Giant Planets: The Case of OGLE-TR-56b, *Astrophysical Journal, Letters* **610**, L53–L56.

Burrows, A., Marley, M., Hubbard, W. B. et al., 1997, A Nongray Theory of Extrasolar Giant Planets and Brown Dwarfs, *Astrophysical Journal* **491**, 856–875.

Burrows, A., Sudarsky, D. & Hubbard, W. B., 2003, A Theory for the Radius of the Transiting Giant Planet HD 209458b, *Astrophysical Journal* **594**, 545–551.

Bussmann, R. S., Holzapfel, W. L. & Kuo, C. L., 2005, Millimeter Wavelength Brightness Fluctuations of the Atmosphere above the South Pole, *Astrophysical Journal* **622**, 1343–1355.

Candidi, M. & Lori, A., 2003, Status of the Antarctic Base at Dome C and perspectives for Astrophysics, *Memorie della Societa Astronomica Italiana* **74**, 29–36.

Cassaing, F., Fleury, B., Coudrain, C. et al., 2000, Optimized fringe tracker for the VLTI/PRIMA instrument, in *Interferometry in Optical Astronomy* (P. Léna & A. Quirrenbach, eds.), *Proc. SPIE*, vol. 4006, 152–163.

Chabrier, G., Barman, T., Baraffe, I. et al., 2004, The Evolution of Irradiated Planets: Application to Transits, *Astrophysical Journal, Letters* **603**, L53–L56.

Chamberlain, M. A., Ashley, M. C. B., Burton, M. G. et al., 2000, Mid-Infrared Observing Conditions at the South Pole, *Astrophysical Journal* **535**, 501–511.

Chamberlin, R. A., Lane, A. P. & Stark, A. A., 1997, The 492 GHz Atmospheric Opacity at the Geographic South Pole, *Astrophysical Journal* **476**, 428–433.

Charbonneau, D., Allen, L. E., Megeath, S. T. et al., 2005, Detection of Thermal Emission from an Extrasolar Planet, *Astrophysical Journal* **626**, 523–529.

Charbonneau, D., Brown, T. M., Latham, D. W. & Mayor, M., 2000, Detection of Planetary Transits Across a Sun-like Star, *Astrophysical Journal, Letters* **529**, L45–L48.

Charbonneau, D., Winn, J. N., Latham, D. W. et al., 2006, Transit Photometry of the Core-dominated Planet HD 149026b, *Astrophysical Journal* **636**, 445–452.

Chauvin, G., Lagrange, A.-M., Dumas, C. et al., 2005a, Giant planet companion to 2MASSW J1207334-393254, *Astron. & Astrophys.* **438**, L25–L28.

Chauvin, G., Lagrange, A.-M., Zuckerman, B. et al., 2005b, A companion to AB Pic at the planet/brown dwarf boundary, *Astron. & Astrophys.* **438**, L29–L32.

Chazelas, B., Brachet, F., Bordé, P. et al., 2006, Instrumental stability requirements for exoplanet detection with a nulling interferometer: variability noise as a central issue, *Applied Optics* **45**(5), 984–992.

Chelli, A. & Petrov, R. G., 1995, Model fitting and error analysis for differential interferometry. I. General formalism., *Astron. & Astrophys., Suppl.* **109**, 389–399.

Chen, C. H. & Jura, M., 2001, A Possible Massive Asteroid Belt around ζ Leporis, *Astrophysical Journal, Letters* **560**, L171–L174.

Chen, C. H., Patten, B. M., Werner, M. W. et al., 2005, A Spitzer Study of Dusty DIsks around Nearby, Young Stars, *Astrophysical Journal* **634**, 1372–1384.

Chiang, E. I. & Goldreich, P., 1997, Spectral Energy Distributions of T Tauri Stars with Passive Circumstellar Disks, *Astrophysical Journal* **490**, 368–376.

Ciardi, D. R., van Belle, G. T., Akeson, R. L. et al., 2001, On the near-infrared size of Vega, *Astrophysical Journal* **559**, 1147–1154.

Claret, A., 2000, A new non-linear limb-darkening law for LTE stellar atmosphere models. Calculations for -5.0 ≤ log[M/H] ≤ +1, 2000 K ≤ T_{eff} ≤ 50000 K at several surface gravities, *Astron. & Astrophys.* **363**, 1081–1190.

Colavita, M., Akeson, R., Wizinowich, P. et al., 2003, Observations of DG Tauri with the Keck Interferometer, *Astrophysical Journal, Letters* **592**, L83–L86.

Colavita, M. M., Swain, M. R., Akeson, R. L. et al., 2004, Effects of Atmospheric Water Vapor on Infrared Interferometry, *Publ. of the Astron. Soc. Pac.* **116**, 876–885.

Conan, J.-M., Rousset, G. & Madec, P.-Y., 1995, Wave-front temporal spectra in high-resolution imaging through turbulence, *J. Opt. Soc. Am. A* **12**, 1559–1570.

Coudé du Foresto, V., Absil, O., Barillot, M. & Swain, M., 2006, ALADDIN: an optimized ground-based precursor for Darwin, in *Direct Imaging of Exoplanet: Science & Techniques* (C. Aimé & F. Vakili, eds.), *Proc. IAU Colloquium*, vol. 200, 305–308.

Coudé du Foresto, V., Bordé, P. J., Mérand, A. et al., 2003, FLUOR fibered beam combiner at the CHARA array, in *Interferometry in Optical Astronomy II* (W. Traub, ed.), *Proc. SPIE*, vol. 4838, 280–285.

Coudé du Foresto, V., Perrin, G., Ruilier, C. et al., 1998, FLUOR fibered instrument at the IOTA interferometer, in *Astronomical Interferometry* (D. Reasenberg, ed.), *Proc. SPIE*, vol. 3350, 856–863.

Coudé du Foresto, V., Ridgway, S. & Mariotti, J.-M., 1997, Deriving object visibilities from interferograms obtained with a fiber stellar interferometer, *Astron. & Astrophys., Suppl.* **121**, 379–392.

Coudé du Foresto, V. & Ridgway, S. T., 1991, FLUOR: a stellar interferometer using infrared fibers, in *High-resolution imaging by interferometry II* (J. Beckers & F. Merkle, eds.), 731–740.

Cox, A., 1999, *Allen's Astrophysical Quantities*, Springer-Verlag.

Creech-Eakman, M. J., Buscher, D. F., Haniff, C. A. & Romero, V. D., 2004, The Magdalena Ridge Observatory Interferometer: a fully optimized aperture synthesis array for imaging, in *New Frontiers in Stellar Interferometry* (W. Traub, ed.), *Proc. SPIE*, vol. 5491, 405–414.

D'Arcio, L. L., Karlsson, A. L. & Gondoin, P. A., 2004, Use of OPD modulation techniques in nulling interferometry, in *New Frontiers in Stellar Interferometry* (W. Traub, ed.), *Proc. SPIE*, vol. 5491, 851–861.

Davis, J., Mendez, A., Seneta, E. B. et al., 2005, Orbital parameters, masses and distance to β Centauri determined with the Sydney University Stellar Interferometer and high-resolution spectroscopy, *Mon. Not. of the Royal Astron. Soc.* **356**, 1362–1370.

Decin, G., Dominik, C., Malfait, K. et al., 2000, The Vega phenomenon around G dwarfs, *Astron. & Astrophys.* **357**, 533–542.

Decin, G., Dominik, C., Waters, L. B. F. M. & Waelkens, C., 2003, Age Dependence of the Vega Phenomenon: Observations, *Astrophysical Journal* **598**, 636–644.

Deming, D., Seager, S., Richardson, L. J. & Harrington, J., 2005, Infrared radiation from an extrasolar planet, *Nature* **434**, 740–743.

den Hartog, R., Absil, O., Gondoin, P. et al., 2004, The simulated detection of low-mass companions with GENIE, in *New Frontiers in Stellar Interferometry* (W. Traub, ed.), *Proc. SPIE*, vol. 5491, 160–168.

den Hartog, R., Absil, O., Gondoin, P. et al., 2006, The prospects of detecting exo-planets with the Ground-based European Nulling Interferometer Experiment (GENIE), in *Direct Imaging of Exo-planet: Science & Techniques* (C. Aimé & F. Vakili, eds.), *Proc. IAU Colloquium*, vol. 200, 233–240.

di Folco, E., Thévenin, F., Kervella, P. et al., 2004, VLTI near-IR interferometric observations of Vega-like stars, *Astron. & Astrophys.* **426**, 601–617.

Domiciano de Souza, A., Kervella, P., Jankov, S. et al., 2003, The spinning-top Be star Achernar from VLTI-VINCI, *Astron. & Astrophys.* **407**, L47–L50.

Domiciano de Souza, A., Kervella, P., Jankov, S. et al., 2005, Gravitational-darkening of Altair from interferometry, *Astron. & Astrophys.* **442**, 567–578.

Dominik, C. & Decin, G., 2003, Age Dependence of the Vega Phenomenon: Theory, *Astrophysical Journal* **598**, 626–635.

Drouet D'Aubigny, C. Y., Walker, C. K. & Golish, D. R., 2004, Mid-infrared spatial filter fabrication using laser chemical etching, in *New Frontiers in Stellar Interferometry* (W. Traub, ed.), *Proc. SPIE*, vol. 5491, 655–666.

Dubovitsky, S. & Lay, O. P., 2004, Architecture selection and optimization for planet-finding interferometers, in *New Frontiers in Stellar Interferometry* (W. Traub, ed.), *Proc. SPIE*, vol. 5491, 284–295.

Dullemond, C. P., Dominik, C. & Natta, A., 2001, Passive Irradiated Circumstellar Disks with an Inner Hole, *Astrophysical Journal* **560**, 957–969.

Dunkin, S. K., Barlow, M. J. & Ryan, S. G., 1997, High-resolution spectroscopy of Vega-like stars - I. Effective temperatures, gravities and photospheric abundances, *Mon. Not. of the Royal Astron. Soc.* **286**, 604–616.

Eisner, J. A., Hillenbrand, L. A., White, R. J. et al., 2005, Observations of T Tauri Disks at Sub-AU Radii: Implications for Magnetospheric Accretion and Planet Formation, *Astrophysical Journal* **623**, 952–966.

Eisner, J. A., Lane, B. F., Hillenbrand, L. A. et al., 2004, Resolved Inner Disks around Herbig Ae/Be Stars, *Astrophysical Journal* **613**, 1049–1071.

Fajardo-Acosta, S. B., Stencel, R. E. & Backman, D. E., 1997, Infrared Space Observatory Mapping of 60 μm Dust Emission Around Vega-type Systems, *Astrophysical Journal, Letters* **487**, L151–L154.

Fajardo-Acosta, S. B., Stencel, R. E., Backman, D. E. & Thakur, N., 1999, Infrared Space Observatory Photometric Search of Main-Sequence Stars for Vega-Type Systems, *Astrophysical Journal* **520**, 215–222.

Fajardo-Acosta, S. B., Telesco, C. M. & Knacke, R. F., 1998, Infrared Photometry of beta Pictoris Type Systems, *Astronomical Journal* **115**, 2101–2121.

Fizeau, H., 1868, Prix Borodin: rapport sur le concours de l'année 1867, *Comptes Rendus de l'Académie des Sciences* **66**, 932–934.

Forveille, T., Ségransan, D., Delorme, P. et al., 2004, An L0 dwarf companion in the brown dwarf desert, at 30 AU, *Astron. & Astrophys.* **427**, L1–L4.

Fridlund, C. V. M., 2004a, Darwin and TPF: technology and prospects, in *New Frontiers in Stellar Interferometry* (W. Traub, ed.), *Proc. SPIE*, vol. 5491, 227–235.

Fridlund, C. V. M., 2004b, The Darwin mission, *Advances in Space Research* **34**, 613–617.

Gai, M., Menardi, S., Cesare, S. et al., 2004, The VLTI fringe sensors: FINITO and PRIMA FSU, in *New Frontiers in Stellar Interferometry* (W. Traub, ed.), *Proc. SPIE*, vol. 5491, 528–539.

Galland, F., Lagrange, A.-M., Udry, S. et al., 2005, Extrasolar planets and brown dwarfs around A-F type stars. I. Performances of radial velocity measurements, first analyses of variations, *Astron. & Astrophys.* **443**, 337–345.

Goldreich, P. & Tremaine, S., 1979, The excitation of density waves at the Lindblad and corotation resonances by an external potential, *Astrophysical Journal* **233**, 857–871.

Greaves, J. S., Holland, W. S., Moriarty-Schieven, G. et al., 1998, A Dust Ring around epsilon Eridani: Analog to the Young Solar System, *Astrophysical Journal, Letters* **506**, L133–L137.

Greaves, J. S., Holland, W. S., Wyatt, M. C. et al., 2005, Structure in the ϵ Eridani Debris Disk, *Astrophysical Journal, Letters* **619**, L187–L190.

Guillot, T. & Showman, A. P., 2002, Evolution of "51 Pegasus b-like" planets, *Astron. & Astrophys.* **385**, 156–165.

Guyon, O., 2002, Wide field interferometric imaging with single-mode fibers, *Astron. & Astrophys.* **387**, 366–378.

Habing, H. J., Dominik, C., Jourdain de Muizon, M. et al., 2001, Incidence and survival of remnant disks around main-sequence stars, *Astron. & Astrophys.* **365**, 545–561.

Haguenauer, P. & Serabyn, E., 2006, Deep nulling of laser light with a single-mode fiber combiner, *Applied Optics* in press.

Haisch, K. E., Lada, E. A. & Lada, C. J., 2001, Disk frequencies and lifetimes in yong clusters, *Astrophysical Journal, Letters* **553**, L153–L156.

Halbwachs, J. L., Mayor, M. & Udry, S., 2005, Statistical properties of exoplanets. IV. The period-eccentricity relations of exoplanets and of binary stars, *Astron. & Astrophys.* **431**, 1129–1137.

Hartmann, L., Kenyon, S. J. & Calvet, N., 1993, The excess infrared emission of Herbig Ae/Be stars - Disks or envelopes?, *Astrophysical Journal* **407**, 219–231.

Hartmann, W. K., Ryder, G., Dones, L. & Grinspoon, D., 2000, The Time-Dependent Intense Bombardment of the Primordial Earth/Moon System, in *Origin of the Earth and Moon* (R. M. Canup & K. Righter, eds.), 493–512, Tucson, Univ. of Arizona Press.

Hatzes, A. P., Cochran, W. D., McArthur, B. et al., 2000, Evidence for a Long-Period Planet Orbiting ϵ Eridani, *Astrophysical Journal, Letters* **544**, L145–L148.

Hauschildt, P. H., Allard, F. & Baron, E., 1999, The NextGen Model Atmosphere Grid for $3000 \leq T_{\rm eff} \leq 10000$ K, *Astrophysical Journal* **512**, 377–385.

Herbst, T. M. & Hinz, P. M., 2004, Interferometry on the Large Binocular Telescope, in *New Frontiers in Stellar Interferometry* (W. Traub, ed.), *Proc. SPIE*, vol. 5491, 383–390.

Herwats, E., 2005, *Study of Young Stellar Objects by optical interferometry*, Diploma thesis, University of Liège.

Hinz, P. M., Angel, J. R. P., Hoffmann, W. F. et al., 1998a, First results of nulling interferometry with the Multiple-Mirror Telescope, in *Astronomical Interferometry* (R. Reasenberg, ed.), *Proc. SPIE*, vol. 3350, 439–447.

Hinz, P. M., Angel, J. R. P., Hoffmann, W. F. et al., 1998b, Imaging circumstellar environments with a nulling interferometer., *Nature* **395**, 251–253.

Hinz, P. M., Angel, J. R. P., Woolf, N. J. et al., 2000, BLINC: a testbed for nulling interferometry in the thermal infrared, in *Interferometry in Optical Astronomy* (P. Léna & A. Quirrenbach, eds.), *Proc. SPIE*, vol. 4006, 349–353.

Hinz, P. M., Hoffmann, W. F. & Hora, J. L., 2001, Constraints on Disk Sizes around Young Intermediate-Mass Stars: Nulling Interferometric Observations of Herbig Ae Objects, *Astrophysical Journal, Letters* **561**, L131–L134.

Högbom, J. A., 1974, Aperture Synthesis with a Non-Regular Distribution of Interferometer Baselines, *Astron. & Astrophys., Suppl.* **15**, 417–426.

Holland, W. S., Greaves, J. S., Dent, W. R. F. et al., 2003, Submillimeter Observations of an Asymmetric Dust Disk around Fomalhaut, *Astrophysical Journal* **582**, 1141–1146.

Holland, W. S., Greaves, J. S., Zuckerman, B. et al., 1998, Submillimetre images of dusty debris around nearby stars., *Nature* **392**, 788–790.

Hummel, C. A., Benson, J. A., Hutter, D. J. et al., 2003, First Observations with a Co-phased Six-Station Optical Long-Baseline Array: Application to the Triple Star η Virginis, *Astronomical Journal* **125**, 2630–2644.

Ireland, M. J., Tuthill, P. G., Davis, J. & Tango, W., 2005, Dust scattering in the Miras R Car and RR Sco resolved by optical interferometric polarimetry, *Mon. Not. of the Royal Astron. Soc.* **361**, 337–344.

Jaffe, W., Meisenheimer, K., Röttgering, H. J. A. et al., 2004, The central dusty torus in the active nucleus of NGC 1068, *Nature* **429**, 47–49.

Jayawardhana, R., Ardila, D. R., Stelzer, B. & Haisch, K. E., 2003, A Disk Census for Young Brown Dwarfs, *Astronomical Journal* **126**, 1515–1521.

Jura, M., Chen, C. H., Furlan, E. et al., 2004, Mid-Infrared Spectra of Dust Debris around Main-Sequence Stars, *Astrophysical Journal, Suppl.* **154**, 453–457.

Kalas, P., Graham, J. R. & Clampin, M., 2005, A planetary system as the origin of structure in Fomalhaut's dust belt, *Nature* **435**, 1067–1070.

Kalas, P., Liu, M. C. & Matthews, B. C., 2004, Discovery of a Large Dust Disk Around the Nearby Star AU Microscopii, *Science* **303**, 1990–1992.

Kaltenegger, L., Eiroa, C., Stankov, A. & Fridlund, M., 2006, Target star catalogue for Darwin: nearby habitable star systems, in *Direct Imaging of Exoplanet: Science & Techniques* (C. Aimé & F. Vakili, eds.), *Proc. IAU Colloquium*, vol. 200, 255–258.

Karlsson, A. & Mennesson, B., 2000, Robin Laurance nulling interferometers, in *Interferometry in Optical Astronomy* (P. Léna & A. Quirrenbach, eds.), *Proc. SPIE*, vol. 4006, 871–880.

Karlsson, A. L., Wallner, O., Perdigues Armengol, J. M. & Absil, O., 2004, Three telescope nuller based on multibeam injection into single-mode waveguide, in *New Frontiers in Stellar Interferometry* (W. Traub, ed.), *Proc. SPIE*, vol. 5491, 831–841.

Kasting, J. F. & Catling, D., 2003, Evolution of a Habitable Planet, *Annual Review of Astron. & Astrophys.* **41**, 429–463.

Kasting, J. F., Whitmire, D. P. & Reynolds, R. T., 1993, Habitable Zones around Main Sequence Stars, *Icarus* **101**, 108–128.

Kelsall, T., Weiland, J. L., Franz, B. A. et al., 1998, The COBE Diffuse Infrared Background Experiment Search for the Cosmic Infrared Background. II. Model of the Interplanetary Dust Cloud, *Astrophysical Journal* **508**, 44–73.

Kervella, P., Bersier, D., Mourard, D. et al., 2004a, Cepheid distances from infrared long-baseline interferometry. II. Calibration of the period-radius and period-luminosity relations, *Astron. & Astrophys.* **423**, 327–333.

Kervella, P., Nardetto, N., Bersier, D. et al., 2004b, Cepheid distances from infrared long-baseline interferometry. I. VINCI/VLTI observations of seven Galactic Cepheids, *Astron. & Astrophys.* **416**, 941–953.

Kervella, P., Ségransan, D. & Coudé du Foresto, V., 2004c, Data reduction methods for single-mode optical interferometry. Application to the VLTI two-telescopes beam combiner VINCI, *Astron. & Astrophys.* **425**, 1161–1174.

Kervella, P., Thévenin, F., di Folco, E. & Ségransan, D., 2004d, The angular sizes of dwarf stars and subgiants: Surface brightness relations calibrated by interferometry, *Astron. & Astrophys.* **426**, 297–307.

Kervella, P., Thévenin, F., Ségransan, D. et al., 2003, The diameters of alpha Centauri A and B. A comparison of the asteroseismic and VINCI/VLTI views, *Astron. & Astrophys.* **404**, 1087–1097.

Koerner, D. W., Sargent, A. I. & Ostroff, N. A., 2001, Millimeter-Wave Aperture Synthesis Imaging of Vega: Evidence for a Ring Arc at 95 AU, *Astrophysical Journal, Letters* **560**, L181–L184.

Koresko, C. D., Mennesson, B. P., Serabyn, E. et al., 2003, Longitudinal dispersion control for the Keck interferometer nuller, in *Interferometry in Optical Astronomy II* (W. Traub, ed.), *Proc. SPIE*, vol. 4838, 625–635.

Kornilov, V., Tokovinin, A. A., Vozyakova, O. et al., 2003, MASS: a monitor of the vertical turbulence distribution, in *Adaptive Optical System Technologies II* (P. Wizinowich & D. Bonaccini, eds.), *Proc. SPIE*, vol. 4839, 837–845.

Kovac, J. M., Leitch, E. M., Pryke, C. et al., 2002, Detection of polarization in the cosmic microwave background using DASI, *Nature* **420**, 772–787.

Krist, J. E., Ardila, D. R., Golimowski, D. A. et al., 2005, Hubble Space Telescope Advanced Camera for Surveys Coronagraphic Imaging of the AU Microscopii Debris Disk, *Astronomical Journal* **129**, 1008–1017.

Kuhn, J. R., Bush, R. I., Scherrer, P. & Scheick, X., 1998, The sun's shape and brightness, *Nature* **392**, 155–157.

Kuo, C. L., Ade, P. A. R., Bock, J. J. et al., 2004, High-Resolution Observations of the Cosmic Microwave Background Power Spectrum with ACBAR, *Astrophysical Journal* **600**, 32–51.

Kurucz, R. L., 1992, Model Atmospheres for Population Synthesis, in *IAU Symp. 149: The Stellar Populations of Galaxies*, 225–232.

Labadie, L., Labeye, P., Kern, P. et al., 2006, Modal Filtering for Nulling Interferometry-First Single-Mode Conductive Waveguides in the Mid-Infrared, *Astron. & Astrophys.* in press.

Labeyrie, A., 1975, Interference fringes obtained on VEGA with two optical telescopes, *Astrophysical Journal, Letters* **196**, L71–L75.

Labeyrie, A., 1996, Resolved imaging of extra-solar planets with future 10-100km optical interferometric arrays, *Astron. & Astrophys., Suppl.* **118**, 517–524.

Lagage, P. O. & Pantin, E., 1994, Dust Depletion in the Inner Disk of Beta-Pictoris as a Possible Indicator of Planets, *Nature* **369**, 628–630.

Lane, B. F. & Muterspaugh, M. W., 2004, Differential Astrometry of Subarcsecond Scale Binaries at the Palomar Testbed Interferometer, *Astrophysical Journal* **601**, 1129–1135.

Laughlin, G., Marcy, G. W., Vogt, S. S. et al., 2005, On the Eccentricity of HD 209458b, *Astrophysical Journal, Letters* **629**, L121–L124.

Laureijs, R. J., Jourdain de Muizon, M., Leech, K. et al., 2002, A 25 micron search for Vega-like disks around main-sequence stars with ISO, *Astron. & Astrophys.* **387**, 285–293.

Lawrence, J. S., 2004, Infrared and Submillimeter Atmospheric Characteristics of High Antarctic Plateau Sites, *Publ. of the Astron. Soc. Pac.* **116**, 482–492.

Lawrence, J. S., Ashley, M. C. B., Burton, M. G. et al., 2003, The AASTINO: Automated Astrophysical Site Testing International Observatory, in *Toward Other Earths: Darwin/TPF and the Search for Extrasolar Terrestrial Planets*, vol. SP-539, 497–501, ESA's Publication Division.

Lawrence, J. S., Ashley, M. C. B., Tokovinin, A. & Travouillon, T., 2004, Exceptional astronomical seeing conditions above Dome C in Antarctica, *Nature* **431**, 278–281.

Lawson, P. R. (ed.) , 2000, *Principles of Long Baseline Stellar Interferometry*, JPL Publication, Pasadena.

Lawson, P. R., Dumont, P. J. & Colavita, M. M., 1999, Interferometer Designs for the Terrestrial Planet Finder, in *Working on the Fringe: Optical and IR Interferometry from Ground and Space*, *ASP Conf. Ser.*, vol. 194, 423–429.

Lay, O. P., 1997, The temporal power spectrum of atmospheric fluctuations due to water vapor, *Astron. & Astrophys., Suppl.* **122**, 535–545.

Lay, O. P., 2004, Systematic errors in nulling interferometers, *Applied Optics* **43**(33), 6100–6123.

Lay, O. P., 2005, Imaging properties of rotating nulling interferometers, *Applied Optics* **44**(28), 5859–5871.

Lay, O. P. & Dubovitsky, S., 2004, Nulling interferometers: the importance of systematic errors and the X-array configuration, in *New Frontiers in Stellar Interferometry* (W. Traub, ed.), *Proc. SPIE*, vol. 5491, 874–885.

Léger, A., Mariotti, J., Mennesson, B. et al., 1996, Could We Search for Primitive Life on Extrasolar Planets in the Near Future? – The DARWIN Project, *Icarus* **123**, 249–255.

Léger, A., Selsis, F., Sotin, C. et al., 2004, A new family of planets? "Ocean-Planets", *Icarus* **169**, 499–504.

Leinert, C., van Boekel, R., Waters, L. B. F. M. et al., 2004, Mid-infrared sizes of circumstellar disks around Herbig Ae/Be stars measured with MIDI on the VLTI, *Astron. & Astrophys.* **423**, 537–548.

Li, A. & Lunine, J. I., 2003, Modeling the Infrared Emission from the HR 4796A Disk, *Astrophysical Journal* **590**, 368–378.

Lineweaver, C. H. & Grether, D., 2003, What Fraction of Sun-like Stars Have Planets?, *Astrophysical Journal* **598**, 1350–1360.

Liu, W. M., Hinz, P. M., Hoffmann, W. F. et al., 2004, Adaptive Optics Nulling Interferometric Constraints on the Mid-Infrared Exozodiacal Dust Emission around Vega, *Astrophysical Journal, Letters* **610**, L125–L128.

Liu, W. M., Hinz, P. M., Hoffmann, W. F. et al., 2005, Resolved Mid-Infrared Emission around AB Aurigae and V892 Tauri with Adaptive Optics Nulling Interferometric Observations, *Astrophysical Journal, Letters* **618**, L133–L136.

Liu, W. M., Hinz, P. M., Meyer, M. R. et al., 2003, A Resolved Circumstellar Disk around the Herbig Ae Star HD 100546 in the Thermal Infrared, *Astrophysical Journal, Letters* **598**, L111–L114.

Lopez, B., Przygodda, F., Wolf, S. et al., 2004, APreS-MIDI, APerture Synthesis in the MID-Infrared with the VLTI, in *New Frontiers in Stellar Interferometry* (W. Traub, ed.), *Proc. SPIE*, vol. 5491, 433–438.

Malbet, F., Benisty, M., de Wit, W.-J. et al., 2006, Disk and wind interaction in the young stellar object MWC297 spatially resolved with VLTI/AMBER., *Astron. & Astrophys.* in press.

Malbet, F., Berger, J.-P., Colavita, M. M. et al., 1998, FU Orionis Resolved by Infrared Long-Baseline Interferometry at a 2 AU Scale, *Astrophysical Journal, Letters* **507**, L149–L152.

Malbet, F., Berger, J.-P., Kern, P. Y. et al., 2004, VITRUV, a second-generation VLTI instrument for aperture synthesis imaging with eight telescopes, in *New Frontiers in Stellar Interferometry* (W. Traub, ed.), *Proc. SPIE*, vol. 5491, 439–446.

Malbet, F., Lachaume, R., Berger, J.-P. et al., 2005, New insights on the AU-scale circumstellar structure of FU Orionis, *Astron. & Astrophys.* **437**, 627–636.

Mamajek, E. E., Meyer, M. R., Hinz, P. M. et al., 2004, Constraining the Lifetime of Circumstellar Disks in the Terrestrial Planet Zone: A Mid-Infrared Survey of the 30 Myr old Tucana-Horologium Association, *Astrophysical Journal* **612**, 496–510.

Mannings, V. & Barlow, M. J., 1998, Candidate Main-Sequence Stars with Debris Disks: A New Sample of Vega-like Sources, *Astrophysical Journal* **497**, 330–341.

Marks, R. D., Vernin, J., Azouit, M. et al., 1999, Measurement of optical seeing on the high antarctic plateau, *Astron. & Astrophys., Suppl.* **134**, 161–172.

Marsh, K. A., Velusamy, T., Dowell, C. D. et al., 2005, Image of Fomalhaut dust ring at 350 microns: the relative column density map shows pericenter-apocenter asymmetry, *Astrophysical Journal, Letters* **620**, L47–L50.

Mayor, M. & Queloz, D., 1995, A Jupiter-Mass Companion to a Solar-Type Star, *Nature* **378**, 355–359.

McAlister, H. A., ten Brummelaar, T. A., Gies, D. R. et al., 2005, First Results from the CHARA Array. I. An Interferometric and Spectroscopic Study of the Fast Rotator α Leonis (Regulus), *Astrophysical Journal* **628**, 439–452.

Mégessier, C., 1995, Accuracy of the astrophysical absolute flux calibrations: visible and near-infrared, *Astron. & Astrophys.* **296**, 771–778.

Meisner, J. A. & Le Poole, R. S., 2003, Dispersion affecting the VLTI and 10 micron interferometry using MIDI, in *Interferometry in Optical Astronomy II* (W. Traub, ed.), *Proc. SPIE*, vol. 4838, 609–624.

Ménardi, S. & Gennai, A., 2001, Technical Specifications for the PRIMA Fringe Sensor Unit, *Tech. Rep. VLT-SPE-ESO-15740-2210*, European Southern Observatory.

Mennesson, B., 1999, *Interférométrie stellaire dans l'infrarouge thermique: observations d'environnements circumstellaires par optique guidé monomode et contributions à la mission spatiale DARWIN*, Ph.D. thesis, Université de Paris VII.

Mennesson, B., Léger, A. & Ollivier, M., 2005, Direct detection and characterization of extrasolar planets: The Mariotti space interferometer, *Icarus* **178**, 570–588.

Mennesson, B. & Mariotti, J. M., 1997, Array Configurations for a Space Infrared Nulling Interferometer Dedicated to the Search for Earthlike Extrasolar Planets, *Icarus* **128**, 202–212.

Mennesson, B., Ollivier, M. & Ruilier, C., 2002, On the use of single-mode waveguides to correct the optical defects of a nulling interferometer, *J. Opt. Soc. Am. A* **19**(3), 596–602.

Mérand, A., 2005, *Étude à haute résolution spatiale des Céphéides*, Ph.D. thesis, Université de Paris VII.

Mérand, A., Kervella, P., Coudé Du Foresto, V. et al., 2005, The projection factor of δ Cephei. A calibration of the Baade-Wesselink method using the CHARA Array, *Astron. & Astrophys.* **438**, L9–L12.

Michelson, A. A. & Pease, F. G., 1921, Measurement of the diameter of alpha Orionis with the interferometer, *Astrophysical Journal* **53**, 249–259.

Millan-Gabet, R., Monnier, J. D., Akeson, R. L. et al., 2006, Keck Interferometer Observations of FU Orionis Objects, *Astrophysical Journal* in press.

Millan-Gabet, R., Schloerb, F. P. & Traub, W. A., 2001, Spatially Resolved Circumstellar Structure of Herbig Ae/Be Stars in the Near-Infrared, *Astrophysical Journal* **546**, 358–381.

Millan-Gabet, R., Schloerb, F. P., Traub, W. A. et al., 1999, Sub-Astronomical Unit Structure of the Near-Infrared Emission from AB Aurigae, *Astrophysical Journal, Letters* **513**, L131–L134.

Millour, F., Vannier, M., Petrov, R. G. et al., 2006, Extrasolar planets with AMBER/VLTI, what can we expect from current performances?, in *Direct Imaging of Exoplanet: Science & Techniques* (C. Aimé & F. Vakili, eds.), *Proc. IAU Colloquium*, vol. 200, in press.

Monnier, J. D., 2000, An Introduction to Closure Phases, in *Principles of Long Baseline Stellar Interferometry* (P. R. Lawson, ed.), 203–229, JPL Publications, Pasadena.

Monnier, J. D., Berger, J.-P., Millan-Gabet, R. & Ten Brummelaar, T. A., 2004, The Michigan Infrared Combiner (MIRC): IR imaging with the CHARA Array, in *New Frontiers in Stellar Interferometry* (W. Traub, ed.), *Proc. SPIE*, vol. 5491, 1370–1378.

Monnier, J. D. & Millan-Gabet, R., 2002, On the Interferometric Sizes of Young Stellar Objects, *Astrophysical Journal* **579**, 694–698.

Monnier, J. D., Millan-Gabet, R., Billmeier, R. et al., 2005, The Near-Infrared Size-Luminosity Relations for Herbig Ae/Be Disks, *Astrophysical Journal* **624**, 832–840.

Moro-Martín, A. & Malhotra, R., 2005, Dust Outflows and Inner Gaps Generated by Massive Planets in Debris Disks, *Astrophysical Journal* **633**, 1150–1167.

Muterspaugh, M. W., Lane, B. F., Konacki, M. et al., 2005, PHASES High Precision Differential Astrometry of delta Equulei, *Astronomical Journal* **130**, 2866–2875.

Natta, A., Prusti, T., Neri, R. et al., 2001, A reconsideration of disk properties in Herbig Ae stars, *Astron. & Astrophys.* **371**, 186–197.

Neuhäuser, R., Guenther, E. W., Wuchterl, G. et al., 2005, Evidence for a co-moving sub-stellar companion of GQ Lup, *Astron. & Astrophys.* **435**, L13–L16.

Nishikawa, J., Yoshizawa, M., Ohishi, N. et al., 2004, MIRA-I.2: recent progress, in *New Frontiers in Stellar Interferometry* (W. Traub, ed.), *Proc. SPIE*, vol. 5491, 520–527.

Noll, R. J., 1976, Zernike polynomials and atmospheric turbulence, *J. Opt. Soc. Am. A* **66**, 207–211.

Ohishi, N., Nordgren, T. E. & Hutter, D. J., 2004, Asymmetric Surface Brightness Distribution of Altair Observed with the Navy Prototype Optical Interferometer, *Astrophysical Journal* **612**, 463–471.

Ollivier, M., 1999, *Contribution à la recherche d'exoplanètes - Coronographie interférentielle pour la mission DARWIN*, Ph.D. thesis, Université de Paris XI.

Ollivier, M., Le Duigou, J.-M., Mourard, D. et al., 2006, PEGASE: a DARWIN/TPF pathfinder, in *Direct Imaging of Exoplanet: Science & Techniques* (C. Aimé & F. Vakili, eds.), *Proc. IAU Colloquium*, vol. 200, 241–245.

Ollivier, M. & Mariotti, J.-M., 1997, Improvement in the rejection rate of a nulling interferometer by spatial filtering, *Applied Optics* **36**(22), 5340–5346.

Oudmaijer, R. D., van der Veen, W. E. C. J., Waters, L. B. F. M. et al., 1992, SAO stars with infrared excess in the IRAS Point Source Catalog, *Astron. & Astrophys., Suppl.* **96**, 625–643.

Ozernoy, L. M., Gorkavyi, N. N., Mather, J. C. & Taidakova, T. A., 2000, Signatures of Exosolar Planets in Dust Debris Disks, *Astrophysical Journal, Letters* **537**, L147–L151.

Paczyński, B., 1980, A model of the subdwarf binary system LB 3459, *Acta Astronomica* **30**, 113–125.

Pan, X., Shao, M. & Kulkarni, S. R., 2004, A distance of 133-137 parsecs to the Pleiades star cluster, *Nature* **427**, 326–328.

Perrin, G., 2003, The calibration of interferometric visibilities obtained with single-mode optical interferometers. Computation of error bars and correlations, *Astron. & Astrophys.* **400**, 1173–1181.

Perrin, G., 2005, An experience in the field of optical interferometry for astronomy, in *SF2A-2005: Semaine de l'Astrophysique Francaise*, 27.

Perrin, G., Ridgway, S. T., Mennesson, B. et al., 2004a, Unveiling Mira stars behind the molecules. Confirmation of the molecular layer model with narrow band near-infrared interferometry, *Astron. & Astrophys.* **426**, 279–296.

Perrin, G. S., Lai, O., Woillez, J. M. et al., 2004b, 'OHANA, in *New Frontiers in Stellar Interferometry* (W. Traub, ed.), *Proc. SPIE*, vol. 5491, 391–404.

Peterson, D. M., Hummel, C. A., Pauls, T. A. et al., 2004, Resolving the effects of rotation in early type stars, in *New Frontiers in Stellar Interferometry* (W. Traub, ed.), *Proc. SPIE*, vol. 5491, 65–72.

Pollack, J. B., 1984, Origin and History of the Outer Planets: Theoretical Models and Observational Contraints, *Annual Review of Astron. & Astrophys.* **22**, 389–424.

Pollack, J. B., Hubickyj, O., Bodenheimer, P. et al., 1996, Formation of the Giant Planets by Concurrent Accretion of Solids and Gas, *Icarus* **124**, 62–85.

Quillen, A. C. & Thorndike, S., 2002, Structure in the ϵ Eridani Dusty Disk Caused by Mean Motion Resonances with a 0.3 Eccentricity Planet at Periastron, *Astrophysical Journal, Letters* **578**, L149–L152.

Quirrenbach, A., Henning, T., Queloz, D. et al., 2004, The PRIMA Astrometric Planet Search project, in *New Frontiers in Stellar Interferometry* (W. Traub, ed.), *Proc. SPIE*, vol. 5491, 424–432.

Racine, R., 2005, Altitude, Elevation, and Seeing, *Publ. of the Astron. Soc. Pac.* **117**, 401–410.

Reach, W. T., Kuchner, M. J., von Hippel, T. et al., 2005, The Dust Cloud around the White Dwarf G29-38, *Astrophysical Journal, Letters* **635**, L161–L164.

Rivera, E. J., Lissauer, J. J., Butler, R. P. et al., 2005, A $\sim$7.5 $M_\oplus$ Planet Orbiting the Nearby Star, GJ 876, *Astrophysical Journal* **634**, 625–640.

Roddier, F., 1981, The effects of atmospheric turbulence in optical astronomy, in *Progress in optics* (E. Wolf, ed.), vol. XIX, 281, North-Holland, Amsterdam.

Roddier, F., Northcott, M. J., Graves, J. E. et al., 1993, One-dimensional spectra of turbulence-induced Zernike aberrations: time-delay and isoplanicity error in partial adaptive compensation, *J. Opt. Soc. Am. A* **10**, 957–965.

Rousselet-Perraut, K., Stehlé, C., Lanz, T. et al., 2004, Stellar activity and magnetism studied by optical interferometry, *Astron. & Astrophys.* **422**, 193–203.

Royer, F., Gerbaldi, M., Faraggiana, R. & Gómez, A. E., 2002, Rotational velocities of A-type stars. I. Measurement of $v \sin i$ in the southern hemisphere, *Astron. & Astrophys.* **381**, 105–121.

Ruilier, C., 1999, *Filtrage modal et recombinaison de grands télescopes. Contributions à l'instrument FLUOR*, Ph.D. thesis, Université de Paris VII.

Ruilier, C. & Cassaing, F., 2001, Coupling of large telescopes and single-mode waveguides: application to stellar interferometry, *J. Opt. Soc. Am. A.* **18**(1), 143.

Sasselov, D. D. & Lecar, M., 2000, On the Snow Line in Dusty Protoplanetary Disks, *Astrophysical Journal* **528**, 995–998.

Schneider, J., 2006, The Extrasolar Planet Encyclopedia, http://www.obspm.fr/planets.

Schuller, P., Vannier, M., Petrov, R. et al., 2003, Direct detection of sub-stellar companions with MIDI, in *Toward Other Earths: Darwin/TPF and the Search for Extrasolar Terrestrial Planets*, vol. SP-539, 583–587, ESA's Publication Division.

Seager, S., Richardson, L. J., Hansen, B. M. S. et al., 2005, On the Dayside Thermal Emission of Hot Jupiters, *Astrophysical Journal* **632**, 1122–1131.

Ségransan, D., Kervella, P., Forveille, T. & Queloz, D., 2003, First radius measurements of very low mass stars with the VLTI, *Astron. & Astrophys.* **397**, L5–L8.

Selsis, F., Despois, D. & Parisot, J.-P., 2002, Signature of life on exoplanets: Can Darwin produce false positive detections?, *Astron. & Astrophys.* **388**, 985–1003.

Serabyn, E., 2000, Nulling interferometry: symmetry requirements and experimental results, in *Interferometry in Optical Astronomy* (P. Léna & A. Quirrenbach, eds.), *Proc. SPIE*, vol. 4006, 328–339.

Serabyn, E., Booth, A. J., Colavita, M. M. et al., 2004, The Keck interferometer nuller: system architecture and laboratory performance, in *New Frontiers in Stellar Interferometry* (W. Traub, ed.), *Proc. SPIE*, vol. 5491, 806–815.

Serabyn, E. & Colavita, M. M., 2001, Fully Symmetric Nulling Beam Combiners, *Applied Optics* **40**, 1668–1671.

Shaklan, S. & Roddier, F., 1988, Coupling starlight into single-mode fiber optics, *Applied Optics* **27**, 2334–2338.

Shao, M. & Colavita, M. M., 1992, Potential of long-baseline infrared interferometry for narrow-angle astrometry, *Astron. & Astrophys.* **262**, 353–358.

Sheret, I., Dent, W. R. F. & Wyatt, M. C., 2004, Submillimetre observations and modelling of Vega-type stars, *Mon. Not. of the Royal Astron. Soc.* **348**, 1282–1294.

Showman, A. P. & Guillot, T., 2002, Atmospheric circulation and tides of "51 Pegasus b-like" planets, *Astron. & Astrophys.* **385**, 166–180.

Skilling, J. & Bryan, R. K., 1984, Maximum Entropy Image Reconstruction - General Algorithm, *Mon. Not. of the Royal Astron. Soc.* **211**, 111–124.

Smith, B. A. & Terrile, R. J., 1984, A circumstellar disk around Beta Pictoris, *Science* **226**, 1421–1424.

Song, I., Caillault, J.-P., Barrado y Navascués, D. & Stauffer, J. R., 2001, Ages of A-Type Vega-like Stars from uvbyβ Photometry, *Astrophysical Journal* **546**, 352–357.

Song, I., Caillault, J.-P., Barrado y Navascués, D. et al., 2000, Ages of Late Spectral Type Vega-like Stars, *Astrophysical Journal, Letters* **533**, L41–L44.

Spangler, C., Sargent, A. I., Silverstone, M. D. et al., 2001, Dusty Debris around Solar-Type Stars: Temporal Disk Evolution, *Astrophysical Journal* **555**, 932–944.

Stapelfeldt, K. R., Holmes, E. K., Chen, C. et al., 2004, First Look at the Fomalhaut Debris Disk with the Spitzer Space Telescope, *Astrophysical Journal, Suppl.* **154**, 458–462.

Stee, P., 2003, Active hot star shells, *Astrophysics and Space Science* **286**, 225–236.

Stencel, R. E. & Backman, D. E., 1991, A survey for infrared excesses among high galactic latitude SAO stars, *Astrophysical Journal, Suppl.* **75**, 905–924.

Storey, J. W. V., Ashley, M. C. B., Burton, M. G. & Lawrence, J. S., 2005, Automated Site Testing from Antarctica, in *EAS Publications Series*, vol. 14, 7–12.

Sudarsky, D., Burrows, A. & Hubeny, I., 2003, Theoretical Spectra and Atmospheres of Extrasolar Giant Planets, *Astrophysical Journal* **588**, 1121–1148.

Sudarsky, D., Burrows, A. & Pinto, P., 2000, Albedo and Reflection Spectra of Extrasolar Giant Planets, *Astrophysical Journal* **538**, 885–903.

Swain, M., Vasisht, G., Akeson, R. et al., 2003, Interferometer Observations of Subparsec-Scale Infrared Emission in the Nucleus of NGC 4151, *Astrophysical Journal, Letters* **596**, L163–L166.

Swain, M. R., Walker, C. K., Traub, W. A. et al., 2004, The Antarctic planet interferometer, in *New Frontiers in Stellar Interferometry* (W. Traub, ed.), *Proc. SPIE*, vol. 5491, 176–185.

Telesco, C. M., Decher, R., Becklin, E. E. & Wolstencroft, R. D., 1988, Resolution of the circumstellar disk of Beta Pictoris at 10 and 20 microns, *Nature* **335**, 51–53.

ten Brummelaar, T. A., McAlister, H. A., Ridgway, S. T. et al., 2005, First Results from the CHARA Array. II. A Description of the Instrument, *Astrophysical Journal* **628**, 453–465.

Thévenin, F., Kervella, P., Pichon, B. et al., 2005, VLTI/VINCI diameter constraints on the evolutionary status of δ Eri, ξ Hya, η Boo, *Astron. & Astrophys.* **436**, 253–262.

Thompson, A. R., Moran, J. M. & Swenson, G. W., 2001, *Interferometry and Synthesis in Radio Astronomy*, Wiley, New-York.

Travouillon, T., Ashley, M. C. B., Burton, M. G. et al., 2003, Atmospheric turbulence at the South Pole and its implications for astronomy, *Astron. & Astrophys.* **400**, 1163–1172.

Tuthill, P. G., Monnier, J. D., Danchi, W. C. et al., 2002, Imaging the Disk around the Luminous Young Star LkHα 101 with Infrared Interferometry, *Astrophysical Journal* **577**, 826–838.

Tycner, C., Lester, J. B., Hajian, A. R. et al., 2005, Properties of the Hα-emitting Circumstellar Regions of Be Stars, *Astrophysical Journal* **624**, 359–371.

Udalski, A., Szymanski, M. K., Kubiak, M. et al., 2004, The Optical Gravitational Lensing Experiment. Planetary and Low-Luminosity Object Transits in the Fields of Galactic Disk. Results of the 2003 OGLE Observing Campaigns, *Acta Astronomica* **54**, 313–345.

Uzpen, B., Kobulnicky, H. A., Olsen, K. A. G. et al., 2005, Identification of Main-Sequence Stars with Mid-Infrared Excesses Using GLIMPSE: β Pictoris Analogs?, *Astrophysical Journal* **629**, 512–525.

Vakili, F., Aristidi, E., Schmider, F. X. et al., 2005, KEOPS: towards exo-Earths from Dome C of Antarctica, in *EAS Publications Series*, vol. 14, 211–217.

van Belle, G. T., Ciardi, D. R., Thompson, R. R. et al., 2001, Altair's Oblateness and Rotation Velocity from Long-Baseline Interferometry, *Astrophysical Journal* **559**, 1155–1164.

van Boekel, R., Kervella, P., Schöller, M. et al., 2003, Direct measurement of the size and shape of the present-day stellar wind of η Carinae, *Astron. & Astrophys.* **410**, L37–L40.

van Boekel, R., Min, M., Leinert, C. et al., 2004, The building blocks of planets within the 'terrestrial' region of protoplanetary disks, *Nature* **432**, 479–482.

Vernin, J. & Munoz-Tunon, C., 1995, Measuring astronomical seeing: The DA/IAC DIMM, *Publ. of the Astron. Soc. Pac.* **107**, 265–272.

Vidal-Madjar, A., Lecavelier des Etangs, A., Désert, J.-M. et al., 2003, An extended upper atmosphere around the extrasolar planet HD209458b, *Nature* **422**, 143–146.

Vink, H. J. P., Doelman, N. J., Flatscher, R. & Sodnik, Z., 2003, DARWIN nulling interferometer breadboard II: design and manufacturing, in *Toward Other Earths: Darwin/TPF and the Search for Extrasolar Terrestrial Planets*, vol. SP-539, 641–645, ESA's Publication Division.

Vinković, D., Ivezić, Ž., Jukić, T. & Elitzur, M., 2006, Near-Infrared and the Inner Regions of Protoplanetary Disks, *Astrophysical Journal* **636**, 348–361.

Wallner, O., Artjuschenko, V. G. & Flatscher, R., 2004a, Development of silver-halide single-mode fibers for modal filtering in the mid-infrared, in *New Frontiers in Stellar Interferometry* (W. Traub, ed.), *Proc. SPIE*, vol. 5491, 636–646.

Wallner, O., Perdigues Armengol, J. M. & Karlsson, A. L., 2004b, Multiaxial single-mode beam combiner, in *New Frontiers in Stellar Interferometry* (W. Traub, ed.), *Proc. SPIE*, vol. 5491, 798–805.

Ward, W. R., 1997, Survival of Planetary Systems, *Astrophysical Journal, Letters* **482**, L211–L214.

Weiner, J., 2004, Mira's Apparent Size Variations due to a Surrounding Semiopaque H_2O Layer, *Astrophysical Journal, Letters* **611**, L37–L40.

Weiner, J., Hale, D. D. S. & Townes, C. H., 2003, Asymptotic Giant Branch and Supergiant Stellar Diameters in the Mid-Infrared, *Astrophysical Journal* **589**, 976–982.

Weingartner, J. C. & Draine, B. T., 2001, Dust Grain-Size Distributions and Extinction in the Milky Way, Large Magellanic Cloud, and Small Magellanic Cloud, *Astrophysical Journal* **548**, 296–309.

Wittkowski, M., Kervella, P., Arsenault, R. et al., 2004, VLTI/VINCI observations of the nucleus of NGC 1068 using the adaptive optics system MACAO, *Astron. & Astrophys.* **418**, L39–L42.

Woolf, N. J. & Angel, J. R. P., 1997, Planet Finder Options I: New Linear Nulling Array Configurations, in *Planets Beyond the Solar System and the Next Generation of Space Missions* (D. Soderblom, ed.), *ASP Conf. Ser.*, vol. 119, 285–193.

Wyatt, M. C., Greaves, J. S., Dent, W. R. F. & Coulson, I. M., 2005, Submillimeter Images of a Dusty Kuiper Belt around η Corvi, *Astrophysical Journal* **620**, 492–500.

Young, J. S., Baldwin, J. E., Boysen, R. C. et al., 2000, New views of Betelgeuse: multi-wavelength surface imaging and implications for models of hotspot generation, *Mon. Not. of the Royal Astron. Soc.* **315**, 635–645.

Ziegler, J. G. & Nichols, N. B., 1942, Optimum Settings for Automatic Controllers, *Trans. ASME* **64**, 759–768.

Appendix

A

Thermal background fluctuations at 10 micron measured with VLTI-MIDI

In the following paper (Absil et al. 2004a), published in the proceedings of the SPIE conference *New Frontiers in Stellar Interferometry* held in Glasgow (June 2004), we analyse the data obtained during a technical observation run performed with the MIDI instrument at the VLTI and dedicated the characterisation of the time fluctuations of the infrared thermal background emission. The rationale for this study is to determine the required chopping frequency for the GENIE experiment (see Section 3.4.3).

Thermal background fluctuations at 10 micron measured with VLTI/MIDI

Olivier Absil[a], Eric J. Bakker[b], Markus Schöller[c] and Philippe Gondoin[d]

[a] Institut d'Astrophysique et de Géophysique, 17 Allée du Six Août, 4000 Liège, Belgium
[b] Leiden Observatory, P.O. Box 9513, 2300 RA Leiden, The Netherlands
[c] European Southern Observatory, Casilla 19001, Santiago 19, Chile
[d] ESTEC, European Space Agency, P.O. Box 299, 2200 AG Noordwijk, The Netherlands

ABSTRACT

We present an experiment to measure the thermal background level and its fluctuations with the European Southern Observatory (ESO) Very Large Telescope Interferometer (VLTI). The Mid Infrared Instrument (MIDI) operating between 8 and 12 micron was used in both dispersed and non-dispersed modes. By using an interferometric instrument, in non-interferometric mode, we probe the same optical path as can be expected for other infrared interferometric instruments, e.g. GENIE and MIDI itself. Most of the infrared thermal background detected with MIDI originates from the VLTI infrastructure. This can be attributed to the absence of a pupil re-imaging mirror. Only for a small region around the optical axis of the system the signal from the VLTI infrastructure can be considered small and the atmospheric background fluctuations can be characterized.

The fluctuations of the thermal emission are described in terms of their power spectral densities (PSD). We have identified two regions in the PSD. For the low frequency range (0-10 Hz) the fluctuations are dominated by the Earth atmosphere. The slope of the log-log PSD is close to -1. For the high frequency (larger than 10 Hz) range the fluctuations are due to photon noise and the PSD flattens off. Many narrow peaks are present in the PSD. Peaks at 1 and 50 Hz occur in almost all data sets and are identified as the effects of the MIDI closed cycle cooler and the power lines respectively. Other peaks at 10 and 30 Hz, as well as peaks above 50 Hz, are assumed to be VLTI or MIDI-specific frequencies.

Keywords: Interferometry, infrared, MIDI, GENIE, thermal background, turbulence

1. INTRODUCTION

Interferometric observations at wavelengths between 3 μm and 25 μm are background limited. This background radiation has the largest contribution at 10 μm. With the exception of very strong astronomical sources the signal from the thermal background emitted by the Earth atmosphere and the telescope is larger than the signal from the astronomical sources. This background signal changes unpredictably on timescales of milli-seconds due to turbulence in the air. Atmospheric blobs at different temperatures and relative humidity passing through the optical path are causing both absorption of the signal and additional emission. In almost all cases scientific instruments operating beyond 3 μm must correct for the background radiation through chopping at a frequency typically between 5 and 20 Hz.

At the Very Large Telescope Interferometer (VLTI) two instruments have to compensate for background radiation: the Mid-Infrared Instrument (MIDI, Ref. 1) and the Ground-based European Nulling Interferometry Experiment (GENIE, Ref. 2). In this paper we present the results of a series of experiments conducted to characterize the thermal background at the VLTI. We have used the only available mid-infrared instrument that sees the full optical path through the interferometer. This instrument operates between 8 and 12 μm and can be used with a filter to see a full image or with a dispersive element (low-resolution prism or high-resolution grism) in combination with a slit to record a dispersed image. The result of our experiments will help decide on the specific parameters to be used for chopping by MIDI and GENIE (e.g. chopping frequency) and whether a more advanced method for background subtraction should be considered.

Send correspondence to absil@astro.ulg.ac.be or bakker@strw.leidenuniv.nl.

We expect several components in the power spectrum of the background radiation (Ref. 3–5): the shot noise of the photon flux itself and a "1/f" noise due to variations in the background caused by temperature drifts and clouds. Additionally we expect read noise, "1/f" noise, and a slow drift in sensitivity of the detector. Fluctuations comparable to a Kolmogorov spectrum would give a slope of $-8/3$ and those comparable to a random intensity walk to a slope of -2 (see details in Ref. 6). For scientific observations we would like to remove all these effects and aim at reaching Background-Limit Performance (BLIP) where the photon noise dominates the other sources.

2. OBSERVATIONS

Measurements of the thermal background of the VLTI with MIDI have been performed on two occasions.

2.1. February 2003

The first set of data was obtained during commissioning of MIDI (18 to 24 February 2003) with UT1-UT3 and SD1-SD2 (Table 1). Data was collected in non-dispersed mode using filters (broad-band N, and narrow band N11.3 and N8.7). Typical frame integration times are 1.2 milliseconds (msec) for the broad-band filter, and 4.0 msec for narrow-band filters. The optical path between the telescopes and the MIDI instrument was not yet optimally aligned. This led to some vignetting of the optical beam by mirror mounts, etc. In addition to this, there was no pupil relay optics available during this experiment. The effect of this is that vignetting of the beams does not only remove part of the light, but the components responsible for the vignetting also emit thermal radiation into the optical path. Since the VLTI infrastructure emits at a temperature significantly warmer than the cold sky (and with a higher efficiency) these observations are very much affected by the absence of pupil transfer optics. For the October 2003 experiment the optical train was much better aligned. This improvement of pupil plane imaging is demonstrated by comparing a pupil plane image recorded in February 2003 (Fig. 1(a)) to one recorded in October 2003 (Fig. 1(b)).

2.2. October 2003

The second data-set was recorded during an observing run between 3 to 10 October 2003 using a single telescope (UT3) (Table 1). This time MIDI was operated in dispersed mode (PRISM mode, $R \approx 30$) with a slit of 0.2 mm. The light was focused on the detector by the field camera lens. Since only one telescope was used only a single window of the MIDI detector was read-out and stored. The lower corner of this window was (x,y)=(1,141) with a size of (δx, δy)=(320,50). The main delay line number 3 was used at a fixed position of 6 meters to have the best pupil matching within the delay tunnel. During the observations no active control of the pupil was available (no variable curvature mirrors in place yet). Therefore the thermal emission from the VLTI infrastructure has affected the measurements. The detector integration time per frame was 2 msec, corresponding to a cycle time (integration, read-out, reset) of 6 msec. A typical detector count rate was 10000 counts/pixel/frame (saturation occurs at 65000, non-linearity starts at 50000). The main difference between this October 2003 and the previous February 2003 experiment was that the VLTI optical train was much better aligned, the main delay lines were positioned at a location which gives the best pupil plane, and MIDI was able to operate in dispersed mode. This latter allows us to study the thermal background characteristics in much greater details than before.

3. DATA ANALYSIS

3.1. Characterization of thermal background characteristics

Turbulent behavior is characterized through a power spectral density (PSD) analysis. In essence, it makes the Fourier Transform of a time series. For each frequency in the PSD, it computes the amplitude and phase needed to characterize the time series. The PSD is plotted as power (square of the amplitude) versus frequency. If the y-axis units of the time series are "ADU/pixel/DIT", the units of the PSD are "(ADU/pixel/DIT)^2/Hz".

The intensity of the pixels within a region are averaged (yielding an average intensity per pixel for that region), and divided by the detector integration time (to be independent of the integration time). With a typical count rate of 10^4 ADU/pixel/DIT, and a typical DIT of 4 ms, a typical count rate of 2.5×10^6 ADU/pixel/second is expected. The conversion from counts to electrons is a factor 145 (electrons per ADU) and a detector efficiency of 0.36. Typical count rates are therefore 10^9 photons/pixel/second.

Table 1. Log of the thermal background fluctuation observations with MIDI. The file names contain the date and universal time of observation. DIT is the detector integration time in msec.

Exp. #	File	DIT	# frames	Filter	Comments
			February 2003		
00	2003-02-18T06:57	4.0	3×100000	N11.3	MIDI black-screen
01	2003-02-19T05:58	4.0	100000	N11.3	SD1, SD2 on Eta Carinae, DL trajectory
02	2003-02-19T08:28	4.0	2×100000	N11.3	SD1, SD2 @ zenith, dome closed
03	2003-02-19T09:31	4.0	100000	N8.7	SD1, SD2 @ zenith, dome closed
04	2003-02-20T06:37	1.2	35000+2×40000	Nband	UT1 standing, UT3 tracking, on sky
05	2003-02-20T07:30	1.2	41000	Nband	UT1 standing, UT3 tracking, dome closed
06	2003-02-20T08:01	4.0	30000+100000	N8.7	UT1 standing, UT3 tracking, dome closed
07	2003-02-20T09:24	4.0	100000	N8.7	Black-plates in DL tunnel
08	2003-02-22T06:32	1.2	3×100000	Nband	UT1 tracking, UT3 standing 45° North, DL fixed, dome closed
09	2003-02-22T07:48	1.2	3×100000	Nband	UT1 and UT3 @ zenith, dome closed, DLs moving
10	2003-02-22T09:17	1.2	70000	Nband	Black-plate in DL, Delay Lines fixed
11	2003-02-23T02:07	1.2	100000	Nband	UT1, UT3 on sky, people at UT3 Coudé, only tracking, no guiding
12	2003-02-23T02:25	1.2	100000	Nband	No people at UT3 Coudé, Z Canis Majoris as source
13	2003-02-24T09:52	1.2	100000	Nband	UT1 Zenith, UT3 45° North, DL1= DL3=7 meters standing
			October 2003		
20	2003-10-07T02:48	2	3×100000	PRISM	Elevation of 90°
	2003-10-07T06:04	2	3×100000	PRISM	Elevation of 80°
	2003-10-07T09:10	2	3×100000	PRISM	Elevation of 70°
	2003-10-07T03:34	2	3×100000	PRISM	Elevation of 60°
	2003-10-07T07:05	2	3×100000	PRISM	Elevation of 50°
	not available			PRISM	Elevation of 40°
	2003-10-07T04:58	2	3×100000	PRISM	Elevation of 30°
	2003-10-07T08:00	2	3×100000	PRISM	Elevation of 20°

The extracted intensity $h_j(t_j)$ has units of ADU/pixel/sec and t_j has units of seconds. Before computing the PSD, we remove the DC offset of the time series. This new signal is noted $V_j(t_j)$ and has units of ADU/pixel/sec. The total energy in V_j is computed by

$$E = \int_{t=0}^{t=\infty} |V(t)|^2 \, dt = \sum_{j=0}^{N-1} |V_j|^2 \cdot \Delta t \tag{1}$$

with Δt being the step size of the time series. The energy E of the signal has units of (ADU/pixel/second)^2. For a simple sine signal $V_j = A \sin(2\pi f t_j - \phi)$, this implies:

$$E = \int_{t=0}^{t=T} A^2 \sin^2(2\pi f t - \phi) = \frac{A^2}{2\pi f} \int_{t=0}^{t=T} \sin^2 x \, dx \, , \tag{2}$$

which gives

$$E = A^2 \frac{T}{2} \, , \tag{3}$$

with A the amplitude of the sine wave in ADU/pixel/sec, T the total time span in sec, f the frequency of the wave in Hz and ϕ the phase offset in radians. The power P of the signal is defined as the energy per second, i.e.,

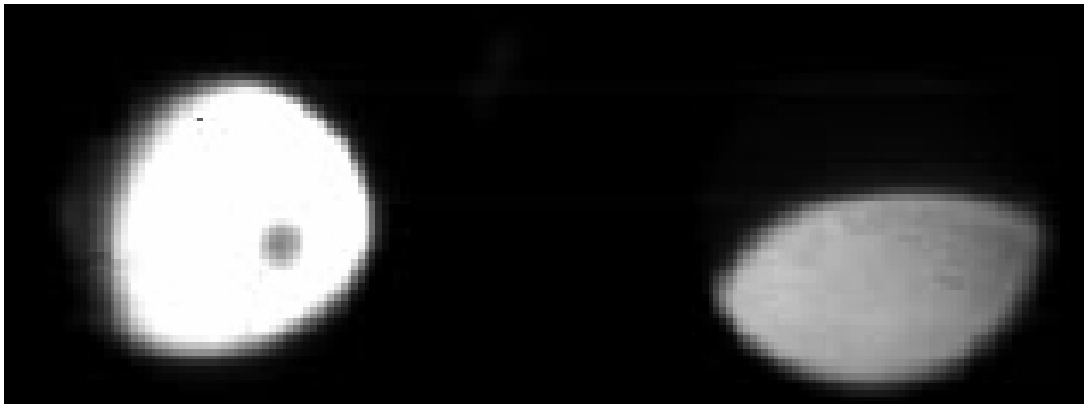

(a) Vignetting of the pupil plane by MIDI during the February 2003 experiment. Left image is UT3 (brightest spot, MIDI beam B), right image is UT1 (MIDI beam A). The different shape is due to vignetting.

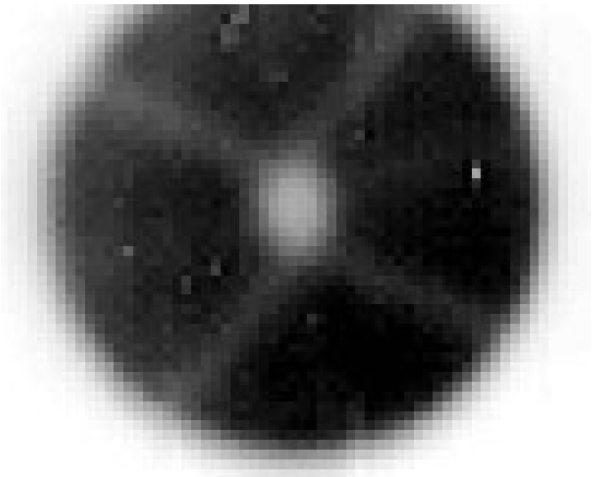

(b) Image of the pupil plane of MIDI obtained with UT3 in October 2003. Note the clear presence of the M2 mirror and the spiders holding this mirror. The read-out window for MIDI was not well centered on the image which left the upper part of the image unrecorded.

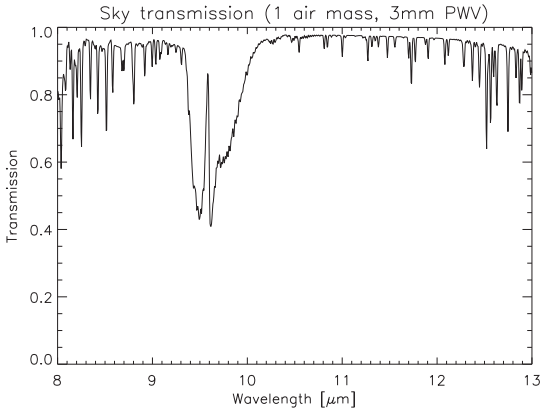

(c) Expected transmission of the atmosphere in the N band based on data obtained at Mauna Kea, taken from the Gemini web-site (http://www.gemini.edu/sciops/ObsProcess/).

Figure 1. Pupil plane images for MIDI and expected sky transmission of the N band for MIDI.

for a discrete signal:

$$P = \sum_{j=0}^{N-1} |V_j|^2 \ . \tag{4}$$

Noting $\widetilde{V_k}$ the Fourier transform of the time signal V_j:

$$\widetilde{V_k} = \sum_{j=0}^{N-1} V_j \exp^{(-2\pi ijk/N)} \ , \tag{5}$$

the power spectrum is given by:

$$\mathrm{PSD}_k = \frac{1}{\Delta f}\left|\widetilde{V_k}\right|^2 \tag{6}$$

in units of (ADU/pixel/sec)^2/Hz, with $\Delta f = \frac{1}{N\Delta t}$ in Hz and k the index of the frequency axis of the power spectrum. In many cases the time series has been split in M sub-series of each 100000 frames. In this case the PSDs are combined to a summed PSD S_k following:

$$S_k = \frac{1}{\Delta f M}\sum_{s=0}^{M}\left|\widetilde{V_k}\right|^2 \tag{7}$$

3.2. Definition of spatial and spectral windows

In order to reduce the amount of data to be handled we have defined several windows on the MIDI detector so as to keep only interesting regions. In Fig. 2 is shown the image of the detector with the definition of the spatial and spectral windows.

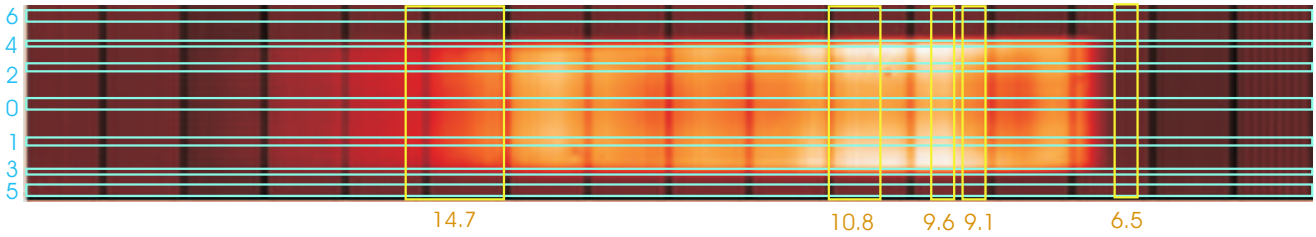

Figure 2. Image of the MIDI detector for one on-sky frame. Spectral information is coded in the horizontal direction (longest wavelength on the left side), while spatial information is in the vertical direction (image of the MIDI slit, 3 arcsecond long). Seven spatial windows have been defined, as well as five spectral windows.

3.2.1. Spatial windows

We have defined seven horizontal spatial windows, corresponding to five different positions in the sky plus two "off-sky" windows.

- Window #0 is on-axis. It is the window in which the contribution of the sky background should be the largest and the contribution from the VLTI thermal emission the smallest;
- Windows #1 and #2 are slightly off-axis, at about 0.65 arcseconds from the optical axis. A significant increase of the background emission can be noticed in these windows due to thermal emission of the VLTI;
- Windows #3 and #4 are chosen at the edge of the slit image on the detector. At this location it is expected that even more VLTI thermal background falls onto the detector, at the expense of sky background;
- Windows #5 and #6 are located outside the slit image. They receive no background emission and are thus only affected by intrinsic detector noise.

3.2.2. Spectral windows

Five spectral regions have been selected for the analysis. Three of them are located within the N band, which is the nominal bandwidth for MIDI: these are the windows in which the sky emission is well transmitted through the instrument down to the detector. We have chosen two of these windows in the "clean" part of the sky spectrum ($8.82 - 9.34$ μm and $10.4 - 11.2$ μm), as illustrated in Fig. 1(c), while the third one has been chosen inside the well-known ozone absorption line ($9.4 - 9.8$ μm). This may allow to detect a different behavior of the sky background at this wavelength because of increased optical depth. Finally, we have defined two windows outside the MIDI bandpass ($6.34 - 6.73$ μm and $14.4 - 15.0$ μm), where the sky emission is strongly attenuated by the low transmission of the instrument. These windows should be sensitive mainly to detector noise.

3.3. Spectrum of the background emission

The raw data obtained during the October 2003 run consist in dispersed images of the background. Useful information on the background emission can already be deduced by comparing the spectra at different elevations and for different spatial windows. In Fig. 3 are illustrated the spectra of the background emission at elevations of 80° and 50° for spatial windows #0, 2, 4 and 6.

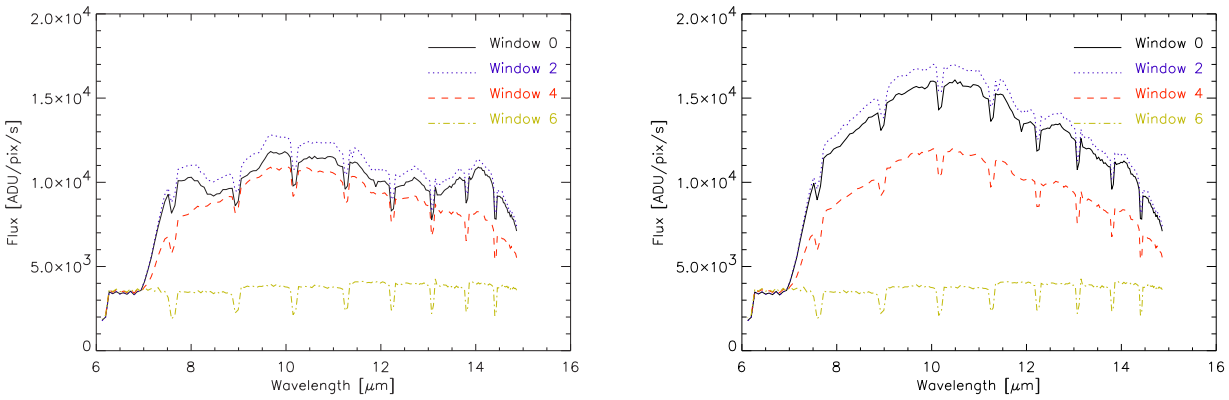

(a) 80° elevation.

(b) 50° elevation.

Figure 3. Cuts through the detector image for spatial windows #0, #2, #4 and #6, at elevations 80° (left) and 50° (right). The spectral structure of the background emission for windows #0 and #2 at 80° are indicative of an important sky contribution, while window #4 seems to be mainly affected by instrumental background (see text). At 50°, the three on-sky windows have the same spectral shape, indicative of a common background source (VLTI thermal emission).

At an elevation of 80°, the structure of the background emission changes between different spatial windows. The spectra for windows #0 and #2, which are quite similar, show a few characteristic features: the two bumps at 8 and 14 μm are most probably associated to the edges of the atmospheric N band, at which the sky emission significantly increases, while the bump at 9.6 μm is related to the contribution of the ozone layer, for which the optical thickness of the atmosphere is larger (see Fig. 1(c)). These bumps are only present in windows #0 and #2, meaning that these windows are more sensitive to sky emission, as expected. Window #4, on the other hand, seems to be mainly affected by VLTI thermal emission, which is expected to have a smoother spectrum. Finally, window #6 has a flat spectrum because it is not exposed to background light and is only affected by detector noise.

The bumps in the background spectrum are not present at low elevations (below 60°), for which the three on-sky windows have almost the same spectral shape. This suggests a common background source for these three windows. It is also noted that the level of background emission has significantly increased for windows #0 and #2 with respect to high elevations, while the level in window #4 is almost the same as before. All these elements suggest that for some reason, the pupil re-imaging was worse at low elevations and that more VLTI infrastructure emission (and less sky emission) was sent to the center of the field-of-view. From this analysis of the background spectra, we conclude that the observations at high elevations (above 60°) are more sensitive to the sky emission than those at lower elevations.

3.4. Power spectrum of the background emission

During the technical run, long exposures of about 1 to 2 hours have been obtained on-sky with a sampling time of about 6 msec. From these series of detector images, we have produced time series for the 35 domains formed by the intersections of the seven spatial windows with the five spectral windows. The intensities recorded by all pixels inside each rectangular box have been averaged to produce the time series. From these time series, we have then produced PSDs for the background emission, which are presented and discussed in the next sections.

3.4.1. Power spectrum at high elevations ($> 60°$)

In Fig. 4, we have plotted the PSD of the background emission registered at an elevation of 80° in the four different types of spatial windows (namely, windows #0, 2, 4 and 6) and for four different wavelengths. A few remarkable features are directly noticed in these PSDs:

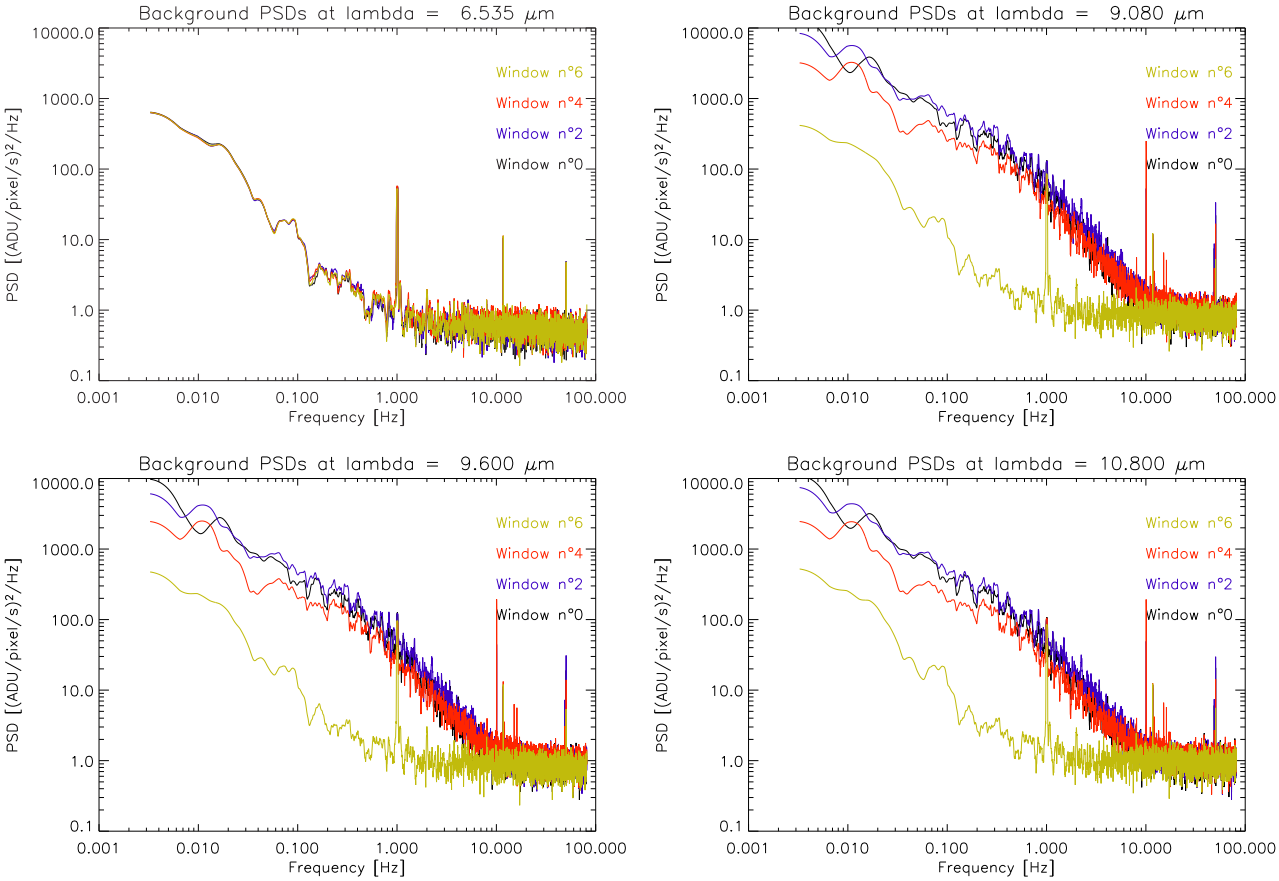

Figure 4. Power spectral densities (PSDs) of background fluctuations computed at an elevation of 80° in the four selected spatial windows, for four different spectral windows.

- Detection noise is an important source of fluctuations, as illustrated by the PSDs taken in window #6, which is not exposed to the sky and instrumental background. Spectral windows outside the MIDI bandwidth (i.e., outside the N band) are only affected by detection noise as expected. At high frequencies, the noise mainly consists in shot noise and has a flat (white) power spectrum, while, at low frequencies, fluctuations associated to the detector itself (drifts, etc) induce a large amount of noise in the recorded intensities. Detection noise can thus be approximated by a two-domain logarithmic power-law. At this particular elevation and moment in time, the slope of the power law at low frequencies is about -1.2 in logarithmic scale. For other measurements at high elevations, the recorded PSD had a log-log slope comprised between -1 and -1.7;

- The presence of background fluctuations is obvious at each of the three wavelengths inside the MIDI bandwidth: the PSDs of the three on-sky windows are largely above the PSD of the off-sky windows, in which only detector noise is present. This means that a large amount of fluctuation comes from the sky and/or instrumental background emission. Background fluctuations are dominant for frequencies below about 10 Hz, and can be described by a power-law with a logarithmic slope of about -1;

- Among the on-sky windows, window #4 has a slightly lower level of fluctuation. As window #4 is expected to be more sensitive to VLTI thermal emission and less sensitive to actual sky background, this indicates that the fluctuations are mainly associated to the sky background and not to the instrumental one. This will be confirmed below when discussing the PSDs at lower elevations;
- Several peaks can be observed in the PSDs. They are related to instrumental effects and will be discussed in section 3.5.

3.4.2. Power spectrum at low elevations ($< 60°$)

In Fig. 5 are plotted the PSDs for an elevation of 50°. Inside the N band, the PSDs of the on-sky windows are still above the detection noise, but their level has strongly decreased. The contribution of actual background fluctuations to the total noise is only noticeable between about 0.1 and 2 Hz and is only slightly larger than detection noise. In this frequency range, it can be fitted with a power law of logarithmic slope −0.8. Since we have shown in section 3.3 that most of the background emission is due to VLTI thermal emission at low elevation, and consequently that the level of sky background is much smaller, this suggests once again that instrumental background is much more stable than the sky background. The large fluctuations observed at high elevations are thus well due to the sky background itself.

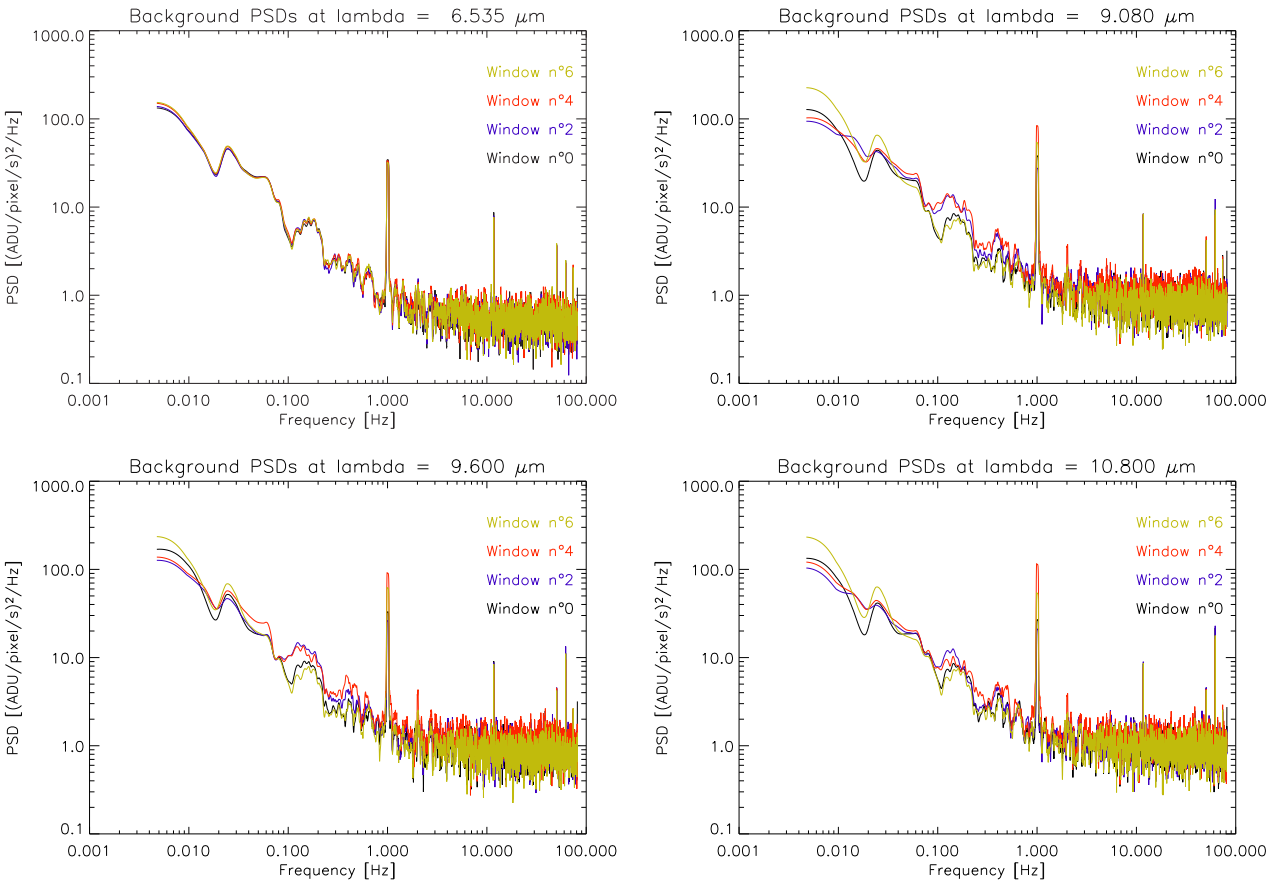

Figure 5. Power spectral densities (PSDs) of background fluctuations computed at an elevation of 50° in the four selected spatial windows, for four different spectral windows.

It can also be noticed that, both at 80° and 50°, the PSDs for the three spectral windows inside the N band are pretty similar. Indeed, background fluctuations show no evidence of wavelength dependence across the N

band. The slope and the precise shape of the PSDs are almost identical in these three spectral windows. There seems to be no influence from the ozone layer on the power spectrum either. Whether this behavior can be extended towards shorter wavelengths is of course debatable, but in first approximation the same slope for the power-law of background fluctuations could be used for the GENIE simulations in the L' band. This would also be in agreement with near-infrared measurements of the sky noise carried out in Siding Springs (Australia) in 1981 (see Ref. 3), for which the measured slope of the power-law was about -1.3 in the L band.

3.4.3. Discussion and consequences for VLTI mid-IR instruments

On the average a slope of -1 to almost -2 is measured for the log-log plot of power versus frequency. This is less steep than a Kolmogorov spectrum (slope is $-8/3$) and that for a random walk signal (-2). We should of course realize that our measurements were made in the image plane and therefore averages intensity fluctuations which exist over the pupil plane are note directly measured, and even averaged. This is consistent with a slope flatter than -2 (Fig. 6).

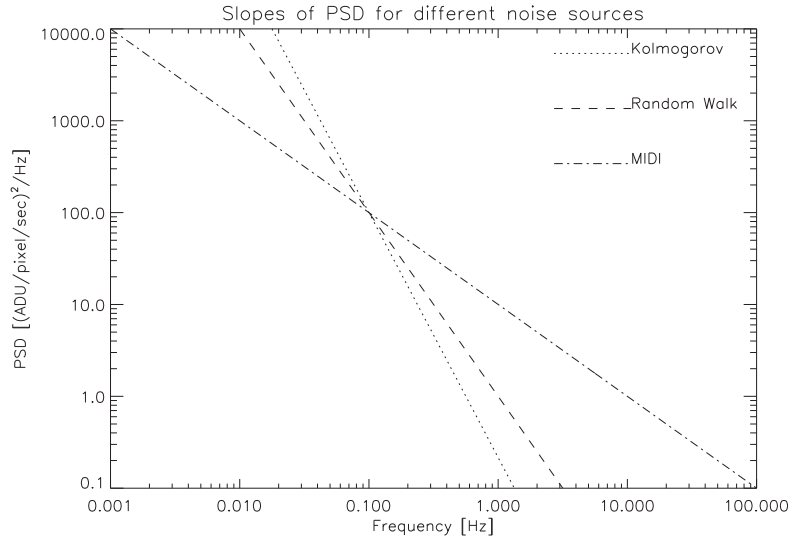

Figure 6. Comparison of the slope for different sources of statistics: Kolmogorov, random walk, and as measured with MIDI in the N band.

In order to study the effects of thermal background fluctuations on the performance of mid-infrared instruments, measuring the background characteristics in the image plane is the relevant method. On the other hand, if one wishes to study the distribution of background emission on the sky, measurements in the pupil plane might be more useful.

The PSDs displayed here show that the transition between fluctuation-limited and photon noise-limited regimes occur around 10 Hz. This is thus the typical frequency that should be used by the VLTI instruments in order to operate in background-limited performance (BLIP) range. In the case of GENIE, BLIP is not sufficient: the background emission must be calibrated with a very high accuracy (typically 10^{-4} to 10^{-5} for an L'-band nulling instrument). Let us try to estimate at which frequency chopping should be carried out in order to reduce the residual background fluctuations below a relative level of 10^{-4}. For this estimation, we will assume that a slope of about -1.5 in log-log scale is valid for the PSD of background fluctuations up to an arbitrary high frequency. This assumption is of course debatable since our data set does not show what happens to background fluctuations at frequencies above 10 Hz, and also because the extrapolation of the PSD observed in the N band towards the L' band is not fully justified. It might well be that the slope becomes steeper at higher frequencies (e.g. because of pupil averaging), which would make the following estimation pessimistic.

We have chosen an uninterrupted on-sky time series of 10 min at an elevation of 80° to compute the mean and standard deviation of the background emission, at a wavelength of 9.6 μm in dispersed mode. A mean

photon rate of 1.7×10^6 ph-el/pix/sec was found, with a standard deviation of 2.8×10^3. This standard deviation contains both the contribution of the photon noise and of the fluctuation noise. Since photon noise is given by the square root of the mean photon arrival rate, we can compute the contribution of fluctuation noise as:

$$\mathrm{RMS}_{fluc} = \sqrt{(2.8 \times 10^3)^2 - 1.7 \times 10^6}\,, \tag{8}$$

which gives $\mathrm{RMS}_{fluc} \simeq 2.5 \times 10^3$ ph-el/pix/sec for the given frequency range ($f > 3.3 \times 10^{-3}$ for a 10-min time series). This represents a fraction of 10^{-3} of the mean background emission. The variance of the residual background fluctuation for a chopping frequency f_c is given by the integral of the PSD for frequencies above f_c, and can be computed as follows:

$$\int_{f_c}^{\infty} \alpha f^{-1.5} \mathrm{d}f = 2\alpha {f_c}^{0.5} \tag{9}$$

$$= \left(\frac{f_c}{3.3 \times 10^{-3}}\right)^{0.5} \int_{3.3\times10^{-3}}^{\infty} \alpha f^{-1.5} \mathrm{d}f \tag{10}$$

with α a normalization factor for the PSD of background fluctuation (PSD$= \alpha f^{-1.5}$) and with the last integral having its square root equal to 2.5×10^3 ph/pix/sec (this is the standard deviation we have just computed above). In order to reach a precision of 10^{-4} in background subtraction, a chopping frequency of about 150 Hz must be used. The precision in background correction increases very slowly, proportionally to ${f_c}^{0.25}$, with our (pessimistic) assumption of a -1.5 slope up to an arbitrary high frequency. Classical chopping with the M2 mirror of the VLTI cannot be performed at such a high frequency, which implies that a more advanced chopping technique, allowing higher chopping frequencies, should be used for GENIE.

3.5. Instrumental effects

Let us briefly discuss the origin of the numerous peaks present in the PSDs of background fluctuations.

- Peaks at 1, 2 and 3 Hz are attributed to the MIDI closed-cycle cooler. The liquid helium expands close to the detector's cold finger. This process slightly modifies the temperature of the detector and hence the efficiency. This leads to a modulation in the detected intensity. A replica of this peak can be observed at 2 Hz, and sometimes even at 3 Hz;

- The strength of the 10 Hz peak seems to be correlated to the strength of the background fluctuations (peak is higher at high elevations) and only present in the off-axis PSD, which means that it is directly affecting the light beams, upstream the detector. Indeed, this peak is very intense for window #4, located at the edge of the slit, and almost absent from window #0 at the center of the slit. These two correlations seem to fit the model that something with the VLTI infrastructure partially blocks the sky light, and has a 10 Hz modulation. Since the vignetting increases with the elevation (probably an effect of the alignment of the beam) this peak is stronger for larger elevation, and also stronger for detector pixels which are more off-axis;

- Peaks at 30.1-30.3 Hz, as well as peaks at 62.3 and 74.0 Hz occurred consistently on one of the observing runs, but not on both. The most likely explanation is that the optical train was different, and that these frequencies are associated with modulation by components of the optical train;

- The 50 Hz, which is observed in both observing runs, is also observed for the experiments where a black-plate was inserted into the beam and also those which looked at the black-screen just in front of the detector. This suggest that the 50 Hz comes from the detector, and most likely from the read-out electronics. Alternatively other equipment may generate fields that effect the detector signal going through the MIDI cables.

Table 2. Census of the instrumental peaks present in the PSDs of the data acquired. If the peak is not always observed at exactly the same frequency but has a certain range of occurrence, it is presented in the frequency column as a range of frequencies. Rate of occurrence is represented by asterisks, each asterisk representing 10 % of the total sample. In addition to the peaks listed hereunder, a large number of peaks (16.0, 16.9, 18.0, 24.2, 26.0, 27.0, 36.0, 53.5, 55.1 and 71.6 Hz) were observed when engineers were present near the Coudé platform to conduct engineering tasks.

Frequency [Hz]	Run 1 Feb.03	Run 2 Oct.03	Occurrence	Origin
1.0	y	y	**********	Closed-cycle cooler
2.0	y	y	********	Replica of the 1 Hz peak
3.0	y		*	Only on 1 event
10.0-10.2	y	y	*****	Infrared emission from components in the optical path
11.8		y	***	
30.1-30.4	y		*****	Only for February 2003, not for October 2003
42.5	y		**	
47.3	y		***	
48.6	y		*****	
50.0-50.4	y	y	**********	Power line frequency
62.3		y	*****	Only for October 2003, not for February 2003
69.2-69.8	y		*****	
74		y	*****	Only for October 2003, not for February 2003
79.7-80.6	y		****	
83.5-83.6	y		****	

3.6. Spatial correlations

Thanks to the spatial extent of the MIDI slit, of about 3 arcseconds, we can investigate the spatial structure of the background emission. We have already seen that the emission peaks at the edges of the slit, where more VLTI thermal emission makes it into the field-of-view. This is illustrated in Fig. 7, where we have plotted the intensity of the background emission as a function of spatial position (i.e., along the vertical direction on the detector). This figure also illustrates that the structure of the background emission is flatter at lower elevations, which could also be attributed to more VLTI thermal emission falling onto the detector.

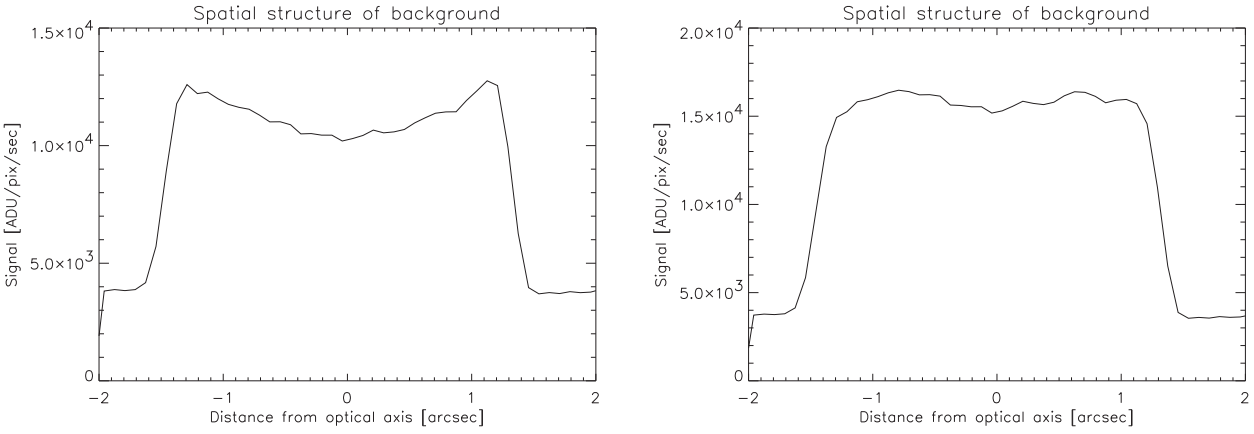

Figure 7. Spatial structure of the background emission, plotted along the slit direction for a wavelength of 9.5 μm, respectively at elevations of 80° (left) and 50° (right).

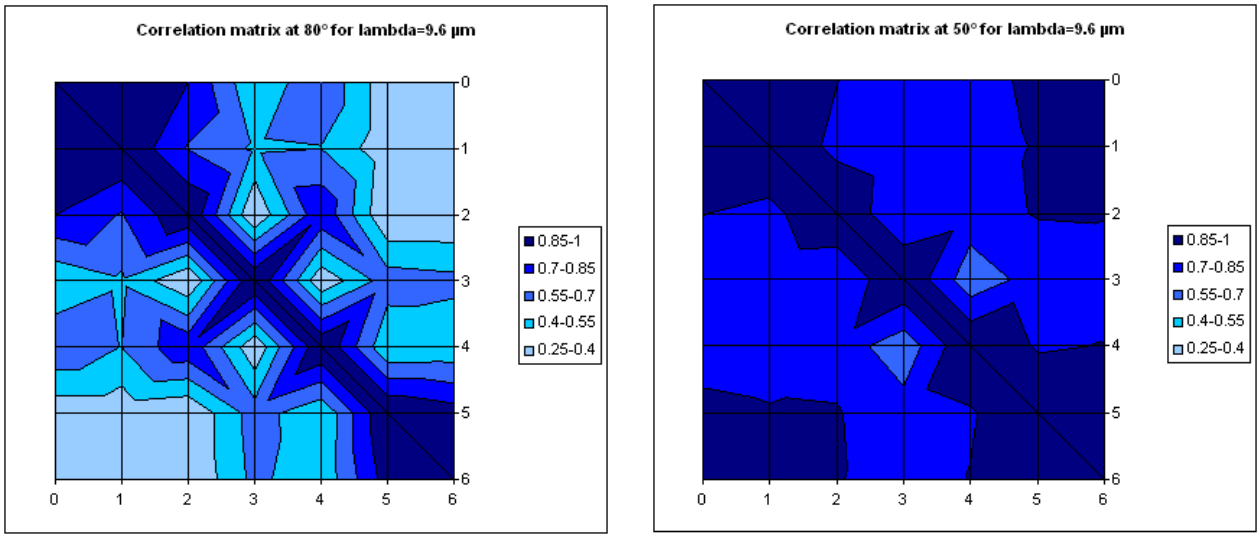

Figure 8. Study of correlation between time series for background emission in different spatial windows (as defined in Fig. 2), respectively at elevations of 80° (left) and 50° (right).

In Fig. 8 we have computed the correlation between the time series for background fluctuations between different spatial windows, at a wavelength of 9.6 μm and for two different elevations. This figure shows that the correlation between spatial windows is much larger at low elevations. This indicates that a common source of background emission affects all spatial windows, and once again suggests VLTI thermal emission to be the main contributor to the background at low elevations. Fig. 8 also shows that a higher correlation exists between spatial windows close together, as expected. For instance, the correlation between windows #0, 1 and 2 is quite high, while the correlation between windows #1 and 4, #2 and 3 or #3 and 4 is rather low (especially at high elevations). This means that some loss of correlation is already detectable in the background emission for an angular distance of 1 arcsecond, which would suggest classical chopping methods to use rather small off-axis angles for background measurements. However, the presence of more VLTI thermal emission in off-axis windows might be the actual reason for this loss of correlation. This statement should thus be refined with further sky background measurements when the Variable Curvature Mirrors come on-line and allow for a clean pupil re-imaging inside the MIDI instrument.

4. CONCLUSIONS

In this paper, we have characterized the fluctuations of the thermal background emission at the VLTI through its power spectral density. The PSD of background fluctuations can be described in terms of a broken power law with two regimes:

- a slope generally comprised between about -1 and -1.5 in log-log scale is identified at low frequencies ($f < 10$ Hz);
- a flat power spectrum is observed at frequencies above 10 Hz, characteristic of pure photon noise.

There are strong indications that the fluctuations at low frequencies are mainly due to the turbulence of the atmosphere outside the VLTI infrastructure.

In addition to the two-domain power law, a series of narrow peaks have been observed in the PSDs. These peaks are suspected to be due to instrumental effects, such as the 1 Hz cycle of the MIDI close cycle cooler, the 50 Hz frequency of the power line, as well as some mechanical vibrations in the VLTI optical train at various frequencies. The results are however limited by the unavailability of a pupil re-imaging device inside the VLTI

delay lines, which caused some spurious thermal light emitted by the VLTI infrastructure to reach the detector and add a significant contribution to the recorded background emission. Moreover, during the February 2003 run, the beams from UT1 and UT3 were vignetted, so receiving even more radiation from the infrastructure.

From this study, we are able to give a few recommendations for the chopping parameters to be used with the VLTI mid-infrared instruments. In order to reach background-limited performance with MIDI, a chopping frequency of about 10 Hz should be used, and in order to sample spatially correlated background regions in the sky, the chopping stroke should not be too large (not more than a few arcseconds*). These two results are in good agreement with a previous study by Käufl et al. (Ref. 4). In the case of GENIE, where a higher precision on background subtraction is mandatory, a higher frequency is needed for chopping (about 150 Hz according to our estimations), requiring a more advanced chopping method than classical chopping with the VLTI M2 mirror.

ACKNOWLEDGMENTS

O. A. acknowledges the financial support of the Belgian National Fund for Scientific Research. E. J. B. is supported by NEVEC, a project of NOVA, the Netherlands Research School For Astronomy. The authors would like to thank the MIDI consortium (principal investigator: Christoph Leinert; project manager: Uwe Graser; software manager: Walter Jaffe, co-PI: Rens Waters, Guy Perrin) to make this experiment possible.

REFERENCES

1. C. Leinert, U. Graser, L. B. F. M. Waters, G. Perrin, W. Jaffe, B. Lopez, F. Przygodda, O. Chesneau, P. A. Schüller, A. W. Glazenborg-Kluttig, W. Laun, S. Ligori, J. A. Meisner, K. Wagner, E. J. Bakker, B. Cotton, J. A. De Jong, R. J. Mathar, U. Neumann, and C. Storz, "Ten-micron instrument MIDI: getting ready for observations on the VLTI," in *Interferometry in Optical Astronomy II*, W. Traub, ed., *Proc. SPIE* **4838**, pp. 893–904, 2003.
2. P. Gondoin, O. Absil, C. V. M. Fridlund, C. Erd, R. H. Den Hartog, N. Rando, A. Glindemann, B. Köhler, R. Wilhelm, A. Karlsson, L. Labadie, I. Mann, A. J. Peacock, A. Richichi, Z. Sodnik, M. Tarenghi, and S. Volonte, "Darwin ground-based European nulling interferometer experiment (GENIE)," in *Interferometry in Optical Astronomy II*, W. Traub, ed., *Proc. SPIE* **4838**, pp. 700–711, 2003.
3. D. A. Allen and J. R. Barton, "A study of sky noise, 1.5-5 microns," *Astronomical Society of the Pacific, Publications* **93**, pp. 381–384, June-July 1981.
4. H. U. Käufl, P. Bouchet, A. Van Dijsseldonk, and U. Weilenmann, "A sky-noise measurement and its implication for ground-based infrared astronomy in the 10μm atmospheric window," *Experimental Astronomy* **2**(2), pp. 115–122, 1991.
5. R. Wilhelm and P. Gitton, "The VLTI environment and GENIE," in *Toward Other Earths: Darwin/TPF and the Search for Extrasolar Terrestrial Planets*, M. Fridlund and T. Henning, eds., **ESA SP-539**, pp. 659–664, ESA's Publication Division, 2003. ISBN 92-9092-849-2.
6. D. F. Buscher, J. T. Armstrong, C. A. Hummel, A. Quirrenbach, D. Mozurkewich, K. Johnston, C. S. Denison, M. M. Colavita, and M. Shao, "Interferometric seeing measurements on Mt. Wilson: power spectra and outer scales," *Applied Optics* **34**, pp. 1081–106, February 1995.

*This statement is still subject to caution because of the bad pupil re-imaging encountered during our technical runs.

Résumé

L'étude des systèmes planétaires extrasolaires a considérablement fleuri durant les vingt dernières années, stimulée par la découverte de poussières circumstellaires et de planètes extrasolaires autour d'étoiles de la séquence principale. Cependant, l'imagerie directe de ces systèmes planétaires n'a été jusqu'à présent possible que dans certains cas particuliers à cause de l'important contraste et de la faible distance angulaire entre les étoiles et leur environnement. Même dans ces cas favorables, les régions internes où les planètes rocheuses sont censées se former et où la vie pourrait se développer n'ont pu être étudiées jusqu'ici de par l'absence d'outils appropriés. L'interférométrie infrarouge est une technique très prometteuse dans ce contexte, car elle fournit la résolution angulaire nécessaire pour séparer le rayonnement des étoiles et de leur voisinage immédiat.

Le présent travail vise à développer les capacités d'imagerie à haute dynamique des techniques interférométriques pour la caractérisation des systèmes planétaires. Dans un premier temps, nous démontrons que les facilités interférométriques actuelles ont le potentiel de détecter la présence de poussières dans les premières unités astronomiques des disques de débris massifs autour d'étoiles proches. Nos observations de Véga avec le recombinateur infrarouge proche FLUOR installé sur l'interféromètre CHARA révèlent la présence de poussières chaudes responsables d'une émission représentant seulement 1/78ème du rayonnement stellaire en bande K. Dans le but d'étendre l'imagerie des systèmes planétaires à des disques plus ténus et aux planètes extrasolaires, nous étudions ensuite les performances au sol de futurs interféromètres en mode destructif en tenant compte de façon réaliste des effets de l'atmosphère. Nos simulations montrent qu'un instrument installé à l'interféromètre du Very Large Telescope de l'ESO et fonctionnant en mode destructif pourrait détecter des structures circumstellaires aussi faibles que quelques 10^{-4} fois le flux stellaire. Finalement, la troisième partie de ce travail se concentre sur l'implémentation de l'interférométrie en mode destructif sur des futures missions spatiales, dans le but de caractériser des planètes extrasolaires aussi petites que la Terre.

Mots-clés: disques circumstellaires – planètes extrasolaires – haute résolution angulaire – imagerie à haute dynamique – interférométrie infrarouge – Darwin

Abstract

The study of extrasolar planetary systems has thrived during the last two decades, stimulated by the discovery of circumstellar dust and extrasolar planets around main sequence stars. However, direct imaging of planetary systems has been possible in only very special cases so far due to the huge contrast and to the small angular separation between stars and their environments. Even for these favourable cases, the inner regions where terrestrial planets are expected to be forming and where life could develop have not been investigated yet due to the lack of appropriate tools. Infrared interferometry is a very promising technique in this context, as it provides the required angular resolution to separate the emissions from the star and its immediate neighbourhood.

The present work aims at developing the high dynamic range capabilities of interferometric techniques for the characterisation of planetary systems. As a first step, we demonstrate that current interferometric facilities have the potential of detecting dust in the first few astronomical units of massive debris disks around nearby stars. Our observations of Vega with the FLUOR near-infrared beam combiner at the CHARA Array reveal the presence of warm dust responsible for a K-band flux 78 times fainter than the stellar photospheric emission. In order to extend the imaging of planetary systems to fainter disks and to giant extrasolar planets, we investigate in a second step the performance of future ground-based nulling interferometers, taking into account atmospheric effects in a realistic way. Our simulations show that a nulling instrument installed at the ESO Very Large Telescope Interferometer would detect circumstellar features as faint as a few 10^{-4} of the stellar flux. Finally, the third part of this work focuses on the implementation of nulling interferometry on future space-borne missions, the goal being to characterise extrasolar planets with sizes down to that of the Earth.

Keywords: circumstellar disks – extrasolar planets – high angular resolution – high contrast imaging – infrared interferometry – Darwin